Innovative impeller design for double suction centrifugal pumps

Department of Mechanics, Mathematics and Management
MECHANICAL AND MANAGEMENT ENGINEERING
Ph.D. Programme
SSD: ING-IND/08–FLUID MACHINERY

Final Dissertation

Innovative impeller design for double suction centrifugal pumps

---

by
Tommaso Capurso

Supervisors:

Prof. Sergio Mario Camporeale

Prof. Marco Torresi

Ph.D Eng. Lorenzo Bergamini

Coordinator of Ph.D. Programme:
Prof. Giuseppe Pompeo Demelio

Course n°31, 01/11/2015-31/10/2018

To my Family

"Ideas are like rabbits
You get a couple and learn how to handle them, and pretty soon you have a dozen”
John Steinbeck

Acknowledgements

FIRST of all, I wish to thank with my most sincere gratitude Prof. Marco Torresi and Prof. Sergio M. Camporeale, who encouraged me all along this arduous journey and constantly inspired me with their distinctive strength and passion. I need to thank them for guiding me through this research and for believing in me when I myself was unhopeful. I express all my gratitude to Dr. Lorenzo Bergamini, who gave me precious suggestions throughout these three years and initiated me to the study of centrifugal pumps, of which I knew (and managed to do) very little when we met four years ago. I thank him for his patience with me and with my simulations.

I need to express special thanks to Prof. Rickard Bensow. I thank him for hosting me at Chalmers University during my period abroad, for introducing me to his kind research group and to share with me all their tools and knowledge about cavitation physics and models. I thank Carlo, Mohammed, Abolfazl and Ebrahim for the time spent in Goteborg after work.

My deepest thanks go to all the people who were beside me all along these three years at the Department of Mechanics, Mathematics and Management. I need to particularly thank Dr. Giovanni Caramia and Dr. Sergio Ranaldo for being always helpful with their precious suggestions about techinical machine problems. I am also grateful to Prof. Giuseppe Pascazio, who helped me to move my first steps in the field of cavitation, centripetal machine and to support me during my first publication. Thanks again for the opportunity to intensively use the Cluster for my numerical simulations.

I will never be able to express my gratitude and affection to Michele, my travelling companion, Pasquale, for sharing with me every day of these three hard and challenging years. I thank ETF team and all the people in my office. Their way of being encouraging and optimistic was reassuring and vital in all the moments in which I felt too weak to go on. My sincere gratitude goes to Master's and Bachelor's candidates for teaching me the importance of clearness and patience. I will take with me their unconsciousness, warmth and kindness.

My deepest and most intimate thanks are addressed to my family, for being always beside me with patience and love, and to Simona, for enjoying together the times of success and facing together the times of failure.

Summary

WORLD'S energy consumption is increasing year by year driven by the industrial and the tertiary sector, where most of the electrical energy is consumed by electrical motors (65%). The latter drive pumps (22%), most of which are centrifugal pumps (73% - world market = 20 billion euro per year). Due to their wide use, a great effort has been spent in the last decades in trying to improve the selection and the efficiency of pump systems with the aim to reduce their energy consumption. Besides, it has been found out that among all the rotating devices in a process plant, centrifugal pumps typically have the best overall potential for energy savings.

In this work, a variety of activities has been carried out in order to introduce innovation in the field of the hydraulic turbomachinery. Firstly, an innovative impeller for double suction centrifugal pumps will be presented and the techniques and methodology adopted to make this geometry feasible will be described. The novel geometry embodiment includes an innovative arrangement of the impeller vanes. The novel impeller has been designed with the purpose of retrofitting the impeller of a conventional pump, preserving its initial size and specific speed. Comparing the baseline and the novel geometry, the latter shows an improvement of the hydraulic efficiency (+1.2%) and a remarkable reduction of the slip phenomenon at the outlet of the impeller (σ- slip factor +8.5%). Thus, it is possible to provide a larger pressure rise with the same size of the pump or alternatively to choose a more efficient and compact system. Moreover, two different prototypes with different number of blades have been designed and their performance has been studied numerically, by means of 3D URANS simulations. Thereafter, they have been manufactured using the lost-foam casting technique, and tested experimentally thanks to the collaboration with the Hydraulic test rig of Nuovo Pignone, Bari (Italy). The novel design is now protected by a patent application.

Furthermore, given the increasing use of centrifugal pumps as turbines (PaT) in water distribution systems, the baseline and the novel geometry have been simulated as turbines with the aim to investigate their performance in reverse mode. This allowed a description of the slip phenomenon at the outlet of centripetal runners. This parameter has proved to be helpful for a 1D performance prediction model based on loss analysis, which works starting from the machine geometrical information; indeed, it allows to

minimize the error in predicting the characteristic curve at part-load (-8% error compared to Busemann and Stodola formulation) and at the best efficiency point (-6% error compared to models which neglect this phenomenon).

Finally, in order to enlarge the operative range of hydraulic pumps and turbines working under cavitating conditions, a passive cavitation control system (PCS) has been proposed. The aim is to guarantee a high performance level, comparable to the single-phase conditions, for these machines in the regions where they usually are affected by performance degradation. The system proposed has been applied to a symmetric 2D hydrofoil which is an archetype of the leading edge of a blade. Even though it appears to induce a loss of performance in terms of lift and drag, it is shown to be helpful for reducing the vapour volume cavity up to 93%. Thus, the introduction of this system to a real impeller (e.g., a centrifugal pump or a turbine) shall be positive to enlarge their operative field towards low suction pressure providing at the same time acceptable level of losses.

Sommario

La domanda mondiale di energia elettrica cresce di anno in anno, spinta dalla crescita del settore industriale e terziario. In questi settori, gran parte dell'energia elettrica è utilizzata da motori elettrici (65%) che trascinano pompe (22%), molte delle quali sono macchine centrifughe (73% - giro d'affari annuo di circa 20 miliardi). A seguito del loro ampio e sempre crescente utilizzo, negli ultimi anni sono stati numerosi gli studi volti alla riduzione dell'energia consumata dalle pompe centrifughe, sia perseguendo il miglioramento delle tecniche di selezione delle macchine per tipo di installazione, sia tentando di incrementarne l'efficienza intrinseca. È noto inoltre che, tra le diverse tipologie di macchine presenti negli impianti di processo, le pompe centrifughe sono quelle con il più ampio margine di miglioramento in termini di efficienza.

In questo lavoro di tesi sono presentate varie attività che introducono innovazione nel campo delle macchine idrauliche. Per prima è descritta una geometria innovativa di girante per pompe centrifughe a doppio flusso e sono illustrate le tecniche e le metodologie che hanno reso questa applicazione realizzabile. La nuova geometria proposta prevede la modifica della classica disposizione dei vani inter-palari di una girante di pompa centrifuga a doppio flusso, a vantaggio di una geometria alternativa di girante, che tuttavia ne conservi gli ingombri e il numero di giri specifico. Confrontando le due geometrie, la geometria qui proposta permette di migliorare l'efficienza idraulica del canale (+1.2%) e ridurre il fenomeno dello scorrimento all'uscita della girante (σ - slip factor +8.5%). Tale soluzione permette dunque di scegliere tra il fornire un valore di pressione più elevato, conservando la dimensione della macchina, o in alternativa optare per una pompa più efficiente e compatta, in grado di fornire le stesse prestazioni di una convenzionale. Sono stati inoltre progettati due prototipi con numero diverso di pale e le loro prestazioni sono state valutate mediante tecniche numeriche, con l'utilizzo di simulazioni 3D URANS. Successivamente le due giranti sono state realizzate mediante una particolare tecnica di micro-fusione (lost-foam casting) e testate sperimentalmente, in virtù della collaborazione con il laboratorio di macchine idrauliche di Nuovo Pignone, Bari, Italia. Visti i buoni risultati la nuova geometria proposta è stata protetta da un brevetto industriale.

In conseguenza del sempre crescente utilizzo di pompe centrifughe come turbine centripete nelle reti di distribuzione idrica, la nuova geometria è stata studiata numericamente come turbina, al fine di valutare eventuali benefici dal suo funzionamento inverso. Attraverso questo studio è stato possibile quantificare numericamente il fenomeno dello scorrimento per le turbine idrauliche centripete convenzionali. Tale parametro risulta utile se applicato all'interno di modelli 1D per la predizione delle prestazioni di pompe come turbine a partire dai soli dati geometrici; esso infatti permette di ridurre gli errori nella stima della caratteristica interna della macchina a flusso parzializzato (-8% rispetto alle formulazioni di Busemann e Stodola) e nel punto di massima efficienza (-6% rispetto al caso in cui il fenomeno è trascurato).

Infine, è stato proposto un sistema di controllo passivo della cavitazione con lo scopo di ampliare il campo operativo delle macchine motrici ed operatrici funzionanti in regime di cavitazione. L'intento è quello di conservare un valore delle prestazioni comparabile con la condizione monofase là dove queste subiscono un rapido decadimento. Tale sistema è stato studiato numericamente mediante l'applicazione a un profilo idrodinamico bidimensionale immerso. Nonostante si noti un peggioramento delle prestazioni del profilo, tale sistema permette una riduzione della bolla di cavitazione fino al 93%. Tale sistema, se applicato a pompe e turbine idrauliche, permetterebbe di ampliare il loro campo operativo in corrispondenza di ridotte pressioni di aspirazione sopprimendo i fenomeni di cavitazione con una perdita accettabile delle performance.

List of publications

International Journals

1. Capurso, T., Bergamini, L., Torresi, M. (2018). Design and CFD performance analysis of a novel impeller for double suction centrifugal pumps. *Journal of Nuclear Engineering and Design*. Elsevier.

2. Capurso, T., Stefanizzi, M., Torresi, M., Pascazio, G., Caramia, G., Camporeale, S.M., Fortunato, B., Bergamini, L. (2018). CFD analysis of the slip factor at the outlet of centripetal turbomachineries. *Water* (Under Review). MDPI.

International Conferences/Workshops with Peer Review

1. Lorusso, M., Capurso, T., Torresi, M., Fortunato, B., Fornarelli, F., Camporeale, S.M., Monteriso, R. (2017). Efficient CFD evaluation of the NPSH for centrifugal pumps. *Energy Procedia*. (Vol. 126, pp. 778–785). Elsevier.

2. Capurso, T., Lopez, M., Lorusso, M., Torresi, M., Pascazio, G., Camporeale, S.M., Fortunato, B. (2017). Numerical investigation of cavitation on a NACA0015 hydrofoil by means of OpenFOAM. *Energy Procedia*. (Vol. 126, pp. 794–801). Elsevier.

3. Capurso, T., Stefanizzi, M., Torresi, M., Pascazio, G., Caramia, G., Camporeale, S.M., Fortunato, B., Bergamini, L. (2018). How to improve the performance prediction of a pump as turbine by considering the slip phenomenon. *Proceedings*. (2(11), 683). MDPI.

4. Stefanizzi, M., Capurso, T., Torresi, M., Pascazio, G., Caramia, G., Camporeale, S.M., Fortunato, B., Monteriso, R. (2018). Development of a 1-D performance prediction model for pumps as turbine. *Proceedings*. (2(11), 682). MDPI.

5. Capurso, T., Lorusso, M., Camporeale, S.M., Fortunato, B., Torresi, M. (2018) Implementation of a passive control system for limiting cavitation around hydrofoils. *IOP Science* (In Press).

6. Capurso, T., Menchise, G., Camporeale, S.M., Fortunato, B., Torresi, M. (2018) Investigation of a passive control system for limiting cavitation inside turbomachinery under different operating conditions. *Energy Procedia*.

7. Capurso, T., Menchise, G., Camporeale, S.M., Fortunato, B., Torresi, M. (2018) CFD analysis of the performance a novel impeller for a double suction centrifugal pump working as a turbine. *ETC 13th* (Under Review).

Patents

1. Bergamini, L., Torresi, M., Capurso, T. (2017). Patent Application – 20180128271 - HIGH EFFICIENCY DOUBLE SUCTION IMPELLER.

List of Abbreviations

E

EC	European Community. 2, 3
EU	European Union. 2

L

LCC	Life cycle cost. 3

N

NPSH	Net Positive Suction Head. 6

Notation

Symbols

A	Area. 51
B	blade height. 47
H	head. 8
$H_{w,1}$	suction head losses. 8
$H_{w,2}$	discharge head losses. 8
N	points. 45
N_b	number of blades. 50
Q	flow rate. 6
Y	specific work. 7
γ	angle between the centre line and axial direction. 46
ω	angular velocity. 10
σ	slip factor. 13
ξ	blade blockage. 51
c_{line}	center line. 42
n	rotor speed. 6, 17
n_q	specific speed. 17

List of Figures

1.1 Global energy consumption. 1
1.2 Split of motor energy consumption, by application. 2

2.1 Single-stage volute pump with bearing frame, Sulzer pumps. 7
2.2 Schematic plant description. 9
2.3 Pump characteristics and system characteristic H_A (dashed curve). . . . 10
2.4 Velocity vectors at the inlet and outlet of an impeller. 11
2.5 Slip phenomenon. a Flow between the blades; b Secondary flow. 11
2.6 Streamline of rela- tive flow in a radial impeller (Navier-Stokes calculation). The broken lines correspond to blade-congruent flow. 11
2.7 Slip and deviation angle. 12
2.8 Cross-section of a blade passage in an axial flow impeller showing the tip leakage flow, boundary layer radial flow, and other secondary flows (adapted from Lakshminarayana 1981). 13
2.9 Photographs of a 10.2cm, 12° helical inducer with a lucite shroud showing the blade surface flow revealed by the running paint dot technique. On the left the suction surfaces viewed from the direction of the inlet. On the right the view of the pressure surfaces and the hub from the discharge. The flow is for 2000 rpm and ϕ_1=0.041. From Bhattacharyya et al. (1993). 14
2.10 Schematic showing secondary flows associated with a typical centrifugal pump operating at off-design conditions (adapted from Makay 1980). . 15
2.11 Schematic of a centrifugal pump with a single, vaneless volute indicating the disturbed and separated flows which can occur in the volute below (left) and above (right) the design flow rate. 15
2.12 Flow patterns in volute casings. 16
2.13 Secondary flow in a square channel a) cross section, b) velocity distributions in sections A-A and B-B (diagonal). 17
2.14 Pump types. 19
2.15 Double-entry vertical pump, Sulzer Pumps, n = 596 rpm, Q_{opt} = 2.4 m^3/s, H_{opt} = 48 m, P_{opt} = 1250 kW, n_q = 36. 20

2.16 Different pumps suitable as turbines. 23
2.17 Direction of rotation and flow in a pump running as turbine. 24
2.18 Velocity triangles at the inlet (2) and at the outlet of the runner (1). At the outlet both actual (solid line) and blade congruent (dashed line) velocity triangles are represented 25
2.19 Phase equilibrium of water 26
2.20 Phase equilibrium of water 27
2.21 Drag coefficient of a circular cylinder versus the Reynolds number and associated cavitation inception patterns and boundary layer state. 28
2.22 Cavitation patterns at inception in the vicinity of the critical Reynolds number for a circular cylinder (a) Re = 270 000, (b) Re = 290 000. . . . 29
2.23 Cavity patterns on a NACA 16012 hydrofoil at $Re = 10^6$ in strongly deaerated water. 31
2.24 An example of active control system for controlling shedding cavities. . 32
2.25 An example of passive control system for limiting cavities oscillation. . 32

3.1 Description of the errors for each quantity measured at the Hydraulic Laboratory, Nuovo Pignone, Bari. 38

4.1 Characteristic curve (H/H_{BEP} - Q/Q_{BEP}) of a conventional double suction impeller obtained by means of transient CFX simulations (Grid size $\cong$ 40 milion cells). Simulations performed by the Nuovo Pignone CFD team. 43
4.2 Front and side views of the 3D CAD model, which includes the inlet duct, the impeller and the double volute. 44
4.3 Flow chart of the design process. 45
4.4 γ inclination of the plane on which the relative velocity vector lies. . . . 46
4.5 w_{tan} and w function assumed for each point in which the path of the particle is discretized. 47
4.6 w_{mer}, w_{rad}, w_{ass} functions assumed for each point in which the path of the particle is discretized. 48
4.7 Velocity vector composition. 48
4.8 The outer diameter (D_2), the hub diameter (d_1) and s_{line} displayed in a radial-tangential plane. 49
4.9 View of the s_{line} on the $x - y$ plane. 50
4.10 View of the s_{line} in the meridional plane, which corresponds to the c_{line} curve. 50
4.11 3D CAD of the vane of a conventional geometry, in which the vane width (α) is highlighted. 51
4.12 Value of the width of the vane (α for a 7 blades impeller for each point in which the path of the particle is discretized. 52
4.13 Evolution of the blade blockage along the c_{line}. 52
4.14 Blade height, resulting from the imposed functions and calculation. . . 53
4.15 Representation of the vertices of the cross section area with tag number at the inlet of the vane. 54
4.16 Plot of the c_{line}, hub and shroud curves in the meridional plane. 55
4.17 Points added to improve the surface drawing of the vanes. 55

4.18 3D CAD of the novel blades. 56
4.19 Chamfer application to channels coming up from the two side of a double suction impeller. 56
4.20 Design tool to inspect channel interpenetration. It is possible to look at the reduction of the interpenetration by increasing the meridional velocity. 57
4.21 3D CAD of the first novel impeller prototype. 57
4.22 Computational domain used for simulating the novel geometry with periodicity equal to $2\pi/N_b$. 58
4.23 Description of the numerical domain and view of the static pressure contours inside the channel on iso-surfaces with constant meridional coordinate. 59
4.24 Trend of the rotary stagnation pressure inside the baseline and the novel geometry. 60
4.25 Relative velocity vector profiles. 61
4.26 Relative axial component of the relative velocity vector. 61
4.27 Relative radial component of the relative velocity vector. 62
4.28 Relative tangential component of the relative velocity vector. 62
4.29 An example of the Harmonic algorithm, on the right the design space with the initial values and on the right the points which minimize the error function. 64
4.30 Plot of the design points for the two impeller. 64
4.31 C_p of the first prototype, comparison between the analytical tool and the CFD results. 65
4.32 C_p of the second prototype, comparison between the analytical tool and the CFD results for Q_{BEP} and $0.8Q_{BEP}$. 66
4.33 3D CAD of the second prototype. 67
4.34 Impeller eye view of the 3D CAD and of the real impeller obtained by means of Lost-foam casting technology. 68
4.35 Outlet view of the 3D CAD and of the real impeller obtained by means of Lost-foam casting technology. 69

5.1 Grid of the entire geometry. 73
5.2 Grid of the impeller. 73
5.3 ψ-ϕ and η-ϕ curves calculated with CFX and OpenFOAM (Circles and rhombuses stand for ψ and η curves respectively). 75
5.4 View of the channels designed with a conventional design tool (up) and the novel impeller for double suction centrifugal pumps covered by patent application (down). 76
5.5 ψ-φ curves of the conventional impeller (CFX - Baseline) and the novel impeller obtained via numerical simulations (OF - Prototype) and experiments (Experiments Prototype); the dashed curves represent the iso-n_q which pass through the BEP of the two impellers. 77
5.6 Efficiency curves of the conventional impeller (CFX - Baseline) and the novel impeller obtained via numerical simulations (OF - Prototype) and experiments (Experiments Prototype). 77

5.7 Comparison of the characteristic curves between the conventional geometry (CFX - Baseline), the novel geometry (Experiments Prototype) and the novel geometry scaled to reach $H_{BEP}/H_{BEP,conv}$ and $Q_{BEP}/Q_{BEP,conv}$ equal to 1. 79
5.8 Contours of the dimensionless velocity magnitude c_2/u_2 at the outlet of the conventional (up) and novel geometry (down). 80
5.9 Averaged velocity profiles at the outlet of the traditional and new geometry along the axial direction, where u_2 is the tangential velocity at the outer diameter. 80
5.10 Iso-surfaces of the vortex criterion Q colored by pressure contours of the static pressure. 81
5.11 Contours of the vorticity field at the outlet of the traditional (up) and novel geometry (down). 82
5.12 View of the impeller outlet with three planes on which velocity and pressure have been calculated. 83
5.13 Averaged velocity profiles at the outlet of the baseline impeller. 84
5.14 Averaged velocity profiles at the outlet of the novel impeller. 84
5.15 Averaged pressure profiles at the outlet of the baseline impeller. 85
5.16 Averaged pressure profiles at the outlet of the novel impeller. 85
5.17 Averaged head (H) evolution over pressure value over a time equal to $(T/T_{final})/N_b = 1/7$ of a complete rotation. 86
5.18 Blade inclination. 86
5.19 Forces due to the interaction between the blades and the volute tongues. 87
5.20 Comparison of the RMS values of the torque (Nm) of the two prototypes. 87
5.21 Waterfall frequency spectrum (f_o = frequency of rotation) of the torque for different flow rate. 88
5.22 Plot of the mean frequencies for torque measured at BEP flow rate at 85%, 50%, 10% and near shut-off. 88
5.23 Plot of the mean frequencies for vibrations measured at BEP flow rate at 85%, 50%, 10% and near shut-off. 89
5.24 ψ-φ curves of the conventional impeller (CFX - Baseline), the first prototype and the second prototype obtained via experiments (Experiments Prototype); the dashed curves represent the iso-n_q which pass through the BEP of the three impellers. 89
5.25 ψ-η curves of the conventional impeller (CFX - Baseline), the first prototype and the second prototype obtained via experiments. 90
5.26 ψ-λ curves of the conventional impeller (CFX - Baseline), the first prototype and the second prototype obtained via experiments. 90
5.27 Comparison of the characteristic curves between the conventional geometry (CFX - Baseline), the second prototype (Experiments Prototype) and the second prototype scaled to reach $H_{BEP}/H_{BEP,conv}$ and $Q_{BEP}/Q_{BEP,conv}$ equal to 1. 91
5.28 Comparison of the RMS values of the torque (Nm) of the two prototypes. 92
5.29 Comparison of the RMS values of the bearing thrust along Vy (mm/s) of the two prototypes. 93

5.30 Comparison of the NPSH curves for the baseline, the first and the second prototype. 93

6.1 Representation of the geometry and with reversed flow. 96
6.2 Pressure coefficient (ψ) vs flow coefficient (ϕ) curves of the two geometries. 97
6.3 Efficiency (η) vs flow coefficient (ϕ) curves of the two geometries. . . . 98
6.4 Power coefficient (λ) vs flow coefficient (ϕ) curves of the two geometries. 98
6.5 $H/H_{BEP,conv}$ vs $Q/Q_{BEP,conv}$ curves of the baseline, the novel impeller scaled by D and the novel impeller scaled by both D and n. 99
6.6 Efficiency (η) and Power coefficient (λ) vs $Q/Q_{BEP,conv}$ curves of the baseline and the novel impeller scaled by D. 100
6.7 Rotary stagnation pressure inside the channel of the two geometries. . . 101

7.1 Plot of the hydraulic turbomachine performance in both pump and turbine operating modes. Head curves with runaway curve with respect to the pump BEP. 104
7.2 Plot of the hydraulic turbomachine efficiency in both pump and turbine operating modes with respect to the pump BEP. 104
7.3 Velocity triangles at the inlet (2) and at the outlet of the runner (1). At the outlet both actual (solid line) and blade congruent (dashed line) velocity triangles are represented. 105
7.4 Velocity triangles at the outlet of the runner. At the outlet both actual (solid line) and blade congruent (dashed line) velocity triangles are represented 105
7.5 Contours of the absolute pressure at the outlet of the runner with pressure gradient. 106
7.6 Velocity profiles of the axial velocity component at the outlet of the runner. 106
7.7 Velocity profiles of the tangential velocity component at the outlet of the runner. 107
7.8 Tangential velocity calculated at different distance from the trailing edge of the blade. 107
7.9 Evolution of the slip factor at various flow rate for a blade with low-medium specific speed and 7 blades. 108
7.10 Application of different definitions of the slip factor (σ =1, σ Busemann and σ Stodola) to a 1D model for predicting the PaT performance curve. 109

8.1 Main dimensions of the numerical domain expressed in mm. 111
8.2 Comparison of the pressure coefficient calculated with three different grids on the suction and pressure side of the NACA0009 hydrofoil with $\alpha = 2.5°$ in fully wetted flow condition with k-kl-ω turbulence model. The results are compared with experimental data. 112
8.3 Mesh details. 113
8.4 NACA0009 hydrofoil modified with the introduction of the slots and representation of the fluid flowing through the slots from the pressure to the suction side. 114

8.5 Pressure coefficient on the suction and pressure side of the NACA0009 hydrofoil with $\alpha = 2.5°$ in fully wetted flow condition with k-ω SST turbulence model. The results of the regular and modified geometry are compared with experimental data [1]. 115
8.6 Contours of the mean velocity around the regular and the modified foil. 115
8.7 Velocity vectors colored by mean pressure on the contours of the mean velocity inside the slots. 116
8.8 Pressure coefficient on the suction side of the NACA0009 hydrofoil with $\alpha = 2.5°$ and $\sigma = 0.81$ with the mass transfer model proposed by Schnerr and Sauer [2] and k-kl-ω turbulence model. The results are compared with experimental data [1]. 117
8.9 Contours of the velocity x component mean ($UMean\ X$) in order to highlight regions affected by flow separation. 118
8.10 Contours of the mean alpha water fraction, with and without the introduction of the passive cavitation control. 118
8.11 Contours of the mean static pressure, with and without the introduction of the passive cavitation control. 119
8.12 Trend of the C_L and C_D coefficients at various angles of attack of the regular and modified geometry. 119
8.13 Trend of the C_L/C_D coefficients at various angles of attack of the regular and modified geometry. 120
8.14 Trend of the volume of the cavity pocket at various angles of attack of the regular and modified geometry. 120
8.15 Contours of the mean liquid volume fraction, α_l, with and without the introduction of the passive cavitation control at different angles of attack. 121
8.16 Contours of the mean liquid volume fraction, α_l, with and without the introduction of the passive cavitation control at different angles of attack. 122

List of Tables

1.1 Losses in pumping system. 4

2.1 Definitions of specific speed. 17

4.1 Main information of the baseline geometry. 43
4.2 Slip factor and hydraulic efficiency calculated for a single blade vane at BEP 59
4.3 Lift coefficient for the three geometries. 66

5.1 Details of three computational grids, values of the hydraulic head at BEP of the centrifugal pump calculated via numerical simulations and results of the GCI method. 72
5.2 Summary of the boundary conditions used in OpenFOAM. 74
5.3 Percentage of the BEP mass flow rate at which the simulations have been run. 74
5.4 Slip factor for the baseline, first and second prototype after single-vane simulations 91

8.1 Comparison of the hydrofoil performance (lift and drag coefficient) in wetted simulation with $U = 20\ m/s$ compared with experimental data [10]. 113
8.2 Comparison of the hydrofoil performance (lift and drag coefficient) under fully wetted condition with and without the passive control system. 114
8.3 Comparison of the cavitation number (σ) and alpha water volume fraction (α_{vapour}) in cavitating flow condition with and without the passive control system. 116
8.4 Comparison of the hydrofoil performance at different angles of attack with and without passive cavitaion system control under multi-phase flow conditions. 117

8.5 Comparison of the hydrofoil performance (lift and drag coefficient) under two-phase condition with the passive control system for three different cases (k-ω SST, k-ω SST + Reboud correction and k-ω SST with periodic conditions). 121

Contents

List of Abbreviations **XI**

Notation **XII**

1 Introduction **1**
1.1 Motivations 1
1.2 Main objectives and thesis outline 4

2 Background **6**
2.1 Introduction 6
2.2 Centrifugal pumps 6
2.2.1 Basic principles and components 6
2.2.2 Net Positive Suction Head 8
2.2.3 Power and efficiency 9
2.2.4 Pump characteristic 10
2.2.5 Flow deflection caused by the blades. Slip factor 10
2.2.6 Secondary flows 13
2.2.7 Pump types 17
2.2.8 Double suction centrifugal pump 20
2.2.9 Attempts to improve centrifugal pumps performance 21
2.3 Pump as Turbine 22
2.3.1 Slip factor in centripetal hydraulic turbine 24
2.4 Cavitation inside hydraulic turbomachinery 25
2.4.1 Cavitation physics 25
2.4.2 Cavitation around hydrofoils 27
2.4.3 Methods for limiting cavitation phenomena 32

3 Numerical models and description of the experimental measurements **33**
3.1 Introduction 33
3.1.1 OpenFOAM 33
3.2 Numerical model for simulating centrifugal pumps 35

3.2.1 Governing equations and turbulence model 36
3.3 Description of the test rig for centrifugal pumps experimental tests . . . 37
3.4 Numerical models for simulating cavitating flows 37
3.4.1 Reboud correction 40

4 Design of the novel impeller - BTC **41**
4.1 Introduction 41
4.2 Design of the novel impeller 42
4.3 Design process 44
4.4 Geometry definition 44
4.4.1 Flow kinematics 44
4.4.2 3D cline 47
4.4.3 Geometry of channels 49
4.5 Numerical simulations of the single vane 56
4.5.1 Losses analysis 59
4.5.2 Velocity distributions 60
4.6 Design of the second prototype 62
4.6.1 Harmonic algorithm to select the nominal values 63
4.6.2 Pressure and Lift coefficients 63
4.7 Lost-Foam Casting 67
4.8 Conclusions 69

5 Performance evaluation and flow analysis of the novel geometry **71**
5.1 Introduction 71
5.2 Results and discussion 71
5.2.1 Domain 71
5.2.2 Boundary conditions 73
5.2.3 Numerical assessment 75
5.2.4 Performance evaluation 75
5.2.5 Flow analysis at the outlet of the impellers 79
5.2.6 Analysis of the pressure fluctuation 81
5.2.7 Torque and vibrations analysis of the first prototype 84
5.3 Performance of the second prototype 86
5.3.1 Scaled geometry 91
5.3.2 Slip facor calibration 91
5.3.3 Comparison of the torque, vibrations and $NPSH_{3\%}$ curves of the two prototypes. 92
5.3.4 Impact of the novel technology on carbon footprint 92
5.4 Conclusions 94

6 Novel Impeller as a Turbine **95**
6.1 Introduction 95
6.2 Results of the novel impeller working as a turbine 96
6.2.1 Scaled geometry 98
6.2.2 Comparison of the performance 100
6.3 Conclusions 100

7 Slip phenomenon at the outlet of hydraulic centripetal turbomachines 102
7.1 Introduction . . . 102
7.2 Characteristic curves . . . 103
7.3 Evaluation of the slip factor for conventional impeller . . . 103
7.3.1 Application to 1D model . . . 107
7.4 Conclusions . . . 108

8 Passive control system for limiting cavitation around hydrofoils 110
8.1 Introduction . . . 110
8.2 Case study . . . 110
8.3 Numerical domain and boundary conditions . . . 111
8.4 Passive control system . . . 113
8.5 Results and Discussion - Flow analysis with AoA = 2.5 deg . . . 114
8.5.1 Single-phase flow . . . 114
8.5.2 Multi-phase flow k-kl-ω . . . 116
8.5.3 Results and discussion at different AoA from 0 to 5 deg . . . 117
8.5.4 Multi-phase flow with k-ω, Reboud correction and hydrofoil cascade . . . 118
8.6 Conclusions . . . 121

9 Conclusions 123

Bibliography 128

CHAPTER 1

Introduction

1.1 Motivations

World's energy consumption is expected to increase by 30% from 2016 to 2030 in order to satisfy the demand associated with the increase in world's population and economy. Global energy usage is estimated to grow from 162,500 ZW in 2015 to 198,654 ZW in 2030 as illustrated in Fig. 1.1 [3]. In the next 15 years (by 2030), the industrial energy consumption alone is expected to reach 71,961 ZW (1.4% per year). Therefore, this concern must be addressed by the researchers and international society to overcome the energy deficit in the future and to identify the energy saving potential [4, 5].

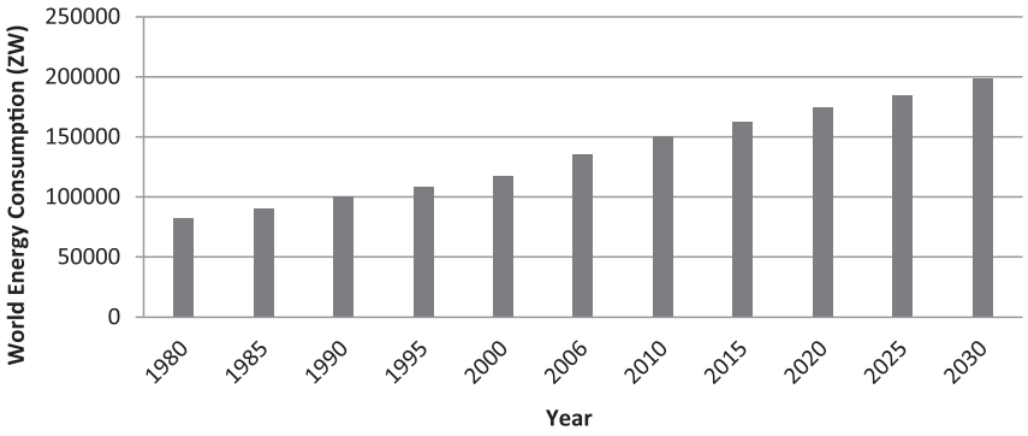

Figure 1.1: *Global energy consumption.*

A study by Dena (Deutsche Energie-Agentur GmbH), a German energy agency,

revealed that in the year 2000 industry in the European Community (EC) consumed 951 TWh of energy (1 TWh = 1 000 000 MWh) in total. About 69% of this energy and approximately 38% of the total energy consumption in the tertiary sector (230 TWh per year) was consumed by machines driven by electric motors, many of which were pumps [6].

Indeed, pumps consume 22% of total motor energy consumption, equivalent to 160 TWh per year. Hence, pumps are the single largest user of electricity in industry in the European Union (EU) accounting for 79 Mt of CO_2. It has been calculated that the energy wasted by all the pumps operating at present in the EU is 46 TWh on a yearly basis. What does this mean? The biggest power station within the Netherlands is the Eemscentrale in Delfzijl, with a generating capacity of 2400 MW. Even when operating 365 days per year, 24 hours per day at full capacity, the electricity production of this station would not amount to more than 21 TWh per year. So, the equivalent of more than two large or several smaller power stations permanently operating is needed just to generate all the energy that is wasted by pumps in Europe [6].

Among all the pumps, centrifugal pumps in the EU use 117 TWh per year of electricity [7]. This represents 73% of all pump energy consumption, see Fig.1.2, and besides it is a known fact that most centrifugal pumps have an overcapacity of 20–30% [8]. Depending on the industry, centrifugal pumps consume between 25% and 60% of a plant electrical motor energy [9]. For instance, the energy consumption due to centrifugal pumps with respect to electrical motor energy demand is 26% in chemical industry, 31% in pulp and paper industry and 59% in petroleum industry [9]. In the field of the energy production, centrifugal pumps are widely used in nuclear and steam power plants as main component of feed-water system (feed-water and primary pumps) and they are responsible for a significant energy absorption (e.g., up to 2% in Hualong One [10]) being directly driven by either steam engines or electrical motors [11].

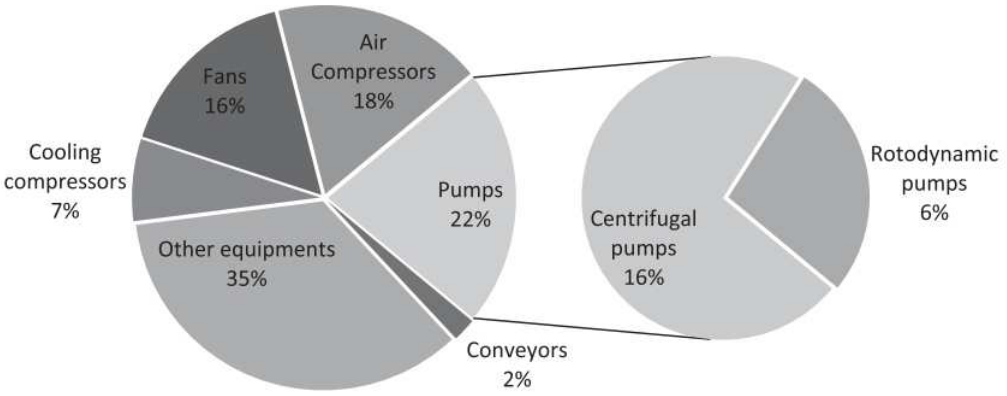

Figure 1.2: *Split of motor energy consumption, by application.*

The last report provided by the EC recommends policy options to improve the selection and maintenance of pumps to reduce their emissions. Thus, in the last decade many researchers and specialized companies worked to improve the energy efficiency of pumps spurred on by the EU. It is estimated an average pumpset cost of 200 €/kW and that an average pumpset runs for 4000 h per year with a lifetime equal to 20 years.

Less efficient pumps are expected to be replaced not earlier than 2020, due to their estimated 20-year lifetime. Following the instructions provided by the EC in 2000, it is estimated that a better pump selection could have given cost effective energy savings of 3% or 1.1 TWh/pa from 2000 to 2015, resulting in cumulative saving of 8.5 TWh/pa by 2015.

Furthermore, one of the key objectives of Europe 2020 growth strategy (Horizon 2020) is to improve the energy efficiency of drinking water and waste water utilities. The annual consumption of the utilities including energy used by pumps and water treatment plants in the USA and the EU is about 4% of the total energy consumption [12].

It is recognized that the largest energy savings are to be achieved through an improvement in the design and control of pump systems. As a consequence, promoting the use of more efficient pumps is very valuable, especially if the diffuse lack of expertise and time to identify best solutions is considered. It is however also recognized that giving simple guidance on the selection of pumps by efficiency, does present particular challenges, in particular that:

- Efficiency may fall off as fast as operation moves from the Best Efficiency Point;
- Pump Efficiency will deteriorate over time;
- Pump operation, and hence efficiency, are determined by principally two parameters (head and flow), in addition to other factors such as properties of the fluid, impeller design and motor speed selected. This compares unfavorably with labeling schemes for products such as lights or electric motors, where the definition of typical operation and hence rated efficiency are much simpler.

A survey of users and specifiers showed the following general order of priorities when considering the purchase of new pumps: 1) time concerns, price, known name, deliveries; 2) reliability, maintenance; 3) energy costs. But in terms of overall costs of ownership, the order of importance of factors is actually the opposite of the priorities listed, Recent studies about Life Cycle Cost (LCC) of pumping system have shown that approximately 50% of the total LCC stems from the energy costs, the remaining part is for maintenance and purchase [9].

The pumping system consists of a pump unit, suction reservoir, delivery reservoir, pipe arrangements and the liquid to be pumped. As well known energy cannot be transformed from one useful form to the other without losses. Losses occurred at each element of the pumping system, (from the transformer to the piping system) was studied by U.S. Department of Energy [13]. U.S. Department of Energy (Table 1.1) shows that the maximum possible losses in the pumping system are due to inefficient piping system design contributing to about 40–50% of losses. The practical efficiency is: for pumps 85–90%; for electric motors (Eff1) more than 90%, and for VFDs (Variable frequency drive) around 95–98% respectively.

In addition, it has been pointed out that, among all the rotating devices in a process plant, centrifugal pumps typically have the best overall potential for energy savings [9].

Table 1.1: *Losses in pumping system.*

Component in pumping system	Efficiency (%)	Losses (%)
Piping system	50-60	40-50
Pump	85-90	10-15
Coupling	99	1
Motors	>90	<10
VFD cables	98	2
VFDs	95-98	2-5
Transformers	99	1

1.2 Main objectives and thesis outline

In this scenario the design of an innovative impeller for double suction centrifugal pumps (BTC impeller) has been proposed, since this kind of centrifugal pumps is widely used (30%) in the following sectors: oil&water pipeline, refinery&petrol-chemical, power generation, onshore and offshore oil&gas production and fire fighting. The main objective has been to introduce a completely new approach for designing novel impellers for double suction centrifugal pumps. The basic idea is to change the vane arrangement of conventional impellers with the aim to increase the number of blades at their outlet. The new vane has lower length and higher hydraulic diameter. Thus, the novel geometry could retrofit conventional impellers allowing the improvement of the performance in terms of hydraulic efficiency and slip phenomena, providing a higher pressure rise and more efficient energy transfer from the impeller to the fluid or, alternatively, it can be downsized with the aim to guarantee the same performance of the conventional one with a more compact system.

A brief outline of this work is described. In the next chapter some background information about centrifugal pumps, pump working as turbine and cavitation inside turbomachinery will be presented. Then the numerical models and the solvers used to analyze the performance of impellers and 2D hydrofoil under cavitation will be described. The fourth chapter deals with a detailed description of the novel geometry. The techniques and the methodologies applied for drawing the new vanes and to overcome design issues due to the innovative arrangement will be presented. After that, a second impeller will be designed by reducing the number of blades and keeping the same specific speed and flow conditions at at the inlet of the volute. In the fifth chapter, the performance of the novel design will be analyzed both numerically, through a detailed flow analysis, and experimentally, thanks to the experiments carried out at the hydraulic test rig of Nuovo Pignone, Bari, Italy.
Given the above mentioned increasing application of pats to water distribution systems and pumped hydroelectric storage systems, in the sixth chapter the novel impeller will be studied working as a turbine. Besides, this will allow to describe the slip factor at the outlet of centripetal runner in order to improve the performance prediction of PaT.
The eight chapter is dedicated to cavitation studies. In order to enlarge the operative range of a centrifugal pump a new passive control system (PCS) will be proposed for limiting cavitation phenomena inside turbomachineries. A preliminary study will be carried out by modifying a 2D hydrofoil. Moreover, different angles of attack will be studied to reproduce centrifugal pumps off-design conditions and the performance

evaluated.
Finally some important conclusions and future work will be summarized.

CHAPTER 2

Background

2.1 Introduction

In this chapter the main background information about centrifugal pumps (2.2), pumps working as turbines (2.3) and cavitation inside hydraulic turbomachinery, in particular around hydrofoils, will be presented [14–16].

2.2 Centrifugal pumps

Centrifugal pumps are used for transporting liquids by raising a specified volume flow to a specified pressure level. Pump performance at a given rotor speed is described by the rate of flow delivered, the pressure rise achieved, the power absorbed at the coupling, the efficiency and the $NPSH$. Depending on the application, a broad variety of pump types is offered by the market. All of these have at least one impeller and a collector where most of the kinetic energy at the impeller outlet is converted into static pressure. Different models of impellers, diffusers, volutes and inlet casings are available to build radial, semi-axial or axial, single- or multistage, pumps mounted in horizontal or vertical position – as most suitable for the specific application.

2.2.1 Basic principles and components

The energy transfer in turbomachines is invariably based on hydrodynamic processes for which characteristically all pressure and energy differences are proportional to the square of the circumferential rotor speed (u_2). By contrast, positive displacement pumps (e.g., piston pumps) essentially deliver the same volume V_{stroke} at each stroke independently of flow velocity or rotor speed n. The flow rate then becomes Q$= nV_{stroke}$; the pressure rise results solely from the imposed back pressure. Positive displacement

pumps are characterised by an operation that moves fluid by trapping a fixed volume, usually in a cavity, and then forces that trapped fluid into the discharge pipe. Positive displacement pumps are usually selected for their ability to handle high viscosity fluids at high pressures and relatively low flows as their efficiency is not affected by pressure. Centrifugal pumps benefit from a simple design with few moving parts, resulting in lower maintenance requirements and costs. This makes them suited to applications where the pump is used often or is even continuously run. The simplicity of the construction also makes centrifugal pumps easy to produce in many different materials including plastics and cast iron for lighter duties, and bronze and stainless steels for more corrosive or hygienic application. The centrifugal pump design is also very compact in comparison to other pump types that produce the same output levels, making them a good option when space saving is an issue.

A centrifugal pump (Fig. 2.1) is essentially composed of a casing, a bearing housing, the pump shaft and an impeller. The liquid to be pumped flows through the suction nozzle to the impeller. The overhung impeller mounted on the shaft is driven via a coupling by a motor. The impeller transfers the energy necessary to transport the fluid and accelerates it in the circumferential direction. This causes the static pressure to increase in accordance with kinetics, because the fluid flow follows a curved path. The fluid exiting the impeller is decelerated in the volute and the following diffuser in order to utilize the greatest possible part of the kinetic energy at the impeller outlet to increase the static pressure. The diffuser forms the discharge nozzle.

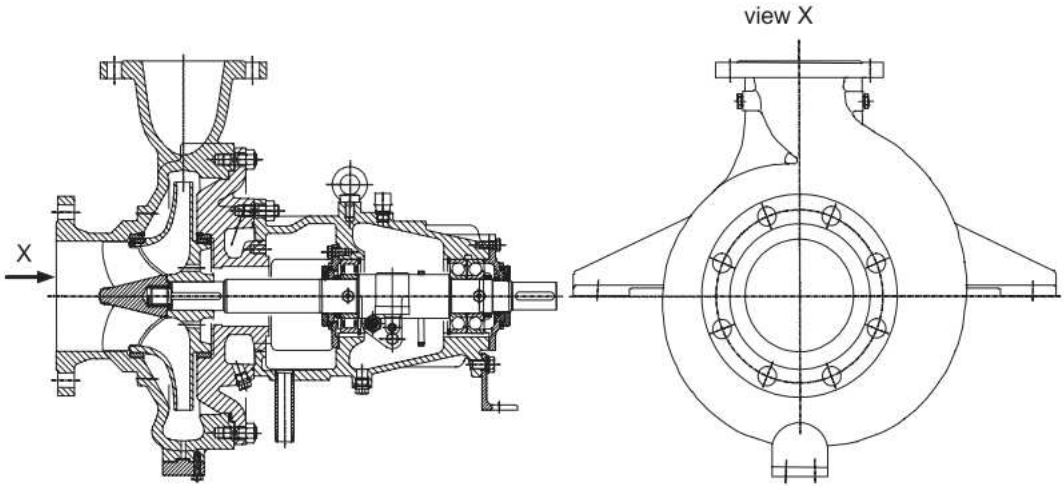

Figure 2.1: *Single-stage volute pump with bearing frame, Sulzer pumps.*

The specific work Y is the total useful energy transmitted by the pump to the fluid per unit of mass. Y is measured between the suction and the discharge nozzle. Y is identical to the total useful (isentropic) enthalpy rise Δh_{tot}. In incompressible flow we have $Y = \Delta h_{tot} = \Delta p_{tot}/\rho$. In practice the head, $H = Y/g$, is commonly used (also termed "total dynamic head"). It has to be comprehended as specific energy unit (or specific work):

$$Y = \Delta h_{tot} = \frac{p_{2,tot} - p_{1,tot}}{\rho} = gH \tag{2.1}$$

The total pressure consists of the static (or system) pressure p, the pressure corresponding to the geodetic head $\rho g z$ and the stagnation pressure $1/2\rho c_2$. The total dynamic head of a pump measured between the suction and the discharge nozzles results from the difference of the total pressures expressed as heads $H = H_2 - H_1$ (subscript 2 = discharge nozzle; 1 = suction nozzle).

$$H = \frac{p_{2,tot} - p_{1,tot}}{\rho g} + z_2 - z_1 + \frac{c_2 - c_1}{2g} \tag{2.2}$$

In this equation all energies are expressed as "energy heads": the static pressure heads $p/(g\rho)$ measurable at the suction or the discharge nozzle, the potential energy z and velocity heads $c_2/2g$. Head and specific work are independent of the density or the type of the medium. Thus a pump (in theory) produces the same head when transporting water, mercury or air. But by no means does it create the same pressure rise $\Delta p = \rho g H$ that could be measured by a manometer. All pressure differences, powers, forces and stresses are proportional to the density. In order to ensure the specified volumetric flow rate through a given pumping plant, the pump must deliver a certain head which is called the required head H_A of the plant. It is calculated from Bernoulli's equation taking into account all head losses in the system (except losses in the pump), see Eq.2.3. During steady operation the head of the pump equals the required head of the plant: $H = H_A$:

$$H_A = \frac{p_{2,tot} - p_{1,tot}}{\rho g} + z_2 - z_1 + \frac{c_2 - c_1}{2g} + H_{w,1} + H_{w,2} \tag{2.3}$$

where $H_{w,1}$, $H_{w,2}$ are the head losses in suction and discharge pipes respectively.

2.2.2 Net Positive Suction Head

When the pressure in a liquid drops below the vapor pressure, a portion of the fluid will evaporate. Excess velocities due to the flow around the blade leading edge cause a local pressure drop, which may lead to such partial evaporation. This phenomenon is called "cavitation" and it will be discussed in detail in paragraph 2.4. Extensive cavitation can impair the performance or even interrupt the flow. Therefore the approach flow conditions at the suction nozzle are an important criterion for the layout and selection of a pump. The relevant parameter is the "net positive suction energy" $NPSE$ or the "net positive suction head" $NPSH$. It is defined as the absolute suction head $H_{1,abs}$ minus the vapor pressure expressed as head $p_v/\rho g$. We distinguish between the (usually measured) $NPSH$ of the pump which is necessary in order to fully or partially suppress cavitation ("$NPSH$ required" or $NPSH_R$) and the $NPSH$ available in the plant ($NPSH_A$). Since the vapor pressure p_v is given in the water/steam tables as an absolute pressure, absolute pressures must be inserted into eqs. 2.4 and 2.5 for calculating the $NPSH$. From Bernoulli's equation we can calculate the absolute pressure at the highest point of the impeller situated at a distance a above the rotor axis. This pressure must never be allowed to fall below a level at which an unacceptably large volume of vapor would form at the impeller inlet due to cavitation. Any given pump has its required $NPSH_R = f(Q)$, which corresponds to a specific amount of cavitation. The $NPSH_A$ or the liquid level z_e which is necessary for the plant to operate properly must be calculated from the condition $NPSH_A > NPSH_R$, eq.2.6.

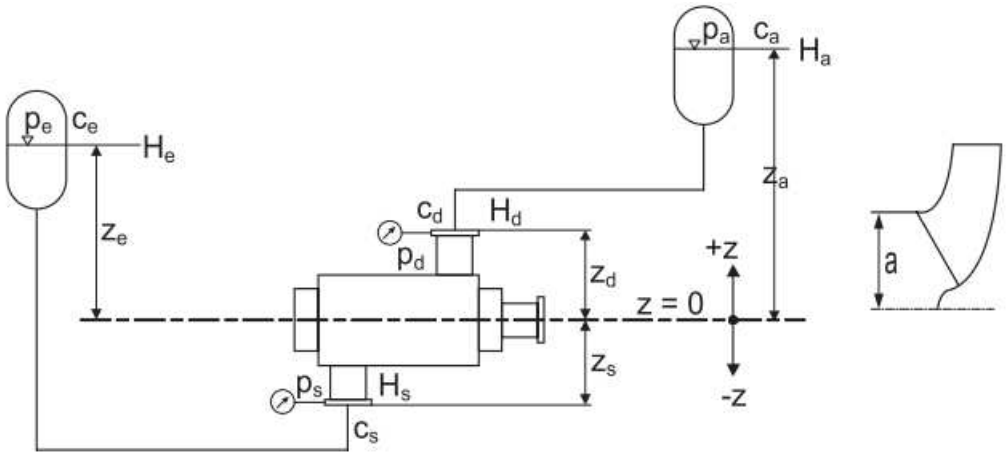

Figure 2.2: *Schematic plant description.*

$$NPSH_R = \frac{p_{1,abs} - p_v}{\rho g} - \frac{c_1^2}{2g} + z_1 \tag{2.4}$$

$$NPSH_A = \frac{p_{e,abs} - p_v}{\rho g} - \frac{c_e^2}{2g} + z_e - H_{w,1} \tag{2.5}$$

$$z_e = NPSH_R + H_{w,1} - \frac{p_{e,abs} - p_v}{\rho g} - \frac{c_e^2}{2g} + a \tag{2.6}$$

- if f_{ze} calculated from eq.2.6 results as negative, this value is the maximum admissible geodetic suction lift: $|z_{s,geo,max}| = -z_e$.
- if eq.2.6 yields a positive value, the pump needs a geodetic suction head, which means that the liquid level must be above the pump. As demonstrated by eq.2.6, this always applies to the pumping of saturated (boiling) liquids, because in that case $p_{e,abs} = p_v$.

With the exception of some special pump types, centrifugal pumps must be filled with liquid for start-up; they are not "self-priming" and thus cannot evacuate the air from the suction pipe. Types of self-priming pumps include side channel and liquid-ring pumps. Radial impellers are sometimes combined with one side-channel stage in order to allow self-priming of radial pumps.

2.2.3 Power and efficiency

Since the specific work represents the energy transferred per unit mass, the useful power P_u of a pump is obtained by multiplying the transported mass flow $m = \rho Q$ by the specific work Y:

$$P_u = \Delta p Q \tag{2.7}$$

The power P needed at the coupling is greater than the useful power because it includes all losses of the pump. The ratio of both values is the pump's efficiency η:

$$\eta = P_u / P \tag{2.8}$$

2.2.4 Pump characteristic

When the flow rate of a pump varies, the head, the power consumption and the efficiency change too. Plotting these quantities against the flow rate, we obtain the "pump characteristics", Fig.2.3. At a certain flow rate the pump efficiency has a maximum value called the "best efficiency point" (BEP). The pump is designed for this BEP which is characterized by Q_{opt}, H_{opt}, P_{opt} and η_{opt} at a given speed. The operation point of a pump is invariably where the head generated by the pump equals the head required by the plant: $H = H_A$. In other words it is at the intersection of the pump characteristic with the system characteristic, (Fig.2.3).

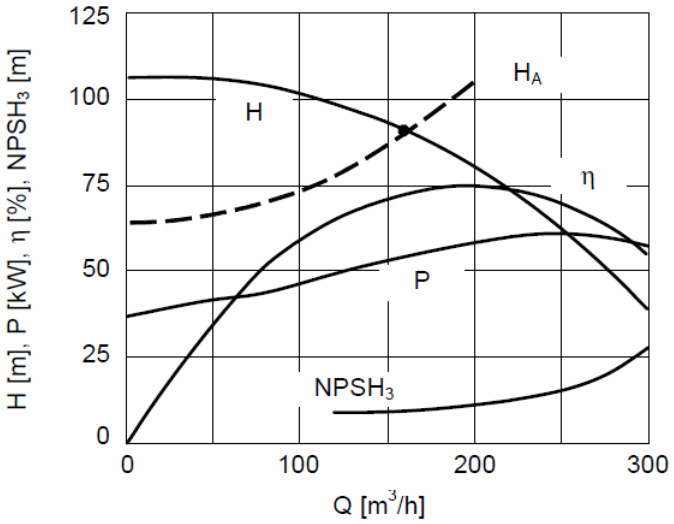

Figure 2.3: *Pump characteristics and system characteristic H_A (dashed curve).*

2.2.5 Flow deflection caused by the blades. Slip factor

When applying the theorem of conservation of momentum, only the average velocities prevailing at the chosen control surfaces are considered . The complicated flow conditions in the interior of the control volume are ignored. The conservation of momentum consequently fails to show how the flow observed at the control surfaces is generated and how the impeller, its outlet width and blade angles must be designed so that these average velocities actually occur at given values of Q and ω. The blade moment results from blade forces which can be imagined as an integral of the pressure and shear stress distributions over the blade surface – much like the lift of a wing is integrated from its pressure distribution. If a blade (or a wing) is to generate a net force, this integral obviously cannot be zero, i.e., greater pressures must be present on the blade pressure surface than on the suction surface. Since the pressure distributions in a turbomachine solely result from the velocity distributions around the blades, it must be concluded that different flow conditions are present on blade pressure and suction surfaces. Hence the flow is not able to follow the blades exactly (the flow is not "blade-congruent"). The work transfer is only made possible through a deviation between the blade and flow angles. In Fig.2.4 a the flow angle β_2 is therefore represented smaller than the blade angle

β_{2B}. The described phenomenon is quantified by the "slip factor" or by the "deviation angle" $\delta = \beta_{2B} - \beta_2$. Both terms implicitly assume the idea of a blade-congruent flow and consider the deviation of the real flow from the blade outlet angle.

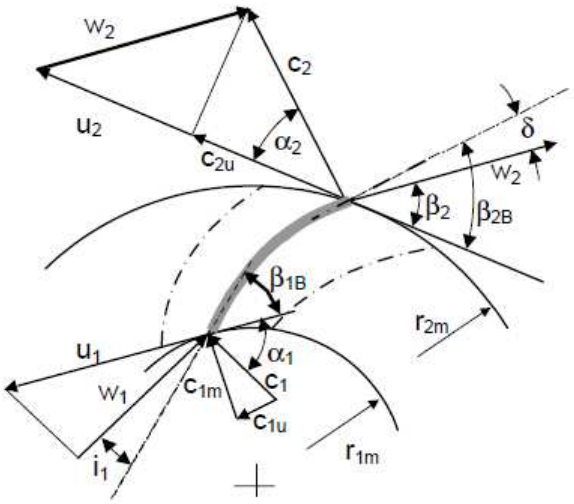

Figure 2.4: *Velocity vectors at the inlet and outlet of an impeller.*

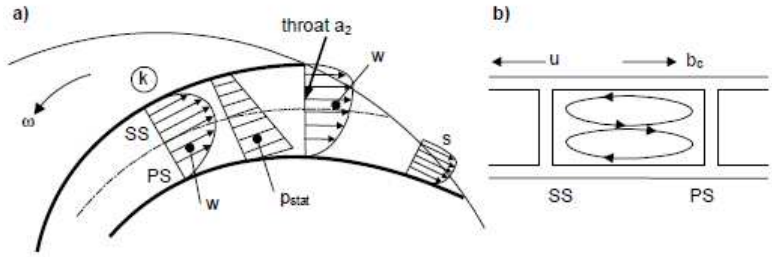

Figure 2.5: *Slip phenomenon. a Flow between the blades; b Secondary flow.*

Figure 2.6: *Streamline of rela- tive flow in a radial impeller (Navier-Stokes calculation). The broken lines correspond to blade-congruent flow.*

As will be discussed in detail in Chap. 5, the flow distribution at the impeller out-

let and consequently the mean flow angle and the slip factor results from a complex equilibrium of forces. The deviation of the real flow from the blade congruent flow is essentially influenced by the following mechanisms:

- The velocity differences between the pressure and suction surfaces of the blades are induced by the transfer of work, Fig.2.5a, Profile k.
- The Coriolis acceleration b_c is opposite to the direction of rotation and causes a secondary flow which transports fluid towards the pressure surface, thus reducing the flow angle β (refer to Fig.2.4a).
- Immediately downstream of the trailing edge, the differences in static pressure acting on the blade pressure and suction surfaces vanish, because pressure differences in the free flow can only be maintained through different streamline curvature. The velocity distribution already adapts in the triangular section downstream of the throat at the impeller outlet in a way that this outflow condition is satisfied and that the circulation around the trailing edge is not excessive. Ahead of the throat, in the actual impeller channel, the flow is guided more effectively and deviates less from the blade angle (refer to profiles k and s in Fig.2.5a). Figure 2.6 illustrates these effects by the paths of the relative velocity calculated with a 3D-Navier-Stokes program. Up to the throat a_2 the flow paths are almost congruent with the blade contour marked by broken lines; in the inclined section after a_2 the flow paths curve in the direction of the pressure surface and the flow angle β is correspondingly reduced toward the impeller outlet. With backward curved blades, the slip factor is to a large extent created in the triangular section at the impeller outlet. Conversely, with radial blades (having inlet and outlet angles of 90°) the slip factor is primarily caused by the Coriolis force.

Since these flow processes cannot be calculated by simple means, empirical data have to be used when calculating the flow outlet angles according to the streamline theory. Figure 2.7 shows the relevant outlet triangle immediately ahead of the trailing edge (i.e., with blockage), where subscript ∞ is used for blade-congruent flow.

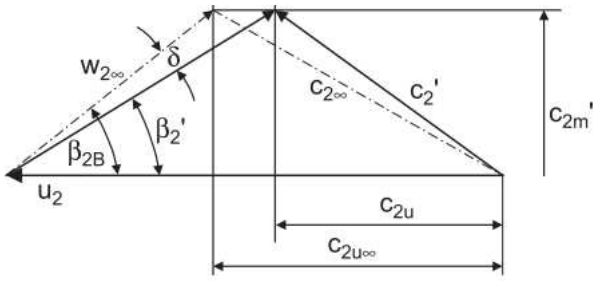

Figure 2.7: *Slip and deviation angle.*

A well-known expression to extimate the slip phenomenon ($c_{2u}/c_{2u\infty}$) for centrifugal pumps is the one proposed by Stodola:

$$\sigma = 1 - \frac{2\pi \sin \beta_2}{N_b \psi_{id}} \tag{2.9}$$

Therefore σ = 1.0 means blade-congruent flow. The smaller σ, the greater is the deviation between flow and blade angles.

2.2.6 Secondary flows

Most pumps operate at high Reynolds numbers, and, in this regime of flow, most of the hydraulic losses occur as a result of secondary flows and turbulent mixing [17]. In the following paragraph an outline of some of the more common secondary flows that occur in pumps will be presented. To do so, we choose to describe the secondary flows associated with three typical pump components, the unshrouded axial flow impeller or inducer, the shrouded centrifugal impeller, and the vaneless volute of a centrifugal pump.

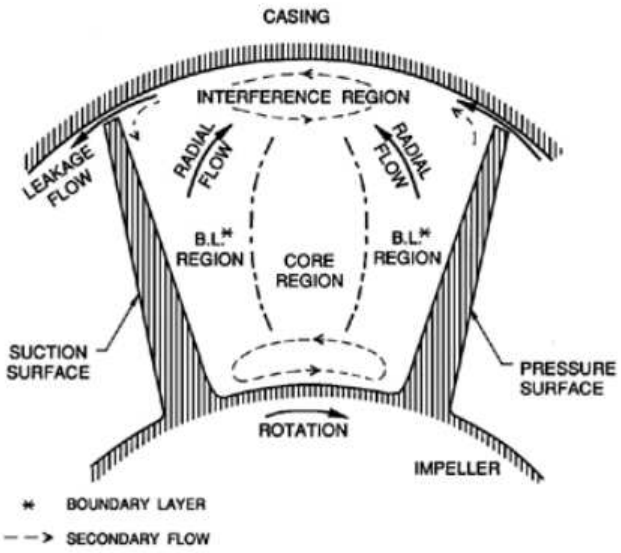

Figure 2.8: *Cross-section of a blade passage in an axial flow impeller showing the tip leakage flow, boundary layer radial flow, and other secondary flows (adapted from Lakshminarayana 1981).*

Secondary flows in unshrouded axial flow inducers have been studied in detail by Lakshminarayana [18, 19], and Fig.2.8, which was adapted from those publications, provides a summary of the kinds of secondary flows that occur within the blade passage of such an impeller. Dividing the cross-section into a core region, boundary layer regions on the pressure and suction surfaces of the blades, and an interference region next to the static casing, Lakshminarayana identifies the following departures from a simple flow following the blades. First, and perhaps most important, there will be a strong leakage flow (called the tip leakage or tip clearance flow) around the blade tips driven by the pressure difference between the pressure surface and the suction surface. Clearly this flow will become even more pronounced at flow rates below design when the blades are more heavily loaded. This leakage flow will entrain secondary flow on both surfaces of the blades, as shown by the dashed arrows in Fig.2.8. Second, the flow in the boundary layers will tend to generate an outward radial component on both the suction and pressure surfaces, though the former may be stronger because of enhancement by the leakage flow. The photographs of Fig.2.9, which are taken from Bhattacharyya et al. [20], show a strong outward radial component of the flow on the

blade surface of an inducer. This is particularly pronounced near the leading edge (left-hand photograph). Incidentally, Bhattacharyya et al. not only observed the backflow associated with the tip clearance flow, but also a "backflow" at the hub in which flow reenters the blade passage from downstream of the inducer. Evidence for this secondary flow can be seen on the hub surface in the right-hand photograph of Fig.2.9 Finally, we should mention that Lakshminarayana also observed secondary vortices at both the hub and the casing as sketched in Fig.2.8. The vortex near the hub was larger and more coherent, while a confused interference region existed near the casing.

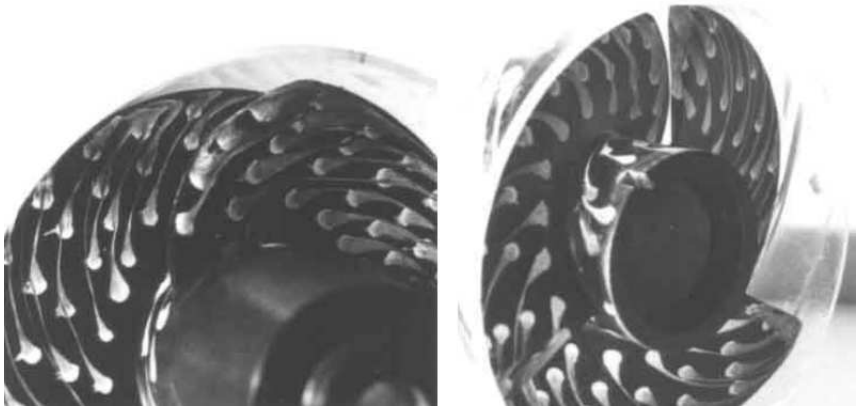

Figure 2.9: *Photographs of a 10.2cm, 12° helical inducer with a lucite shroud showing the blade surface flow revealed by the running paint dot technique. On the left the suction surfaces viewed from the direction of the inlet. On the right the view of the pressure surfaces and the hub from the discharge. The flow is for 2000 rpm and ϕ_1=0.041. From Bhattacharyya et al. (1993).*

Additional examples of secondary flows are given in the descriptions by Makay [21] of typical flows through shrouded centrifugal impellers. Figure 2.10, which has been adapted from one of Makay's sketches, illustrates the kind of secondary flows that can occur at off-design conditions. Note, in particular, the backflow in the impeller eye of this shrouded impeller pump. This backflow may well interact in an important way with the discharge-to-suction leakage flow that is an important feature of the hydraulics of a centrifugal pump at all flow rates. As testament to the importance of the backflow, Makay cites a case in which the inlet guide vanes of a primary coolant pump in a power plant suffered structural damage due to the repeated unsteady loads caused by this backflow. Note should also be made of the secondary flows that Makay describes occurring in the vicinity of the impeller discharge.

Flow in a volute

It is also important to mention the disturbed and separated flows that can often occur in the volute of a centrifugal pump when that combination is operated at off-design flow rates [22–25]. As described in the preceding section, and as indicated in Fig.2.11, one of the commonest geometries is the spiral volute, designed to collect the flow discharging from an impeller in a way that would result in circumferentially uniform pressure and velocity. However, such a volute design is specific to a particular design flow coefficient. At flow rates above or below design, disturbed and separated flows can occur particularly in the vicinity of the cutwater or tongue. Some typical phenomena are

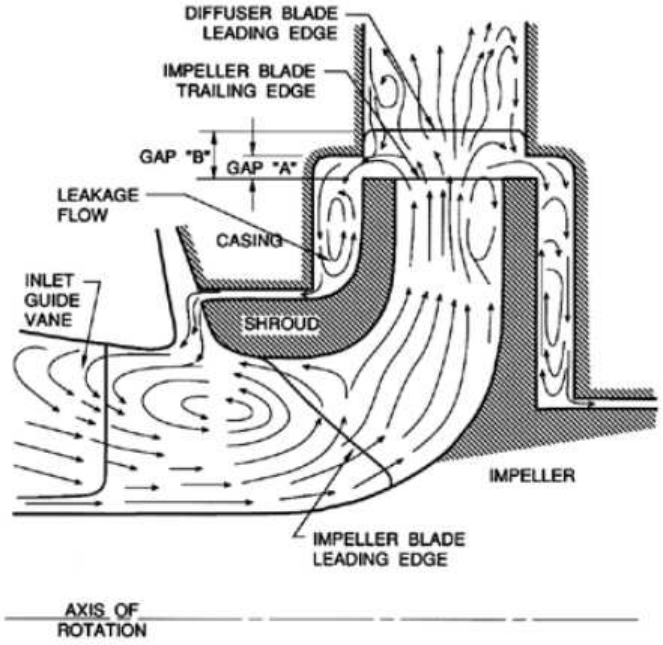

Figure 2.10: *Schematic showing secondary flows associated with a typical centrifugal pump operating at off-design conditions (adapted from Makay 1980).*

sketched in Fig.2.11 which shows separation on the inside and outside of the tongue at flow coefficients below and above design, respectively. It also indicates the flow reversal inside the tongue that can occur above design [24]. Moreover, as Chu et al. [26] have recently demonstrated, the unsteady shedding of vortices from the cutwater can be an important source of vibration and noise.

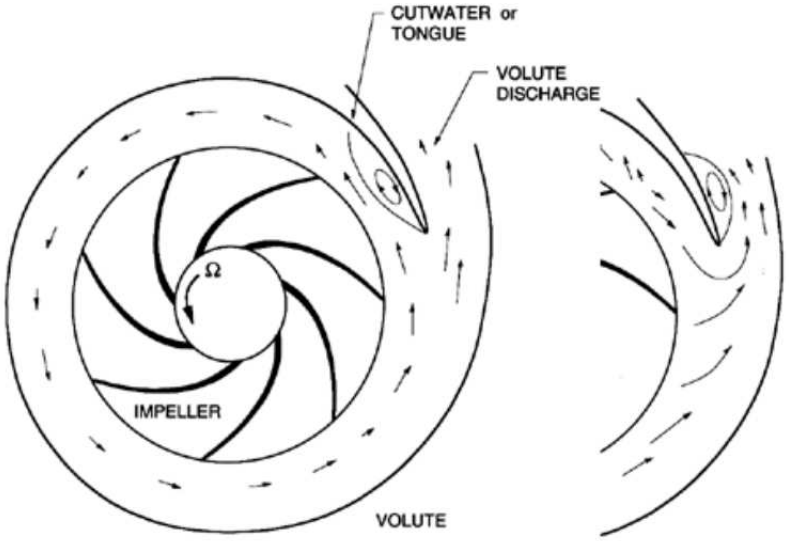

Figure 2.11: *Schematic of a centrifugal pump with a single, vaneless volute indicating the disturbed and separated flows which can occur in the volute below (left) and above (right) the design flow rate.*

A fluid element downstream of the impeller outlet moves in accordance with the conservation of angular momentum $c_u \times r = c_{2u} \times r_2$ = constant. Consequently, the circumferential velocity in the volute drops with growing radius, while the static pressure increases from the inside to the outside. These pressure and velocity distributions, shown qualitatively in Fig.2.12, are confirmed by experiments near the best efficiency point, e.g., [27]. At overload and partload operation, the volute cross sections do not match the impeller discharge velocities and the flow patterns in the volute deviate from the behavior shown in Fig.2.12. The pressure gradients over the radius become flatter at partload, while they increase at overload. Similar to the flow through a bend or any curved channel, secondary flows are generated in a volute. The flow pattern has the shape of a double vortex according to Fig.2.12; it becomes increasingly asymmetrical with growing non-uniformity of the impeller outflow. In flat, rectangular or trapeze-shaped volute cross sections a less intensive secondary flow is expected than in a volute of circular or square cross section (because of the smaller radius ratio). The deceleration of the flow in the volute is governed by similar mechanisms for diffusers. Volute casings react in a less sensitive manner to a non-uniform impeller outflow than diffusers. Saddle-type instabilities of the Q-H-curve are therefore rarely found with volute casing pumps below n_q = 70 (unless the characteristic $H_p = f(Q)$ is unstable).

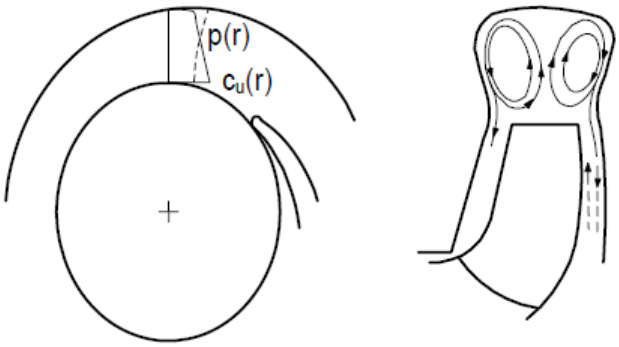

Figure 2.12: *Flow patterns in volute casings.*

Flow in a channel

If the channel cross section is other than circular, the velocity distribution is not rotational-symmetric. Different velocity profiles are expected in sections A-A and B-B (diagonal) of a square channel (Fig.2.13). Consequently, the wall shear stresses change over the channel perimeter. The shear stresses are lowest in the diagonal B-B and greatest in section A-A. Since the static pressure (with flow in straight channels) is constant over the cross section, the eq.2.10 can only be satisfied if fluid is transported through compensatory flows normal to the channel axis from locations with low shear stress to zones with higher shear stress. Such secondary flows occur, for example, in triangular or square channels (Fig.2.13), hence also in the impeller or diffuser channels. Vortices ("corner vortices") develop in the corners of a channel, between blades and shroud or between pillar and baseplate. Their effect can be observed when abrasive particles are carried with the flow giving rise to erosion. Corner vortices can also play a role in cavitation, since the pressure in the vortex core drops relative to the pressure in the main

flow. The velocity components of the secondary flow attain approximately 1 to 2% of the velocity in mid channel, [28]. By rounding the corners the losses can be somewhat reduced.

$$\Delta p = \tau U \Delta L = \rho c_f \frac{w^2}{2} U \Delta L \tag{2.10}$$

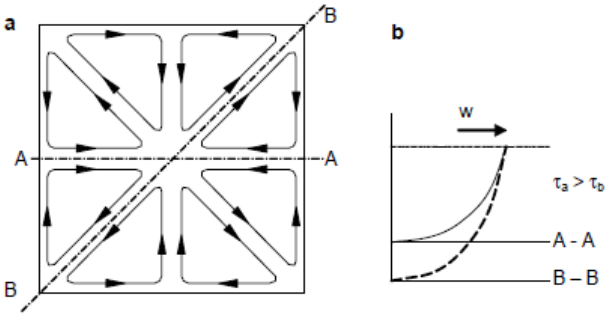

Figure 2.13: *Secondary flow in a square channel a) cross section, b) velocity distributions in sections A-A and B-B (diagonal).*

2.2.7 Pump types

Centrifugal pumps are of eminent technical and economic importance in many areas of life and industry (the world market volume for centrifugal pumps is in the order of 20 billion US-dollars per year). Their application range comprises small pumps of a few watts, such as central heating circulation pumps or cooling water pumps for automobiles, as well as 60 MW storage pumps and pump turbines with more than 250 MW when operating in the pumping mode. The term "centrifugal pumps" comprises radial, semi-axial and axial pumps, but also side channel, peripheral and liquid-ring pumps whose working principles are fundamentally different from that of the first group. Centrifugal pumps in the narrow sense are designed for flow rates from 0.001 to 60 m^3/s, heads of 1 to 5000 m and speeds from a few hundred to about 30000 revolutions per minute. These values are intended to illustrate the broad range of applications; they do not define the absolute limits of actual or future pumps. Any pump application is characterized by the flow rate Q_{opt}, the head H_{opt} and the rotor speed n. To a large extent these parameters determine which impeller type and pump design to choose. These three performance parameters are interrelated by the "specific speed" n_q, N_s or ω_s which is of great importance for the selection and design of a pump, see Tab.2.1.

Table 2.1: *Definitions of specific speed.*

$n_q = n\frac{\sqrt{Q/f_q}}{H^{0.75}}$	$N_s = 51.6\, n_q$	$\omega_s = \omega\frac{\sqrt{Q/f_q}}{gH^{0.75}}$
Q in m^2/s	Q in gpm	Q in m^2/s
H in m	H in ft	H in m
n in rpm	n in rpm	ω in $1/s$

In Europe n_q is most popular, while N_s is defined in US customary units. The truly non-dimensional quantity ω_s should be preferred for theoretical considerations or for deriving general equations, but is not yet used in practice by the majority of pump engineers. This is because the available documentation is often prepared with either n_q or N_s. Unfortunately, a variety of other definitions of the specific speed can be found in the literature.

$H_{st} = H_{tot}/z_{st}$ is the head per stage where z_{st} is the number of stages. f_q is the number of impeller entries, that is f_q = 1 for single-entry and f_q = 2 for double-entry impellers. The choice of radial, semi-axial or axial impellers depends on the specific speed as well as on the pump type. A pump with medium specific speed (e.g., n_q = 60) may be built with a radial or a semi-axial impeller depending on the pump type which is most economical for the expected application. Looking at specific speed expressions it can be seen that:

- For supplying small flow rates at high pressures, pumps with low specific speeds are required. Below $n_q < 20$ the efficiency drops rapidly with diminishing specific speed. Therefore, the lower economic limit for a centrifugal pump application is generally n_q = 5 to 8 for small pumps, but $n_q = 10$ to 15 for larger performances, depending on the application and the importance of keeping energy costs low. Below this limit the speed must be increased, or a multistage pump must be used raising thus the specific speed as in Tab.2.1. Otherwise another pump type must be selected.

- Special pumps with radial blades or Pitot-tube pumps may be built with specific speeds as low as $n_q = 1$, albeit with low efficiencies.

- Large flow rates and low heads require pumps with high specific speeds. The upper limit for economical operation is typically in the region of $n_q = 350$ to 450. Above that limit, costs and hydraulic losses may become unacceptably high. But the economical application is not determined by the specific speed alone. Approach flow conditions and the pump size must also be taken into consideration when selecting the type of pump. If a given application would require an excessively high specific speed, the flow rate must be divided among two or more parallel pumps in order to reduce unit size and n_q. Distributing the flow to several units may prove advantageous in view of the driver cost, plant layout and standby requirements to maintain operation in case of a pump failure.

Fig.2.14 lists the different impeller types and their properties in order to illustrate the influence of the specific speed on the design and the range of performance.

Explanations to Fig.2.14:

- The head per stage at BEP given in the table represents approximately the feasible maximum. Attainable peripheral speed, head per stage and head coefficient fall with increasing specific speed.

- The head coefficient is defined as $\Psi_{opt} = 2gH_{opt,st}/u_2^2$

- The efficiency of a pump depends not only on the specific speed but also on the pump type, design and absolute size. For extremely small pumps it might even be less than the lower limit listed in Fig.2.14.

n_q	Type	Impeller shape	Maximum $H_{st,opt}$	ψ_{opt}	η_{opt} [%]	
< 0.5	Piston pumps	Positive displacement pumps	Limited by mechanical constraints		85 - 95	
< 2	Gear pumps				75 - 90	
2-10	Screw pumps				65 - 85	Also for gas/liquid mixtures
0.5-4	Peripheral pumps	Figure 2.19	400 m	5 - 15	30 - 35	Single and multistage
2-11	Side channel pumps	Figure 2.18	250 m	3 - 10	34 - 47	
1-10	Friction pumps	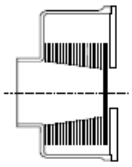		0.5	25 - 35	
7-30	Radial pumps	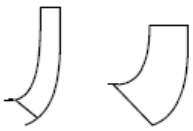	800 m (1200)	1 to 1.2	40 - 88	Below n_q < 10 usually small pumps only
50			400 m	0.9	70 - 92	In most cases: $H_{st,opt}$ < 250 m
100		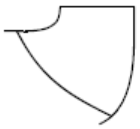	60 m	0.65	60 - 88	n_q = 100 is essentially the upper limit for radial impellers
35	Semi-axial-pumps		100 m	1	70 - 90	For n_q < 50 often multistage For n_q > 75 seldom multistage
160			20 m	0.4	75 - 90	For n_q > 100 only single-stage
160 to 400	Axial pumps	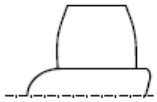	2 m to 15 m	0.4 to 0.1	70 - 88	Flow rates up to 60 m^3/s, only single-stage

Figure 2.14: *Pump types.*

- Radial, semi-axial and axial pumps are built in a range of $7 < n_q < 400$ for a wealth of universal applications.

- Multistage pumps are commonly built as horizontal units with radial impellers, while in vertical machines often semi-axial impellers are used. Their specific speed does not generally exceed $n_q = 50$, because the multistage design yields

better efficiencies below that figure.

2.2.8 Double suction centrifugal pump

Pumps with double-entry impellers require distinctly lower suction pressures (or $NPSH_A$) than single-entry pumps for delivering a specified flow rate at a given speed. Also the efficiencies of double-entry pumps are often superior to those obtained with single entry pumps (at n_q < 40). With a double-entry design the hydraulic forces acting axially on the impeller are to a great extent balanced for symmetry reasons. Thus a smaller axial bearing is sufficient. Figure 2.15 shows a double-entry vertical booster pump feeding a pump in a pipeline for the transport of drinking-water. The double volute used considerably reduces the hydraulic radial forces as compared to a single volute design thereby reducing shaft deflection and increasing the service life of bearings, seals and wear rings. As the lower radial bearing is water lubricated, there is no need for a lower shaft seal. This bearing is cooled with water taken from the volute casing.

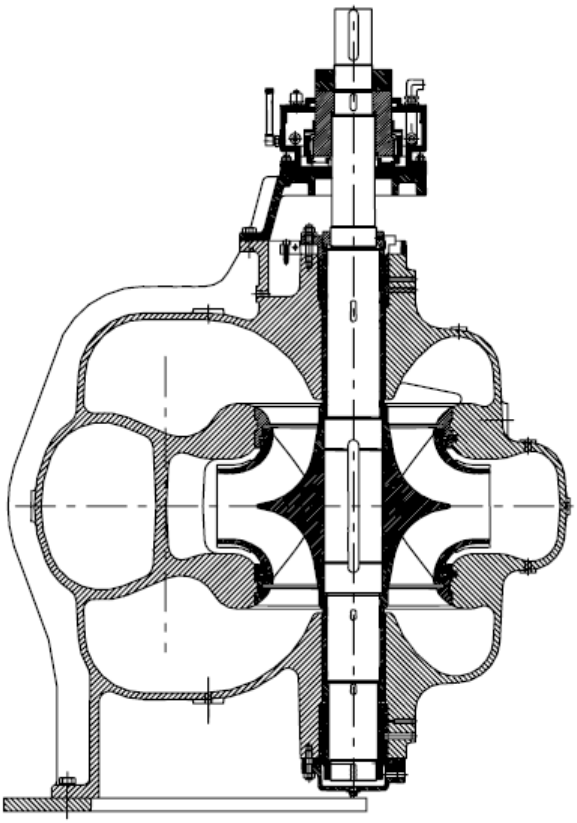

Figure 2.15: *Double-entry vertical pump, Sulzer Pumps, n = 596 rpm, Q_{opt} = 2.4 m^3/s, H_{opt} = 48 m, P_{opt} = 1250 kW, n_q = 36.*

The upper radial bearing is a plain journal bearing while the axial forces are carried by a tilting-pad thrust bearing. Both are oil lubricated. As this is a low speed pump with a large shaft diameter, a stuffing box is a good solution for the shaft seal. Single-stage, double-entry pumps are designed for specific speeds between approximately n_q = 10 to 100. Mostly they are built as horizontal units with the suction and discharge nozzles in line. Thus the pump can be installed in a straight pipeline without elbows

or additional fittings. For large-bore piping this is an important cost advantage if the installation concept is compatible with this arrangement. For cold liquids (nonetheless up to 130 °C) double-entry pumps are mostly built as "axial-split" designs. In this type, a flange splits the pump casing through the rotor axis and allows the removal of the complete rotor assembly after lifting off the upper half of the casing. Discharge and suction nozzles are below the split flange and do not hinder the opening of the pump. For high temperatures, high pressures and for chemical processes, single-stage, double-entry pumps are also designed with barrel casings and one or two casing covers which support the bearings and house the shaft seals.

2.2.9 Attempts to improve centrifugal pumps performance

Centrifugal pumps are probably among the most often used machinery in industrial facilities as well as in common practice. After being invented, they passed long evolutionary way until they became accessible for various applications. A few centuries ago, Euler described their physical principle through a well-known equation named after him "Euler's equation for turbomachinery". Since then, many studies have been conducted to improve the centrifugal pump performance. These studies used a lot of methods and ideas seeking a better centrifugal pump performance through attempts to increase the pump total efficiency and slip factor. One of these methods that took a lot of interest was to improve the pump performance by impeller trimming [14, 29–31]. These studies found that as the diameter is reduced, the head and power curves decrease continuously. The efficiency, however, will increase at first and then drop for a certain value of diameter. The main reason for this might be attributed to the growth of the gap between the impeller and stator as the impeller diameter is reduced. Another attempt to improve the centrifugal pump performance lies in adding splitter blades between the main blades [32–34]. Unfortunately, such solution was found to render negative and positive effects on the pump behavior. It increases the head as compared to the original impeller. This was explained by the fact that increasing the impeller slip factor in effect of the splitter would help better conduct energy to the flow. However, a drop in total efficiency has been noticed in some cases due to the increase of the hydraulic friction between the pumping fluid and the splitter blades. The pump geometrical parameters remain the greatest interest of all researchers looking for improving the centrifugal pump performance. Some authors made optimization on the blade exit angle and they found that with increasing the blade exit angle the head increases but the efficiency decreases [35–39].

There are authors that proposed geometry modifications by not acting on common design parameters (e.g., β_2, l_2, etc.), but modifing other features with respect to the conventional ones. For instance, with this regard, J. Skrzypacz et al. [40] suggested the introduction of micro grooves, performed on the front and rear disks, for low specific speed impellers in order to reduce the hydraulic losses. The application of micro grooves, which work as additional blades, should increase the ability of the impeller to transmit power to the liquid, particularly in the region of the boundary layer. Some other authors conducted optimization on the number of blades [41–43]. They concluded that when increasing the number of blades, both head and efficiency increase until a certain number of blades at which the efficiency decreases. Other authors considered the blade outlet width (l_2) in their optimization research [44, 45]. It was found that at the design

flow rate, the head increases gradually with the progressive increments of blade outlet width. In addition, the high efficiency area in the large flow rate region gets bigger and the area in low flow rate region changes a little with the increase of blade outlet width. Some authors tried to improve the pump performance by making a slot in the impeller blade. The first one who start adopting this technique was E.A. Ahmed [46]. Then, M. Saffaa and his group [47] developed this work using their own 2-D numerical code to solve a laminar flow inside the pump impeller. In an attempt to examine the effect on the pump performance, Hongxun [48] used a similar technique and made a comparison between the draughting technique and the splitter blades. Recent works investigate the effect of three slot geometrical parameters, namely slot radial position (R_s), slot height (h_s) and slot inclination angle (θ_s) on the impeller performance.
Nowadays the research about centrifugal pumps also comprises the design of multi-objective algorithms for pump definition and geometry optimization in order to improve impeller efficiency (reducing losses and enlarging the operative range with both single-phase and cavitating flows) and to develop less time consuming design tools. The first field includes, e.g., multi-objective optimization method using a Simulation-Kriging model-Experiment (SKE) approach [40, 49]. The latter includes global optimization method based on Artificial Neural Network (ANN), Artificial Bee Colony (ABC) [50] and analytical models based on potential flow theory [51]. In addition, there are works that introduce new design methodologies based on Energy Loss Models and Computational Fluid Dynamics (ELM/CFD) [52].

2.3 Pump as Turbine

If the system head imposed on the pump exceeds the shut-off head, liquid flows back through the pump from the discharge to the suction nozzle in the "pumping- brake mode". There are a number of other abnormal modes of operation which are described by the "general characteristics". These include a turbine mode where the liquid transfers power to the rotor, which can be used to drive an electrical generator or any other machine. Reverse-running centrifugal pumps can be used as turbines for energy recuperation (in [53] termed "Hydraulic Power Recovery Turbines", HPRT). Applications are processes where a large amount of fluid energy is dissipated in valves or other throttling devices. In some processes dissolved gases separate from the fluid or liquid is flashed into steam during the expansion. Higher energy differences are then available for power recovery than in pure liquid flow. The preceding chapters dealt with centrifugal pumps which transfer energy to the liquid. The direction of rotation and flow for this type of operation are defined as positive. But a centrifugal pump can also transform liquid energy into mechanical power as a prime mover if the directions of rotation and flow are reversed, i.e., both become negative.

The application of a pump instead of a turbine seems to be an alternative solution in terms of easy implementation and reduced cost of equipment [54]. The pumps in turbine mode have various advantages over conventional hydro turbines viz. low cost, less complexity, mass production, availability for a wide range of heads and flows, short delivery time, availability in a large number of standard sizes, ease of availability of spare parts, easy installation, etc. [55]. For low and very low capacity power plants (up to 500 kW), the PAT deserves thoughtfulness due to considerable reduction in the

capital cost of the plant of the order of 10–1 or even more in spite of having slightly reduced efficiency [20]. In this range, the investment cost for conventional hydro turbines is relatively high. The payback period of such hydro turbine can be as high as 15 years which can be reduced to 2 years using PAT for similar capacity [56]. Selection of appropriate type of pump depends on head and discharge available at the site, initial and maintenance cost, ease of availability of pump, etc. Lueneburg and Nelson [57] reported that all centrifugal pumps from low to high specific speed, single or multistage, radially or axially split, horizontal or vertical installations can be used in reverse mode. The pump to be used as turbine can be selected, based on head and discharge, as shown in Fig. 2.16. It can be seen that multistage radial flow pumps are suitable for high head and low discharge sites; whereas, axial flow pumps are appropriate in low head and high discharge range. Similar chart was also presented by Orchard and Klos [56] (range: 5–750 kW) [58, 59].

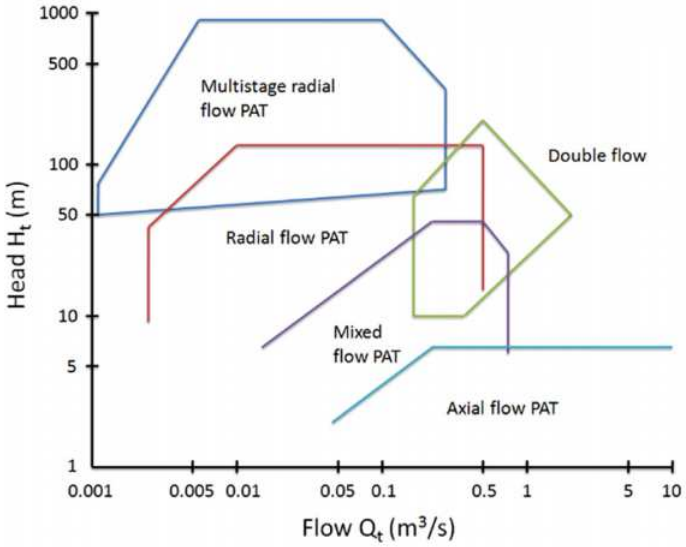

Figure 2.16: *Different pumps suitable as turbines.*

In turbine operation the pressure in the inlet nozzle is higher than in the outlet nozzle. The diffuser ("guide wheel") or volute feeds the liquid to the outer diameter of the runner. The discharge nozzle of the pump is thus an inlet nozzle to the turbine, while the pump suction nozzle becomes the turbine outlet (or "exhaust") nozzle, Fig.2.17. The velocity vectors at the inlet and outlet of a runner blade are depicted in Fig.2.17 on the right. The relative velocity w_2 at the inlet hits the blade with an incidence i_2 while the liquid leaves the blade with the relative velocity w_1 at a deviation angle δ_1. Let us consider the resultant flow conditions by comparing the velocity triangles for pump and turbine operation for an impeller with back-swept blades. In pump operation the inflow angle to the impeller α_1 and the outflow angle β_2 from the impeller are largely independent of the flow. The reasons are: (1) angle α_1 is determined by the inlet geometry upstream from the impeller; (2) β_2 is essentially given by the impeller blade outlet angle β_{2B}. This is borne out by the observation that the slip factor γ depends little on the flow rate for $q^* > 0.7$. As a result, the absolute velocity c_2 at the impeller outlet-and therefore the specific work of the pump drop with increasing flow.

In turbine operation the guide wheel or volute determines the runner inflow angle α_2 which is largely independent of the flow q^* when fixed guide vanes are used. The fluid leaves the runner with the angle β_1, which likewise depends little on the flow rate. Consequently, the inflow velocity c_2 to the runner increases with the flow rate. The specific work increases proportionally to the flow through the turbine. This is demonstrated by eq.2.11. In this way $c_{2u} = c_{2m} \cot \alpha 2$ and $c_{1u} = u_1 - w_{1u} = u_1 - c_{1m} \cot \beta_1$. The specific work of a turbine runner thus becomes:

$$Y = u_2 c_{u2} - u_1 c_{u1} = u_2 c_{2m} \cot \alpha_2 - u_1^2 + u_1 c_{m1} \cot \beta_1 \tag{2.11}$$

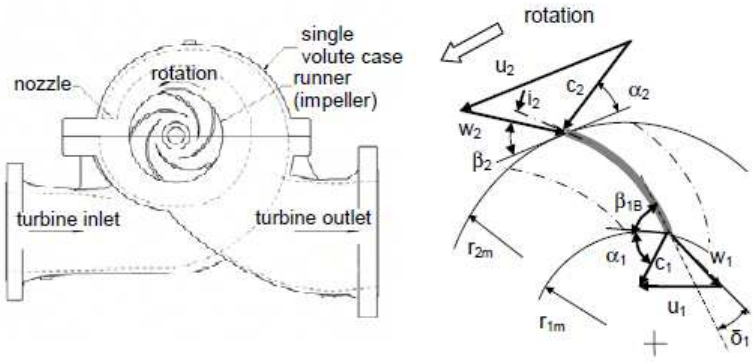

Figure 2.17: *Direction of rotation and flow in a pump running as turbine.*

The angles α_2 and β_1 in eq.2.11 are flow angles. The inflow angle α_2 to the runner can be determined from the guide wheel or volute geometry.

While the total flow rate Q entering the turbine inlet nozzle flows through the guide wheel, the actual flow through the runner is reduced by the volumetric efficiency $Q' = Q\eta_v$ due to leakage losses. The angle β_1 of the fluid exiting from the runner differs from the blade angle β_{1B} because a vane-congruent flow cannot be expected in turbine operation either.

2.3.1 Slip factor in centripetal hydraulic turbine

A the outlet of centripetal hydraulic turbomachinery the relative flow undergoes a deflection with respect to the blade direction, as explained in paragraph 2.2.5, as well as at the outlet of a centrifugal pump. However, the deflection occurs in the rotational direction and the β_1 angle becomes bigger than the β_{1B}. This phenomenon is negligible for conventional hydrulic turbines such as Francis turbine,due to their high number of blades, but it can be relevant for pumps working as turbines.
As shown by Ventrone [60] and Shi et al. [61], under proper hypotheses, the fluid flow inside a blade channel in a rotating machine is subject to a counter rotating vortex with an intensity equal to:

$$\nabla \times \bar{w} = -2\bar{\omega} \tag{2.12}$$

Thus, vorticity is twice the angular velocity (ω) of the rotating machine eq.2.12. This leads to a deviation of the relative velocity (w_1) with respect to the blade congruent angle (β_{1B}) at the outlet of the impeller, see Fig.2.18.

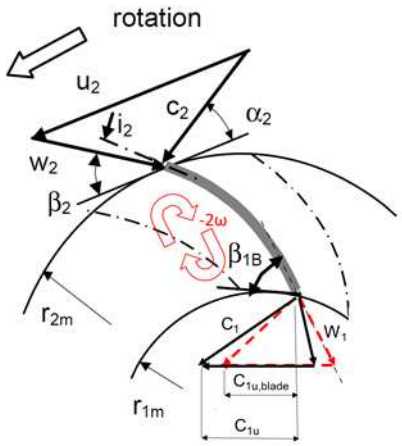

Figure 2.18: *Velocity triangles at the inlet (2) and at the outlet of the runner (1). At the outlet both actual (solid line) and blade congruent (dashed line) velocity triangles are represented*

In Fig.2.18 both the actual and the blade congruent velocity triangles are represented. Actually, the main flow is subject to a deflection in the same direction of the machine rotation, which could be justified by the vorticity inside the channel. This deflection leads to an increase of the absolute tangential velocity component (c_{u1}) at the outlet of the machine and therefore to a reduction of the work extracted by the runner according to Euler's equation (see 2.11).

2.4 Cavitation inside hydraulic turbomachinery

Cavitation means the partial evaporation of liquid in a flow system. A cavity filled with vapor is created when the static pressure in a flow locally drops to the vapor pressure of the liquid due to excess velocities, so that some fluid evaporates and a two-phase flow is created in a small domain of the flow field. The vapor condenses suddenly ("implodes") as soon as it is transported downstream into zones where the static pressure again exceeds the vapor pressure. With increasing extension of the cavitating zone with two-phase flow, the head and efficiency of the pump may be impaired, noise and vibrations excited and components damaged through cavitation erosion under certain conditions. When using the term "cavitation" the "cavitating flow"-i.e. the occurrence of local zones with two-phase flow-and "cavitation erosion" or cavitation damage must be well distinguished. The term "hydrodynamic cavitation intensity" is used for the totality of the implosion energy of all bubbles. If this exceeds the "cavitation resistance", the material will be damaged by "cavitation erosion" if it is exposed sufficiently long to the attack. The cavitation resistance is a material property which is independent of the flow system.

2.4.1 Cavitation physics

Any substance can exist in the phases solid, liquid and gaseous. The transition from one phase to another (e.g., "formation of ice" or "evaporation") is described through phase equilibriums in a $p - T$ diagram. Accordingly, the vapor pressure curve $p_v(T)$ characterizes the equilibrium (the "saturation status") between liquid and vapor from

the triple point to the critical point (Fig.2.19).

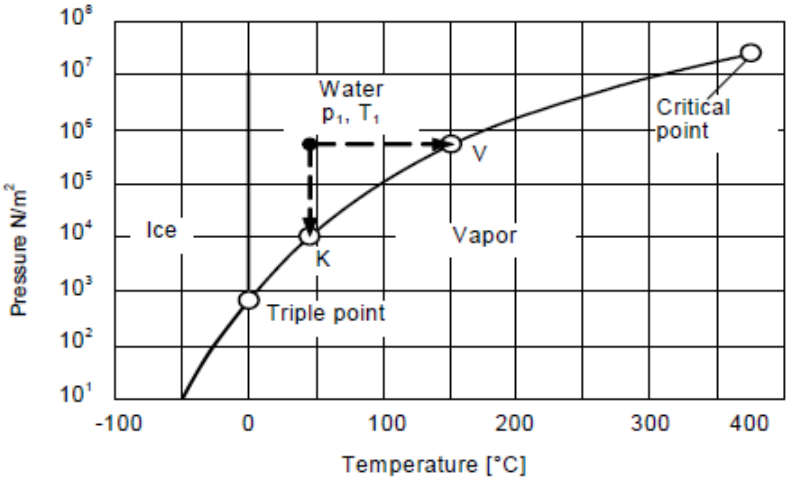

Figure 2.19: *Phase equilibrium of water*

A liquid in condition p_1, T_1 with $p_1 > p_v(T1)$ can be evaporated, if it is heated at constant pressure to the saturation temperature $T_v(p1)$ (point V), or expanded to the vapor pressure $p_v(T1)$ at constant temperature (point K in Fig.2.19)). During phase conversion from liquid to vapor the evaporation enthalpy must be added. In the reverse process, i.e., condensation, the evaporation enthalpy is liberated. During cavitation a small portion of the liquid is expanded at constant temperature (in Fig.2.19) from p_1 to K), to the extent that some liquid evaporates. Downstream of the low-pressure zone, the pressure rises again so that the saturation pressure is exceeded and the vapor condenses. This distinguishes cavitation from evaporation by "flashing". The nature of cavitating flows therefore implies that: (1) the static pressure in a system initially drops locally to the vapor pressure as a result of flow acceleration; (2) subsequently the flow is decelerated so that the pressure increases and the vapor bubbles implode. To illustrate the cavitation process, Fig.2.20 shows the development of the static pressure in a Venturi nozzle. The minimum pressure, p_min, is reached in the throat area. Let the temperature of the fluid in otherwise identical conditions vary in four stages from T_1 to T_4 with the relevant vapor pressures p_{v1} to p_{v4}: in condition 1 with $p_{min} > p_{v1}(T1)$ the vapor pressure is not reached and consequently no evaporation oc- curs. With $p_{min} \leq p_{v2}(T2)$ saturation is reached and initial vapor bubbles develop. At $p_{v3}(T3)$ the zone with $p_{min} \leq p_{v3}$ takes up roughly one half of the diffuser length; this domain is covered with a large cavity which influences the flow in the channel. In condition 4 the pressure recovery in the diffuser is smaller than $p_{v4} - p_{min}$, so that the vapor created no longer condenses; the two-phase flow is maintained and covers the entire channel downstream of the diffuser. In accordance with the pressure loss and the thermodynamic equilibrium some fluid evaporates with increasing pipe length (only a fraction of the flowing fluid mass evaporates). Such a process is called expansion evaporation or "flashing". Because of the shear stresses between the flowing liquid and the cavity, the latter cannot be at rest. Bubbles develop continuously and are transported downstream to the end of the cavity where they implode when $p > p_v$ applies again. For evaporating the corresponding amount of liquid, the required evaporation enthalpy must be transported

by heat conduction and convection from the surrounding liquid to the boundary of the vapor bubble. The heat transport requires a finite temperature difference ΔT_u. This temperature difference corresponds to a pressure difference Δp_u between the pressure in the bubble and the vapor pressure as shown in Fig.2.20. Let us assume that the water flowing through the nozzle in Fig.2.20 is saturated with dissolved air corresponding to the inlet pressure. As soon as the local pressure in the nozzle falls noticeably below the vapor pressure, air is liberated in accordance with Henry's law. This produces finely distributed individual bubbles when the pressure throughout the channel is sufficiently lowered or a cavity is formed as in Fig.2.20. Consequently, gas separation can also create cavitation without the pressure dropping below the vapor pressure. However, a vapor component is always present in any gas-filled volume having an interface with a liquid. The partial pressure of the vapor is equal to the vapor pressure resulting from the fluid temperature. If the effect of gas separation is significant, the phenomenon is also called "gaseous cavitation". Non-condensable gases weaken the intensity of the implosion, thereby reducing the potential for noise, vibrations and material erosion.

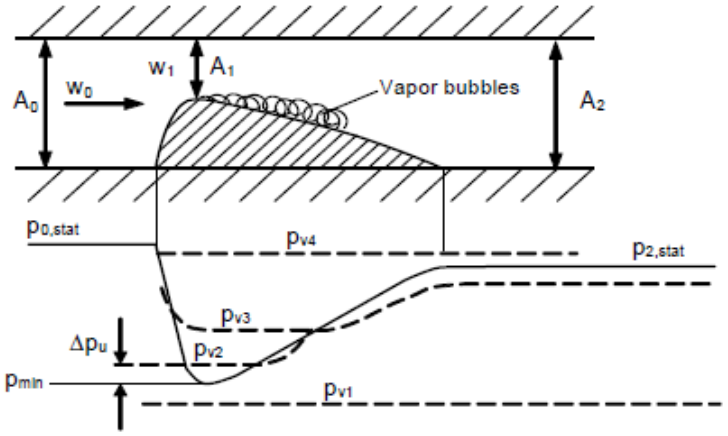

Figure 2.20: *Phase equilibrium of water*

2.4.2 Cavitation around hydrofoils

This paragraph is mainly concerned with developed cavitation on two-dimensional hydrofoils as it occurs on blades of rotating machinery or lifting hydrofoils. It is shown that attached cavities are strongly connected to the boundary layer, while bubble cavitation chiefly depends on the pressure distribution and the liquid nuclei content. From an experimental viewpoint, the control of cavitation patterns requires specific control of the water quality by means of equipment devoted to de-aeration, nuclei seeding and nuclei measurement.

The volume region affected by cavitation is called cavity. Cavities can be either steady, i.e., attached to the surface or unsteady, i.e., partially or totally separated from the surface, and transported downstream by the flow towards regions with higher pressure where they collapse. The main types of cavitation are here briefly summed up: bubble cavitation, sheet cavitation, cloud cavitation, super-cavitation and vortex cavitation. Each one shows a peculiar behavior and occurs depending on the operating conditions and the fluid properties [62, 63]. Consequently, the prediction of cavitation

can help in forecasting the most stressed regions.

Cavitation inception on a circular cylinder

The case of a circular cylinder or a sphere is particularly representative of the connection between cavitation inception and the boundary layer. In non-cavitating conditions, the drag coefficient of a cylinder presents a sudden decrease for a critical value of the Reynolds number. This value depends to a small extent upon the operating conditions (such as wall roughness or turbulence level) but usually lies around 3×10^5. It is well-known that this drop corresponds to the transition to turbulence of the boundary layer flow. Figure 2.21 shows the corresponding states of the boundary layer, as observed from visualizations, together with the variation of the drag coefficient versus the Reynolds number.

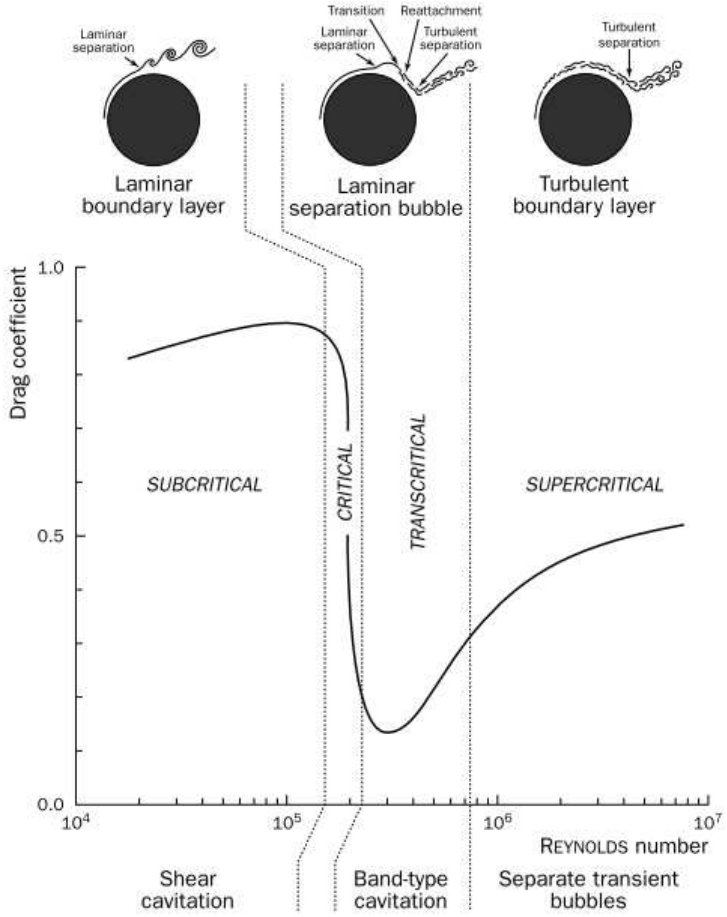

Figure 2.21: *Drag coefficient of a circular cylinder versus the Reynolds number and associated cavitation inception patterns and boundary layer state.*

Below the critical value of the Reynolds number, the boundary layer is laminar and separates from the body at an angle of between 70 and 80 degrees with respect to the stagnation point. The wake is thick and the drag is large. Transition to turbulence occurs away from the wall, in the free shear layer. It progressively approaches the

separation point as the Reynolds number is increased. In the transcritical region, the boundary layer is dramatically modified. Transition to turbulence is so close to the cylinder that the boundary layer reattaches on the wall. Laminar separation, transition to turbulence and turbulent reattachment are concentrated within a small region and form the so-called "separation bubble". The boundary layer, which has become turbulent, can withstand a stronger adverse pressure gradient than if it were laminar and separates later, at about 130 degrees. The wake becomes narrower and the drag smaller. Photographs on Fig.2.22 show the corresponding cavitation patterns at inception. Although the difference in Reynolds numbers is very small, the cavitation looks very different. At Re = 270 000, cavitation is not attached to the body, but appears in the wake, in the form of vapor filaments which are characteristic of shear cavitation.

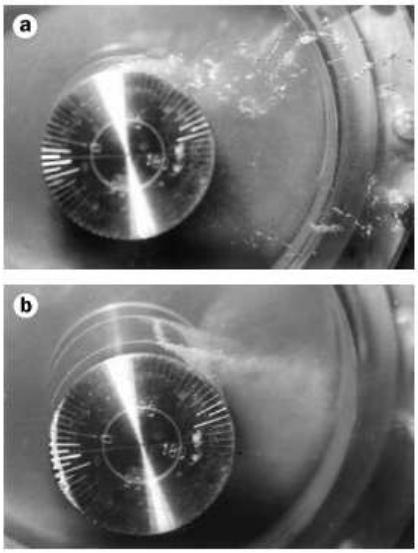

Figure 2.22: *Cavitation patterns at inception in the vicinity of the critical Reynolds number for a circular cylinder (a) Re = 270 000, (b) Re = 290 000.*

Conversely, for a slightly higher Reynolds number of 290,000, cavitation appears as a narrow sheet of vapor attached to the wall at an angle of about 115 degrees (visible on Fig.2.22b on the upper surface of the cylinder). It is generally referred to as band-type cavitation. It is initially made up of small bubbles, originating in nuclei trapped in the laminar separation bubble, where they grow slowly by diffusion of dissolved air. A further decrease in the ambient pressure results in the transformation of the band into a continuous attached vapor cavity. In this transcritical regime, the cavitation band, in which the pressure is close to the vapor pressure, develops downstream of the minimum pressure location. Hence, the liquid particles are in a metastable state while traveling through a region where the pressure is lower than the vapor pressure. For large values of the Reynolds number, the flow regime is supercritical. Transition to turbulence moves upstream of the laminar separation and suppresses the laminar separation bubble. Cavitation appears as separate transient bubbles –on the condition that water contains nuclei which can actually be activated by the minimum pressure– or as three-dimensional vapor cones attached to isolated roughness elements.

Cavity patterns on a two dimensional foil

In the case of hydrofoils, various cavity flow patterns can be observed according to the angle of attack and the cavitation number. For a proper observation of attached cavities in a hydrodynamic tunnel, it is essential to eliminate as much as possible traveling bubble cavitation in favor of attached cavities, and hence to use strongly deaerated water, so that almost no nucleus is activated. Figure 2.23 gives a mapping of the various cavity flow patterns which have been observed on a NACA 16012 hydrofoil, for a fixed Reynolds number, when the incidence and the cavitation number (or simply the ambient pressure) are modified. The cavitation number is defined as:

$$\sigma = \frac{p_{in} - p_v}{1/2\rho U_\infty^2} \tag{2.13}$$

For small values of the cavitation number, supercavitation is observed for any angle of attack. The supercavity detaches itself from the rear part of the foil for an angle of attack of around zero (region 1), and the detachment point progressively moves upstream, towards the leading edge, as incidence increases. The detachment line is almost straight in the spanwise direction in regions 1 and 3, whereas it becomes strongly three-dimensional in the intermediate zone 2. In region 1, the detachment point is far downstream of the point of minimum pressure, which is close to the point of maximum foil thickness. Thus, as for trans- critical flow around a cylinder, the liquid particles are in a metastable state in front of the cavity. This is why deaerated water is needed to observe this cavity flow regime. For high values of the cavitation number, the pattern progressively evolves from a partial pure vapor cavity (region 3'), to a two-phase cavity (region 4) with a smaller void fraction (α) and, finally, to cavitation in the shear layer bordering the recirculating zone due to stall at high angle of attack (region 5). Within a very narrow domain of attack angles (around 4 degrees), the behavior of the cavity flow is rather unexpected. When the cavitation number is decreased from non-cavitating conditions, a leading edge cavity appears first. As the cavitation number is further decreased, the leading edge cavity completely disappears before a new cavity develops, at sufficiently low values of the cavitation number. The disappearance of the leading edge cavity is associated with an unexpected displacement of the detachment point, which moves downstream as σ decreases until the cavity disappears. This behavior, connected to the S-shaped limiting curve, results from the strong interaction between the cavity and the boundary layer. Similar behavior of the detachment point was also observed by Michel [16] on a different foil, for velocities of up to 30 m/s, and approximately the same σ-values.

Cavitation inception

The connection between laminar separation and attached cavitation was first put forward in 1968 by Alexander in order to explain the difference between the minimum value of the pressure coefficient on the wall and the cavitation number at inception svi. In 1973, Arakeri and Acosta demonstrated experimentally, using schlieren and holographic methods, that the inception of attached cavitation on ogives occurs in the small recirculating bubble following laminar separation of the boundary layer, as it does for the transcritical flow around a circular cylinder. Thus, at inception, the pressure at the

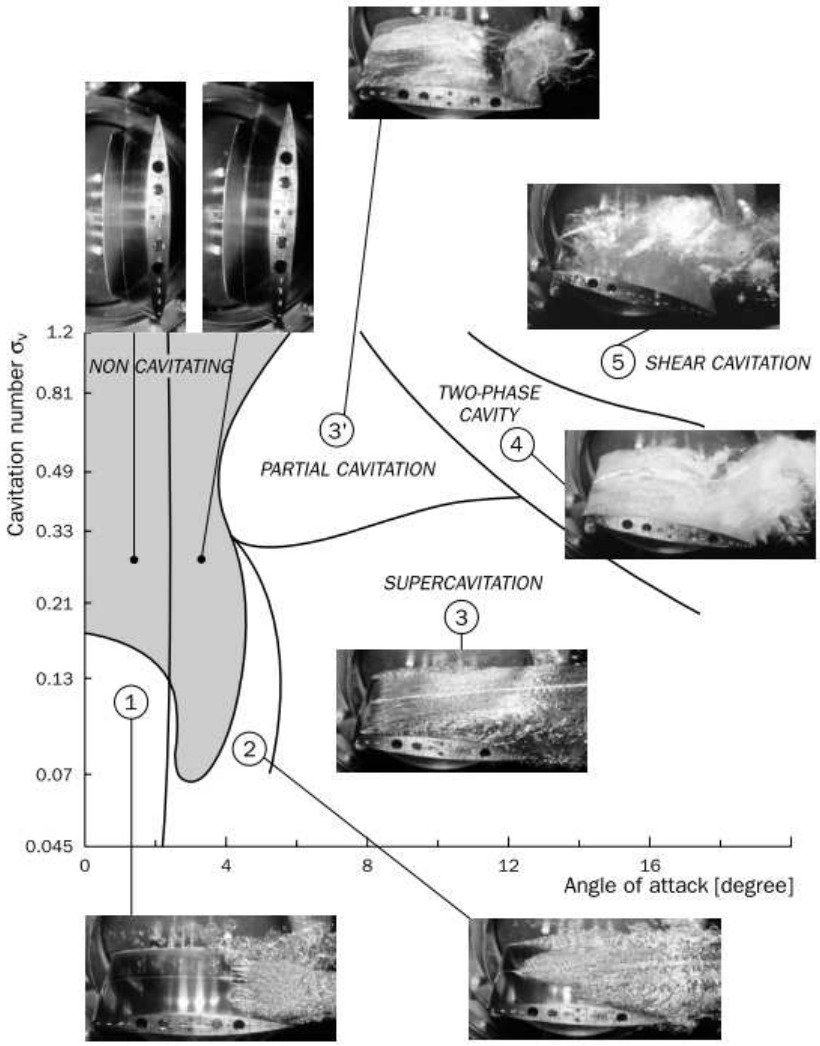

Figure 2.23: *Cavity patterns on a NACA 16012 hydrofoil at $Re = 10^6$ in strongly deaerated water.*

laminar separation point is equal to the vapor pressure, so that the cavitation inception number is equal in magnitude to the pressure coefficient at laminar separation:

$$\sigma = -C_{p,LS} \tag{2.14}$$

With reference to the minimum pressure coefficient, one can write:

$$\sigma = -C_{p,min} - \Delta C_p \tag{2.15}$$

with

$$\Delta C_p = \frac{p_{LS} - p_v}{1/2\rho U_\infty^2} > 0 \tag{2.16}$$

Hence, there is a delay in cavitation inception with respect to the expected inception at the minimum pressure point. This delay corresponds to the additional decrease in

pressure necessary for the pressure at the laminar separation point to reach the vapor pressure.

2.4.3 Methods for limiting cavitation phenomena

In the past, either active or passive cavitating flow control systems have been proposed with the aim of limiting cavitation phenomena inside turbomachines and around hydrofoils. The formers are intentionally activated by the operator like in the case of continuous water injection with different flow rates through a slot channel in order to reduce vapour shedding and bubble collapse [64]. The latters are systems which work autonomously with the aim of modifying the boundary layer behaviour. In this second class, we can find the application of external elements, e.g., trip bars installed along the bodies in order to modify their boundary layer behaviours [65].

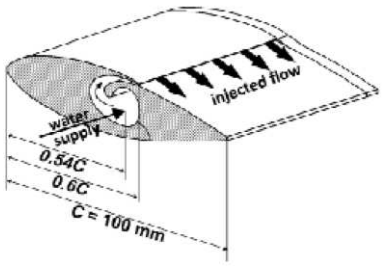

Figure 2.24: *An example of active control system for controlling shedding cavities.*

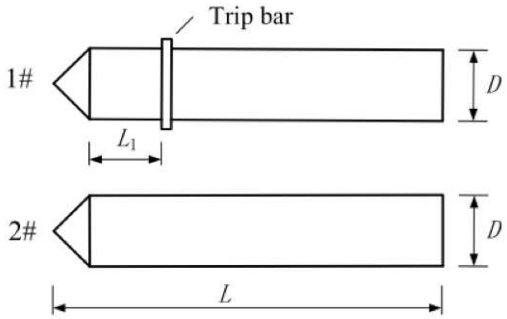

Figure 2.25: *An example of passive control system for limiting cavities oscillation.*

CHAPTER 3

Numerical models and description of the experimental measurements

3.1 Introduction

The novel impeller for a double suction pump, whose geometry will be presented in the next chapter, has been designed writing a specific 1D code and performing simplified (single channel) numerical simulations carried out by means of the commercial CFD code ANSYS Fluent®. After having completed the preliminary design came to an end, the novel impeller has been investigated both numerically and experimentally. The entire centrifugal pump geometry has been modeled and investigated by means of the CFD open-source code OpenFOAM in order to validate the results previously obtained via single channel simulations and to evaluate the influence of the actual suction pipe and double volute on the overall performance. The results have been validated by experiments carried out at the Hydraulic test rig of Nuovo Pignone. In the second part of this work the same geometry has been simulated with the same numerical technique in reverse mode, i.e., as a turbine. Finally, simulation of 2D hydrofoil under two-phase flow condition has been carried out by means of OpenFOAM in order to investigate a new passive cavitation control system for hydraulic turbomachinery.

3.1.1 OpenFOAM

OpenFOAM (Open Source Field Operation and Manipulation) is an open source code written in C++ to model and simulate fluid dynamics and continuum mechanics. It is possible to adopt the code and build new functionalities, libraries, solvers, and utilities. The software is community driven, and the various communities work on different fields of applications. This has expedited the progress and development of the software. Another advantage is the ability to use the software in parallel. In OpenFOAM, the

spatial discretization is performed using a cell centered co-located finite volume (FV) method for unstructured meshes with arbitrary cell-shapes, and a multi-step scheme is used for the time derivatives. To complete the FV-discretization the face fluxes need to be reconstructed from grid variables at adjacent cells, requiring interpolation of the convective fluxes and difference approximations for the inner derivatives of the diffusive fluxes; see Weller et al. [66], Jasak [67] and Rusche [68] for more details on the discretization and the numerics used in OpenFOAM. In this work, the OpenFOAM version 2.3.x is used.

OpenFOAM requires three directories to be present in any case file: system, constant, and "time" directories. These three files contain all the information needed to run a simulation. A constant directory contains two important subdirectories - the polyMesh folder, which contains the mesh information, and at least one file containing the physical properties of the system, typically the transportProperties file. Additional files may be present that contain thermodynamic properties, rotational parameters, or any initial constants the user wishes to specify. A system directory is composed of files that control the solution procedure. At a minimum, this directory includes the files: controlDict which is where the start and end time, time steps, and data output parameters are set; fvSchemes that contains the discretization schemes; and, fvSolution which stores the equation solvers, tolerances and other algorithm controls. The 'time' directories contain the data files for particular fields of interest. These data can either be initial or boundary conditions that the user has specified (in time step 0 file), or written data as the solution progresses [69].

Solvers

Numerous solvers are included with OpenFOAM that can all be modified to suit the user's specific requirements. They range from basic CFD solvers, to compressible, incompressible, multiphase, LES, DNS, combustion, heat transfer, stresses, electromagnetics, and even financial solvers. Many pre- and post-processing utilities are available ranging from mesh manipulation, velocity field analysis, to surface data sampling. A list, and a brief description, of the solvers that have been used in this work is shown below.

PotentialFoam: potentialFOAM is a useful solver to validate OpenFOAM since the assumptions of potential flow are such that an analytical solution exists for cases whose geometries are relatively simple (continuity equation $\nabla \cdot \overrightarrow{\mathrm{U}} = 0$ and pressure equation $\nabla^2 p = 0$). PotentialFoam can also be run more like a utility to provide a (reasonably) conservative initial U field for a problem. When running certain cases, this can be useful for avoiding instabilities due to the initial field being unstable. In short, potentialFoam creates a conservative field from a non-conservative initial field supplied by the user

SimpleFoam: simpleFoam is a steady-state Navier-Stokes solver which is based upon the SIMPLE [70] algorithm. This solver is ideal for rapidly converging to steady state solutions; this is the reason why it was used to produce all OF generated single phase results. The overall SIMPLE algorithm can be summarized as follows:

- Set all field values to some initial values.
- Begin the global iteration loop.

- Assemble and solve the under-relaxed momentum predictor equation.
- Solve the pressure equation and calculate the conservative fluxes. Update the pressure field with an appropriate under-relaxation. Perform the explicit velocity correction.
- Solve the other equations in the system using the available fluxes, and the updated pressure and velocity fields.
- Check the convergence criterion for all equations. If the system has not converged, start a new global iteration.

PimpleDyMFoam: pimpleDyMFoam is an implementation of the pimpleFoam solver that allows for dynamic meshes. Like pimpleFoam, the solver is transient, allowing for relatively large time steps thanks to the hybrid PISO-SIMPLE (PIMPLE) algorithm.
CavitatingFoam: cavitatingFoam is a fully compressible two-phase flow solver in which a barotropic equation of state is used. This solver was discarded because of the excessive computational execution time necessary for the physical conditions considered in this work.
InterPhaseChangeFoam: InterPhaseChangeFOAM models two incompressible, isothermal immiscible fluids with phase change and incorporates the VOF phase-fraction based interface capturing approach. One momentum equation is solved which incorporates the fluid properties of the mixture. The Kunz, Merkle, and Schnerr-Sauer models are included to simulate phase change, primarily for cavitation.
The first three solvers have been used to simulate the geometry of a centrifugal pumps starting from initialization and steady state solutions to dynamic mesh solutions. Among the multi-phase flow the solver interPhaseChangeFoam has been chosen.

3.2 Numerical model for simulating centrifugal pumps

Computational Fluid Dynamics (CFD) has an important role in predicting hydraulic turbomachinery performance and designing new impellers since it allows for a reduction of both design costs and time. As shown by S. Shah [71], there are many possibilities to simulate hydraulic turbomachinery. Steady-state simulations are useful to extend the basic understanding of the flow, but unsteady simulations are needed in order to take into account the actual flow interaction between steady (diffusers or volutes) and rotating (impeller) parts. The relative movement between impeller and volute generates an unsteady interaction which affects not only the overall pump performance but is also responsible for pressure fluctuations. Pressure fluctuations interact with the volute casing and give rise to dynamic effects (mainly unsteady forces) over the mechanical parts, which are one of the most important sources of vibration and hydraulic noise. Gonzalez et al. [72] showed the capability of a numerical simulation in capturing the dynamic and unsteady flow effects inside a centrifugal pump due to impeller-volute interaction. Viscous Navier-Stokes equations along with sliding mesh technique were applied to consider the impeller-volute interaction. The amplitude of the fluctuating pressure field at the blade passing frequency was successfully captured by the model for a wide range of operating flow rates. Both experiments and numerical predictions showed the presence of a spatial fluctuation pattern at the blade passing frequency as

a function of the flow rate. Wang and Tsukamoto [73] developed a numerical method for more realistic prediction of pressure fluctuations due to rotor-stator interaction in a diffuser pump by considering the change in operating point of the pump. The pressure fluctuations were predicted in 2-D unsteady incompressible flow using a vortex method, in which vortices shed from solid boundary were determined based on the momentum equations. It was reported that the pressure in the diffuser passage fluctuates with the basic frequency of the impeller blade passing frequency.
The use of OpenFOAM for CFD calculations is widely growing nowadays because it is opensource and it can be easily parallelized. OpenFOAM is able to perform steady, but also unsteady, simulations by using DNS (Direct Numerical Simulations), LES (Large Eddy Simulations) and RANS (Reynolds Averaged Navier-Stokes) approaches which are already available in OpenFOAM, but also by implementing hybrid methods, e.g., Detached Eddy Simulations, DES, and Partially Averaged Navier-Stokes, PANS. Furthermore, H. Nilsson [74] showed that OpenFOAM is able to reach good agreement with results obtained by commercial codes (e.g., CFX) for hydraulic turbomachinery, such as turbines, pumps and propellers.
Among the previously listed methods ,the RANS approach is the most common technique used to solve the flow field inside centrifugal pumps, but LES simulations are becoming more and more attractive especially when complex geometries and flow phenomena are involved [75]. In the last decade also the Immersed Boundary Method (IBM) [76] became more popular. It has been applied to simulate centrifugal pumps [77] and it has been implemented in OpenFOAM as shown by M. Specklin et al. [78]. This method allows one to handle multi-phase flows or fluid-structure interaction problems, in a single-phase framework. One of the main interests in IBM lies in the simplification of the model and especially in its suitability for use with Cartesian meshes of perfect orthogonal quality.
In this work the RANS method has been used because it is less time consuming compared to methods which require more detailed and finer grids and it is appropriate to get a reasonable estimation of the general performance of the centrifugal pump, from an engineering point of view, with typical errors below 10 percent compared to experimental data [71]. In order to verify the performance improvement prior to the construction and test of the impeller, a numerical investigation has been run with the open source code OpenFOAM by solving the 3D U-RANS equations. However, in order to validate the computational procedure, a simulation of the baseline geometry and a comparison of the results against the consolidated ones, obtained by means of the commercial CFD code CFX have been performed.

3.2.1 Governing equations and turbulence model

The unsteady RANS equations have been considered adequate in order to model the flow through the pump [71], where quantities have to be considered averaged over a time period short enough with respect to global unsteady phenomena, but long enough for statistical significance.
The turbulence model applied for the system closure is the k-ω SST, as proposed by Menter [79]. This turbulence model is a standard to perform numerical analysis in hydraulic turbomachinery [80]. It automatically uses the k-ω model in the near wall region and the k-ϵ model in the regions away from the walls. The k-ω SST model can

give accurate prediction of flow separation, hence explaining its common use for the numerical investigations of flow inside centrifugal pumps.
In the OpenFOAM computational environment either steady-state or transient simulations can be run in order to study hydraulic machines, as proposed by Shah et al. [71]. For steady-state simulations the application simpleFoam can be used. This application works with incompressible, stationary flows and it is based on the SIMPLE (semi-implicit method for pressure linked equation) algorithm. Moreover, the multiple-reference-frame (MRF) technique can be employed which actually neglects the rotor stator interaction since it does not allow the relative motion of the moving meshes (Frozen Rotor).
Because of the significant impeller-volute interaction, for the case under investigation, transient simulations have been preferred with respect to stationary ones [71]. Transient simulations in OpenFOAM involve the use of the application pimpleDyMFoam, which is based on the PIMPLE (merged PISO-SIMPLE scheme) algorithm. Rotating meshes have been considered for taking into account the impeller motion.
In the following simulations the convection, diffusion and gradient terms have been computed by using second-order upwind schemes, whereas the time derivative terms have been calculated by using a second-order backward scheme.

3.3 Description of the test rig for centrifugal pumps experimental tests

Experimental tests have been carried out at the test rig of Nuovo Pignone (Bari, Italy). Once realized by means of lost-foam casting technique, see paragraph 4.8, the prototype has been tested to verify the performance improvement pointed out by the numerical simulations and to validate the entire design process.
The facility is characterized by maximum flow rate = 600 m^3/h, maximum pressure = 35 bar, maximum rotational speed = 4800 rpm and maximum electrical motor power = 200 kW. Data have been collected at 1 s interval for a duration of 30 s, after having reached steady state conditions. The experimental setup for the characterization is constituted of a series of electronic measurement devices: two electromagnetic flow meter (accuracy 0.25%), three redundant static (accuracy 0.15%) pressure transducers either upstream and downstream the section test. A torque meter with integrated angular speed encoder, characterized by an accuracy class of 0.05%, has been used to calculate the pump efficiency. The measurement errors for Q, H, P and η at different flow rate are summurized in Fig. 3.1.

3.4 Numerical models for simulating cavitating flows

Cavitation includes complex phenomena such as the interaction of turbulence with phase-changes, steep pressure variations and pressure wave propagation, which can activate surface erosion. Indeed, several experimental tests have been carried out on Venturi ducts [81, 82] and hydrofoils [83, 84] in order to develop theoretical models helping in the prediction of the basic cavitation mechanisms. Moreover, various numerical algorithms have been developed with the aim of simulating cavitating flow, mainly based on one of the following two approaches [63]: 1) density based compressible solvers with an equilibrium cavitation model; 2) two-phase incompressible

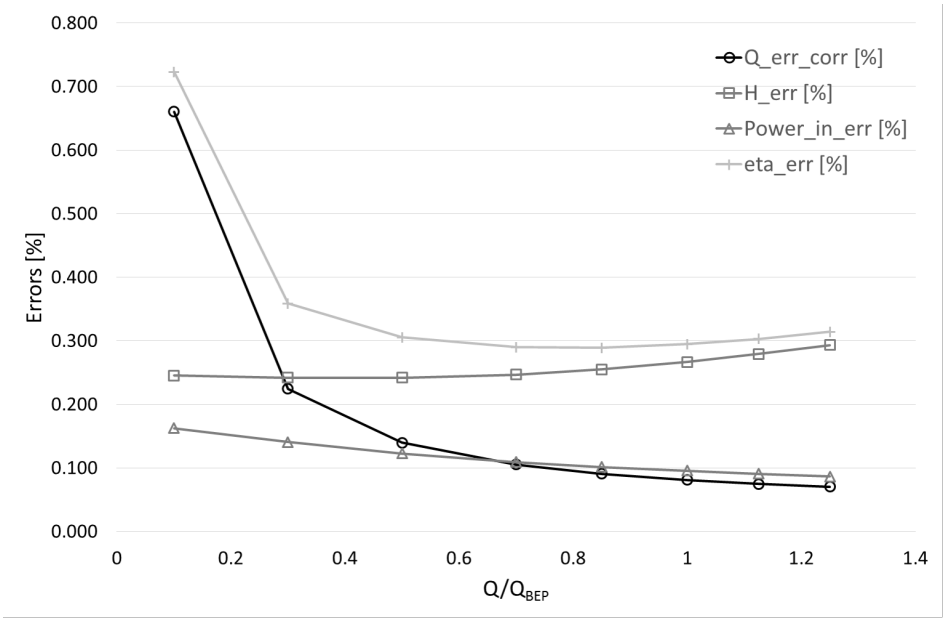

Figure 3.1: *Description of the errors for each quantity measured at the Hydraulic Laboratory, Nuovo Pignone, Bari.*

Navier-Stokes equation solvers in combination with mass transfer equations. Different studies have been carried out on 2D hydrofoils according to this latter approach. Various mass-transfer models are available in the literature and they normally include several empirical parameters that must be tuned for a particular flow condition and geometry by means of several experiments [81]. Moreover, various turbulence models have been tested in order to find the best combination between mass transfer models and turbulence models [85–87].

As far as simulation of two-phase flows is concerned, in this work simulations have been performed by means of OpenFOAM by solving the 2D Unsteady Reynolds-Average Navier-Stokes (U-RANS) equations for incompressible flow with the mass transfer model proposed by Schnerr and Sauer [88]. The attached cavities are strongly connected to the boundary layer behavior, while the bubble cavitation chiefly depends on the pressure distribution and the liquid nuclei content [16]. Because of the small angles of attack (max $5°$), this activity deals with quasi-steady cavitation and periodic cavitation. These phenomena require a transient approach. Even if high Reynolds numbers are considered, laminar to turbulent transition is crucial in order to capture the inception of attached cavitation, which occurs in the small recirculating bubble following laminar separation of the boundary layer, as it does for the transcritical flow around a circular cylinder [16]. The Unsteady RANS equations have been solved in order to model the quasi-steady sheet cavitation case studied here. These equations, in their conservative unsteady formulation, for Newtonian fluids without body forces and heat transfer, are presented in the Cartesian coordinates (eq.3.1) along with the continuity equation (eq.3.2) and the mass transport equation (eq.3.3) for liquid:

$$\frac{\partial \rho_m u_i}{\partial t} + \frac{\partial (\rho_m u_j u_i)}{\partial x_j} = -\frac{\partial p}{\partial x_j} + \frac{\partial}{\partial x_j}\left[\mu_m \left(\frac{\partial u_i}{\partial x_j} + \frac{\partial u_j}{\partial x_i}\right) - \mu_m \frac{2}{3}\frac{\partial u_k}{\partial x_k}\delta_{ij}\right] \tag{3.1}$$

$$\frac{\partial \rho_m}{\partial t} + \frac{\partial (\rho_m u_j)}{\partial x_j} = 0 \tag{3.2}$$

$$\frac{\partial (\rho_l \alpha_l)}{\partial t} + \frac{\partial (\rho_l \alpha_l u_j)}{\partial x_j} = \dot{m}^+ + \dot{m}^- \tag{3.3}$$

$$\rho_m = \rho_l \alpha_l + \rho_v \alpha_v \tag{3.4}$$

$$\mu_m = \mu_l \alpha_l + \mu_v \alpha_v \tag{3.5}$$

The subscript (l, v, m) refers to the liquid, vapour and mixture phases, respectively. The subscripts (i, j, k) denote the directions of the Cartesian coordinates. The source term, $(\dot{m}^+)$, and the sink term, $(\dot{m}^-)$, in eq.3.3 represent the condensation and evaporation rates, respectively. In OpenFOAM, the application, which allows one to solve this set of equations, is named InterPhaseChangeFoam. It is based on the Volume of Fluid (VoF) technique, which considers two incompressible, isothermal and immiscible flows and solves one global momentum equation and a transport equation for each flow adopting a PIMPLE algorithm. Moreover, this solver can perform simulations according to one of the following approaches: RANS, LES (Large Eddy Simulation) and DNS (Direct Numerical Simulation).

The surface tension force (f_σ) is added into momentum equation, and it is calculated per unit volume via Continuum Surface Force (CSF) mode [89] as:

$$f_\sigma = \sigma k \nabla \alpha \tag{3.6}$$

where σ is the surface tension coefficient defined as:

$$\sigma = -\nabla \frac{\nabla \alpha}{|\nabla \alpha|} \tag{3.7}$$

and k is the mean curvature of the free surface defined before in eq.3.6. In the used OpenFOAM version an improved version of VOF technique called "Compressive Interface Capturing Scheme for Arbitrary Meshes (CICSAM)" [89] is implemented and used in interPhaseChangeFoam solver. In this model an additional parameter "interface-compression velocity (U_c)" in the surroundings of the interface is described to promote the interface resolution by steepening the gradient of the volume fraction function.

The mass transport models (i.e., the cavitation models) available in OpenFOAM are those developed by Kunz et al. [90], Merkle et al. [91], and Schnerr and Sauer [2]. In these simulations the condensation and the evaporation rates are modeled according to Schnerr and Sauer [2]:

$$\dot{m}^- = 3 C_v \rho_v \rho_l \sqrt{\frac{2}{3\rho_l}} \frac{1}{R \rho_m \sqrt{|p - p_v|}} (1 - \alpha_m + \alpha_l) min(p - p_v, 0) \tag{3.8}$$

$$\dot{m}^+ = 3 C_c \rho_v \rho_l \sqrt{\frac{2}{3\rho_l}} \frac{1}{R \rho_m \sqrt{|p - p_v|}} \alpha_l max(p - p_v, 0) \tag{3.9}$$

which are based on the Rayleigh-Plesset equation. The volume fraction of the water vapour nuclei, α_{nuc}, and the radius of the bubble, R_B, used in the previous equations (6, 7) are calculated as follows:

$$\alpha_{nuc} = \frac{n_0 \pi d_{nuc}^3/6}{1 + n_0 \pi d_{nuc}^3/6} \tag{3.10}$$

$$R_B = \sqrt[3]{\frac{3}{4\pi n_0} \frac{1 + \alpha_{nuc} - \alpha_l}{\alpha_l}} \tag{3.11}$$

The Schnerr and Sauer model assumes that several vapour bubbles (called nuclei) inside the liquid act as the initial sources of the phase change, and cavitation inception starts from their locations and due to their presence. The number, size and distribution of these bubbles can be determined during water quality experimental tests. To simplify the numerical modelling, it is assumed that the initial nuclei have been evenly distributed throughout the liquid, and they have the same size corresponding to the smallest size that vapour bubbles can assume. It is known that the quantity of nuclei (n) and the bubble diameters (d_{nuc}) can strongly affect the results of the simulations [92]. For these simulations n and d_{nuc} are set equal to $1.6 \cdot 10^{13}$ and $2 \cdot 10^{-6}$, respectively and both the condensation coefficient, C_c, and the evaporation coefficient, C_v, coincide to 1, the default value in OpenFOAM. These mass transfer model equations have been solved in combination with either k-ω SST or k-kl-ω models for turbulence closure [87, 93, 94]. The Courant number for all the simulations is approximately the same and it is equal to 0.3. The gradient terms have been computed using a second-order upwind scheme and a cell limited scheme for the pressure. The convection terms have been computed using a second-order backward scheme and a first-order upwind scheme for the turbulence. The laplacian terms have been resolved using a limited corrected scheme while the time integration scheme is a first-order Euler scheme.

3.4.1 Reboud correction

A key point to compute the unsteadiness of the cavitation pocket is linked to the overproduction of eddy viscosity by standard turbulence models. Goncalvès illustrated the importance of using an eddy-viscosity limiter to capture the re-entrant jet dynamics. In this study, the Reboud limiter is added to the turbulence model [95]. Reboud proposed an arbitrary limiter by introducing a function $f(\rho)$ in the computation of the turbulent viscosity for the k-ϵ model:

$$\mu_t = f(\rho) C\mu \frac{k^2}{2} \tag{3.12}$$

with

$$f(\rho) = \rho_v + (1 - \alpha)^{n'} (\rho_l - \rho_v) \tag{3.13}$$

where n' is a parameter fixed to 10. This correction is extended to other turbulence models with the same function $f(\rho)$. For a correct simulation of the re-entrant jet, the Reboud eddy-viscosity limiter is added [96, 97]. In this work for simulating 2D hydrofoils with various angles of attack (α), the Rebound eddy-viscosity limiter has been used applied to k-ω SST turbulence model.

CHAPTER 4

Design of the novel impeller - BTC

4.1 Introduction

This work deals with low-medium specific speed double suction pumps and it describes a 1D design procedure coupled with computational fluid dynamics (CFD) with the purpose to improve the efficiency of their impellers with respect to conventional designs. Low-medium specific speed double suction impellers ($n_q < 60$) are chiefly used when medium-high hydraulic heads ($40\,m < H < 250\,m$) and low-medium flow rates ($Q < 2$ m^3/s) are required.
Commonly, a double suction impeller is made of two single suction impellers in a back-to-back arrangement [14], each one having a lower specific speed number and a marked radial impeller shape. At low-medium specific speeds, in order to ensure higher values of the flow rate, a double suction impeller is preferred to a mixed axial-radial impeller with the same specific speed, the latter being more subject to the risk of cavitation. Furthermore, a double suction impeller is able to balance the axial hydraulic thrust resulting in a compact system.
The performance of a centrifugal pump is strongly affected by disparate sources of loss (performance degradation), e.g., fluid dynamic friction losses. Concerning the impeller, the above mentioned losses mainly depend on the shape of the vanes. Furthermore, slip depends on the number of blades of the impeller, which is finite, and on the pressure conditions acting on both pressure and suction sides of the blades [14].
In line with the works concerning geometry optimization of centrifugal pumps, previously described in paragraph 2.2.9, in this chapter the techniques and the methodologies applied to design a novel impeller for double suction centrifugal pumps are described. The design procedure is based on the assumption that slip at the outlet of the impeller can be reduced by increasing the number of blades [14]. Indeed, in the past, different impeller geometries have been proposed trying to increase the number of the blades

along the circumferential direction at the outlet of the impeller in order to improve the efficiency of double suction pumps and to reduce secondary flows at part load [98–101]. They show completely new blade arrangements with respect to the ones conventionally used. Nevertheless, these proposals lack of simplicity, do not introduce detailed descriptions of the channel shape and give no information about the flow velocity control inside the impeller channels [102, 103].
The new impeller design allows to double the number of blades at the outlet of the impeller in a way that the channel outlets, coming from the two sides, are circumferentially arranged and therefore the flow guidance is increased. The basic idea behind the novel impeller is its compatibility with the casing of a conventional impeller. The channels not only intersect each other without interference but also have a specific cross sectional area distribution along the center line (c_{line}). As it will be shown, this results in an increase of the slip factor, which leads to a higher value of the hydraulic head with respect to a conventional configuration with the same impeller outlet diameter. Other results are a higher value of the hydraulic diameter (D_h) and a lower length of the channels (L), which allow for a lower amount of losses inside the new channel, hence improving the hydraulic efficiency. This will be highlighted by evaluating the rotary stagnation pressure inside the channel.
The novel geometry, presented in this work, has been designed writing a specific 1D code and performing simplified (single vane) numerical simulations carried out by means of the commercial CFD code ANSYS Fluent®. Once the preliminary design came to an end, the novel impeller was investigated both numerically and experimentally (see Chapter 5). The entire centrifugal pump geometry has been modeled and investigated by means of the CFD open-source code OpenFOAM in order to validate the results previously obtained via single vane simulations and to evaluate the influence of the stator parts, suction pipe and double volute, on the overall performance.

4.2 Design of the novel impeller

The new double suction impeller is supposed to be used in substitution of a conventional one, defined as “baseline”, whose characteristic curve in non-dimensional form is shown in Fig.4.1.

The pump specific speed (n_q), defined as follows (paragraph 2.2.7):

$$n_q = n\frac{\sqrt{Q_{BEP}/f_q}}{H_{BEP}^{0.75}} \tag{4.1}$$

is equal to 21.3. In eq.4.1, *n* is the rotational speed (rpm), *Q* is the volumetric flow rate (m^3/s), f_q is the number of impeller entries (f_q = 2 for a double suction one), *H* is the hydraulic head (m) and BEP stands for Best Efficiency Point. In the next paragraphs, the comparison between different machines will be performed by means of two dimensionless parameters, namely the head coefficient, which is equal to:

$$\psi = \frac{2gH}{u_2^2} \tag{4.2}$$

and the flow coefficient, which is defined as follows:

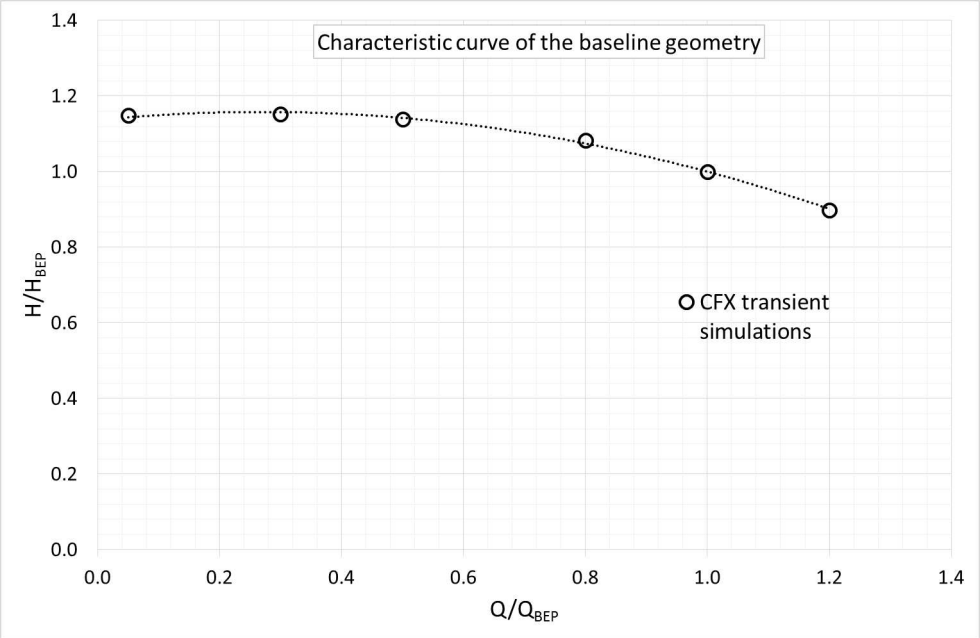

Figure 4.1: *Characteristic curve (H/H_{BEP} - Q/Q_{BEP}) of a conventional double suction impeller obtained by means of transient CFX simulations (Grid size ≅ 40 milion cells). Simulations performed by the Nuovo Pignone CFD team.*

$$\varphi = \frac{Q}{\pi D_2^2 u_2/4} \tag{4.3}$$

In eq.4.3 D_2 is the outer diameter of the impeller, $u_2 = \pi D_2 n/60$ is the tangential velocity calculated at the outer diameter and *g* is the standard gravity. Furthermore, the efficiency of these machine has been calculated as follows:

$$\eta = \frac{\rho g H Q}{C\omega} \tag{4.4}$$

where ρ is the density of the fluid (kg/m^3), ω is the rotational speed in (rad/s) and *C* is the torque (Nm) exchanged by the fluid and the impeller, including the shear stress acting on the internal and external surfaces of the impeller (disk friction losses). These parameters allow to compare the performance of various centrifugal pumps, regardless their dimensions and operating conditions.

The main features of the baseline geometry are summarized in Tab.4.1.

Table 4.1: *Main information of the baseline geometry.*

$D_2(mm)$	$l_2(mm)$	N_b	$\beta_2(^\circ)$	$\alpha_1(^\circ)$	η_v	$n(rpm)$
252	25 (2×12.5)	7	28	25	0.964	3900

4.3 Design process

The novel geoemtry has been designed to retrofit a conventional one. To this aim the stator parts, which are shown in Fig.4.2, represent design constraints to the outer diameter and the axial size. According to these constraints, the new impeller has been designed together with other three important restrictions to be satisfied:

- preserving the same specific speed number (n_q) of the baseline geometry;
- guaranteeing at the Best Efficiency Point (BEP) a kinematic flow angle at the inlet of the volute (α_3) in accordance with the optimum α_3 of the volute (there is no bladed diffuser);
- satisfying the matching of the relative inlet flow angle with the inlet geometric angle of the impeller.

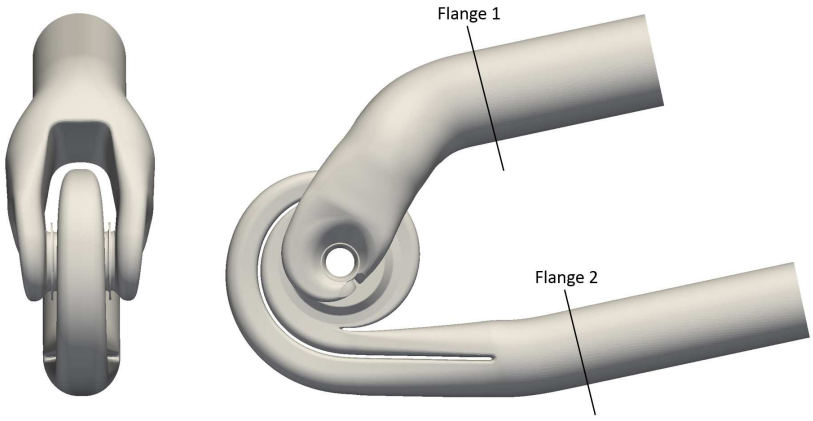

Figure 4.2: *Front and side views of the 3D CAD model, which includes the inlet duct, the impeller and the double volute.*

The design process of the new double suction impeller has been developed by writing a specific 1D code. Initially, the code empirically estimates the slip factor, the hydraulic efficiency and the losses between the outer diameter and the volute inlet. After that the geometry is genereted (see paragraph 4.5) and simulations are then run (see paragraph 4.6) on a single blade channel in order to define the correct value of the flow angles and fluid dynamics parameters peviously assumed. In Fig. 4.3, the design process is described in detail.

4.4 Geometry definition

4.4.1 Flow kinematics

Firstly, the velocity triangles at the inlet and the outlet of the impeller have been calculated according to geometry details (Tab.4.1) and constraints described in paragraph 4.3. An initial value for the slip factor has been assumed to predict the current value of c_{u2} at the outer diameter of the novel impeller. A modified empirical formulation has been proposed for the slip. Its expression is:

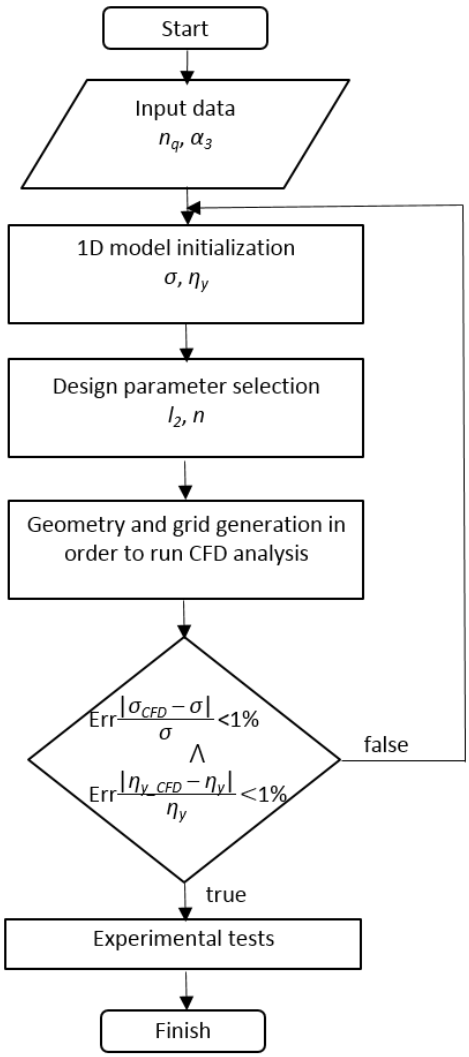

Figure 4.3: *Flow chart of the design process.*

$$\sigma = 1 - \frac{\sin \beta_2{}^{0.5}}{(aN_b + b2N_b)^{0.7}} \tag{4.5}$$

where a and b are two coefficients that take into account the new vane design according to the embodiments described in the introduction of this chapter. If $a = 1$ and $b = 0$, the modified σ definition shall be equivalent to the one commonly used for conventional centrifugal pumps. This parameter acts directly on the values of w_{u2} and β_2, respectively the value of the w_u and β at the outlet of the channel.

When this preliminary 1D calculation has been concluded, a study of the motion of a single particle of fluid started. The whole time that a particle of fluid would spend through the channel has been split into 20 time steps (corresponding to 21 points in the space (N). This number of steps has been chosen as a good compromise between curves refinement and 1D model complexity. For this purpose, a specific particle has been chosen, whose starting point at the impeller eye coincides with the c_{line}. The hypothesis is that the locus of points, defined by its motion, coincides with the c_{line} in

a meridional plane. The c_{line} is the line which divides the projection of the channel on the meridional plane into two parts both supplying half of the flow rate, $Q/2$. At the inlet of the impeller the definition of c_{line} leads to:

$$R_{cline} = \sqrt{\frac{R_s + R_h}{2}} \tag{4.6}$$

where R_s and R_h are the shroud and hub radius, respectively. Working with c_{line}, a more accurate calculation of the particle kinematis will be obtained, since it is more representative of the fluid behavior inside the channel than the m_{line}.

Under the hypothesis that the flow at the impeller eye has a purely axial direction, the velocity triangle at the inlet (c_{line}) lies on the blade-to-blade plane (axial-tangential) where the meridional direction coincides with the axial one. This triangle of velocity evolves in time and space, it goes from a purely axial to a purely radial direction. Its components (meridional, tangential), but also the inclination of the plane on which it lies, change. A function called γ has been defined to describe the variation of this plane; it represents the angle between two vectors, the axial direction and the vector tangent to the c_{line}. The assumed γ function is showed in Fig.4.4.

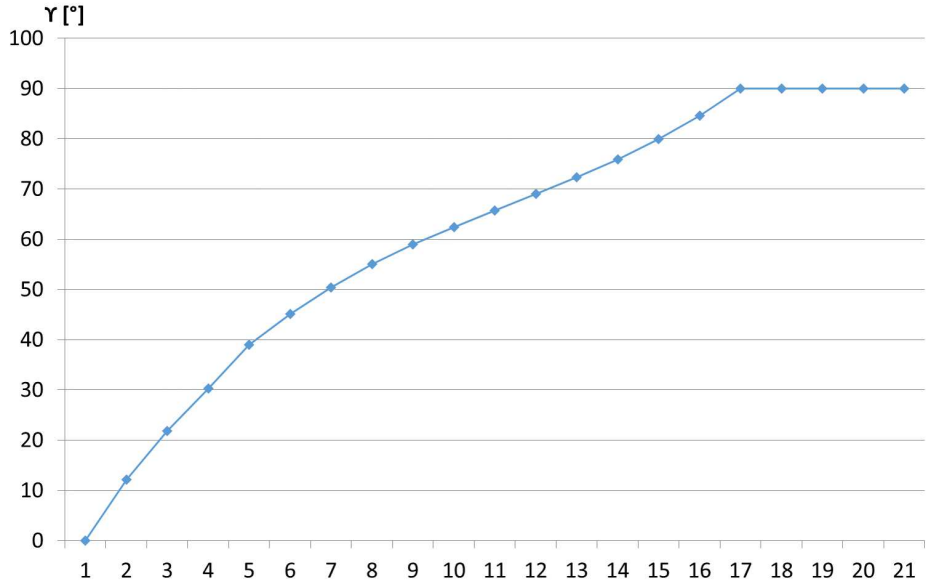

Figure 4.4: *γ inclination of the plane on which the relative velocity vector lies.*

The components of the triangle of velocity are constrained at the inlet and the outlet of the channel, in order to guarantee the constancy of the performance (in terms of $L_i = c_{u2}u_2 - c_{u1}u_1$), whereas the path described by the particle inside the impeller vane has been obtained by assigning specific functions to the velocity vectors. It is important to highlight that every little change in these functions can affect significantly the entire geometry, but not the performance since the velocity vectors at the inlet and the outlet are fixed. The three components of the relative velocity vector (w) are: w_{tan} (circumferential component - also known as w_u), w_{axi} (axial component) and w_{rad} (radial component). The vectorial sum of the second and the third component gives w_{mer} (meridional component) (Figs.4.6 and 4.7) while $w = w_{tan} + w_{mer}$ (Figs.4.5 and 4.6).

For the w_{tan}, a linear function has been imposed, see Fig.4.5. Its final value depends on the slip factor formulation:

$$w_{u2} = u_2 - \frac{c_{u2}}{\sigma} \tag{4.7}$$

where c_{u2} depends on Q and α_2, the latter derives from the constraint α_3 at the inlet of the volute.

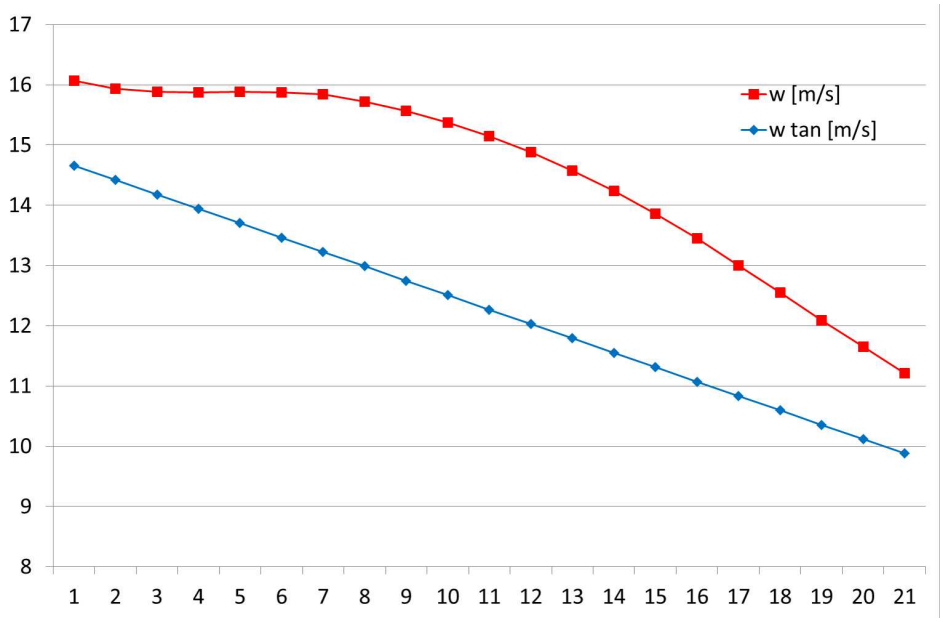

Figure 4.5: *w_{tan} and w function assumed for each point in which the path of the particle is discretized.*

In this model the w_{mer} function is composed of three different curves: a "Bézier" curve, a section of parabola and a line. As will be shown later, this combination is useful to avoid unexpected shape of the blade height, B. Moreover, the values for the meridional velocity are comprehensive of the blade blockage effect due to the blade thickness.

As can be easily deduced, w_{axi} and w_{rad} result by a simple calculation involving the assumed values of w_{mer} and γ at each point (N), as shown in Figs.4.7 and 4.6 for a generic couple of w_{mer} and γ. At this point, the velocity triangle can be drawn in every single point from the inlet to the loutlet of the vane.

$$w_{rad} = w_{mer} \sin \gamma \tag{4.8}$$

$$w_{axi} = w_{mer} \cos \gamma \tag{4.9}$$

4.4.2 3D cline

In order to obtain the 3D domain, time information has to be introduced. It is necessary to calculate the position of the fluid particle once the values of the velocity vectors have been imposed. The results are the coordinates (x, y, z) of the points representing the c_{line} in the three dimensional space.

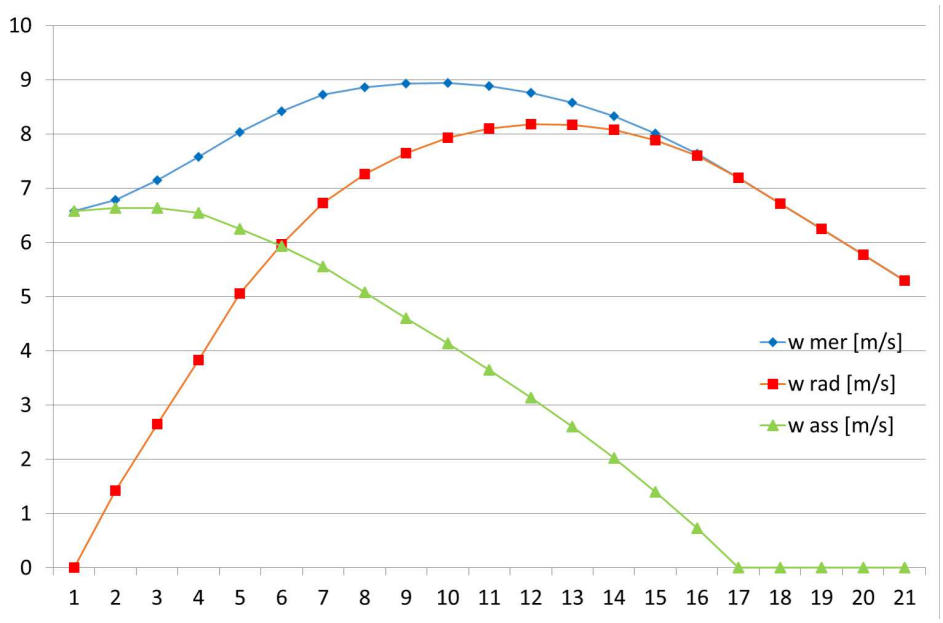

Figure 4.6: *w_{mer}, w_{rad}, w_{ass} functions assumed for each point in which the path of the particle is discretized.*

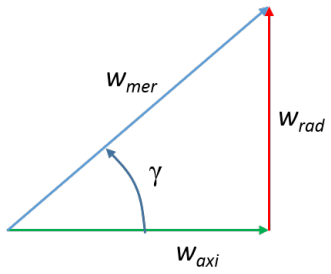

Figure 4.7: *Velocity vector composition.*

As explained at the beginning of the paragraph 4.4, the main dimensions, i.e., the radial (D_2) and the axial (Δx) dimensions, are given once the stator parts have been chosen. Thus, to begin this calculation a maximum axial c_{line} allowable displacement is required. It represents the difference in the meridional plane between the x-projections of the first and the last point of the c_{line} (where the impeller is totally radial $\gamma = 90°$). The Δx value has been assumed equal to half of the axial size of the double suction impeller of the baseline geometry. Under the hypothesis that the particle will move from one point to another (of the 3D c_{line} called s_{line}) with a constant time step Δt, two different Δt have been defined: the first one, Δt_1, concerns the time in which the particle flows in the mixed (axial-radial) zone, from 0 to N_1; the latter, Δt_2,concerns the totally radial zone, from N_1 to N. They have been defined as follows:

$$\Delta t_1 = \frac{\Delta x}{\sum_{N1} w_{axi_i}} \tag{4.10}$$

$$\Delta t_2 = \frac{R_2 - R_{x,max}}{\sum_{N} w_{rad_i}} \tag{4.11}$$

The line describing the particle path in the space is called s_{line} (stream line):

$$S = \sum_{N-1} \Delta s_i \tag{4.12}$$

where each Δs (displacement in the space) is obtained by the vectorial sum of three independent displacements along the axial, the radial and the circumferential directions. Herein, the equations used are based on polar coordinate system (x, ρ, ϕ), eq. 4.13, 4.14 and 4.15. In the following equations the subscript i goes from 1 to 21, the number of steps in which the path of the fluid particle has been divided.

$$x_{i+1} - x_1 = w_{axi}\Delta t_1 \tag{4.13}$$

$$\begin{cases} \phi_{i+1} - \phi_i = \tan^{-1}\left[\frac{w_{axi}\Delta t_1}{\rho_i}\right] & \text{for } \gamma < 90°, \\ \phi_{i+1} - \phi_i = \tan^{-1}\left[\frac{w_{axi}\Delta t_2}{\rho_i}\right] & \text{for } \gamma > 90°\text{-} \end{cases} \tag{4.14}$$

$$\begin{cases} \rho_{i+1} - \rho_i = w_{rad_i}\Delta t_1 & \text{for } \gamma < 90°, \\ \rho_{i+1} - \rho_i = w_{rad_i}\Delta t_2 & \text{for } \gamma > 90°, \end{cases} \tag{4.15}$$

In the following Figs.4.8,4.9,4.10, 3 different views of the s_{line} are shown. The c_{line} (Fig.4.10) results from the composition of axial and radial displacements.

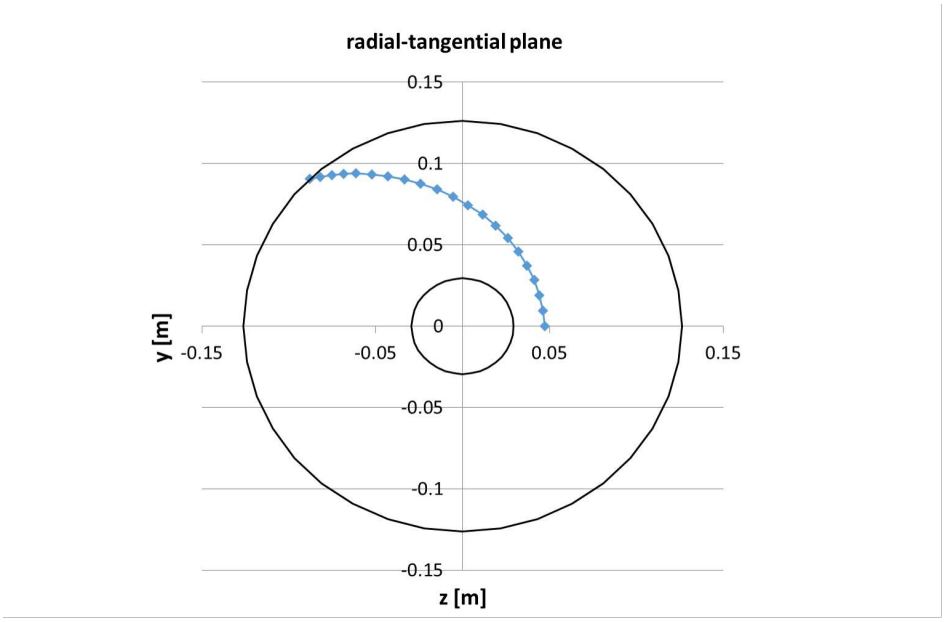

Figure 4.8: *The outer diameter (D_2), the hub diameter (d_1) and s_{line} displayed in a radial-tangential plane.*

4.4.3 Geometry of channels

Another important step towards the complete 3D design is to define the shape of the channel. The design of the channel starts from the s_{line}. As shown in Fig.4.10, the s_{line} without tangential components degenerates in the c_{line}.

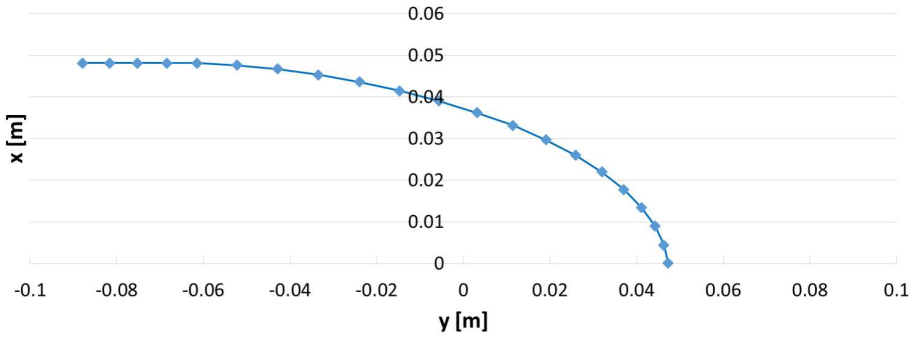

Figure 4.9: *View of the s_{line} on the $x - y$ plane.*

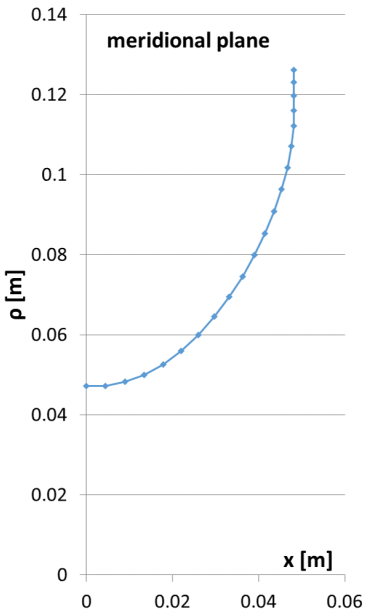

Figure 4.10: *View of the s_{line} in the meridional plane, which corresponds to the c_{line} curve.*

Hence, around each point of the c_{line} a four-sided polygonal cross section area of the channel has been drawn. The new design is possible by means of the variation of a particular parameter, namely α. The α parameter usually defines the width of a single vane, i.e., the angular distance from two blades of an impeller, see Fig.4.11. Generally, a conventional vane is characterized by a constant value of α, which is equal $2\pi/N_b$, from the inlet to the outlet of the channel.

One of the purposes in the design of new geometry has been that of improving the slip factor of conventional machine, which is generally achieved by increasing the number of blades. However this induces loss of performance due to higher friction losses, as for instance occurs with the introduction of slitter blades. In this case the number of blades, belonging to the two impellers of a double suction pump which are arranged in a back-to-back configuration, does not change; on the other hand, the circumferential distance between each trailing edges of the single impeller is reduced. This modification introduces the risk of interpenetration of the two vanes coming from the opposite sides. To draw a geometry in which, at the outer diameter (D_2), the vanes'

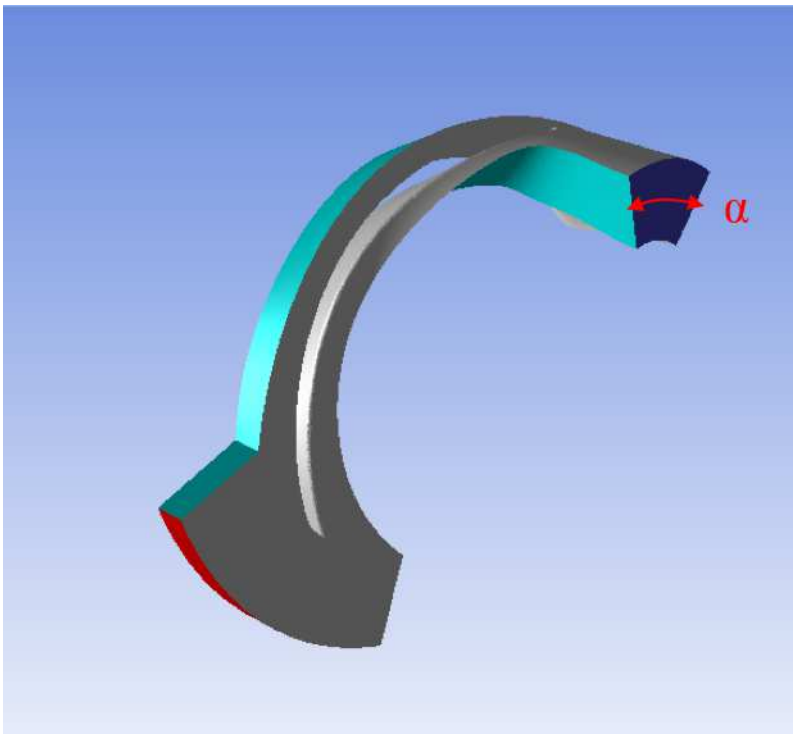

Figure 4.11: *3D CAD of the vane of a conventional geometry, in which the vane width (α) is highlighted.*

outlets are arranged in a way that they come up alternately from the two sides of the double suction pump, a different definition of α was needed. Actually, in this work α goes progressively from $2\pi/N_b$ to π/N_b. Furthermore, the α parameter needs to reach the value of π/N_b where the c_{line} is completely radial, but in this case to avoid the interpenetration of the channels it quickly reaches its half value.

At the inlet the channel section is basically made of two arcs of circumference (the hub and the shroud) and 2 radial segments (the leading edge of two blades), whereas the outer section, is made of 2 arcs of circumference and 2 axial segments which represent the trailing edge of the blades.

Starting from the value of the mass flow rate (Q), which is obviously constant in every section of the channel, a value of the blade blockage (ξ) has been calculated in each section with the relative velocity angle β, see Fig.4.13, by means of the eq.4.16.

$$\xi_i = 1 - \frac{N_{b_i}\delta_i}{\sin\beta_i \pi \rho_i} \tag{4.16}$$

In eq.4.16, δ_i is the blade thickness and ρ_i is the radial coordinate. This allows to evaluate the correct cross-sectional areas (A) of the vane taking into account the blade thickness, that will be added in the following. Indeed, the size of these areas does not include the blade size. Therefore, the value of the area A_i is calculated as:

$$A_i = \frac{Q_{channel}}{\xi_i w_{mer_i}} \tag{4.17}$$

The value of the area is necessary to arrange the four vertices of the channel section with respect to the c_{line}. It is worth stressing the point that the parameter ξ depends

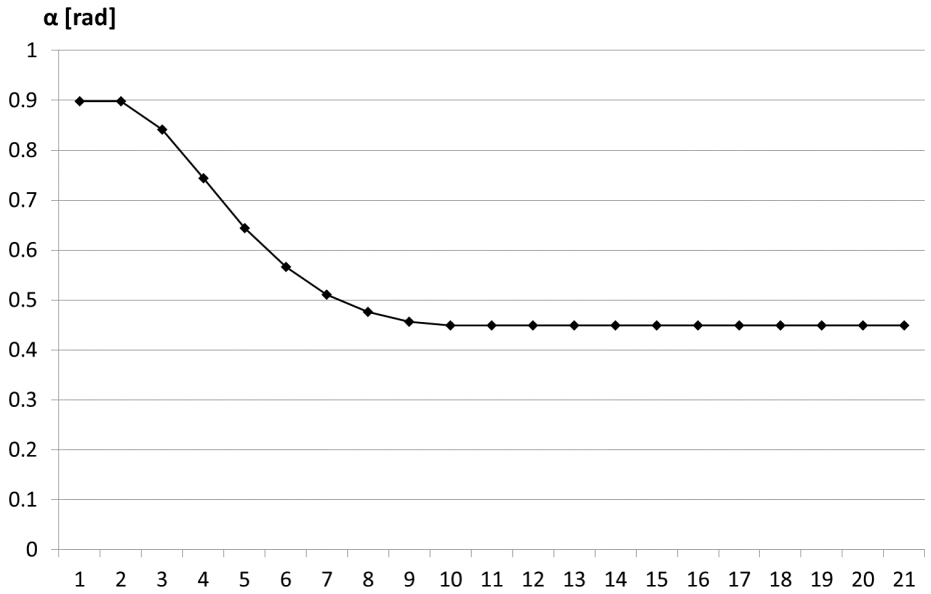

Figure 4.12: *Value of the width of the vane (α for a 7 blades impeller for each point in which the path of the particle is discretized.*

also on the number of blades (N_b). Because of the complexity of the geometry, it might be supposed that the number of blades is not constant but varies from the inlet towards the outer diameter (for this reason a subscript is present for N_b in eq.4.16). A way of considering the N_b evolution is to derive it proportionally from the α function.

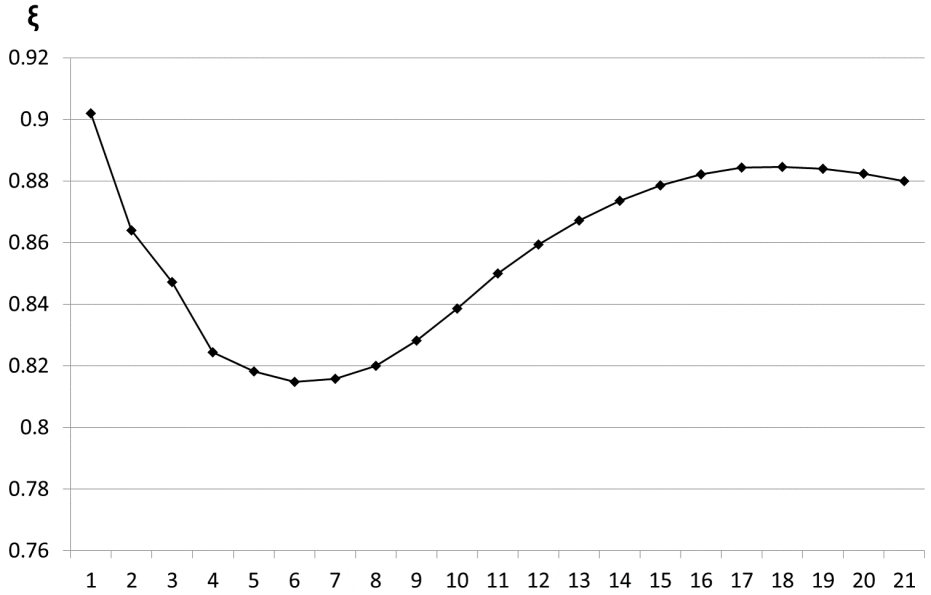

Figure 4.13: *Evolution of the blade blockage along the c_{line}.*

In order to define the blade height, two values, B_1 and B_2, have been introduced, the first to be added up and the latter to be added down the c_{line} curve, their sum being

equal to B. Their expression has been derived from a second order equation:

$$\frac{A_i}{2} = (\rho_{c_i} \pm \frac{B_i}{2}) B_i \theta_i \tag{4.18}$$

where only one result is meaningful.

$$B_1 = \frac{\frac{\rho}{\cos\gamma}\Delta\theta - \sqrt{(\frac{\rho}{\cos\gamma}\Delta\theta)^2 + 4\frac{\Delta\theta}{2}\frac{A}{2}}}{-\Delta\theta} \tag{4.19}$$

$$B_2 = \frac{\frac{\rho}{\cos\gamma}\Delta\theta - \sqrt{(\frac{\rho}{\cos\gamma}\Delta\theta)^2 + 4\frac{\Delta\theta}{2}\frac{A}{2}}}{\Delta\theta} \tag{4.20}$$

The results of the blade height calculated for each point are displayed in Fig.4.14.

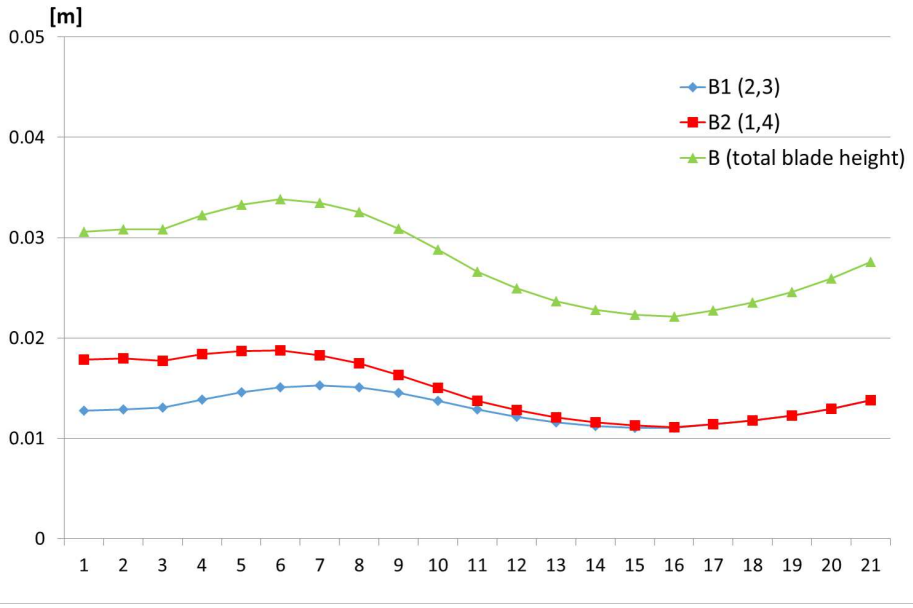

Figure 4.14: *Blade height, resulting from the imposed functions and calculation.*

To localize the four vertices of the cross section area of the channel another set of equations expressed in cylindrical coordinates has been used, eq. 4.21, 4.22, 4.23 and 4.24. The following equations refers to the vertices 1, 2, 3 and 4 in Fig. 4.15:

$$\begin{cases} x_{1_i} = x_{c_i} + B_{2_i}\cos\frac{\Delta\theta_i}{2}\sin\gamma_i + \frac{\rho_{c_i}}{\sin\gamma}(1-\cos\frac{\Delta\theta_i}{2})\sin\gamma_i \\ \rho_{1_i} = \frac{\rho_{c_i} - B_{2_i}\cos\gamma_i\cos\frac{\Delta\theta_i}{2}}{\cos\frac{\alpha}{2}} \\ \phi_{1_i} = \phi_c - \frac{\alpha_i}{2} \end{cases} \tag{4.21}$$

$$\begin{cases} x_{2_i} = x_{c_i} - B_{1_i}\cos\frac{\Delta\theta_i}{2}\sin\gamma_i - \frac{\rho_{c_i}}{\sin\gamma}(1-\cos\frac{\Delta\theta_i}{2})\sin\gamma_i \\ \rho_{2_i} = \frac{\rho_{c_i} + B_{1_i}\cos\gamma_i\cos\frac{\Delta\theta_i}{2}}{\cos\frac{\alpha}{2}} \\ \phi_{2_i} = \phi_c - \frac{\alpha_i}{2} \end{cases} \tag{4.22}$$

$$\begin{cases} x_{3_i} = x_{c_i} - B_{1_i} \cos\frac{\Delta\theta_i}{2} \sin\gamma_i - \frac{\rho_{c_i}}{\sin\gamma}(1 - \cos\frac{\Delta\theta_i}{2}) \sin\gamma_i \\ \rho_{3_i} = \frac{\rho_{c_i} + B_{1_i} \cos\gamma_i \cos\frac{\Delta\theta_i}{2}}{\cos\frac{\alpha}{2}} \\ \phi_{3_i} = \phi_c + \frac{\alpha_i}{2} \end{cases} \tag{4.23}$$

$$\begin{cases} x_{4_i} = x_{c_i} + B_{2_i} \cos\frac{\Delta\theta_i}{2} \sin\gamma_i + \frac{\rho_{c_i}}{\sin\gamma}(1 - \cos\frac{\Delta\theta_i}{2}) \sin\gamma_i \\ \rho_{4_i} = \frac{\rho_{c_i} - B_{2_i} \cos\gamma_i \cos\frac{\Delta\theta_i}{2}}{\cos\frac{\alpha}{2}} \\ \phi_{4_i} = \phi_c + \frac{\alpha_i}{2} \end{cases} \tag{4.24}$$

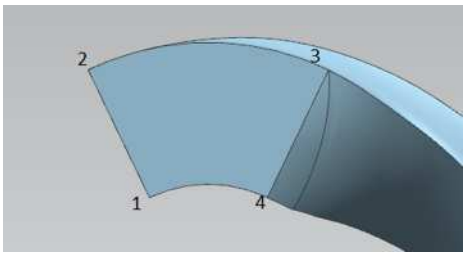

Figure 4.15: *Representation of the vertices of the cross section area with tag number at the inlet of the vane.*

The segments that link vertex 1 to vertex 2 and 3 to 4 represent the blades, while the arcs that connect 1 to 4 and 2 to 3 represent the hub and shroud, respectively. In the previous equations the angle θ is defined as:

$$\theta = tan^{-1}(\tan\alpha \cos\gamma) \tag{4.25}$$

The resulting channel shape is shown in the meridional plane, Fig.4.16.

To improve the surface design of the blades, four more points for each section and thus four more splines have been added to the first model ($u, d, bd1, bs1$), see Fig.4.17. These splines allow to draw more appropriate blade surfaces, without steep curvatures, and to maintain the desired channel cross section area along the entire impeller.

Blade thickness

This kind of geometry does not have conventional shape of vanes and blades, but two important characteristics are left unchanged: the leading edge and the trailing edge blade thickness. The leading edge has been designed by means of the NACA five digits foil 16012. Differently form the common blade that constitutes a centrifugal pump, for this purpose the blade thickness has been kept constant from the end of the leading edge(maximum thickness of the NACA foil) to the trailing edge. The surfaces of the blades diverge from the leading edge and, once they reach the outer diameter, they assembly the trailing edge of the blades with surfaces belonging to vanes coming up from the opposite site of the impeller, see Fig.4.18. The blade profile has been defined starting from the splines $1 - bs1 - 2$ and $4 - bd1 - 3$, which delimit the channel, see Fig. 4.18.

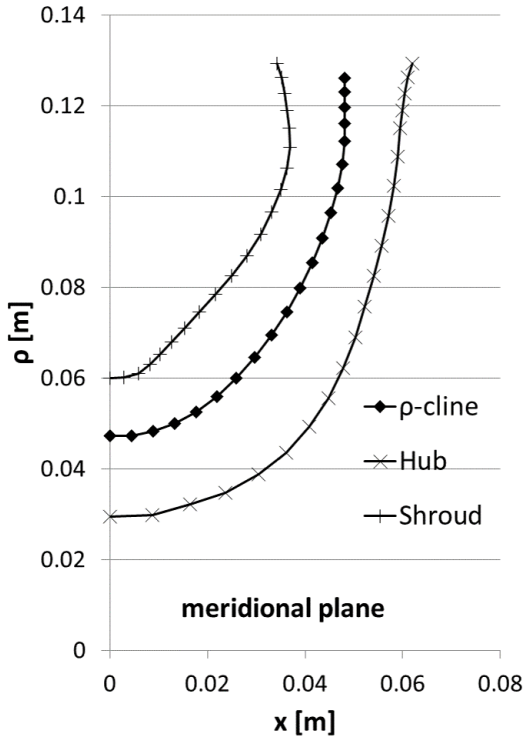

Figure 4.16: *Plot of the c_{line}, hub and shroud curves in the meridional plane.*

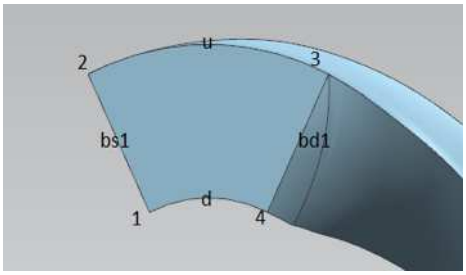

Figure 4.17: *Points added to improve the surface drawing of the vanes.*

Chamfer

Once the α development is fixed, the size of the channel can be modified by varying the function by which the w_{mer} is defined, see Fig.4.6 paragraph 4.4.1. The higher is the velocity, the higher is the reduction of the blade height, thus avoiding the channel interpenetration, which is one of the complexity of the novel geometry. However, the improvement obtained through the increase of the mean value of the w_{mer} does not succeed in avoiding the channel interpenetration. To completely avoid the interpenetration between channels, a chamfer has been introduced on the right corner (4) at the bottom of the section. This geometry modification is not necessary for all the length of the channel, but it has been designed only for a short region, where the intersection is more probable. Therefore, the four-sided polygonal channel section becomes a five-sided polygonal one. Two parameters have been introduced to define the width of the chamfer along the tangential ($\Delta\gamma$) and radial direction ($\Delta\rho$).

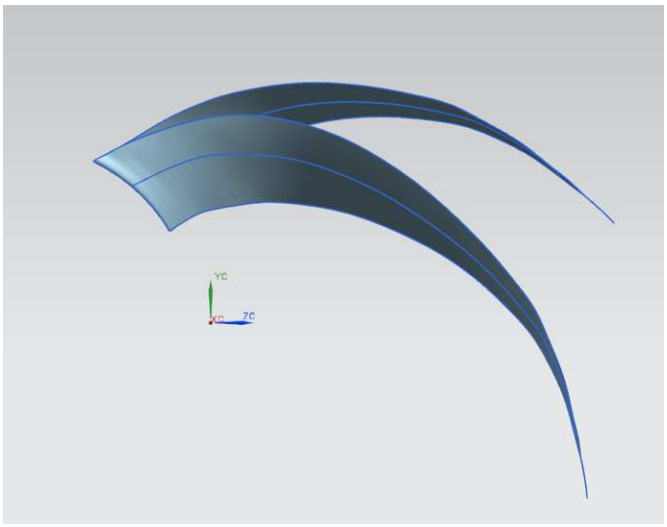

Figure 4.18: *3D CAD of the novel blades.*

Therefore, the control parameters necessary to avoid channel interpenetration are essentially three: the cross section area of the channel and its shape, function of w_{mer} and α, and a chamfer placed on the bottom right side of the channel.

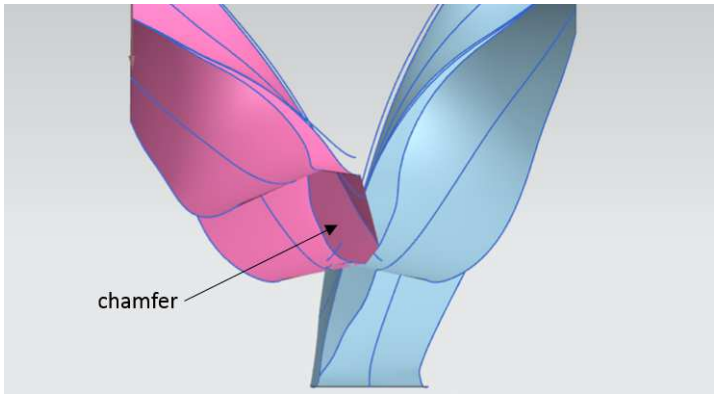

Figure 4.19: *Chamfer application to channels coming up from the two side of a double suction impeller.*

In order to monitor the channel interpenetration, an on-purpose strategy has been developed. It consists in looking for the intersections between two adjacent channels and a cylindrical surface with the possibility to change the radius of this cylinder. This allows one to inspect the channel deformation at various radii. In Fig.4.20 the view of the channel section at ρ=0.09 and how its size changes by increasing the meridional velocity (w_{mer}) are represented .

The design strategy described in this chapter allowed to draw the first prototype, see Fig.4.21.

4.5 Numerical simulations of the single vane

During the design process described in the flowchart, Fig.4.3, CFD simulations have been run on single vane in order to correct the values of slip factor and the efficiency,

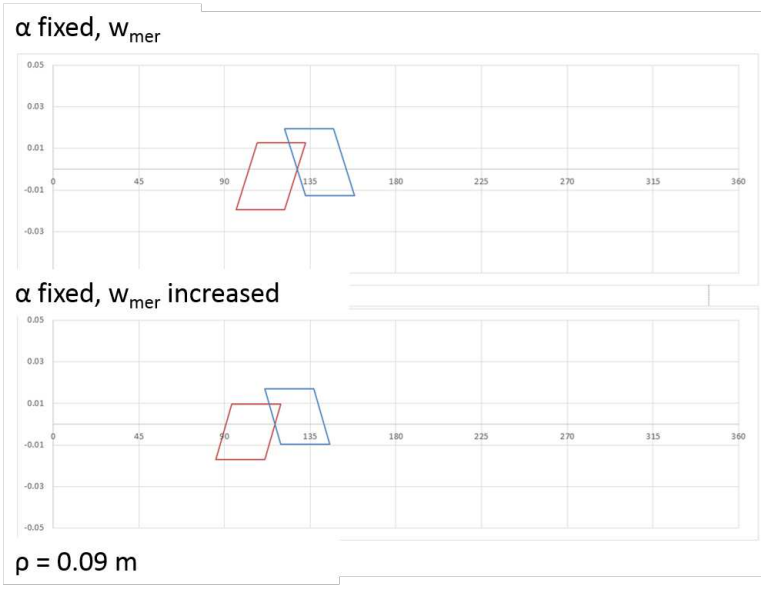

Figure 4.20: *Design tool to inspect channel interpenetration. It is possible to look at the reduction of the interpenetration by increasing the meridional velocity.*

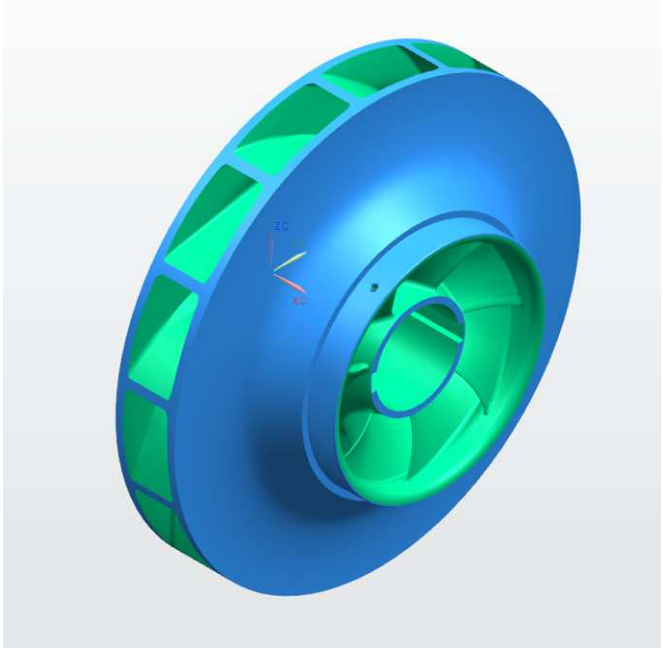

Figure 4.21: *3D CAD of the first novel impeller prototype.*

assumed at the beginning of the work. The computational domain, adopted for these calculations, comprises a short pipe upstream the blade channel inlet and a vaneless diffuser downstream the channel outlet with the aim to reduce the influence of the boundary conditions on the results, see Figs.4.22, 4.23.

Contrary to the baseline geometry (Fig.4.11), in this case to simulate a single vane with periodicity equal to $2\pi/N_b$ two channels have to be included in the numerical domain, see 4.22.

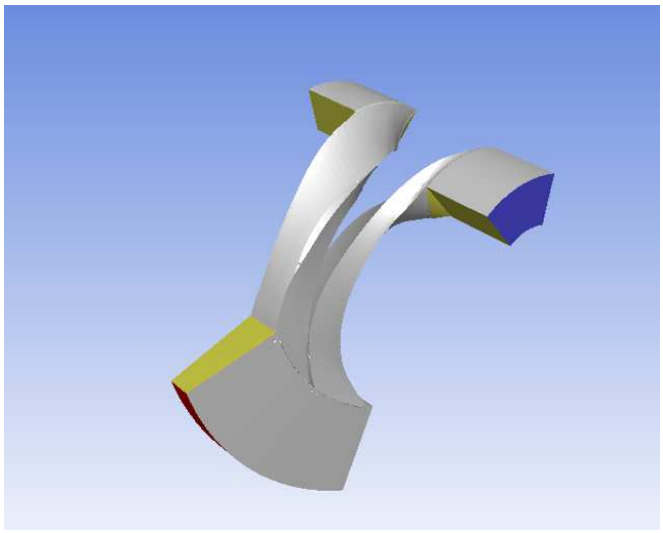

Figure 4.22: *Computational domain used for simulating the novel geometry with periodicity equal to* $2\pi/N_b$.

All the grids have been generated with the same grid generation strategy by means of Icem CFD® and they are made of 1 milion cells with $y^+ = 1$. CFD analyses have been run with the commercial code ANSYS Fluent® in steady-state configuration by means of the Multiple Reference Frame (MRF) technique and the k-ω SST model for turbulence closure [79]. Regarding the boundary conditions, velocity components have been imposed at the inlet and uniform pressure distribution at the outlet, whereas a constant turbulence intensity equal to 3% has been imposed at the inlet. For all the simulations concerning the desing process the convection, diffusion and gradient terms have been computed by using second-order upwind schemes.

For each iteration, see Fig.4.3, at the end of the numerical simulations the hydraulic efficiency and the slip factor have been calculated and the coefficient a and b in eq.4.5 have been calibrated. These values are then passed back to the 1D code where the new value of the slip factor is applied to eq.4.7. The process continues until convergence is reached, as summarized in Fig.4.3. The slip factor calculated via CFD simulations is defined as follows:

$$\sigma = \frac{c_{u2}^{CFD}}{c_{u2}^{th}} \tag{4.26}$$

where c_{u2}^{CFD} is the absolute tangential velocity evaluated via area-weighted calculations on surfaces placed at the exit of the impeller, whereas c_{u2}^{th} derives from the blade congruent flow theory. The hydraulic efficiency of the channel is calculated as:

$$\eta_y = \frac{Q' \Delta P_{tot}}{C\omega} \tag{4.27}$$

where ΔP_{tot} is the total pressure difference between the inlet and the outlet of the channel (N/m^2), $Q' = Q/\eta_v$ is the volumetric flow rate (m^3/s) comprising flow leakages, ω is the rotational speed (rad/s) and C is the torque calculated on the blade, the hub and the shroud (Nm).

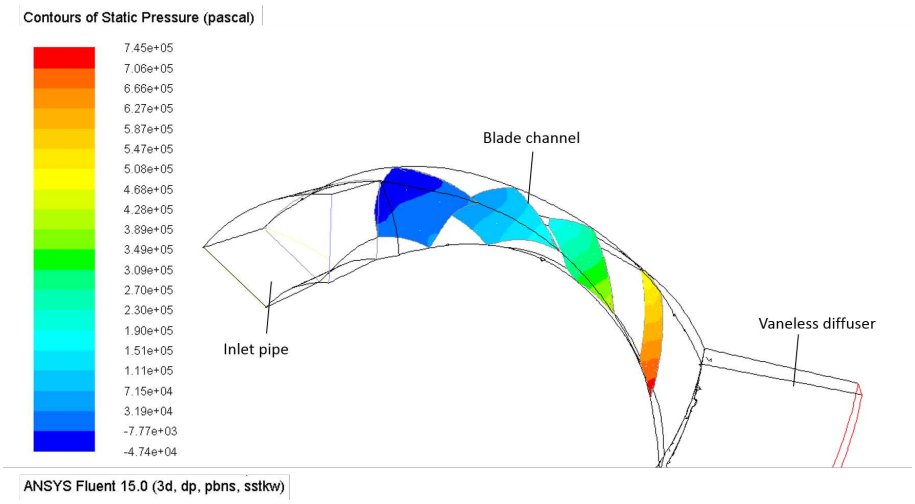

Figure 4.23: *Description of the numerical domain and view of the static pressure contours inside the channel on iso-surfaces with constant meridional coordinate.*

As expected, the numerical results of the flow field concerning the novel geometry, obtained at the end of the convergence process, have shown an improvement in the slip factor ($+8.5\%$) and in the hydraulic efficiency ($+1.2\%$). In Tab.4.2, data obtained at the BEP of the two geometries are reported.

Table 4.2: *Slip factor and hydraulic efficiency calculated for a single blade vane at BEP*

Tag name	Conventional	novel Geometry
hydraulic efficiency (η_y)	0.917	0.928 (+1.2%)
slip factor (σ)	0.782	0.854 (+8.5%)

4.5.1 Losses analysis

In order to quantify the energy loss, L_w, the rotary stagnation pressure drop, ΔP^*, has been calculated inside the vane. In a rotating system, the rotary stagnation pressure is defined as:

$$-L_w = \frac{\Delta P^*}{\rho} = \Delta\left(\frac{P_{abs}}{\rho} + \frac{w^2}{2} - \frac{u^2}{2}\right) \tag{4.28}$$

where u is the local rotational speed defined as $u = \omega R$, P_{abs} is the absolute static pressure, and w is the relative velocity. For incompressible, inviscid flow, the value of P^* shall be constant along a streamline. For the viscous flow, the change of this parameter between two points on the same streamline represents the viscous loss.

The trend of the rotary stagnation pressure has been evaluated on surfaces with iso-meridional coordinates along the blade channel of the two geometries, i.e., the baseline and the novel one. Figure 4.24 points out that when the fluid flows through the baseline geometry, it is subjected to a more than linear reduction of the rotary stagnation pressure mainly in the first part (first 10% length) and towards the outlet (last 40% length) of the channel, whereas it experiences a linear reduction in the central part of the channel. On the contrary, the novel design shows a mild linear reduction of the rotary stagnation

pressure along the entire channel length. This is due to the shape of the novel vane and its reduced length: the new cross sections are close to a square shape and have larger hydraulic diameters compared to the baseline, thus contrasting the development of secondary flows (paragraph 2.2.6).

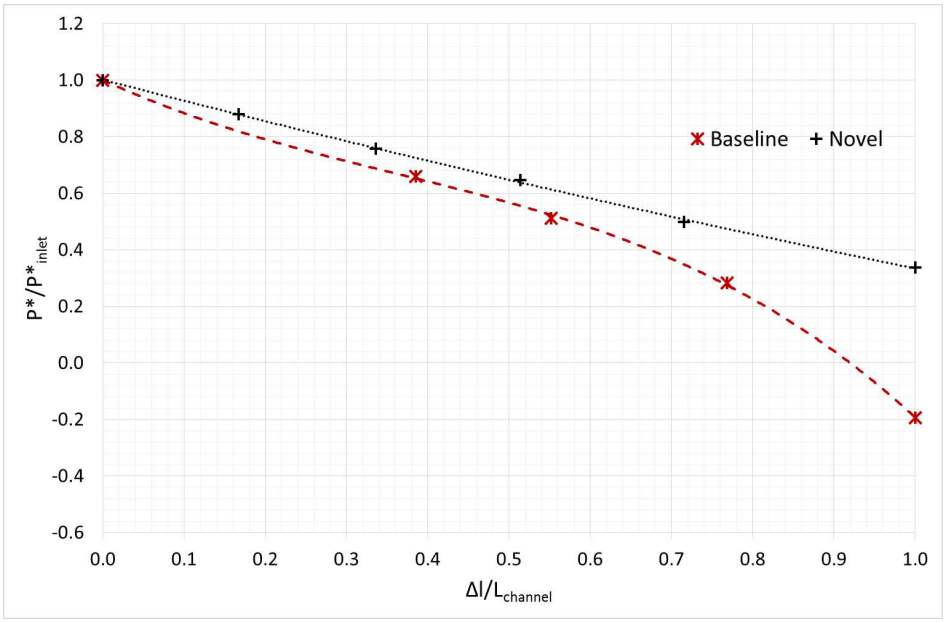

Figure 4.24: *Trend of the rotary stagnation pressure inside the baseline and the novel geometry.*

4.5.2 Velocity distributions

As shown in paragraph 4.4.1, to make the new geometry feasible a velocity distribution has been set up. The evolution of the relative velocity vector w, described herein, is completely different from that of a conventional impeller. In this case the relative velocity vector is imposed since it results from the combination of the w_{tan} and the w_{mer} functions. The w_{tan} is represented by a linear function, so that the blades are proportionally loaded from their leading edge to the trailing edge. Another possible way may be to vary the w_{tan} values proportionally to the radial coordinate; a decreasing wrap angle and a more stressed blade would be expected in this case at higher radii. On the other hand, w_{mer} has been chosen to avoid the channels intersection, as illustrated in the previous paragraphs, but other reasons have been taken into account. The first purpose is to smooth as much as possible the B trend (Fig.4.14), avoiding stings and cuspids; this usually happens in the first part of the channel where α decreases rapidly. The second purpose is to control the blade height, B, where the impeller is totally radial.
By comparing the velocities inside the vanes of the baseline (an averaged value between the PS and the SS) and the novel geometry, it can be pointed out that the novel configuration has globally a higher velocity, see Fig.4.25. Despite this unusual shape, which may suggest higher losses since the mean value of w is much higher, the losses inside the channel are reduced; indeed the vane has higher hydraulic diameter and lower length (lower wrap angle) than the baseline vane.

Besides, the functions of the w_{tan} and w_{mer} applied for designing the novel geometry

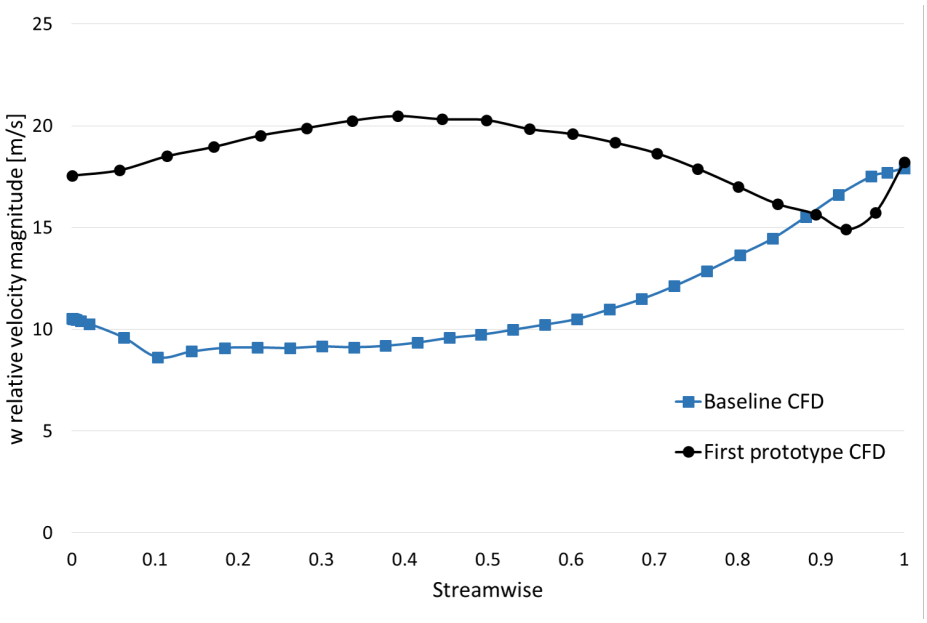

Figure 4.25: *Relative velocity vector profiles.*

have been validated by comparing their functions with the velocities calculated along the c_{line} of the vane. Even though the velocity function have been applied to the centre line of the vane neglecting the 3D flow phenomena inside the channel, the results point out a good agreement between the values of velocity function and the 3D distribution of the flow inside the channel calculated via CFD simulations, see Fig.4.26, 4.27 and 4.28.

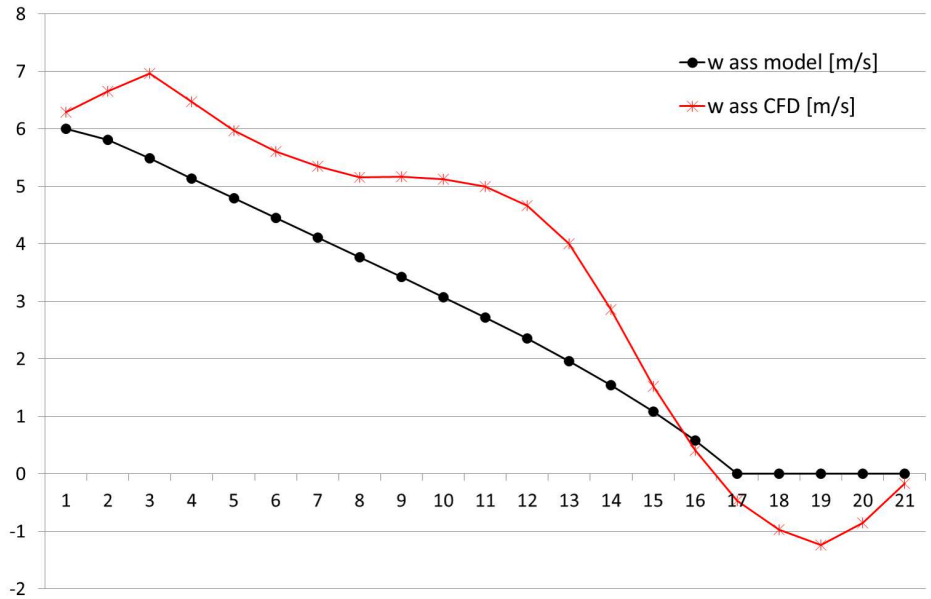

Figure 4.26: *Relative axial component of the relative velocity vector.*

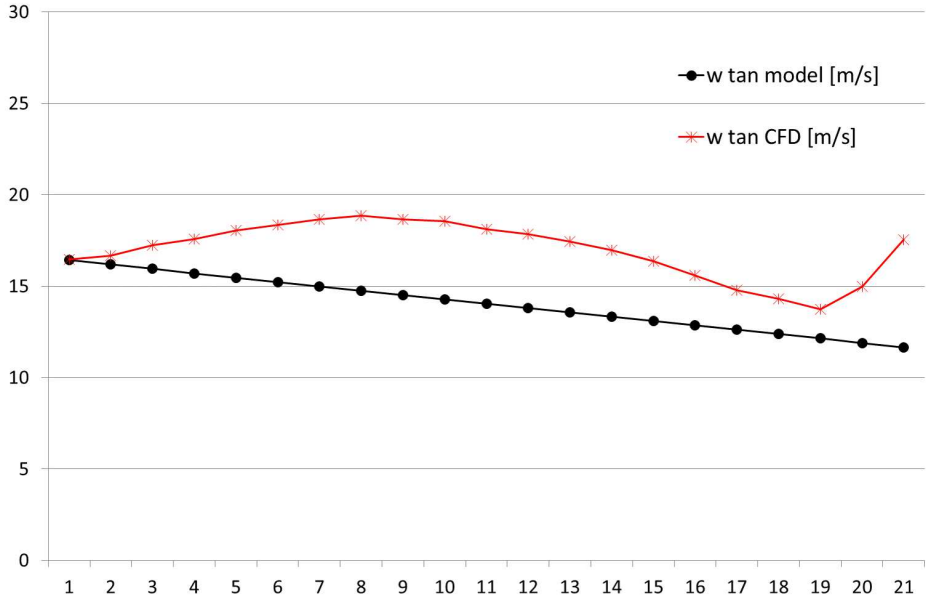

Figure 4.27: *Relative radial component of the relative velocity vector.*

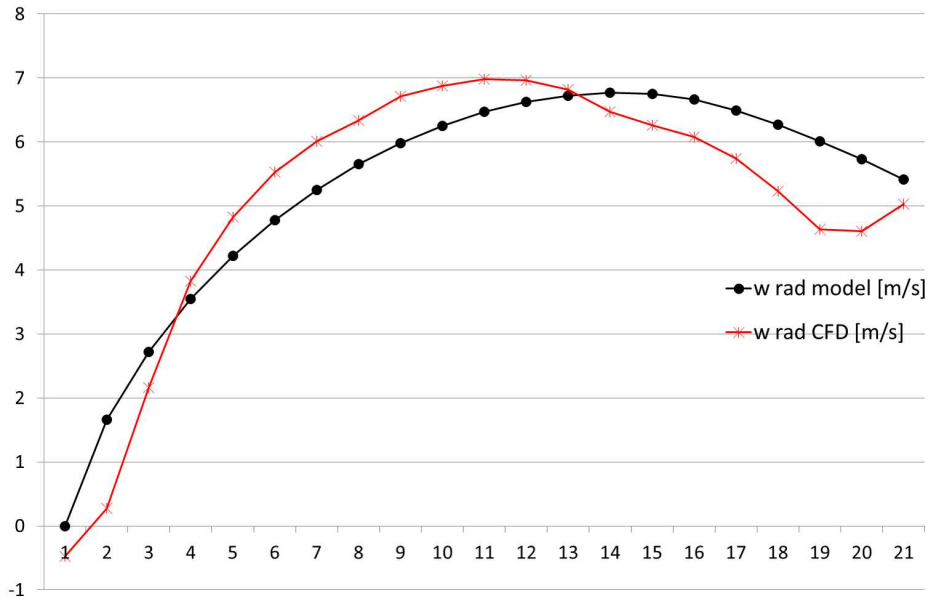

Figure 4.28: *Relative tangential component of the relative velocity vector.*

4.6 Design of the second prototype

A second prototype has been designed with the aim to rotate at a lower rotational speed with a higher blade loading (with a reduced number of blades) than the first prototype. As in the first case, the second prototype should have the same specific speed of the first geometry at its BEP, keeping the same absolute angle at the outlet of the impeller (α_2) and at the inlet of the volute (α_3).

It will be shown in the next chapter that the first prototype has its BEP at 115%

of the Q_{design} producing an error in the value of the n_q. The first prototype has been designed with 7 blades, whereas 5 blades have been chosen for the second one. The design process has been updated in order to further improve the shape of the vanes and some features have been added at the design tool to take control of the blade loading and to detect any separation flow points inside the channel (C_p and C_L prediction).

Firstly, the design tool has been calibrated by matching the expected values of head (H) and efficiency (η) of the first prototype with those obtained from the experimental tests illustrated in the previous chapter, paragraph 3.3, whereas the characteristic curves will be displayed in the fifth chapter. This can be done by adjusting two parameters, the hydraulic efficiency and the slip factor. The first has been corrected by considering the BEP deviation and the CFD results on the single-vane; the latter has been modified by changing the value of a and b in the modified slip factor formulation eq.4.5, in order to match the results obtained by the CFD simulations on the entire pump geometry and the experimental results. This means that the flow seems to be guided by a higher N_b thus proving that the novel design works as if the number of blades at the impeller outlet were doubled. The tuning process has also given information about the best absolute angle at the inlet of the volute, α_3. The values of the slip factor will be analyzed in the next chapter.

4.6.1 Harmonic algorithm to select the nominal values

To find the operating conditions for the second prototype geometry, a tool based on *Harmony search algorithm*, has been written in Matlab® and used to find the values of Q and n that minimize the error function, eq.4.29. The Matlab tool has been coupled with the 1D code.

$$f_{err} = \left| \frac{\alpha_3 - \alpha_{3_{(1^{st}prototype)}}}{\alpha_{3_{(1^{st}prototype)}}} \right| + \left| \frac{n_q - n_{q_{(1^{st}prototype)}}}{n_{q_{(1^{st}prototype)}}} \right| \tag{4.29}$$

The tool is able to minimize various error functions by varying also geometric design parameters, e.g., l_2 blade height at the outer diameter. In this case, Q and n have been chosen as variables. This tool allows to keep the same specific speed and to guarantee the best angle at the inlet of the volute because of the previous calibration process described in paragraph 4.7.

Firstly, the limits of the design space have been set up; after that, random couples of Q and n have been generated, see Fig.4.29,a. In the end, the algorithm provides a family of points which minimize the error function, eq.4.29, see Fig.4.29,b. The best among all the possible solutions, highlighted in red in Fig.4.29, has been chosen as input data and design point for the design of the second impeller prototype.

In Fig.4.30 the values of ψ and ϕ of the second prototype lie on the iso-n_q curve passing through the BEP of the first geometry (115%Q_{design}). This point is below the BEP of the first prototype in order to reduce the blade loading and to avoid $H - Q$ instability at low flow rates.

4.6.2 Pressure and Lift coefficients

The design generator tool has been updated with the possibility to calculate the pressure and the lift coefficients (C_p and C_L). This allows the designer to predict and inspect:

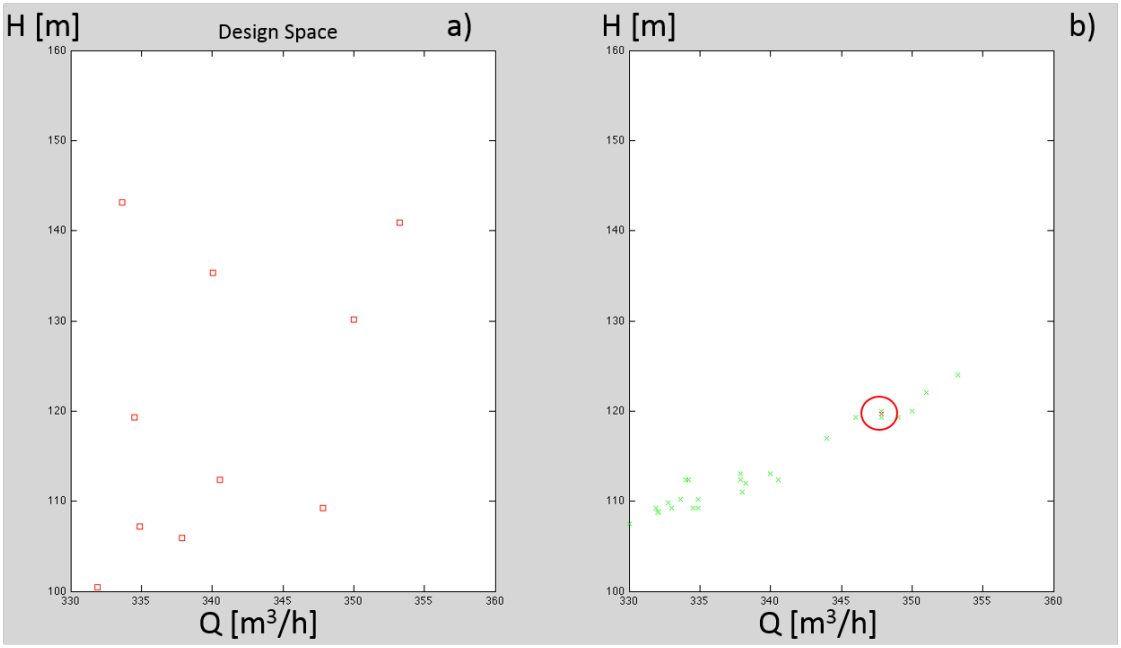

Figure 4.29: *An example of the Harmonic algorithm, on the right the design space with the initial values and on the right the points which minimize the error function.*

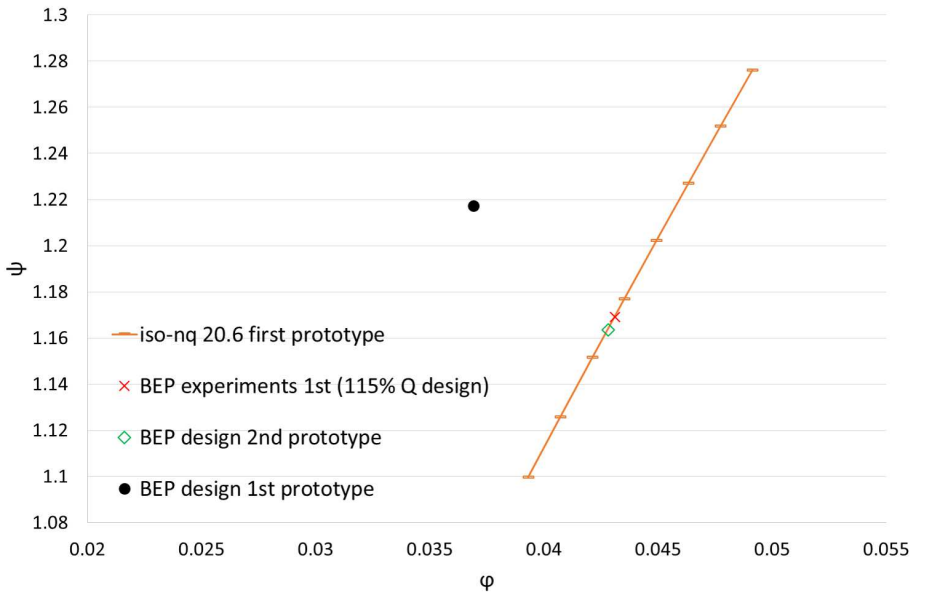

Figure 4.30: *Plot of the design points for the two impeller.*

pressure distribution on the blade, if the blades are over-loaded and flow separation can occur.

The pressure coefficient C_p is usually obtained by calculating the pressure value along the pressure, P_{PS}, and the suction side, P_{SS}, of the blade. It is defined as follows:

$$C_p = \frac{P_{PS} - P_{SS}}{1/2\rho u_2^2} \tag{4.30}$$

To perform this calculation a CFD simulation shall be run and the C_p can be obtained by post-processing. In the design tool proposed in this thesis, an analytical function has been added to predict this value before drawing the geometry, to take control of the velocity. The local velocities determine the pressure distribution which, when integrated, yields the forces acting on the airfoil. A novel expression, eq.4.31, has been introduced for this calculation:

$$C_p \cong \frac{2Q\Delta(c_u r)}{u_2^2 Br\Delta s} \tag{4.31}$$

This expression as been calculated as:

$$C_{p_{poliba}} = \frac{2Q}{u_2^2(c_{tan_{i+1}}\rho_{i+1} - c_{tan_i}\rho_i)c_{tan_{mean}}\rho_{mean}\sqrt{\Delta\rho^2 + \Delta x^2}} \tag{4.32}$$

This is a 1D model and the c_{tan_i} used are the ideal values of the absolute tangential velocity along the c_{line} imposed by the velocity functions described in paragraph 4.5. The comparison between the Cp of the first prototype obtained from the 1D tool and the CFD results is displayed in Fig.4.31. Figure 4.31 shows a good agreement between the two curves. Moreover, the 1D tool provides the $C_{p,max}$ and $C_{p,max}$ positions along the channel with errors equal to 4% and 1.3%, respectively, compared to the CFD results. The same procedure has been applied to the second prototype and the results are shown in Fig.4.32.

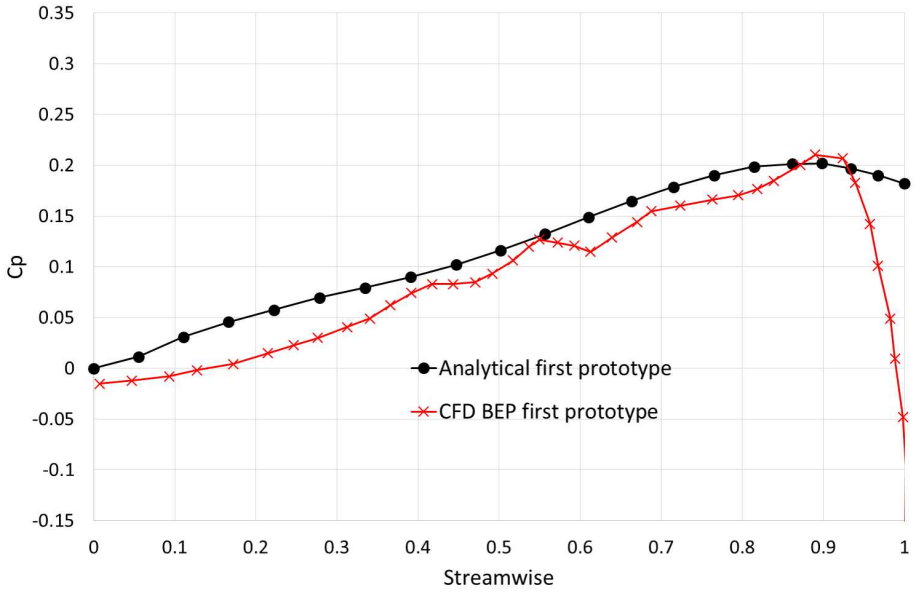

Figure 4.31: *C_p of the first prototype, comparison between the analytical tool and the CFD results.*

The new geometry has a $C_{p_{max}}$ 10% higher than the baseline, but still acceptable (Tab.4.3).

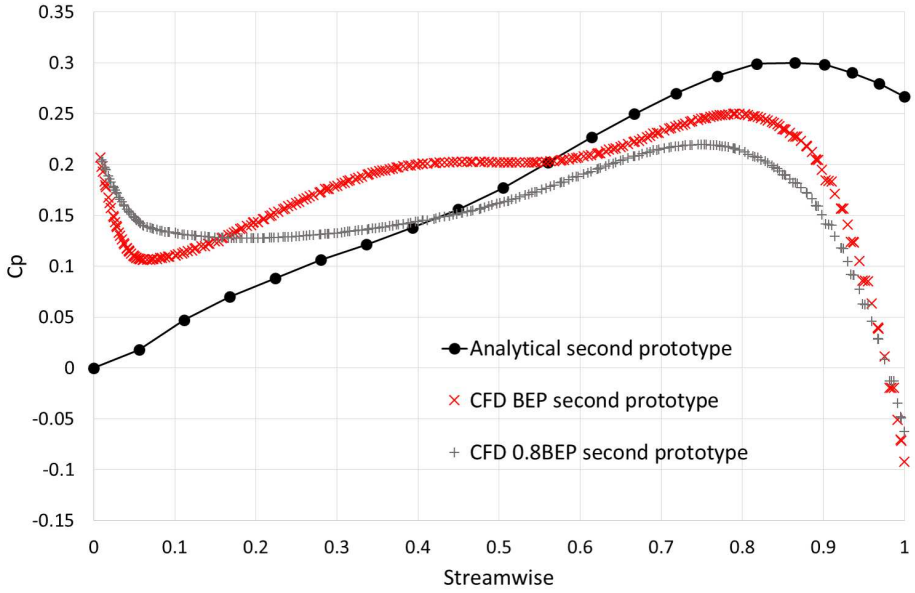

Figure 4.32: *C_p of the second prototype, comparison between the analytical tool and the CFD results for Q_{BEP} and $0.8Q_{BEP}$.*

Before starting the design of the second impeller, the lift coefficient has been calculated to estimate the blade loading. The lift coefficient is defined as follows:

$$C_L = 2gH\frac{60}{n}\frac{1}{L_{can}f_bN_b(w_2 + w_{1tip})/2} \tag{4.33}$$

The reduction of number of blades, N_b, and the new nominal value show an increase of C_L of the second geometry with respect to the first one; however, its value is still under the baseline C_L and the maximum allowable value, which is $C_{L_{max}} = 1.25$ (Tab.4.3).

Considering the new arrangement of the channels, the number of blades in eq.4.33 can be considered a value between the number of blades at the impeller eye and at the outlet. In this work a value of f_b equal to 0.87 has been used. It derives from the α function set up during the vane design. In the following the values of the lift and the pressure coefficients are summed up.

Table 4.3: *Lift coefficient for the three geometries.*

Imepeller.	baseline	1^{st}	2^{nd}
C_L	1.1627	0.9248	1.170
$C_{p_{max}}$ analytical	0.225	0.208	0.300
$C_{p_{max}}$ CFD		0.200	0.250

Once these parameters have been verified, the second prototype has been drawn, see Fig.4.33.

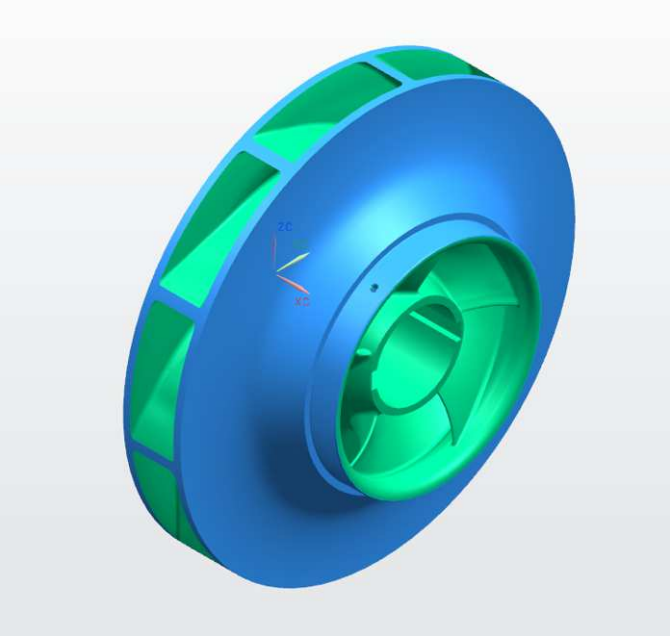

Figure 4.33: *3D CAD of the second prototype.*

4.7 Lost-Foam Casting

Due to the complexity of the geometry, the simplest way to make the impeller is by casting. Lost-foam casting (LFC) is a type of evaporative-pattern casting process that is similar to investment casting, except foam is used for the pattern instead of wax. This process takes advantage of the low boiling point of foam to simplify the investment casting process by removing the need to melt the wax out of the mold [104, 105]. First, a pattern is made from polystyrene foam, which can be done in many different ways. For small volume runs the pattern can be hand cut or machined from a solid block of foam; if the geometry is simple enough it can even be cut using a hot-wire foam cutter. If the volume is large, then the pattern can be mass-produced by a process similar to injection molding. Pre-expanded beads of polystyrene are injected into a preheated aluminum mold at low pressure. Steam is then applied to the polystyrene which causes it to expand more to fill the die. The final pattern is approximately 97.5% air and 2.5% polystyrene. Pre-made pouring basins, runners, and risers can be hot glued to the pattern to finish it. Next, the foam cluster is coated with ceramic investment, also known as the refractory coating, via dipping, brushing, spraying or flow coating. This coating creates a barrier between the smooth foam surface and the coarse sand surface. Secondly, it controls permeability, which allows the gas created by the vaporized foam pattern to escape through the coating and into the sand. Controlling permeability is a crucial step to avoid sand erosion. Finally, it forms a barrier so that molten metal does not penetrate or cause sand erosion during pouring. After the coating dries, the cluster is placed into a flask and backed up with un-bonded sand. The sand is then compacted using a vibration table. Once compacted, the mold is ready to be poured. Automatic pouring is commonly used in LFC, as the pouring process is significantly more critical than in conventional foundry practice. There is no bake-out phase, as for

lost-wax. The melt is poured directly into the foam-filled mold, burning out the foam as it pours. As the foam is of low density, the waste gas produced by this is relatively small and can escape through mold permeability, as for the usual outgassing control. Commonly cast metals include cast irons, aluminium alloys, steels, and nickel alloys; less frequently stainless steels and copper alloys are also cast. The size range is from 0.5 kg (1.1 lb) to several tonnes (tons). The minimum wall thickness is 2.5 mm (0.098 in) and there is no upper limit. Typical surface finishes are from 2.5 to 25 μm (100 to 1000 μin) RMS.[3] Typical linear tolerances are $\pm$0.005 mm/mm (0.005 in/in). This casting process is advantageous for very complex castings that would regularly require cores. It is also dimensionally accurate, maintains an excellent surface finish, requires no draft, and has no parting lines so no flash is formed. The un-bonded sand of lost foam casting can be much simpler to maintain than green sand and resin bonded sand systems. Lost foam is generally more economical than investment casting because it involves fewer steps. Risers are not usually required due to the nature of the process; because the molten metal vaporizes the foam the first metal into the mold cools more quickly than the rest, which results in natural directional solidification. Foam is easy to manipulate, carve and glue, due to its unique properties. The flexibility of LFC often allows for consolidating the parts into one integral component; other forming processes would require the production of one or more parts to be assembled. The two main disadvantages are that pattern costs can be high for low volume applications and the patterns are easily damaged or distorted due to their low strength. If a die is used to create the patterns there is a large initial cost.

A certain extra-amount of material has been needed for casting the impeller in order to guarantee a ceratin gap between the channles.Thus, the smallest gap left between channels during the design has been over 3 mm. The parasolid of the entire geometry had been draw at the Polytechnic of Bari and sent to Sheffild for casting. Two photos (Fig.4.34 and 4.35) show the inlet and the outlet of the unconventional geometry. It is a one solid body. In the future a geometry made of two parts could be built. Each part would include the channels coming from the two sides of the impeller. In Fig. one of the two parts, which will constitute the impeller, is shown. This solution may lead to a considerable weight reduction. Obviously a cover of sheet metal may be necessary to give to the impeller the same resemblance as in Fig.4.35.

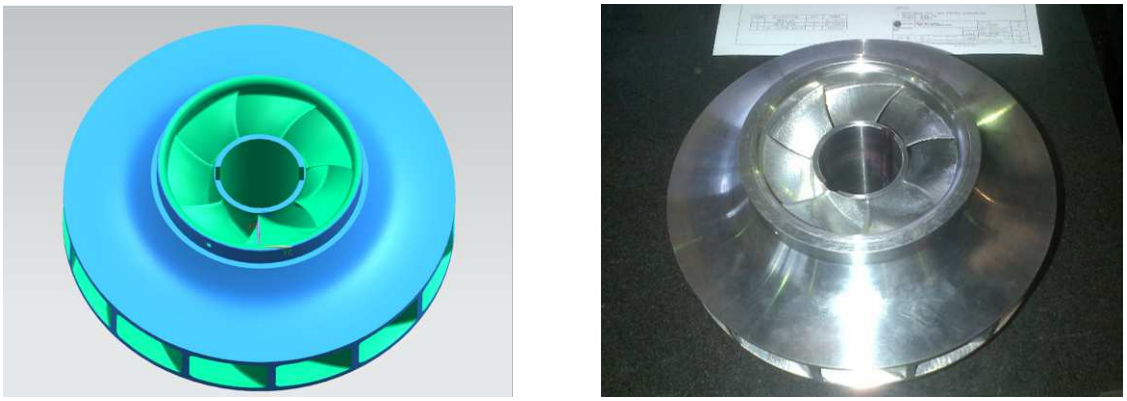

Figure 4.34: *Impeller eye view of the 3D CAD and of the real impeller obtained by means of Lost-foam casting technology.*

Figure 4.35: *Outlet view of the 3D CAD and of the real impeller obtained by means of Lost-foam casting technology.*

4.8 Conclusions

In this work a novel impeller, that can easily retrofit a conventional one, for a low-medium specific speed double suction centrifugal pump has been presented. Considering that double suction centrifugal pumps are the main devices involved in the feedwater system of nuclear power plants and they are responsible for a significant share of their energy consumption (by affecting the balance of both the gross and net electrical energy production), the obtained efficiency increase, even if of only a few percentage points, is a relevant result in the economy of these power plants.
This new geometry has been designed respecting the following geometric and fluid dynamic constrains: to have the same specific speed number (n_q) of the baseline geometry; to guarantee a kinematic flow angle at the inlet of the volute (α_3) in accordance with the optimum α_3 of the volute and to satisfy the matching with the absolute inlet flow angle at the outlet of the inlet duct.

The novel impeller is characterized by having the channels between the blades starting from inlets, crossing the symmetry plane, normal to the rotational axis, and ending in such a way that the equivalent blades number at the impeller outlet is actually doubled with respect to a conventional configuration obtained by the back-to-back coupling of two single suction impellers (see Figs.4.34 and 4.23). In the novel impeller, the slip reduction permits a higher pressure rise or optionally to downsize the impeller, thus reducing the manufacturing cost of the pump. Furthermore, the reduction of the impeller diameter brings also a significant reduction of the losses due to disk friction, thus increasing the overall pump efficiency.
Compared to a conventional double suction impeller provided with splitter blades, embodiments of the new impeller do not introduce any additional leading edge and corresponding losses [14]. For low-medium specific speed pumps, the new shape of the inter-blade channels of the impeller is such that the cross section hydraulic diameter is increased and the length of each channel reduced, thus reducing the hydraulic losses with respect to conventional configurations. The cross section area of the channel is designed to have control over the velocity of the flow inside the channel (see paragraph

4.4.1). Moreover, its shape is designed in order to avoid any channel interpenetration when they twist from the axial to the radial direction and at the same time to match a target area law (continuous in its first and second order derivative) along the flow path, in order to avoid too high velocity gradients inside the channels. This leads to higher performance in terms of hydraulic head and global efficiency compared to other solutions, e.g., [102] and [103]. In particular, the channels start essentially with a quadrilateral cross-section which becomes a five-sided polygon. When the channels become parallel to the radial tangential plane, their cross-sections return to be essentially quadrilateral. The additional side is introduced between the so called suction side and the hub surfaces of the channel. Its length starts from zero, reaches its maximum at about half of the channel length, and then goes back to zero. This novel vane design is covered by a patent application [106].

CHAPTER 5

Performance evaluation and flow analysis of the novel geometry

5.1 Introduction

In this chapter the main results of the numerical simulations and experimental tests carried out on the novel impellers will be shown. The characteristic curves, velocity and pressure profiles will be compared to highlight the benefits from using the novel geometry. The benefits go from the higher pressure rise to the lower $NPSH_R$ curves with respect to the baseline geometry.

5.2 Results and discussion

As explained in the previous paragraph a campaign of simulations has been run by means of the open-source CFD code OpenFOAM with the purpose of simulating the entire centrifugal pump including the novel impeller. This analysis aim to evaluate the performance of the novel impeller, to quantify the improvement with respect to the baseline and to perform a flow analysis. Moreover, The numerical results have been compared against the experimental tests of the novel geometry carried out in the Hydraulic test rig at Nuovo Pignone (Modugno, Italy). Firstly, the numerical models assessment has been performed by running transient simulations on the baseline geometry and comparing the numerical results with those calculated by means of the commercial code ANSYS® CFX by a different CFD team at Nuovo Pignone.

5.2.1 Domain

The computational grid has been generated by means of the grid generator Icem CFD®. The grid is a hybrid mesh. The volume has been discretized by means of unstructured

tetrahedral elements with prism layers close to the walls in order to guarantee a wall y^+ equal to 30. The wall y^+ is defined as:

$$y^+ = \frac{yU_\tau}{\nu} \tag{5.1}$$

where y is the cell centroid distance to the nearest wall, ν is the local kinematic viscosity of the fluid and U_τ is the friction velocity:

In eq.5.2 τ_w is the wall shear stress, defined as follows:

$$\tau_w = \mu \left(\frac{\partial u}{\partial y} \right)_{y=0} \tag{5.2}$$

where μ is the dynamic viscosity, u is the flow velocity parallel to the wall and y is the distance from the wall. The y^+ selected for this application corresponds to a correct use of the wall-functions, which involve modelling the boundary layer using a log-law distribution. Moreover, the mesh density has been increased at the leading edge of the blades and at the tongues of the volute by decreasing the value of the maximum cell dimension on these wall surfaces without changing the y^+.

Three different meshes in the *.msh* format have been generated and exported for each part of the model (namely, the suction, the impeller and the volute). Then the three *.msh* files have been converted into the OpenFOAM format with the command *fluent3DMeshToFoam* and checked with *checkMesh* routine. The entire grid is characterized by no aspect ratio problem (values < 1000 - The ratio between the longest and the shortest length), no skewness problem (values < 0.98 - Measurement of the distance between the intersection of the line connecting two cell centres with their common face and the centre of that face - smaller is better) and an orthogonality lower than 70° (Measurement of the angle between the line connecting two cell centers and the normal of their common face - 0.0 is the best) [107]. This avoids the use of *nonOrthogonalCorrectors* giving more accurate numerical results. Finally, the three parts have been merged together using the *mergeMesh* command.

To perform a grid refinement study three computational grids with different mesh refinement levels have been generated, see Table 5.1, and the results have been analyzed by means of the Grid Convergence Index (GCI) method, proposed by Roache [108]. The grids have been systematically refined with a global factor of $f_{GCI} = 1.33$. Eventually a grid made of 11 millions of cells has been chosen because of small deviations in the results and a good compromise between the geometry refinement and the computational costs (see Table 5.1).

Table 5.1: *Details of three computational grids, values of the hydraulic head at BEP of the centrifugal pump calculated via numerical simulations and results of the GCI method.*

	Coarse	Medium	Fine	GCI_{coarse}	GCI_{fine}
Impeller (x10^6)	3	6	10		
Suction (x10^6)	1	2	4		
Volute (x10^6)	2	3	6		
Total number of elements (x10^6)	6	11	20		
Head at BEP (m)	139.8	140.8	141.0	4.87%	0.55%

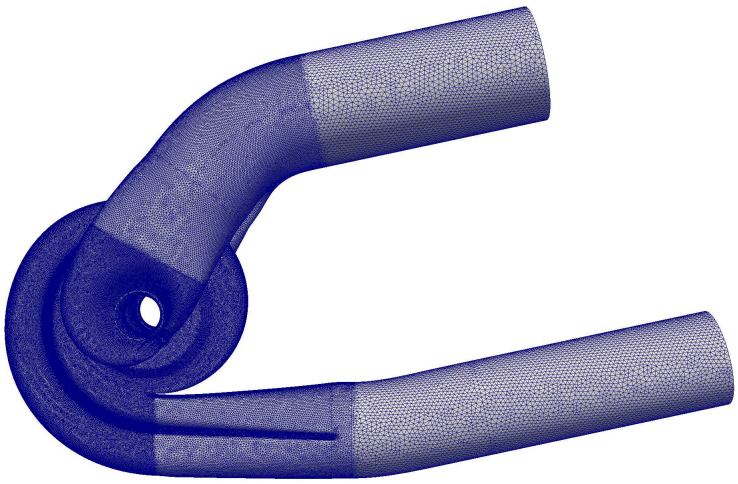

Figure 5.1: *Grid of the entire geometry.*

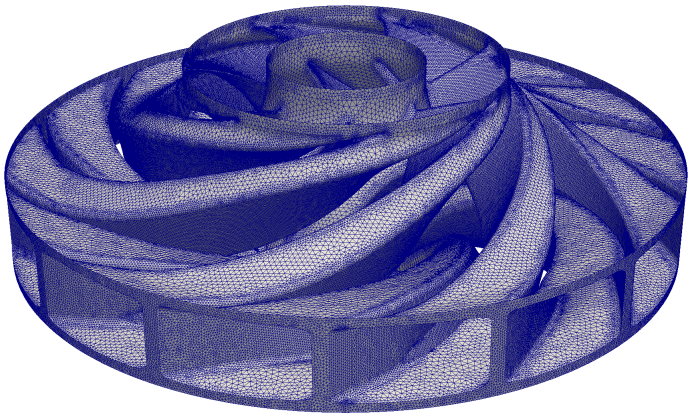

Figure 5.2: *Grid of the impeller.*

5.2.2 Boundary conditions

For all the analyzed cases, the flow rate has been imposed at the inlet considering a uniform inlet velocity distribution. Moreover, the value of the flow leakage, which flows

through the annular seal, has been modeled as exiting from the impeller case and incoming axially upstream the impeller eye with a $45°$ of swirl with respect to the tangential direction; it has been calculated a priori, according to a consolidated one-dimensional empirical model, because the geometry of the seal has not been modeled [14]. A uniform pressure distribution has been imposed at the outlet of the domain. The three part of the geometry, which have been merged together, communicate each other by means of interfaces. In OpenFOAM the boundary condition used on these interfaces is named cyclicAMI (Arbitrary Mesh Interface).
Furthermore, for this test case the turbulent intensity has been assumed constant and equal to 3% at the inlet of the domain. At the inlet and outlet of the pump straight pipes have been added to reduce influence of boundary conditions.
Another critical aspect was the definition of the wall roughness in OpenFOAM; the value of the *equivalent sand grain roughness* is equal to $5.6 \cdot 10^{-5}\ m$ and $5.6 \cdot 10^{-6}\ m$ respectively for the walls of the stator and rotor parts; the same values are used for all the tested geometries. For the purpose of activating the wall roughness, the *nutURoughWallFunction* has been applied to the walls in the *nut* file together with *kqRWallFunction* and *omegaWallFunction*, respectively for k and ω wall boundary conditions (see Tab.5.2). The *nutURoughWallFunction* provides a turbulent viscosity condition based on U^+ calculation and one of its argument requires the *equivalent sand grain roughness*. The *kqRWallFunction* derives from the zeroGradientFvPatchField, which means it provides Neumann boundary (the only Neumann boundary of wall functions) while *omegaWallFunction* provides the constraint on turbulence specific dissipation applying the combination of viscous and log equation.

Table 5.2: *Summary of the boundary conditions used in OpenFOAM.*

	Inlet	Outlet	Wall	Flow leakage inlet	Flow leakage out
p	zeroGradient	fixedValue	zeroGradient	zeroGradient	zeroGradient
U	massFlow	zeroGradient	fixedValue	swirlFlowRateInletVelocity	flowRateInletVelocity
k	turbulence intensity	zeroGradient	kqRwallFunction	fixedValue	fixedValue
ω	fixedValue	zeroGradient	omegaWallFunction	fixedValue	fixedValue
nut	calculated	calculated	nutURoughWallFunction	calculated	calculated

The performance of the conventional impeller (the baseline) has been evaluated at different mass flow rates, see Tab.5.3:

Table 5.3: *Percentage of the BEP mass flow rate at which the simulations have been run.*

Simulation n.	1	2	3	4	5	6
mass flow rate	5%	30%	50%	80%	100%	120%

All the transient flow simulations have been carried out with a time step $\Delta t = (T/N_b)/256 = 4.5 \cdot 10^{-6}\ s$ where T is the time of a complete rotation for a duration total time equal to 0.085 s, which corresponds to five complete impeller revolutions. The results in terms of head and efficiency have been averaged over the last 3 revolutions. The mean and the maximum values of the Courant number result approximately equal to 0.03 and 6, respectively, in all the simulations.

5.2.3 Numerical assessment

To assess the numerical models and methods applied for simulating the entire geometry of a centrifugal pump a comparison between OpenFOAM and a commercial code commonly used to simulate hydraulic turbomachineries (ANSYS CFX ®) has been done. The baseline geometry, which is property of Nuovo Pignone, Bari, has been investigated by means of numerical simulations on a grid with 40 million cells by means of the CFD commercial code ANSYS CFX ® by solving the unsteady fluid dynamic equations with a high resolution method. The same geometry has been investigated with OpenFOAM by setting boundary conditions equivalent to the ones adopted in CFX, see paragraph 5.2.2 and 5.2.1. The results of the simulations, which have been obtained with the two software for the conventional geometry are illustrated in Fig.5.3 in terms of head and global efficiency. The comparison between different machines has been performed by means of two dimensionless parameters, namely the head coefficient and the flow coefficient which have been defined in paragraph 4.2, eq.4.2 and 4.3. The curves show a good agreement with each other.

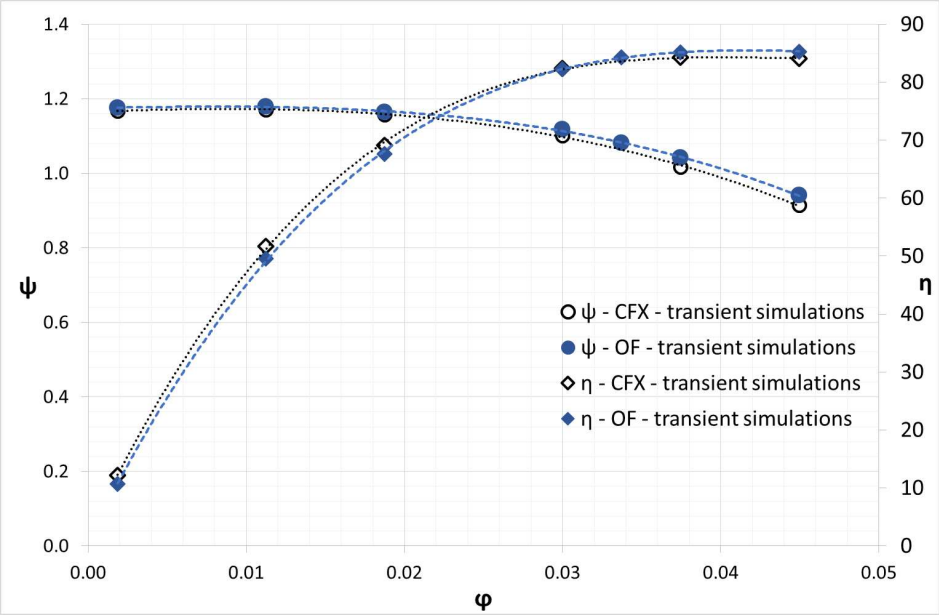

Figure 5.3: *ψ-ϕ and η-ϕ curves calculated with CFX and OpenFOAM (Circles and rhombuses stand for ψ and η curves respectively).*

5.2.4 Performance evaluation

In Fig.5.4 the two impellers are represented with the plot of the static pressure contours. Besides, this view points out the main differences between the 2 impellers from the impeller eye to the outer diameter. Looking at the vane outlet, in the new arrangement, the geometrical elements (chamfer) introduced to avoid vanes interpenetration is visible.

In order to highlight the benefits from using this novel impeller configuration the characteristic curves of the two machines, the baseline and the novel, have been plotted on two non dimensional planes. Firstly, the ψ-φ and the η-φ curves (Fig.5.5 - Fig.5.6) obtained with OpenFOAM for the new prototype have been compared against

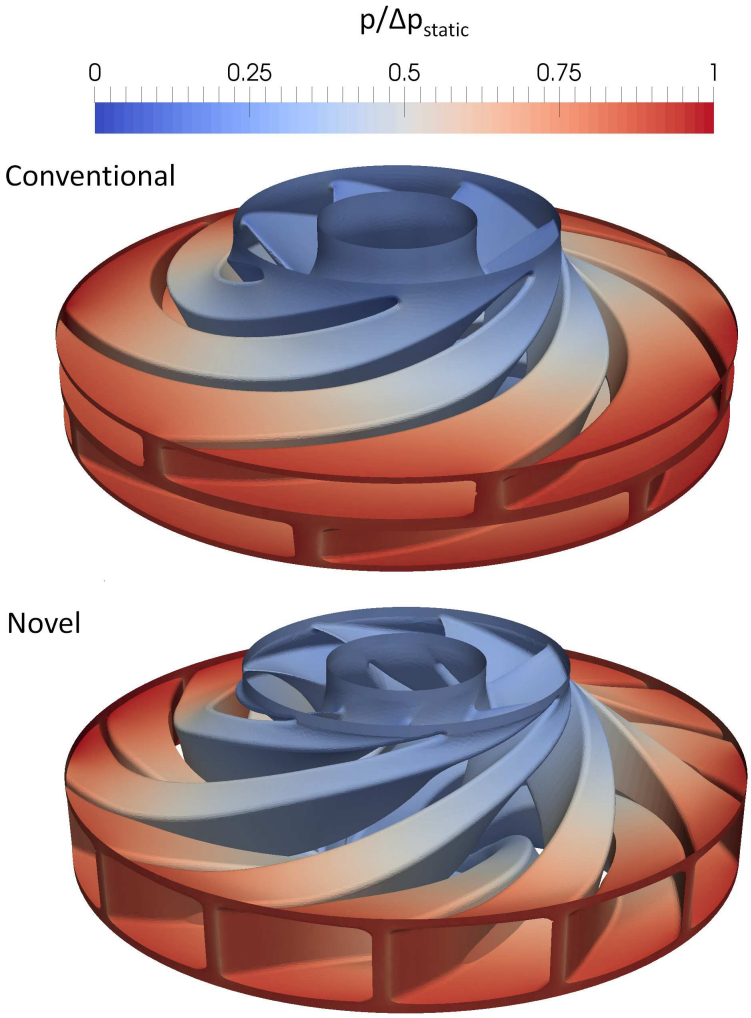

Figure 5.4: *View of the channels designed with a conventional design tool (up) and the novel impeller for double suction centrifugal pumps covered by patent application (down).*

the experimental ones and the performance of the conventional geometry in order to quantify the performance improvement. The numerical results obtained with the set up described in the previous paragraph confirm the benefits previously pointed out by the single vane simulations in terms of slip factor and efficiency, see Figs. 5.5, 5.6; in fact the novel impeller shows greater values of ψ vs φ and higher global efficiency over the full range compared to the baseline geometry. Furthermore, the numerical results show a good agreement with the experimental tests. This confirms the goodness of the numerical set-up.

In Fig. 5.5 two n_q iso-curves, corresponding to the n_q of the two impellers, have been calculated according to eq. 5.3. The specific speed is a parameter which is useful to select the right type of machine for a given application and it permits a comparison of geometrically dissimilar impellers. As shown in Fig.5.5, where two n_q iso-curves passing through the BEP of the two pumps are represented, the design process proposed

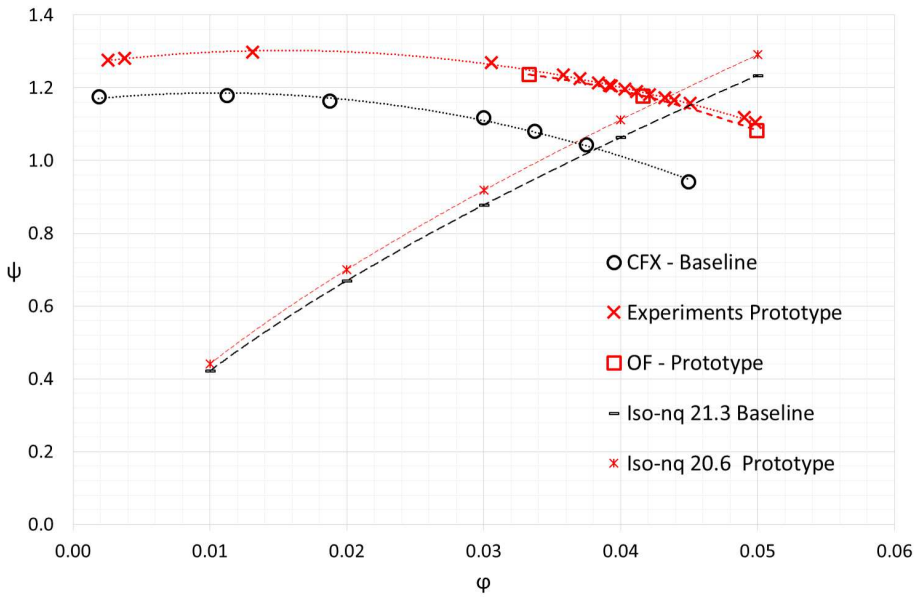

Figure 5.5: *ψ-φ curves of the conventional impeller (CFX - Baseline) and the novel impeller obtained via numerical simulations (OF - Prototype) and experiments (Experiments Prototype); the dashed curves represent the iso-n_q which pass through the BEP of the two impellers.*

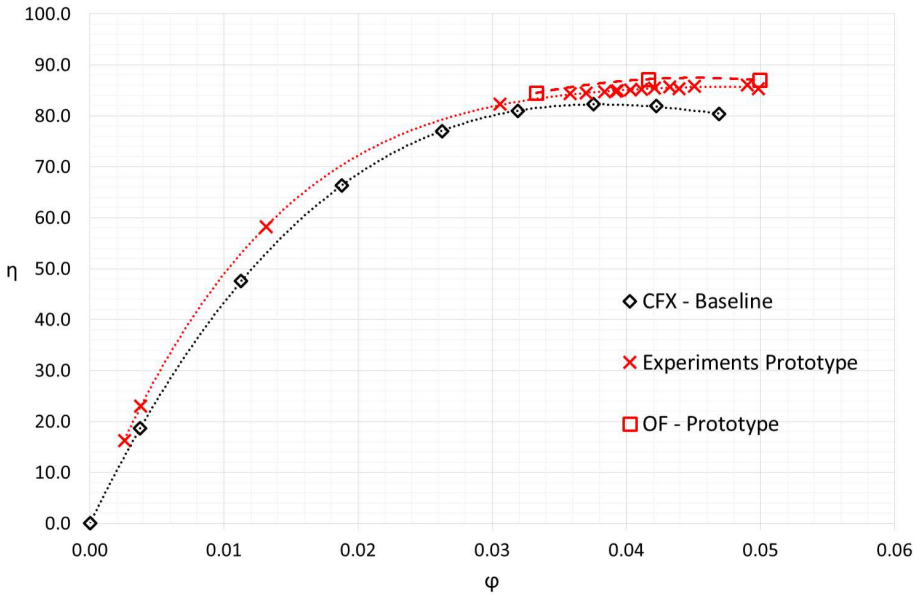

Figure 5.6: *Efficiency curves of the conventional impeller (CFX - Baseline) and the novel impeller obtained via numerical simulations (OF - Prototype) and experiments (Experiments Prototype).*

for centrifugal pumps, having specific speed (n_q) comparable to the one of the baseline, is able to guarantee a relative specific speed error (n_q error) lower than 3.4%. Therefore it is possible to make a comparison between their performance.

$$n_q = \frac{\varphi^{1/2} cost}{\psi^{3/4}} \tag{5.3}$$

Considering this, it can be stated that preserving the stator parts and just substituting the baseline impeller with the novel one, the new hydraulic machine provides a higher value of the head coefficient (see Fig.5.5); this means that the novel impeller is able to transfer energy to the fluid more efficiently and this substantial difference can be justified by the higher value of its slip factor, Tab.4.2.
Another reason behind the performance improvement can be found in the enhancement of the shape and the length of the impeller channels, as explained in the paragraph 2.2. The values of the efficiency, shown in Fig.5.6, are calculated by means of the following expression:

$$\eta = \frac{Q\Delta P_{tot}}{C\omega} \tag{5.4}$$

where Q is the flow rate expressed in (m^3/s), ΔP_{tot} is the total pressure difference between two flanges downstream and upstream the impeller (N/m^2) (Fig.4.2), ω is the rotational speed in (rad/s) and *C* is the torque (Nm) exchanged by the fluid and the impeller, including the shear stress acting on the internal and external surfaces of the impeller (disk friction losses). As explained in paragraph 5.2.2 flow leakages are considered, thus their effect is included in the efficiency calculation. Only the shaft mechanical losses are neglected, hence:

$$\eta = \frac{\eta_g}{\eta_m} = \frac{\eta_y \eta_v \eta_m}{\eta_m} \tag{5.5}$$

In eq.5.5 η_y is the hydraulic efficiency, η_v is the volumetric efficiency and η_m is the mechanical efficiency.

Whereas the increase in ψ coefficient shall be due to the slip phenomenon, the efficiency improvement can be justify by looking at the shape of the novel vanes. Indeed, the new shape of the channel section along with its reduced length allow the reduction of the hydraulic losses ($h_{w-channel}$) inside the channels (eq.5.6, where ϵ is the friction factor which depends on the Reynolds number and the relative roughness $\epsilon = f(Re, r/D)$).

$$h_{w-channel} = \epsilon \frac{L}{D_h} \frac{w^2}{2} \tag{5.6}$$

The cross sections of the new channels have generally larger hydraulic diameters (D_h). This contribute is meaningful in Fig.5.6 where the efficiency curves are compared. The second comparison proposed is done in the $H/H_{BEP,conv}$ - $Q/Q_{BEP,conv}$ plane, where $H_{BEP,conv}$ and $Q_{BEP,conv}$ are the values of head and flow rate of the conventional geometry in correspondence of its BEP. All the curves represented in Figure 5.7 are scaled at the same rotational speed. In this plane are plotted: the curve obtained for the conventional geometry by means of CFD simulations and the characteristic curves of the novel geometry, one extracted experimentally and then the same geometrically scaled in order to reach the value $H_{BEP}/H_{BEP,conv}$ and $Q_{BEP}/Q_{BEP,conv}$ equal to 1, see Fig.5.7.

In order to reach $H_{BEP}/H_{BEP,conv}$ and $Q_{BEP}/Q_{BEP,conv}$ equal to 1, the new geometry needs a size reduction equal to 5.5%, applied along the three coordinates (x, y, z). This means that the novel impeller would lead to a machine smaller than the conventional one and consequently to a reduction of the industrial cost and of the volume

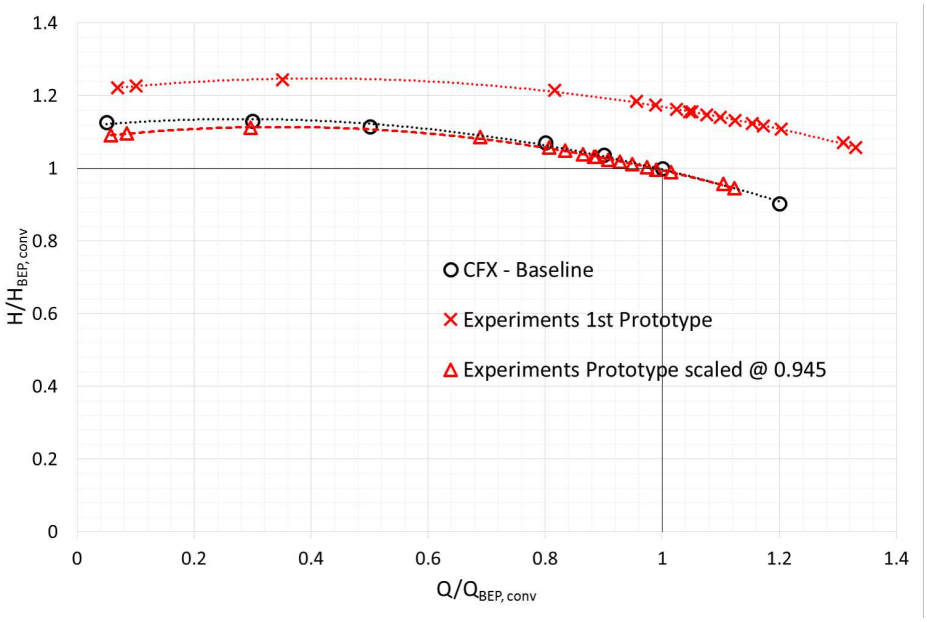

Figure 5.7: *Comparison of the characteristic curves between the conventional geometry (CFX - Baseline), the novel geometry (Experiments Prototype) and the novel geometry scaled to reach* $H_{BEP}/H_{BEP,conv}$ *and* $Q_{BEP}/Q_{BEP,conv}$ *equal to 1.*

occupied. Thus, it is possible to provide a larger pressure rise with the same size of the pump or alternatively to choose a more efficient and compact system. An example of the impact of these conclusions will be presented in paragraph 5.3.3.

5.2.5 Flow analysis at the outlet of the impellers

First of all a study of the velocity (Figs.5.8, 5.9) and the vorticity (Fig.5.11,5.10) field at the outlet of the impeller has been carried out with the aim to verify the benefits of the novel configuration. Figure 5.8 shows the contours of the dimensionless velocity magnitude (c_2/u_2) at the outlet of the two impellers; the velocity contours at the outlet of the novel impeller configuration are particularly more homogeneous than in the traditional one. Indeed, the standard deviation of the velocities along the axial direction is equal to 0.68 and 0.45 for the conventional and the novel impeller, respectively.

It is well known that a square duct limits the secondary flows compared to a rectangular one, hence velocity unbalances between the corners of cross section are reduced. This means a reduction of the secondary losses and a better flow guidance [14]. Velocity profiles have been calculated on surfaces at the outlet of the impeller along the axial direction averaged over $360°$. These are reported in Fig.5.9 and point out that the velocity profile at the outlet of the novel impeller follows a flatter profile; on the other hand the baseline shows a velocity ripple in the middle, therefore the division element influences the mixing flow in the baseline configuration. Moreover, the theoretical values of the absolute velocity magnitude (c_2) calculated at the outlet of the impellers are represented in Fig.5.9. It can be stated that the velocity profile at the outlet of the novel geometry is closer to the target value, calculated by means of the blade congruent theory, compared to the baseline geometry. The relative errors between the mean velocities calculated by means of CFD and the theoretical velocities are equal to 4.8% and 9.6%

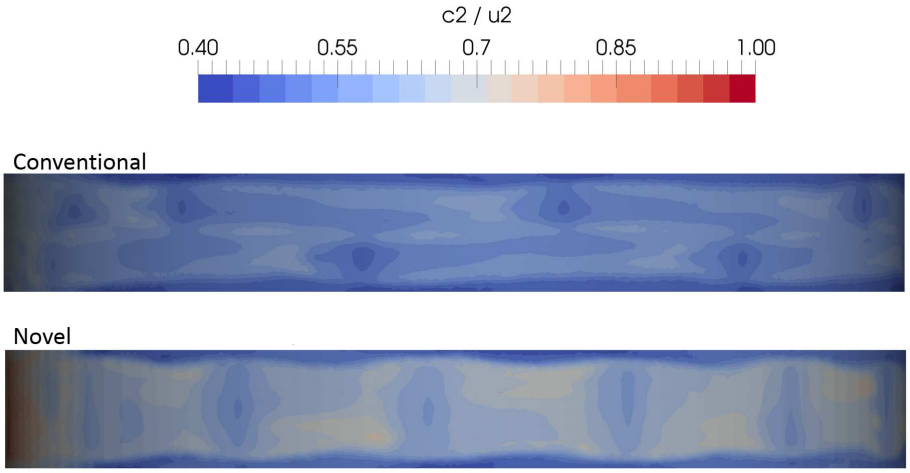

Figure 5.8: *Contours of the dimensionless velocity magnitude c_2/u_2 at the outlet of the conventional (up) and novel geometry (down).*

for the novel and the baseline, respectively.

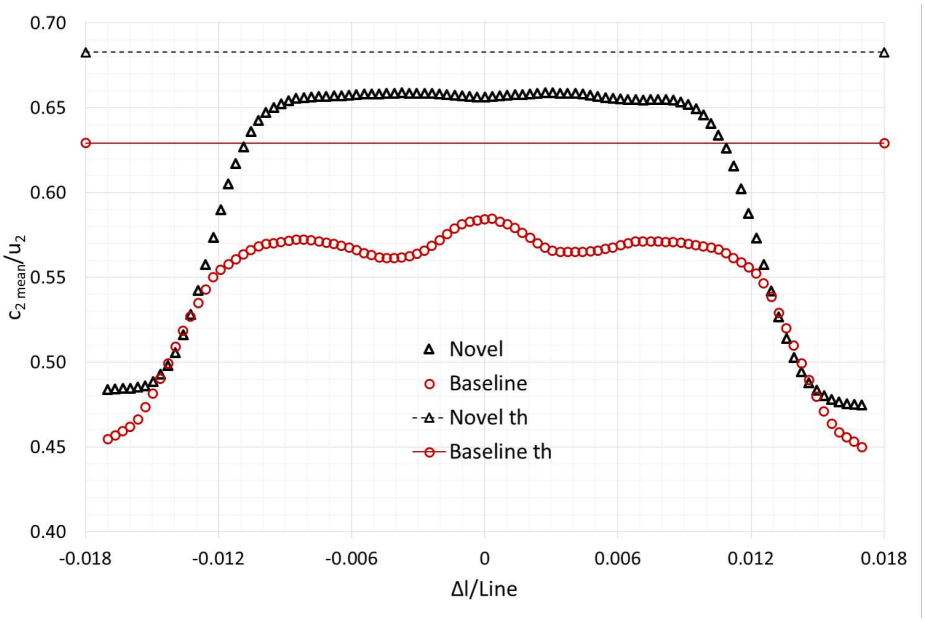

Figure 5.9: *Averaged velocity profiles at the outlet of the traditional and new geometry along the axial direction, where u_2 is the tangential velocity at the outer diameter.*

In order to evaluate the fluid characteristics in the region between the impeller outlet and the volute inlet and to understand how the flow field is influenced by the design of the novel impeller, iso-surfaces of the "Q-criterion vortex" [109] are shown in Fig.5.10. These iso-surfaces describe the wake structures. In the conventional geometry these occur in correspondence of the division element between the two impeller in back-to-back configuration, Fig.5.10,a. On the other hand, in the novel configuration, only vertical structures remain as well as in the conventional geometry in correspondence of the leading edge of the blades.

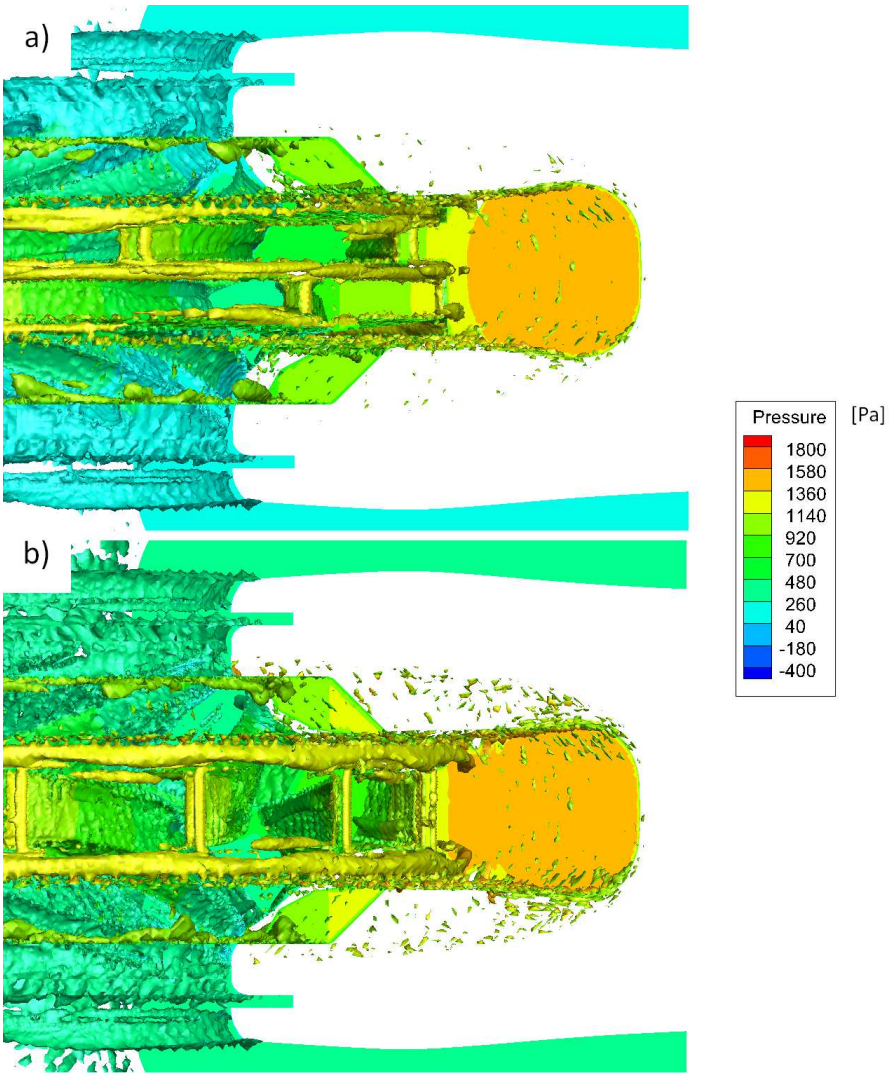

Figure 5.10: *Iso-surfaces of the vortex criterion Q colored by pressure contours of the static pressure.*

A study of the vorticity field points out that the vorticous structures that develop between the left and right side of the baseline impeller vanish when the novel geometry is employed. This might help the flow guidance and it also reduces the secondary flows, which develop inside the volute, diminishing the losses inside of it. Moreover, the absence of the division element allows a better flow mixing between the two side of the impeller. It is well known that inside the volute secondary flows develop and the flow pattern has the shape of a double vortex. This secondary flow becomes increasingly asymmetrical with growing non-uniformity of the impeller outflow, see Figs.5.9 and 5.11 (paragraph 2.2.6).

5.2.6 Analysis of the pressure fluctuation

To investigate the pressure pulsations inside the volute, the velocity and the pressure profiles at the outlet of the impeller have been plotted. In this case velocity and pressure have been plotted along the circumferential direction over 360° by cutting a cylindrical

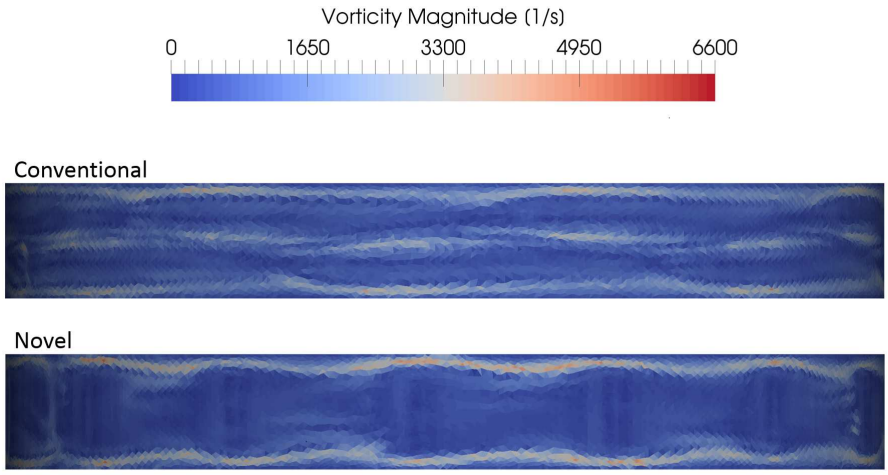

Figure 5.11: *Contours of the vorticity field at the outlet of the traditional (up) and novel geometry (down).*

surface between the impeller outlet and volute inlet with three planes, see Fig.5.12. The first plane is at the half of the impeller (middle plane), the other two are at different axial distance ($\pm l_2/2$) with respect to the middle one. The results (Fig.5.13, 5.14, 5.15 and 5.16) are averaged over the last 5 rotations of the machine.

The baseline configuration shows a velocity profile calculated at the middle plane with a frequency equal to $2N_b f_{rotation}$, on the other hand the velocity profile of the two back-to-back impellers displays a saw-tooth evolution with $f = N_b f_{rotation}$. The novel impeller has a quite flat velocity profile except that close the trailing edge of the blades where the velocity increases. The analysis of the velocity points out a different behavior in the middle plane, the novel impeller displays a smooth oscillation of the velocity, whereas the baseline presents oscillation higher than at the half of the vanes' exit. The velocity peaks coincide with suction side of the impeller.

Contrary to the velocity trends, the pressure profile of the baseline shows a saw-tooth evolution in the middle plane, with a $2N_b f_{rotation}$. The novel geometry displays a pressure profile identical for each position of the planes. Even if the baseline impeller tends to smooth the pressure peaks and valleys due to the arrangement of the two single suction impellers, the baseline shows locally higher pressure amplitude than the novel impeller (55.1 Pa and 47.2 Pa, respectively).

Moreover, the head, calculated via numerical simulations has been studied in order to further investigate pressure fluctuations inside the volute. This represents the dynamic interaction between the blades and the tongues of the double volute. The evolution of the head over an interval corresponding to the time necessary to complete a portion of a complete rotation equal to $360°/N_b$ has been plotted in Fig.5.17. The novel geometry shows a higher pressure fluctuation, i.e., the values of the standard deviation over the mean value of the head (σ_{Head}/H_{mean}) are 2.29% and 3.71% for the baseline and the novel impeller, respectively. This result confirms what pressure profiles highlight along the circumferential direction, namely the arrangement of the baseline geometry is prone to cut pressure peaks.

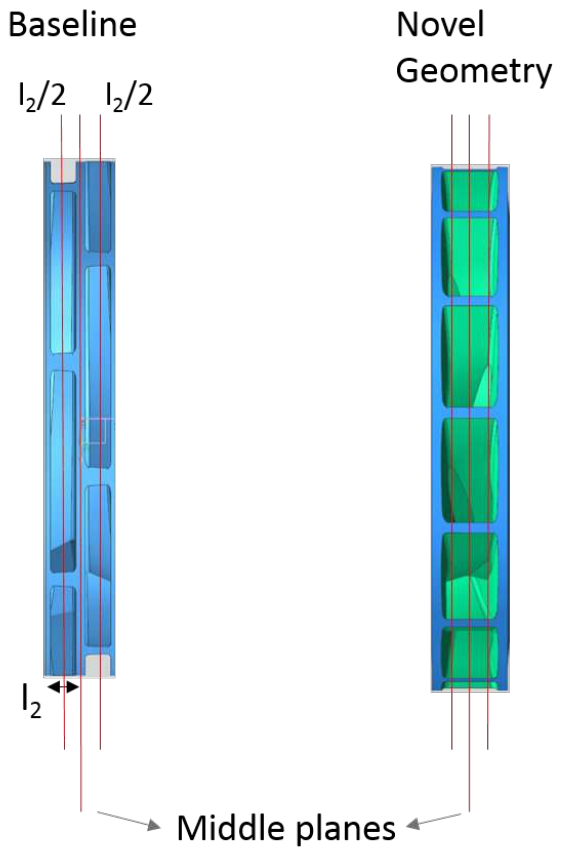

Figure 5.12: *View of the impeller outlet with three planes on which velocity and pressure have been calculated.*

The frequencies of the two curves are equal to $2N_b f_{rotation}$, whereas the amplitude of the head fluctuation is higher for the novel geometry. A higher amplitude could drive the piping system to oscillate with greater amplitude at specific frequencies if the frequencies of the pulsations are equal to the system's resonant frequencies. Even though the novel impeller shows higher pressure fluctuations these can be reduced by changing the blade inclination, see Fig.5.18. This allows to distribute the forces on a longer surface. Typically, λ_{La} can vary from 70 to 90 °. Moreover, in case the frequency coincides with that of the piping system, to avoid resonance frequencies at least three parameters can be changed: the number of blades of the impeller, the system's resonant frequencies and the rotational speed.

It is worth highlighting the dynamic forces generated by the interaction between the blades and the two tongues of the volute during a complete rotation. Analyzing the novel geometry dynamic behavior, the forces results coaxial and symmetric with respect to the rotation axis, Fig.5.19,a, on the other hand the baseline shows eccentric forces that generates a momentum which changes its verse with a frequency equal to $2N_b f_{rotation}$ during a complete rotation, see Fig.5.19,b. This oscillating phenomenon could impair the performance of the bearings.

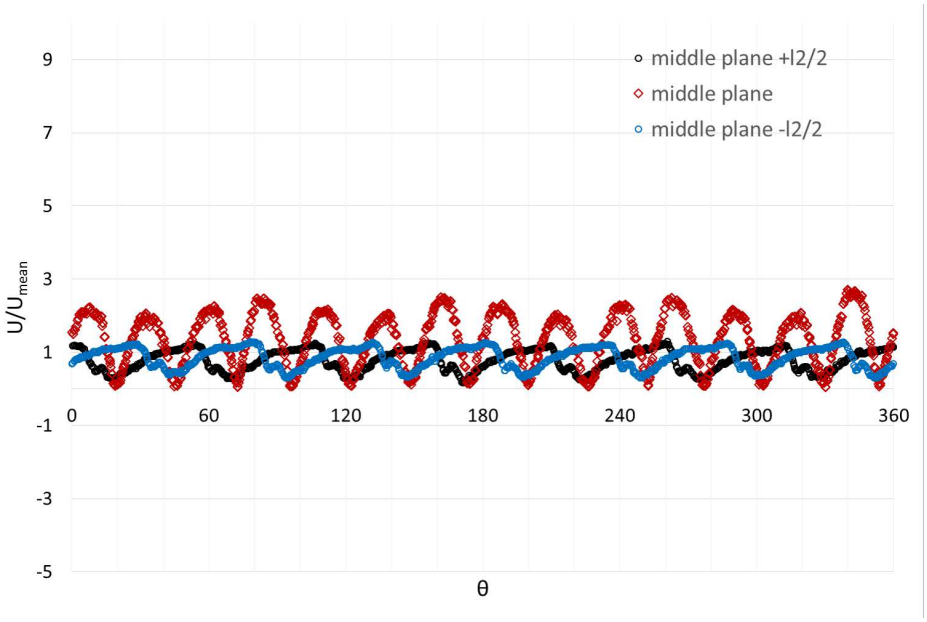

Figure 5.13: *Averaged velocity profiles at the outlet of the baseline impeller.*

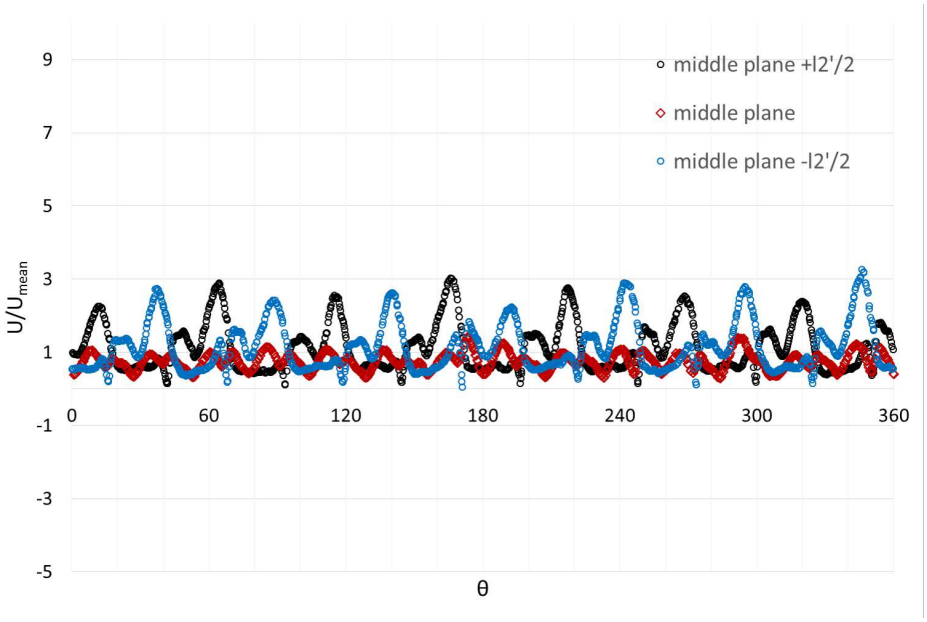

Figure 5.14: *Averaged velocity profiles at the outlet of the novel impeller.*

5.2.7 Torque and vibrations analysis of the first prototype

The first prototype has been tested at Hydraulic test rig of Nuovo Pignone, Bari. In the following paragraph the experimental data analysis will be shown. Torques, vibrations and pressure upstream and downstream of the impeller have been analyzed. Data acquisition has been carried out at different flow rate: 125%, 112.5%, 100%, 85%, 70%, 50%, 30%, 10% and 6%. Vibrations have been measured on a bearing in order to detect radial forces due to pressure fluctuation inside the volute. Furthermore, a statistical

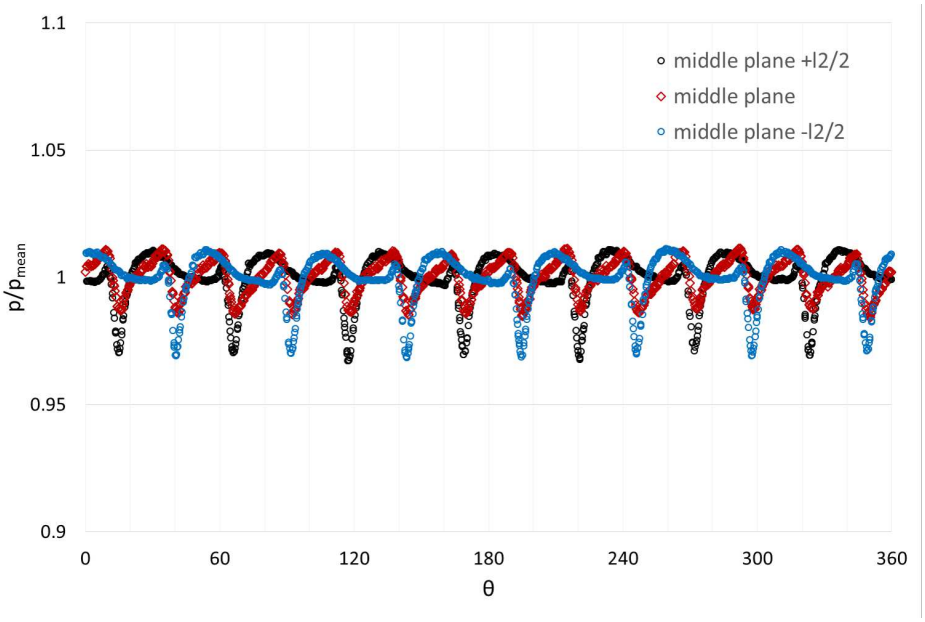

Figure 5.15: *Averaged pressure profiles at the outlet of the baseline impeller.*

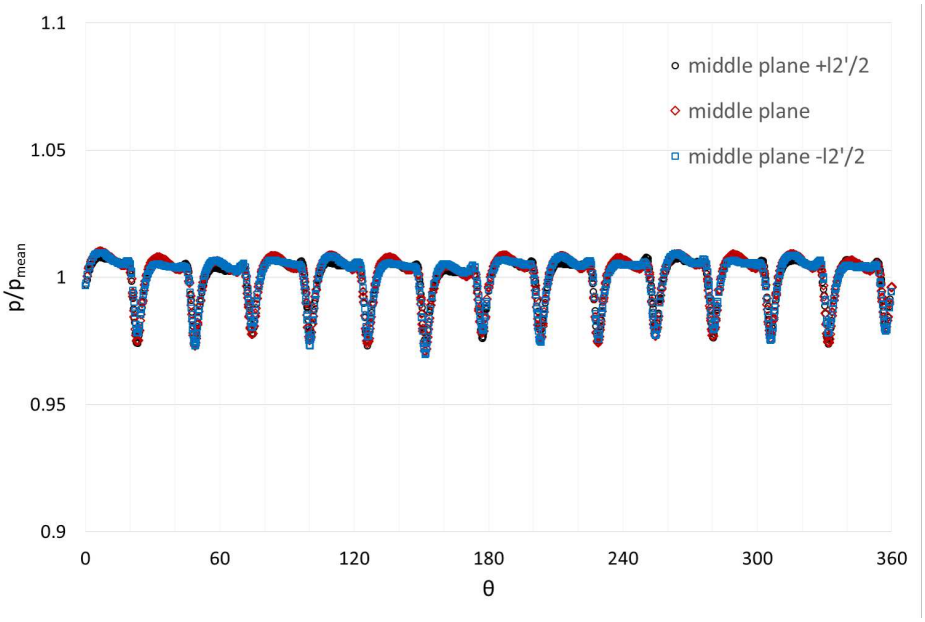

Figure 5.16: *Averaged pressure profiles at the outlet of the novel impeller.*

analysis and the Fast Fourier Transform (FFT) have been applied to data in order to investigate resonance phenomena, flow instabilities and blade stall related to the first prototype geometry.

Firstly, analyses of the torque and vibrations ($V_{ythrust}$) for the new prototype have been performed. In Fig.5.20 the standard deviation has been plotted over flow rate. It can be stated that in the range of part-load and over-load the torque has low oscillation, on the contrary torque oscillations increases towards the shut-off condition. On the other hand vibrations remain almost the same for all the flow rate.

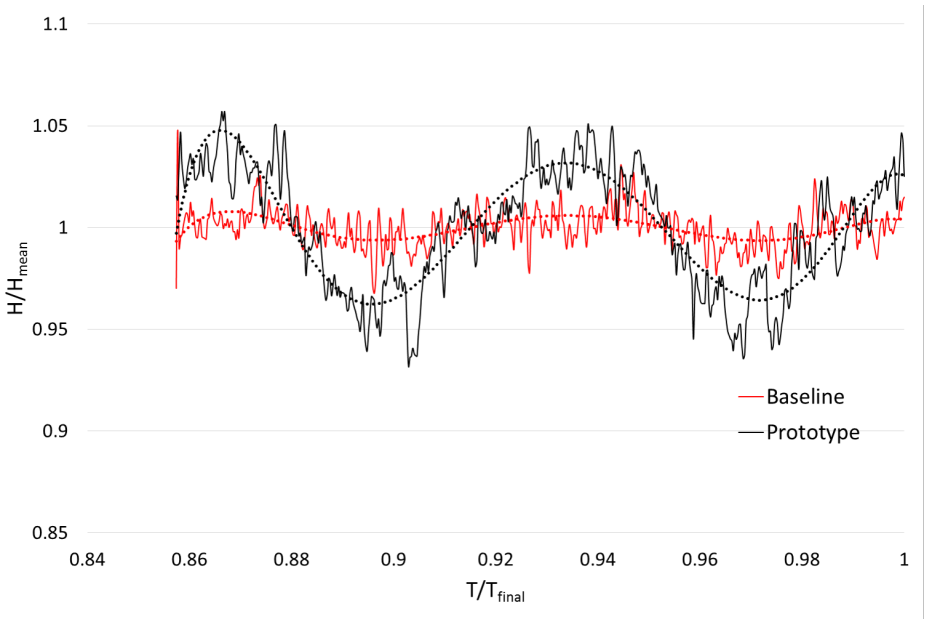

Figure 5.17: *Averaged head (H) evolution over pressure value over a time equal to $(T/T_{final})/N_b = 1/7$ of a complete rotation.*

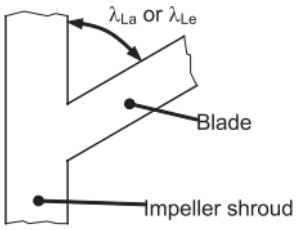

Figure 5.18: *Blade inclination.*

The signal spectra are plotted on dimensionless abscissa referred to the rotation frequency, f_0. Looking at the frequency spectrum of the torque signal, Fig.5.21, 5.22, the highest frequency's amplitude appear to be localized at 2x and 3x, 7x and 8.3x, close to 23.4x and 33.4x of the rotational frequency.

The frequency spectrum of the vibrations is slightly different and it shows the highest peaks amplitude 1x, 4x, 14x and 28x of the rotational frequency. Some of these coincides or are multiple of the number of blades. Low frequencies, such as 2x may be related to the double volute configuration.

This analysis does not show phenomena, which could be related to instability and stall inside the impeller, allowing the design of a novel impeller with a higher blade loading. Therefore, a new geometry with 5 blades has been developed, as previously discussed in Chapter 4.

5.3 Performance of the second prototype

THe second prototype has been designed with geometry improvements and numerical simulations have been carried out. Once the impeller has been manufactured, it has

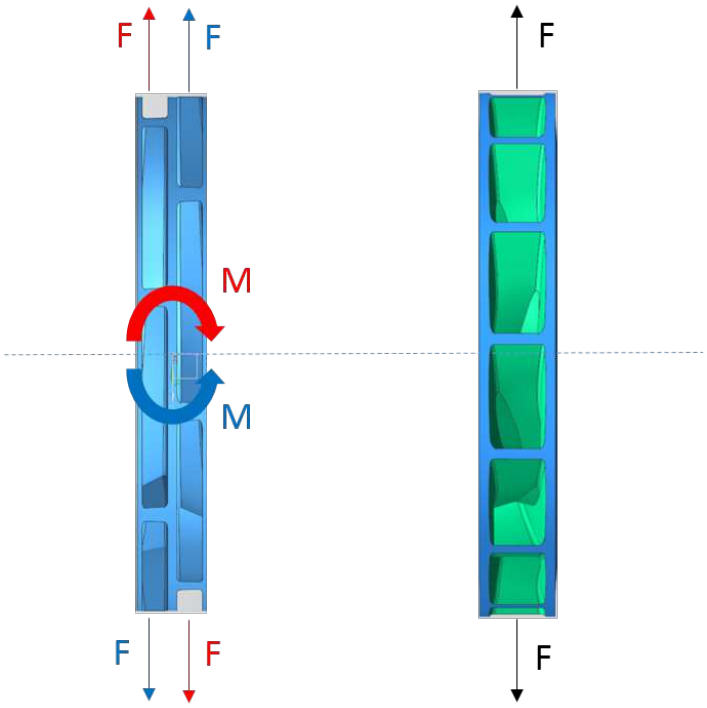

Figure 5.19: *Forces due to the interaction between the blades and the volute tongues.*

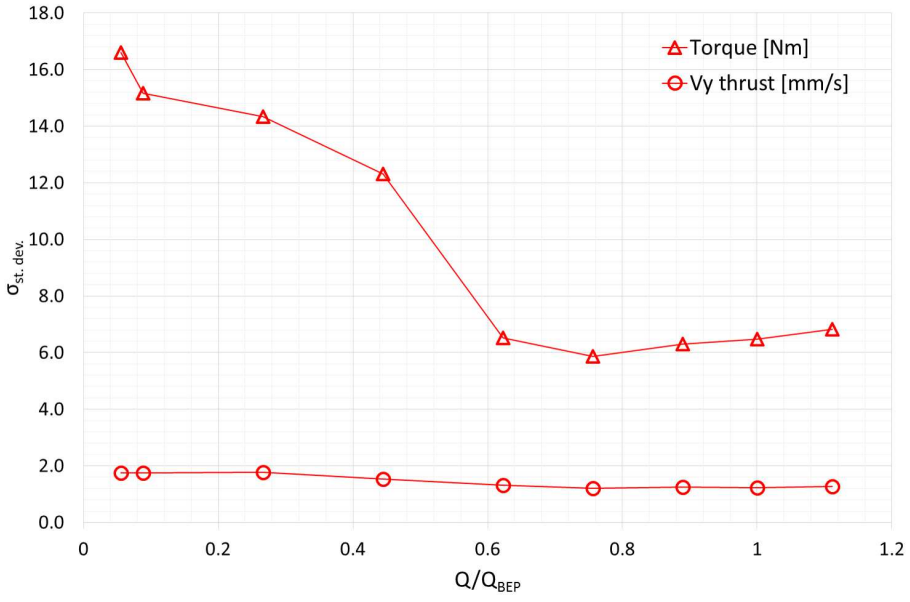

Figure 5.20: *Comparison of the RMS values of the torque (Nm) of the two prototypes.*

been tested at the hydaulic test rig of Nuovo Pignone. As in the previous case, paragraph 5.2.4, the second geometry shows an improvement in terms of ψ vs. ϕ, Fig.5.24 and 5.25, that is due to the reduction of the slip phenomenon at the outlet of the impeller. This is a remarkable result considering that the number at the impeller eye is lower than the baseline. The second prototype shows an efficiency globally higher than the

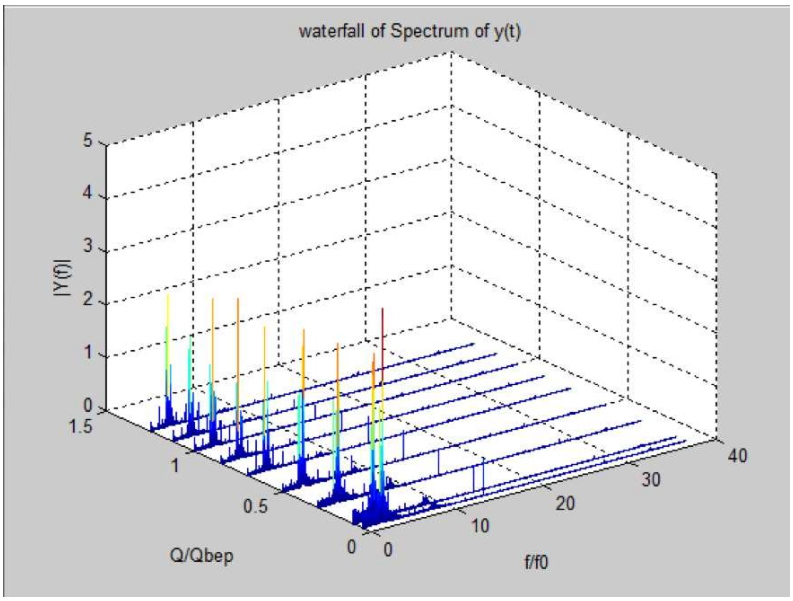

Figure 5.21: *Waterfall frequency spectrum (f_o = frequency of rotation) of the torque for different flow rate.*

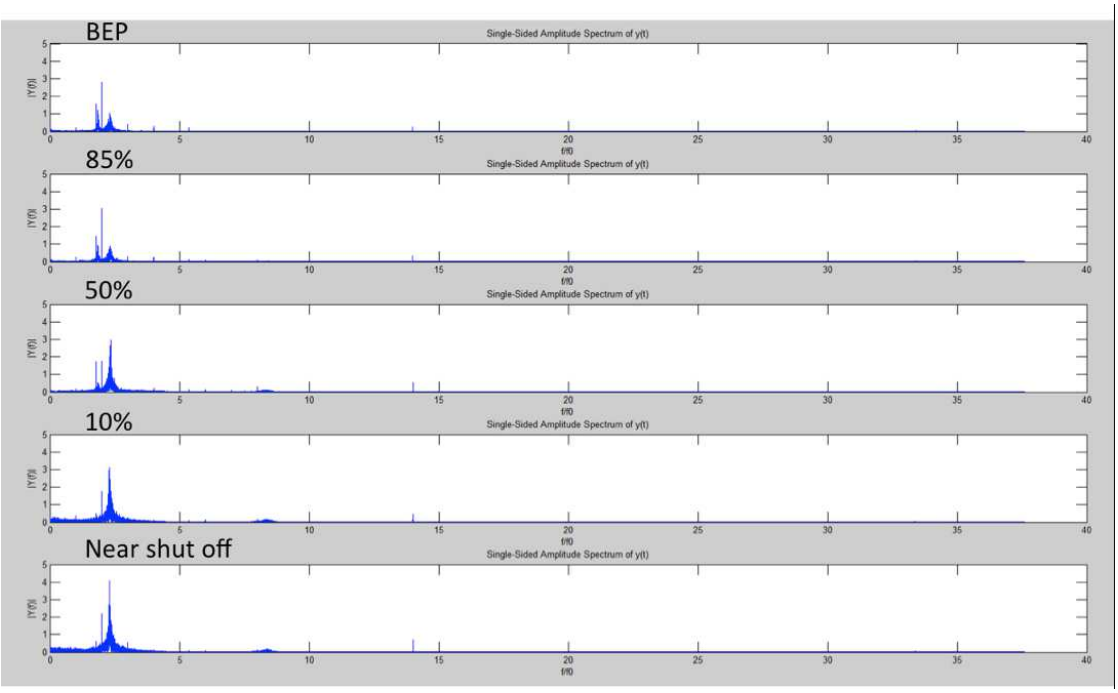

Figure 5.22: *Plot of the mean frequencies for torque measured at BEP flow rate at 85%, 50%, 10% and near shut-off.*

baseline, close to the value obtained by the first prototype. The specific speed of the second prototype is equal to 22.5 with an error equal to 5.75% and 9.34% with respect to the baseline and the first impeller. These errors can be due to the coefficients used to calibrate the slip factor modified expression used in the design process. Nevertheless, the second prototype do not show instable curve towards zero flow rate.

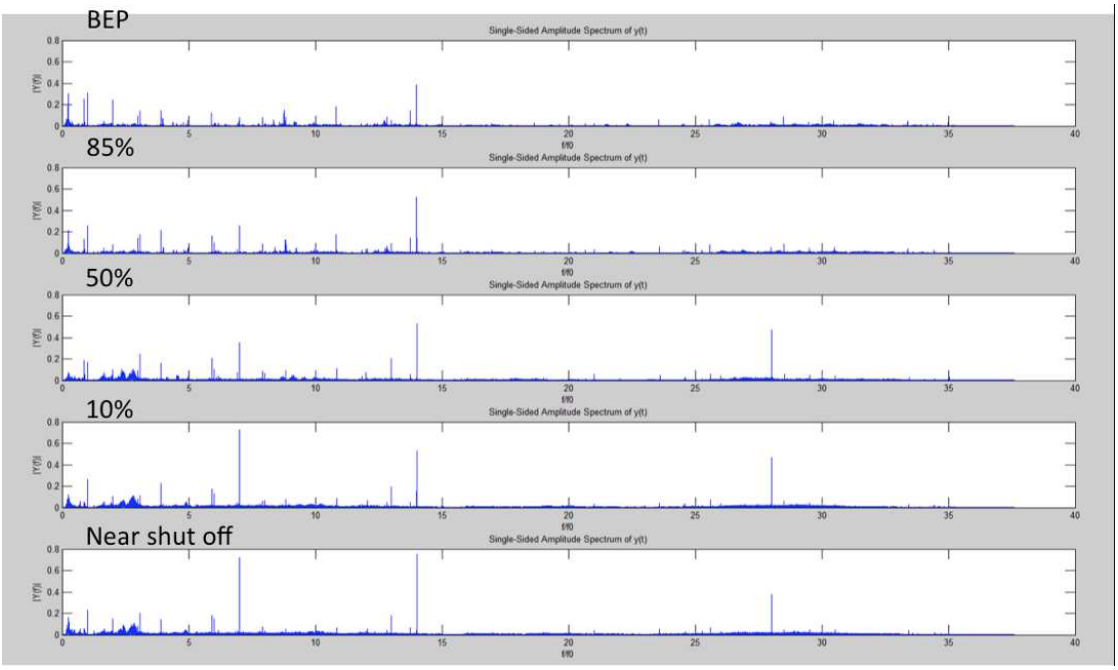

Figure 5.23: *Plot of the mean frequencies for vibrations measured at BEP flow rate at 85%, 50%, 10% and near shut-off.*

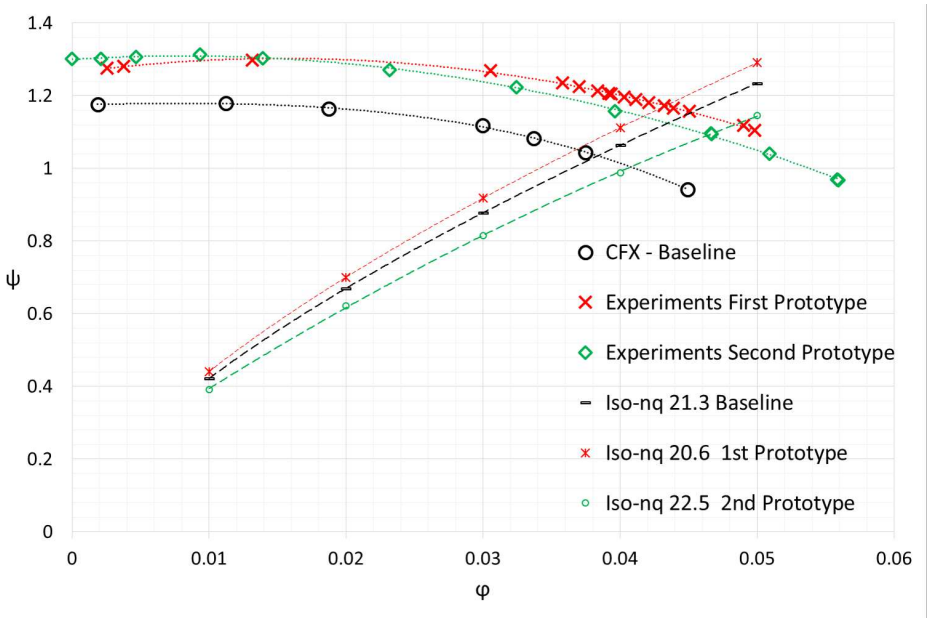

Figure 5.24: *ψ-φ curves of the conventional impeller (CFX - Baseline), the first prototype and the second prototype obtained via experiments (Experiments Prototype); the dashed curves represent the iso-n_q which pass through the BEP of the three impellers.*

Moreover, the power coefficient (λ) has been calculated for the three pumps; it is defined as follows:

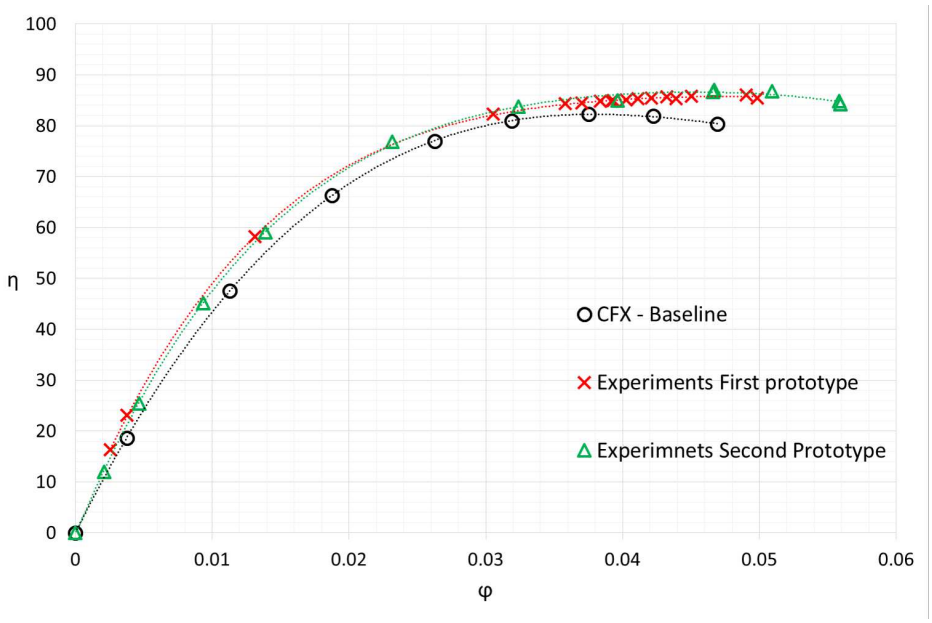

Figure 5.25: *ψ-η curves of the conventional impeller (CFX - Baseline), the first prototype and the second prototype obtained via experiments.*

$$\lambda = \frac{\psi\phi}{\eta} \tag{5.7}$$

The two new prototypes present higher power coefficient compared to the baseline. This is obvious if we consider that the novel geometries provide simultaneously higher ψ and ϕ, eq.5.7.

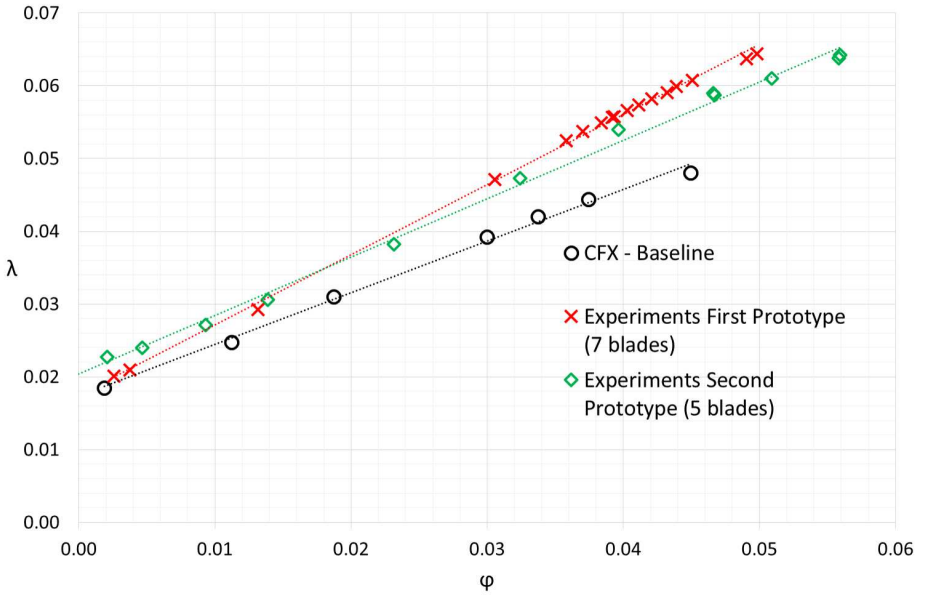

Figure 5.26: *ψ-λ curves of the conventional impeller (CFX - Baseline), the first prototype and the second prototype obtained via experiments.*

5.3.1 Scaled geometry

As previously described for the first prototype, also in this case the novel impeller can be downsized to reach the same performance of the baseline $H_{BEP}/H_{BEP,conv}$ and $Q_{BEP}/Q_{BEP,conv}$ = 1. To do this the impeller has to be downsized by 4%, Fig.5.27. The size reduction means a compact system with higher power density (W/m^3) than the baseline.

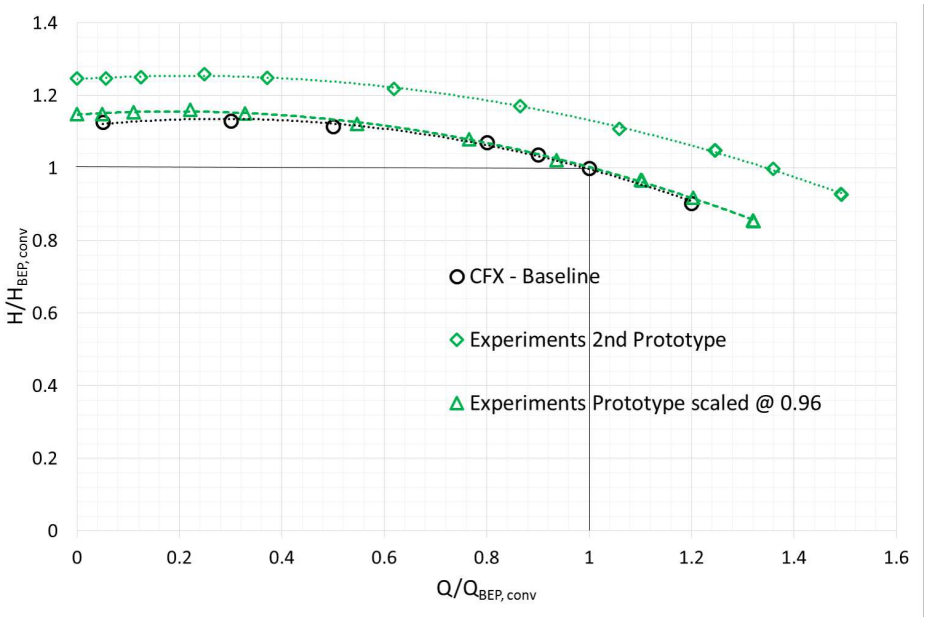

Figure 5.27: *Comparison of the characteristic curves between the conventional geometry (CFX - Baseline), the second prototype (Experiments Prototype) and the second prototype scaled to reach $H_{BEP}/H_{BEP,conv}$ and $Q_{BEP}/Q_{BEP,conv}$ equal to 1.*

5.3.2 Slip facor calibration

Herein the values of the slip factor calculated by means of the standard expression and the modified one are summed up.

Table 5.4: *Slip factor for the baseline, first and second prototype after single-vane simulations*

	Baseline	First prototype	Second prototype
N_b	7	7	5
σ (eq.4.5 with a=1 and b=0)	0.8101	0.7943	0.7504
σ single-vane CFD	0.7816	0.8538	0.7645
a		0.65	1.06
b		0.35	-0.06
$a + 2b$		0.675	0.47
operating N_b	4.65	9.45	4.7

The analysis of the results in Tab.5.4 suggests that the slip factor calculated by neglecting the novel shape of the vanes underestimates the actual value. Decreasing the number of blades, the error between the two formulation decreases. Besides, the novel

design impeller with 5 blades has an actual number of blades higher than a conventional one with 7 blades.

5.3.3 Comparison of the torque, vibrations and $NPSH_{3\%}$ curves of the two prototypes.

In the following figures (5.28 and fig:vibrations2) a comparison of the torques and the vibrations of the two impellers, tested at the Hydraulic test rig of Nuovo Pignone, have been done. It can be stated that the torque does not show high oscillation amplitude. The same thing appears in the vibrations graphic. Thus strange fluid dynamic phenomena seem not to be present by employing the novel configuration.

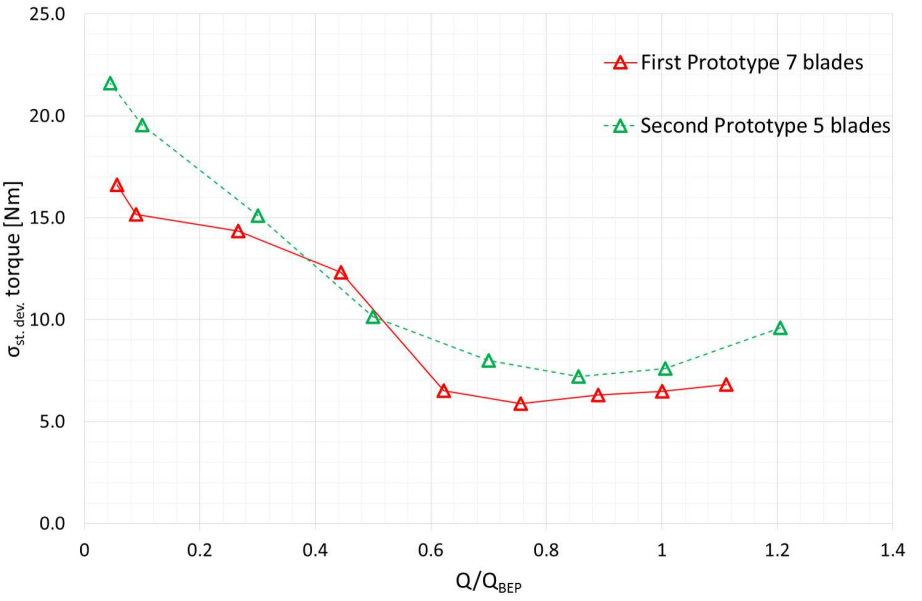

Figure 5.28: *Comparison of the RMS values of the torque (Nm) of the two prototypes.*

Experimental test have been carried out to measure the Net Positive Suction Head, $NPSH_{3\%}$. The curve of the two prototype (7 and 5 blades) have been measured via experimental test at Hydraulic test rig of Nuovo Pignone and have been compared with the baseline geometry calculated via CFD simulation by the CFD team of Nuovo Pignone, see Fig.5.30. The curves show that the novel geometry requires a lower $NPSH_R$ over the range from part to over load than the baseline and the novel geometry shows a flat curve towards shut-off zero flow rate. Furthermore, due to the improvement in the design the second prototype has a lower $NPSH_R$ around the BEP than the first prototype.

5.3.4 Impact of the novel technology on carbon footprint

According to the results shown in this thesis, it can be stated that the introduction of this technology, instead of the conventional one, can allow a reduction of the total electric motor energy consumption in industry due to centrifugal pumps, which nowadays in UE corresponds to 120 $TWh/year$. Under the hypothesis that the novel geometry provides an efficiency improvement in the order of $1-2\%$ and the number of double

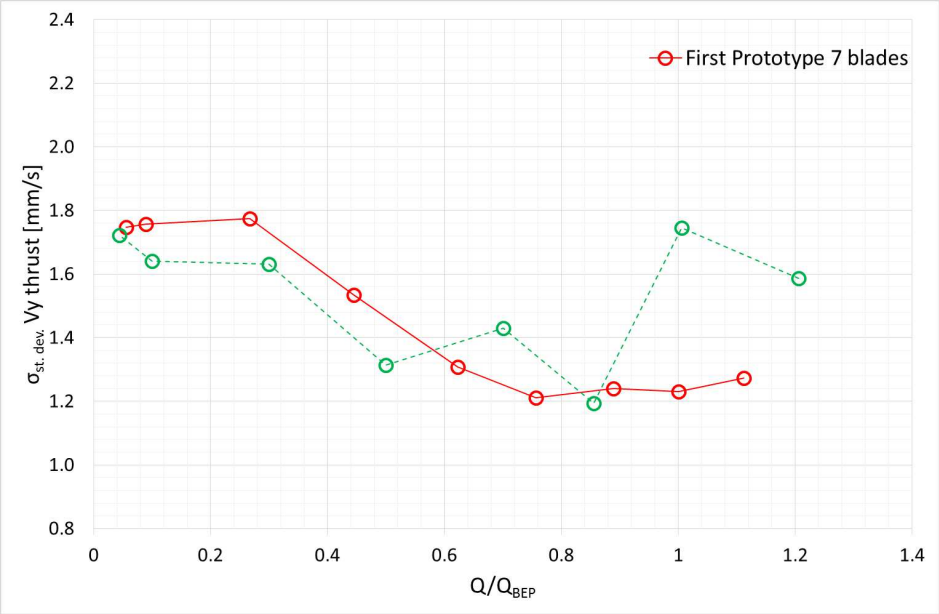

Figure 5.29: *Comparison of the RMS values of the bearing thrust along Vy (mm/s) of the two prototypes.*

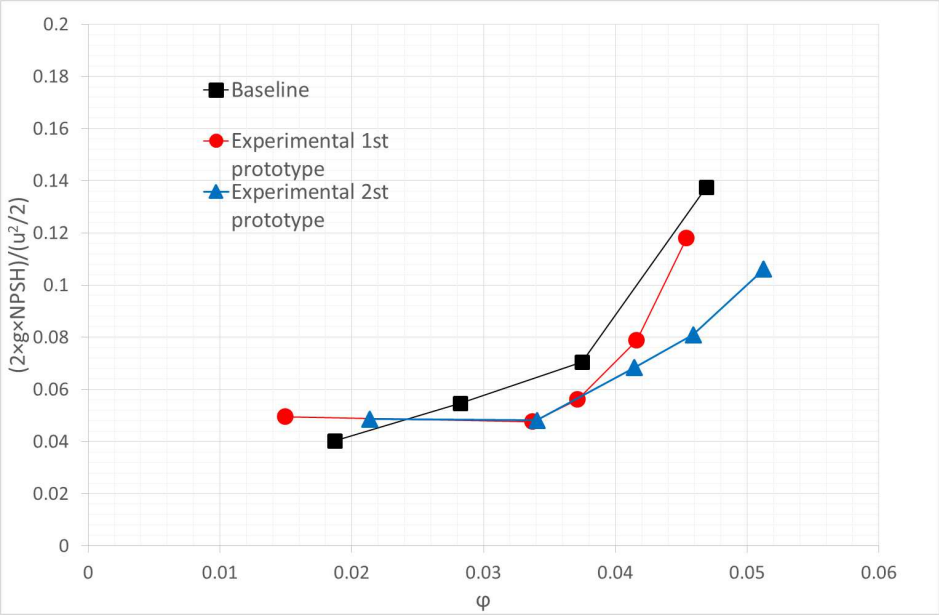

Figure 5.30: *Comparison of the NPSH curves for the baseline, the first and the second prototype.*

suction pumps were 30% of the total number of centrifugal pumps used in industry, then the amount of energy saved would be equal to $0.36\ TWh/year$. This amount of energy is equivalent to 600 units of 300 MW gas turbine power plants for electricity generation. The carbon footprint data related to gas-fired electricity generation is equal to 500 gCO_2eq/kWh [110], [111], thus the novel geometry could allow a reduction of the CO_2 emission up to $90 \cdot 10^3\ t_{CO_2}/year$. This would give a cumulative saving of $3.96\ TWh$ and $1980 \cdot 10^3\ t_{CO_2}$ by 2040. Norrowing it down to a Nuclear power plant, for instance the China's Hualong One. This plant has three primary coolant

loops with pump each driven by 6.6 MW electric motors (110 t each). Its gross energy production is 1170 MWe and the energy consumed by the pumps is equal to 19.8 MW. Under the hypotesis that the conventional and the novel geometry have the same weight, considering a 5.5% size reduction to provide the same pressure rise and the price of stainless steel = 1200 €/t a money saving of the 28000 € (-15.6%) concerning the cost of the pumps can be reached by substituting the three conventional geometry with novel ones. In terms of efficiency the retrofit of the conventional geometries could lead to 0.198 MW of energy saving in the global energy consumption.

5.4 Conclusions

In this chapter the main results of the numerical simulations and experimental test of a novel impeller have been shown. Firstly, the design process show a good prediction of the slip factor, indeed the CFD simulations before and the experimental after verify the performance of the two prototypes. The two geometries provide higher values of the head factor with almost the same value of specific speed. Moreover the two geometries show major values of efficiency compared to the baseline. This leads to high power factor. Before designing the second prototype potential flow instabilities, flow separation and dangerous resonance frequencies have been evaluated by means of experimental data analysis. The torque and vibrations have been studied. These do not show clear signs of instability. A remarkable results is that the novel impellers can provide a higher pressure rise keeping the same size of the baseline or a compact system can be installed with higher power density. This leads to a reduction in costs and emission. Moreover, the novel design displays a lower $NPSH_R$ and a flat curve towards zero flow rate. Finally the application of this technology has been hypotized to a real nuclear power plants with three pumps by 6.6 MW showing the advantages in terms of costs (-15.6% pump costs) and emissions.

CHAPTER 6

Novel Impeller as a Turbine

6.1 Introduction

World's energy consumption is increasing year by year and much attention is paid to renewable energy sources (such as hydroelectric) in order to replace fossil fuels consumption. In the field of Micro Hydropower Plants (MHP) where turbines are critical technological components, many researchers in the last decades proposed the use of pump as turbine (PaT) [112] and applied them to a real sites. Moreover, a significant amount of energy in petrochemical plants and water distribution networks is often wasted when Pressure-Reducing Valves (PRV) or other restriction mechanisms are used. Indeed, these devices can be effectively replaced by pumps used as turbines for waste energy recovery. Furthermore, pump as turbine are used in combination with renewable energy plants in order to storage energy during off-peak demand due to the intermittency [113]. Thus, they can be used as energy storage systems (ESSs). One of them is the Pumped Hydro Energy Storage (PHES), which is characterized by predictable energy characteristics, long-term reliability and reduced global environmental effects. Moreover, thanks to its storage capacity and flexibility it can support the installation of other intermittent renewable power plants [114, 115]. The use of PaT is strongly suggested because pumps are mass-produced, cheaper than turbines and covers wide range of specific speeds and sizes. Moreover, from an economical point of view, it is often stated that PaTs, in the range of 1 to 500 kW, are profitable and allow capital payback periods of two years or less, which is considerably less than that of a conventional hydraulic turbine [116].
Herein the novel impeller deeply described in the previous chapters has been studied numerically in reverse mode. The novel geometry, which has been previously studied as a pump showing an efficiency improvement with respect to a conventional geometry (a baseline impeller with the same specific speed) in the order of 1-2% associated

to a slip factor increase, secondary losses reduction and impeller outflow homogeneity improvement, has been thought to provide higher performance under turbine operating mode (Capurso, 2018). The new channel arrangement can help in guiding the flow at the inlet of the runner of a PaT in absence of diffuser and their novel shape allows the reduction of the hydraulic losses providing more energy to the shaft. Numerical analyses of both a baseline and the novel impeller operating in turbine mode have been performed by means of OpenFOAM and solving the 3D U-RANS equations with the k-ω SST model for turbulence closure (Menter, 2003). Eventually, their characteristic curves have been compared. The novel geometry shows an increase of the head coefficient (+4.33%) and the global efficiency (+0.83%); specifically the latter improvement is justified by evaluating the disk friction losses and the hydraulic losses inside the vanes. To do this the rotary stagnation pressure variation has been calculated along the channels of the two geometries. The results show that the novel geometry is able to extract energy from the fluid more efficiently. Furthermore, the new geometry can be downsized (-3.5%) to work at the same flow coefficient of the baseline providing both higher power coefficient (+5.53%) and space saving.

6.2 Results of the novel impeller working as a turbine

The novel and the baseline geometry have been simulated by inverting the inlet with the outlet, Fig.6.1. The boundary conditions have been set as the pump case, see chapter 5.

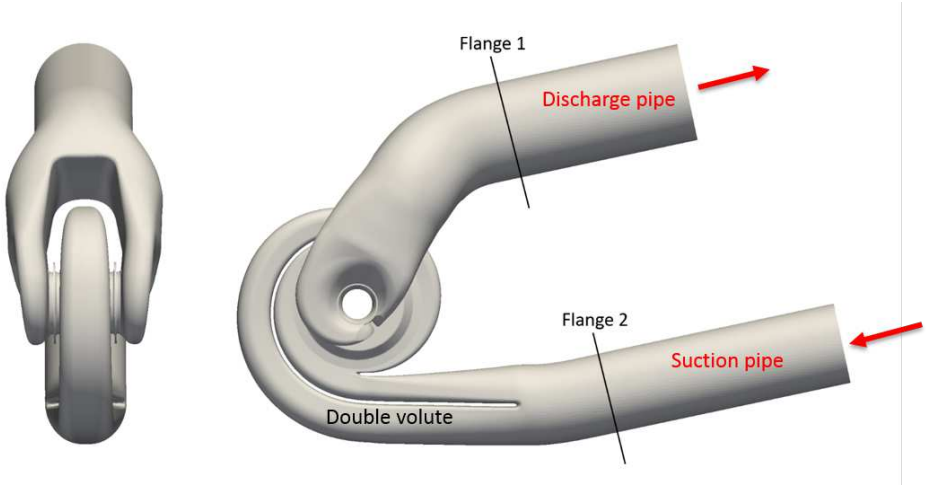

Figure 6.1: *Representation of the geometry and with reversed flow.*

All the transient flow simulations have been carried out with a time step $\Delta t = (T/N_b)/256$ = 4.5E-6 s where T is the time period of a complete rotation and N_b the number of blades for a duration total time equal to 0.085 s, which corresponds to five complete impeller revolutions. Once convergence has been reached, the results in terms of head and efficiency have been averaged over the last 3 revolutions. The mean and the maximum values of the Courant number have been found to be approximately equal to 0.03 and 6, respectively, in all the simulations.
The performance of the two geometries have been compared on dimensionless plane. The head and the flow coefficients have been used, whose expressions have been de-

scribed in the previous chapter (eq.4.2, 4.3). For pumps working as turbines the expression of the efficiency is defined as:

$$\eta = \frac{C\omega}{Q\Delta p_{tot}} \tag{6.1}$$

The runaway curve, represented in Fig.6.2, has been calculated by means of the empirical equations provided by [14]. The novel geometry has been designed in order to guarantee the same specific speed (n_q) of the conventional one (chapter 4). Experimental results have shown that the design process proposed by the authors provides pump impellers with specific speed deviation lower than 3.66% compared to the target one. From the numerical simulations carried out in this work, the specific speeds for the baseline and the novel impeller are equal to 21.88 and 21.08, respectively, with the same error that would have been obtained if the impellers had worked in pump operating mode.
In Figs6.2 and fig:eta pat it can be pointed out that the BEP of the novel impeller is placed at higher phi and that the global efficiency is higher (+0.83%) than the baseline. This shall be due to the novel shape of the vanes.

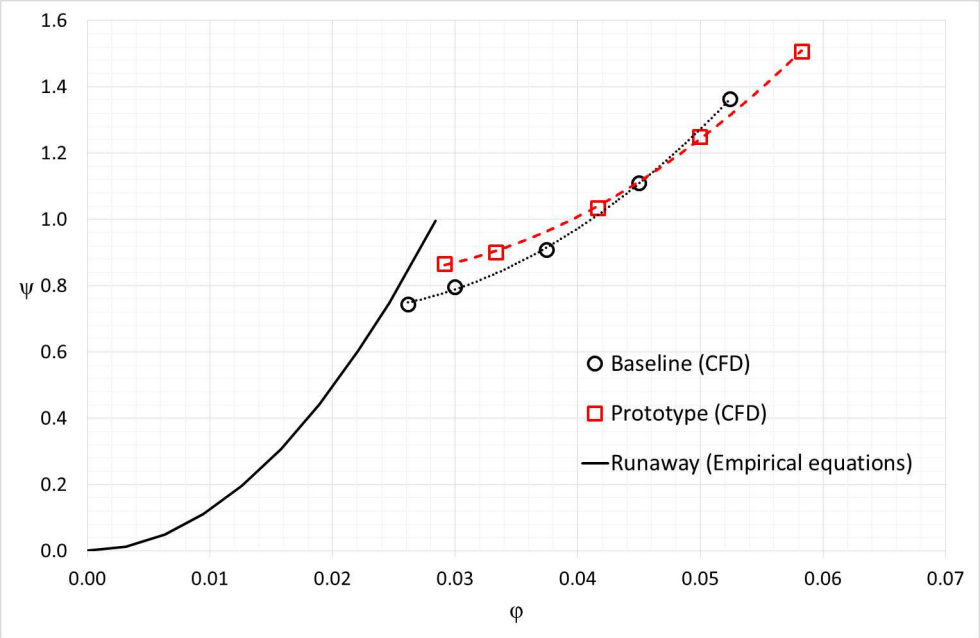

Figure 6.2: *Pressure coefficient (ψ) vs flow coefficient (ϕ) curves of the two geometries.*

Moreover, the power coefficient (λ) has been evaluated for the turbines; it is defined as follows:

$$\lambda = \psi\phi\eta \tag{6.2}$$

Looking at Fig.6.4, the power coefficient curve of the novel impeller displays higher flow coefficients as well as the $\psi - \phi$ curve.

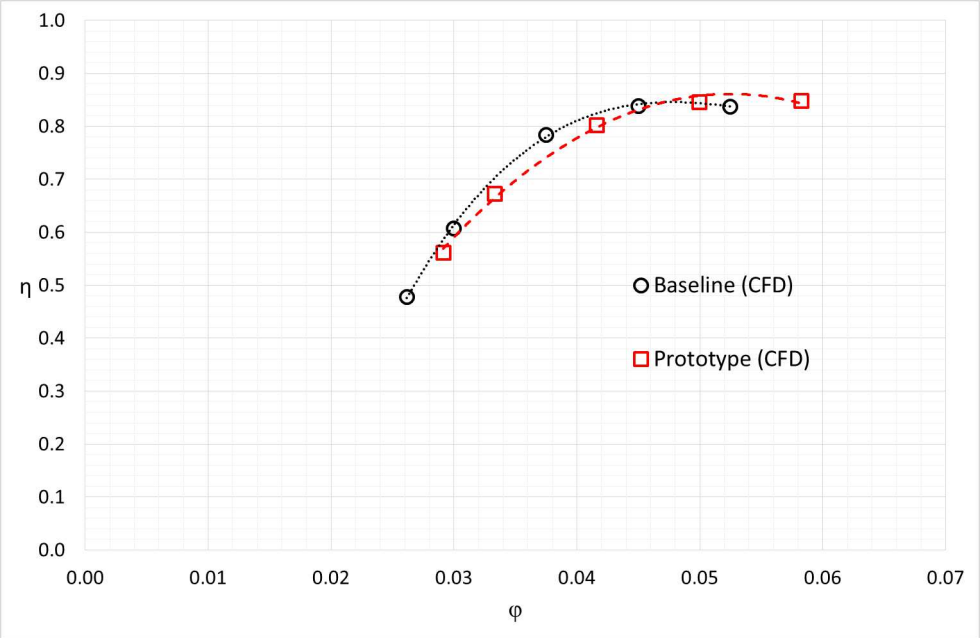

Figure 6.3: *Efficiency (η) vs flow coefficient (ϕ) curves of the two geometries.*

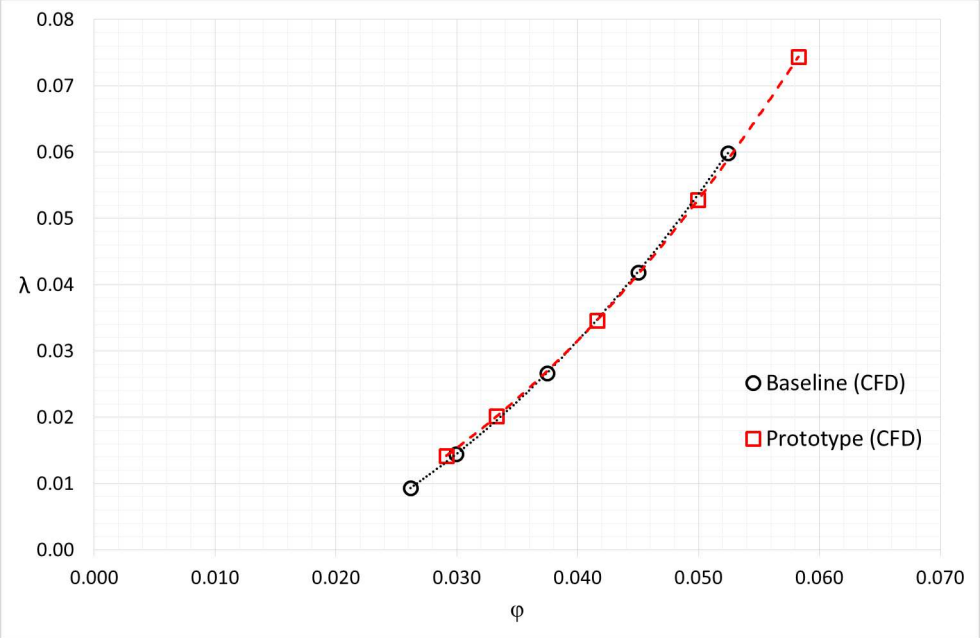

Figure 6.4: *Power coefficient (λ) vs flow coefficient (ϕ) curves of the two geometries.*

6.2.1 Scaled geometry

In order to overlap the novel impeller BEP with the one of the baseline, the former has been downscaled by -3.5%. After downscaling, the two machines have their $BEPs$ placed at $Q/Q_{BEP,conv}$ = 1, with the difference that the novel impeller provides higher head (Fig.6.5). This means that the runner is able to extract a larger amount of energy

from the fluid than the traditional one, ΔH = +4.70%. To overlap the two characteristic curves a further scaling is necessary. In addition to the size scaling a reduction of the rotational speed is needed (-4%). Thus, the new impeller allows to guarantee the same performance of the baseline with size saving and an efficiency improvement. Indeed, it is well known that the power losses due to friction losses is proportional to the angular velocity and the diameter of the machine in the way described by the eq.6.3:

$$P_{RR} \propto \omega^5 r^5 \tag{6.3}$$

Thus, both scaling diameter and angular velocity we obtain a machine, which provides the same performance of the baseline with a remarkable improvement of the efficiency, in particular a disk friction losses reduction equal to -25.96%.

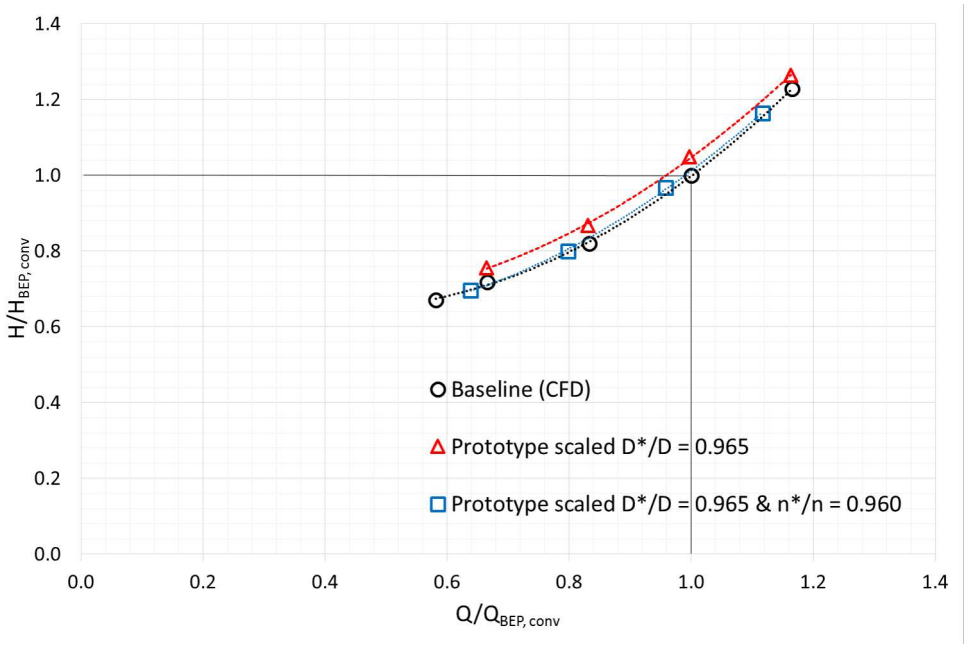

Figure 6.5: *$H/H_{BEP,conv}$ vs $Q/Q_{BEP,conv}$ curves of the baseline, the novel impeller scaled by D and the novel impeller scaled by both D and n.*

Moreover, looking at the efficiency curve (Fig.6.6) the novel geometry is more prone to convert hydraulic energy in mechanical energy than the baseline. This occurs at BEP (+0.83%), at overload but especially at part loads (+14.9%). The novel shape of the channel and their width can reduce instabilities at the inlet of the runner at part loads [117], that are responsible of static pressure reduction. Thus, the novel impeller not only reduces the losses when it works at the BEP, but also when the fluid at the outlet of the volute is not perfectly guided (part-load). Indeed, the novel vanes work better at off-design. Eventually, the evaluation of the power coefficient (λ) shows another important advantage. The novel geometry presents a higher curve over the entire range of flow rate; in particular an increase of 5.53% at the BEP, see Fig.6.6.

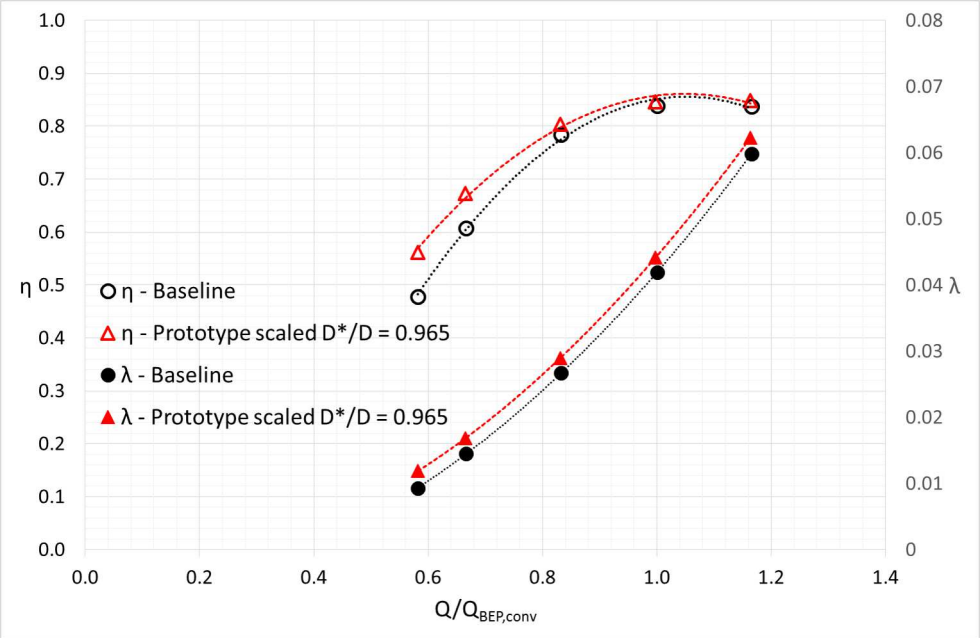

Figure 6.6: *Efficiency (η) and Power coefficient (λ) vs $Q/Q_{BEP,conv}$ curves of the baseline and the novel impeller scaled by D.*

6.2.2 Comparison of the performance

To further investigate the performance improvement, the rotary stagnation pressure shown in the previous chapter (eq.4.28) has been calculated inside the channels of the baseline and the novel geometry at their best efficiency points ($BEPs$). The rotary stagnation pressure has been calculated along the channels as area-weighted integral on iso-surfaces with constant meridional coordinates. Looking at Fig.6.7, when the fluid flows through the novel impeller, it is subjected to a smooth reduction of the rotary stagnation pressure, $\Delta p^*/\rho$. This means that the hydraulic efficiency of the new channels is higher than the baseline one. This result has also a positive impact on the global efficiency of the PaT, see Fig.6.6.

6.3 Conclusions

In this work a comparison of the performance of a baseline and a novel impeller, proposed by the authors to retrofit conventional impellers for double suction centrifugal pump, is presented. The novel geometry has been designed with a new arrangement of the channels with the aim to improve the efficiency and the slip factor in pump operating mode. Firstly, 3D U-RANS simulations have been run with the open source CFD code OpenFOAM. The characteristic curves of the two machines have been calculated and their specific speeds compared. From the results analysis a size scaling (-3.5%) is proposed in order to reach the same performance of the baseline geometry. Once done, this size reduction moves the BEP of the novel geometry at the same value of $Q/Q_{BEP,conv} = 1$, pointing out that the novel geometry is able to extract excess energy from the fluid ΔH = +4.33%. Thus, to reach the same performance of the baseline an

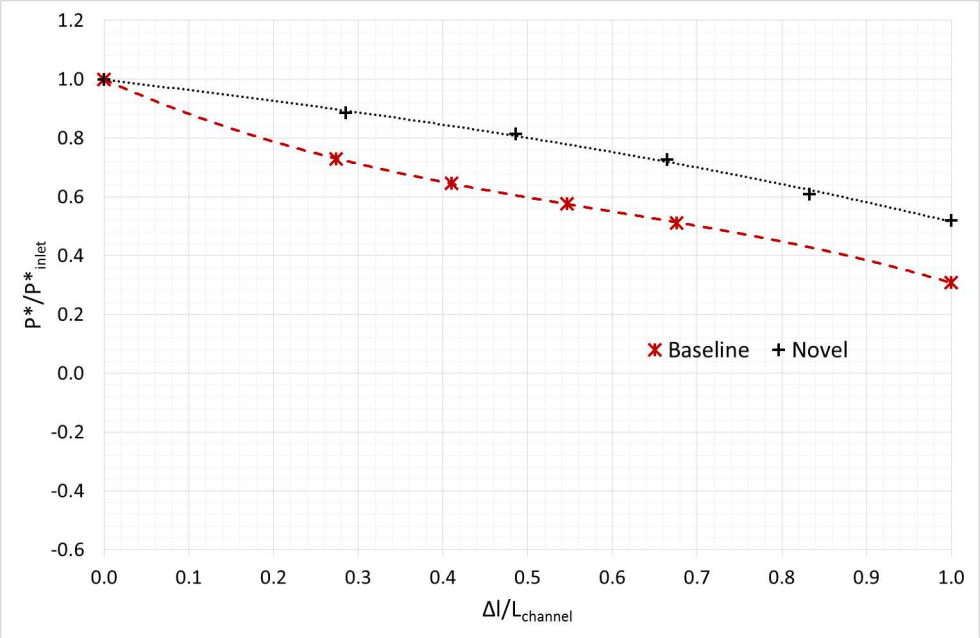

Figure 6.7: *Rotary stagnation pressure inside the channel of the two geometries.*

additional scaling is required. By reducing both the size (D) and the rotational speed (n) an overlapping of the curves of the two machines is possible. This leads to a remarkable reduction of the disk friction losses and an improvement of the global efficiency. The novel geometry seems to be more prone to extract hydraulic energy over the entire range of flow rate.
Moreover, the rotary stagnation pressure has been studied inside the two impeller vanes working at their $BEPs$ showing a reduced level of losses from the inlet to the outlet of the runner. In the future, further analyses of the rotary stagnation pressure will be carried out at part loads in order to investigate the benefits from using the novel geometry in reverse mode. Moreover, velocity profiles at the inlet and at the outlet of the runners will be compared to analyze the behavior of the novel vanes in guiding the fluid exiting from the volute and to quantify slip phenomena at the outlet of the novel runner.

CHAPTER 7

Slip phenomenon at the outlet of hydraulic centripetal turbomachines

7.1 Introduction

As discussed in the previous chapter, the oscillations of the power produced by renewable sources is going to promote the need for energy storage such as micro hydro where the same machine needs to be operated both in pump mode and in turbine mode. Nowadays, the prediction of the performance of a PaT is crucial in order to select the suited machine starting from its geometric information and its specific speed. Several models have been proposed for the prediction of the characteristic curve of a PaT; those based on statistic and normalization approaches are adopted when the geometric properties of the runner are unknown [118, 119] and that are useful to evaluate the flow rate and the head exploited by the PaTs running at their BEP, whereas, the models based on the evaluation of the flow characteristics through the machine are used by constructors [120, 121]. The latter models currently show a lack of accuracy in the prediction of the head vs flow rate curve especially at part-loads and over-loads.

The following chapter deals with the prediction of the performance of a centrifugal pump, property of Nuovo Pignone, tested in both direct and inverse mode, by means of numerical simulations with emphasis on the flow field through the impeller. The computational domain reproduces the baseline geometry of a commercial pump, presented in the previous chapters. As shown by Ventrone [60] the relative velocity vector at the outlet of a centripetal turbine, e.g., Francis turbine and PaT, is subject to a deflection with respect to the blade congruent angle (slip). Ventrone [60] and then Shi et al. [61] justify the slip phenomenon by demonstrating the presence of fluid flow vorticity between the blades in planes orthogonal to the rotational axis. Thus, counter rotating vortices appear inside the impeller channels. The proposed numerical investigation aim

to inspect and quantify the slip phenomenon at the outlet of runners with low number of blades.

The introduction of a slip factor, $\sigma_{turbine}$, whose definition is equivalent to the one used for centrifugal pumps [14], accounts for the difference between the real work and the theoretical one, due to the reduced number of the blades in PaTs compared to conventional turbines (e.g., Francis turbines) [60]. This analysis is based on the evaluation of the axial and tangential velocities at the c_{line} radius of the trailing edge of the blades at the outlet of the centripetal impeller. Moreover, this analysis shows the presence of different phenomena, e.g., pressure gradient and secondary flows, which can occur at the outlet of a centripetal turbine and affect the performance of the machine.

The introduction of $\sigma_{turbine}$ provides a great support in developing and tuning 1D models for the prediction of the turbine performance. Moreover, this analysis could provide the guidelines to successfully improve PaT geometries. A relationship between the new parameter ($\sigma_{turbine}$) and the mass flow rate for the baseline geometry is presented and discussed. Eventually, 1D models with and without the new corrections are applied and the deviations discussed [14, 118, 122, 123].

7.2 Characteristic curves

Firstly a campaign of simulations of the "baseline" geometry, (see Chapter 4) has been carried out with the machine operating in reverse mode by applying the same set up, previously described for the pump mode. In Fig.7.1 and 7.2 the characteristic curves of the impeller working either in pump or in turbine mode are represented on a H/H_{BEP} vs Q/Q_{BEP} plane, where H_{BEP} and Q_{BEP} are the head and the flow rate at the BEP of the pump. $H_{BEP,P}/H_{BEP,T}$ and $Q_{BEP,P}/Q_{BEP,T}$ are equal to 0.958 and 0.832, respectively. PaTs work with higher mass flow rate than the same machine operating in pump mode. Therefore, numerical simulations have been performed starting from $Q/Q_{BEP,P}$ equal to 70%, which is a value close to the runaway curve calculated according to the empirical model proposed by Gülich [14] (Fig.7.1), to $Q/Q_{BEP,P}$ equal to 140%. The maximum flow rate allows us to identify the BEP of the turbine (Fig.7.2). Just as in chapter 6, the mass flow leakages have been calculated by means of the equations provided by Gülich [14] for centrifugal pumps. Applying this model the volumetric efficiency (η_v) for a PaT results constant at various flow rate.

7.3 Evaluation of the slip factor for conventional impeller

With the aim to quantify this phenomenon, at the end of the numerical simulations, absolute tangential and axial velocity components have been evaluated at section 1, see Fig.7.3, by means of area-weighted averages on surfaces downstream the impeller exit. These values have been averaged over the last 3 rotations of the machine. The mean value of the absolute tangential velocity is 4.40 m/s. This value has been compared with the theoretical value [121] computed at the same flow rate, congruently with the blade angle at the outlet of the impeller (β_{1B}). For the machine studied in this work, the theoretical tangential velocity, calculated by means of the blade congruent flow theory at the BEP of the turbine, is equal to 2.08 m/s. Furthermore, the presence of the blades induces a strong and localized deviation of the flow field, see Fig.7.4. It has been noted

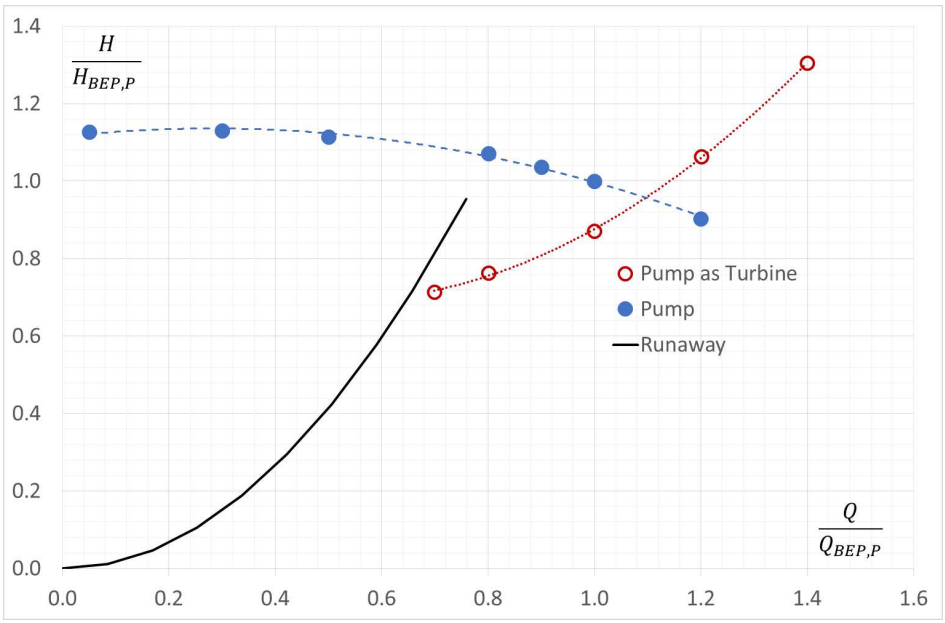

Figure 7.1: *Plot of the hydraulic turbomachine performance in both pump and turbine operating modes. Head curves with runaway curve with respect to the pump BEP.*

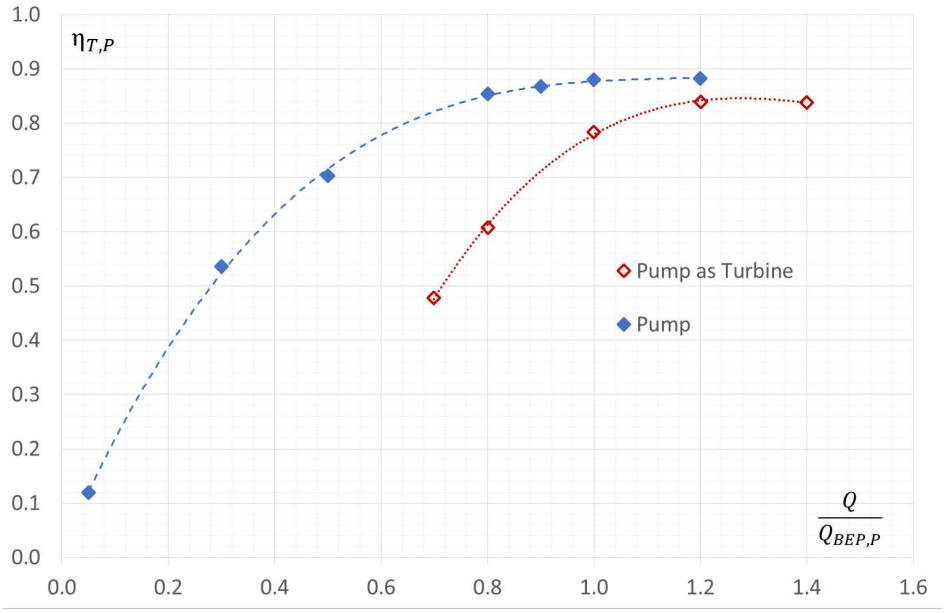

Figure 7.2: *Plot of the hydraulic turbomachine efficiency in both pump and turbine operating modes with respect to the pump BEP.*

that this might be justified by the pressure gradient that occurs between pressure and suction side of the blades (Fig.7.5).

To point out this contribution, axial and tangential velocity components have been evaluated along the c_{line} radius of the blades close to their trailing edge. The curves show a periodicity due to the presence of the blades (see Figs.7.6 and 7.7). This means that the main flow at the outlet of the turbine is subject to a deviation not only due to

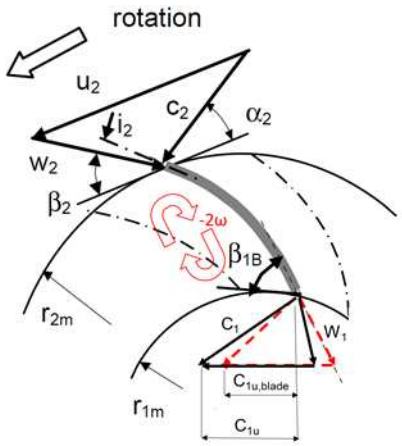

Figure 7.3: *Velocity triangles at the inlet (2) and at the outlet of the runner (1). At the outlet both actual (solid line) and blade congruent (dashed line) velocity triangles are represented.*

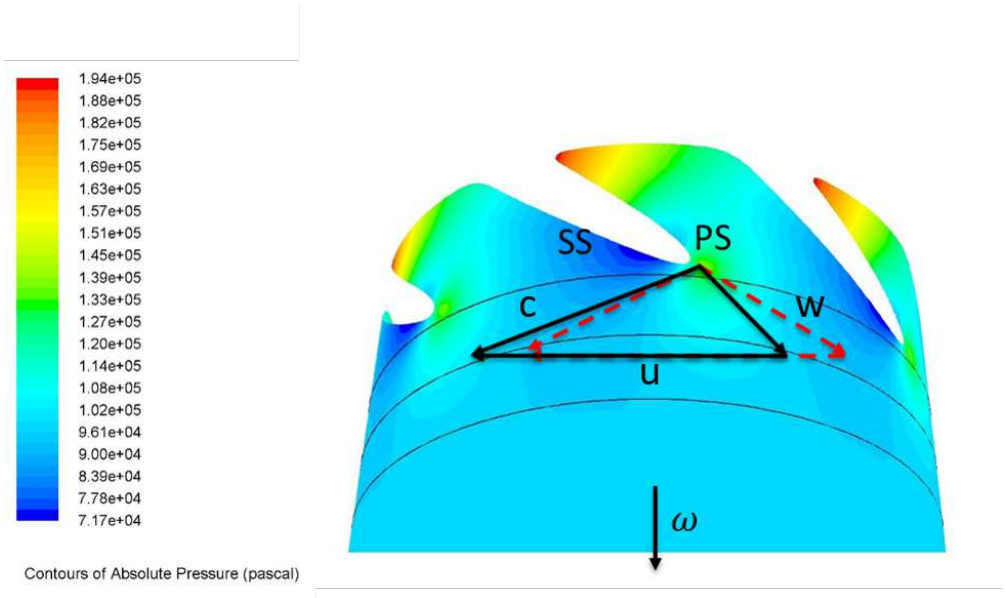

Figure 7.4: *Velocity triangles at the outlet of the runner. At the outlet both actual (solid line) and blade congruent (dashed line) velocity triangles are represented*

the vortex inside the channel, as described by Ventrone [60] and Shi et al. [61], but also to the pressure gradient acting in the same direction of the peripheral velocity. The velocity profiles highlight that the velocity triangles close to the trailing edge of the blade undergo a distortion in both axial and peripheral direction.

In order to quantify the flow deflection at the outlet of a centripetal hydraulic turbo machine, the turbine slip factor, $\sigma_{turbine}$, has been introduced:

$$\sigma_{turbine} = \frac{Y_{real}}{Y_{th}} \tag{7.1}$$

Moreover, a velocity analysis close to the trailing edge of a blade has been performed. The absolute tangential velocity has been plot on an arc with length $2\pi r/N_b$

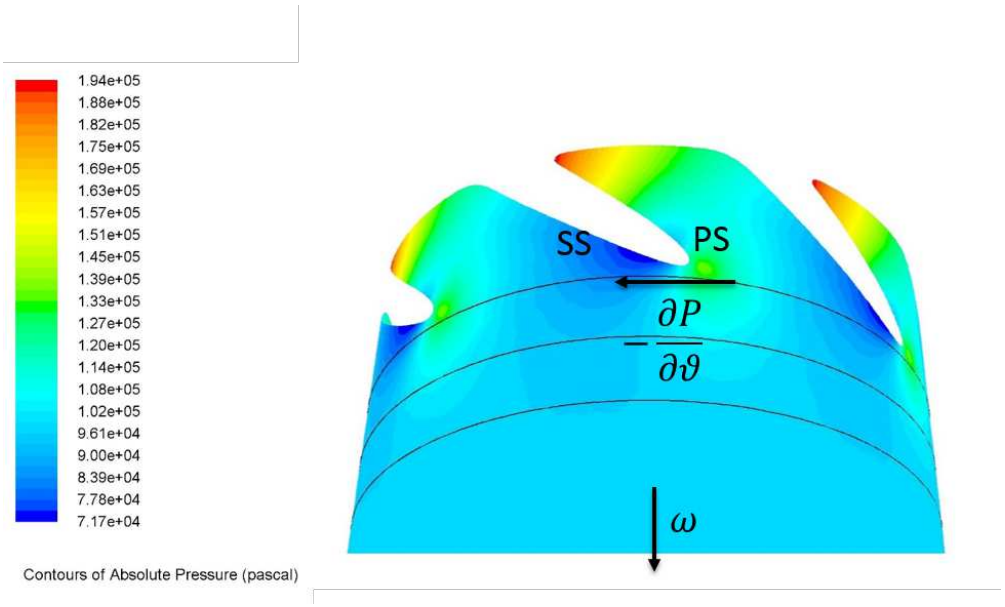

Figure 7.5: *Contours of the absolute pressure at the outlet of the runner with pressure gradient.*

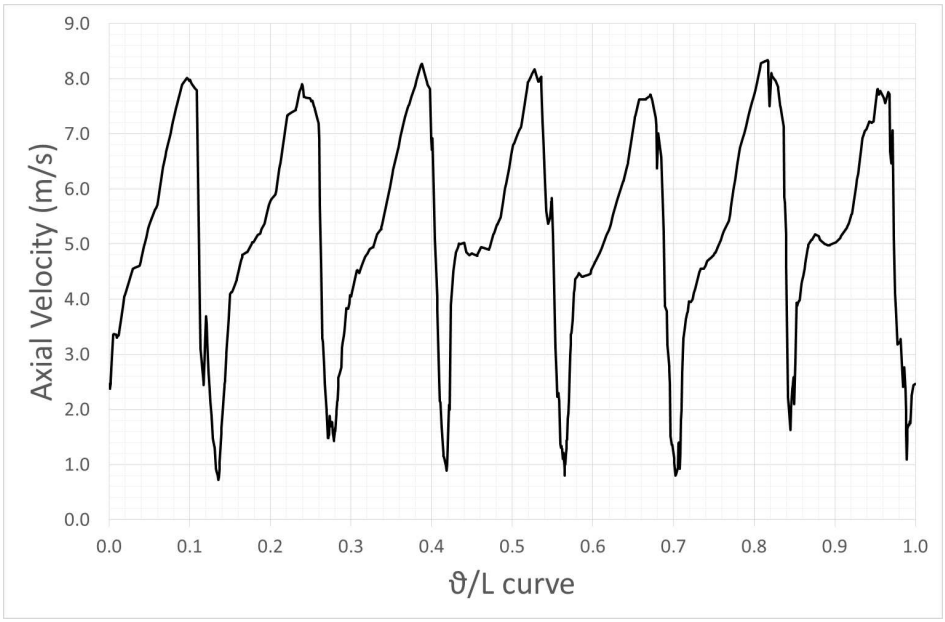

Figure 7.6: *Velocity profiles of the axial velocity component at the outlet of the runner.*

and radius (r) equal to the c_{line} radius at different axial distance downstream of the blade leading edge ($a, 2a$), see Fig.7.8. Looking at the graphs, closer the arc, higher the velocity deflection, as expected. Flowing trough the discharge pipe, the velocity peaks become smoother. This is confirmed by the standard deviation of the velocity along the three arcs, its value is equal to 2.23, 0.31 and 0.16 m/s, respectively moving from the vane outlet towards the discharge pipe.

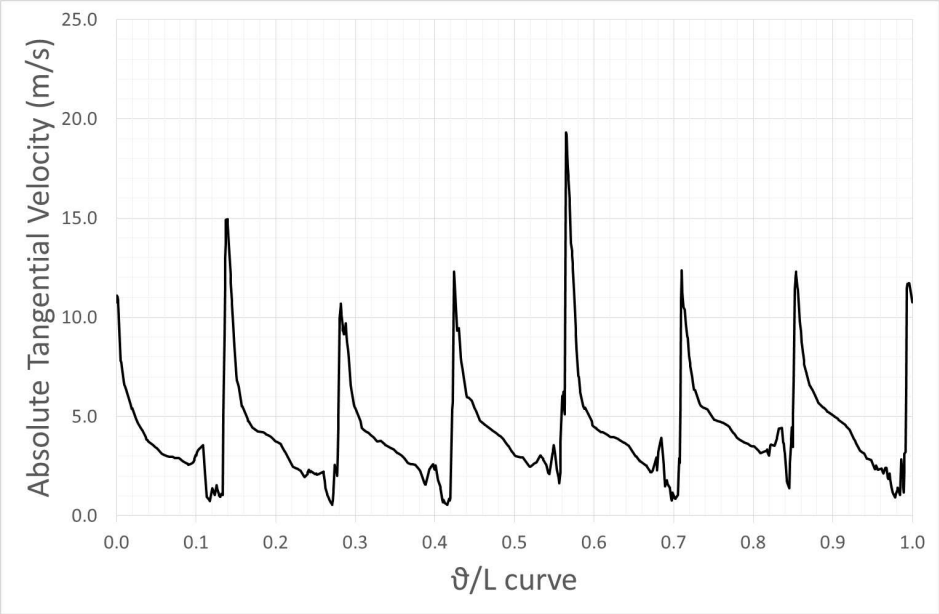

Figure 7.7: *Velocity profiles of the tangential velocity component at the outlet of the runner.*

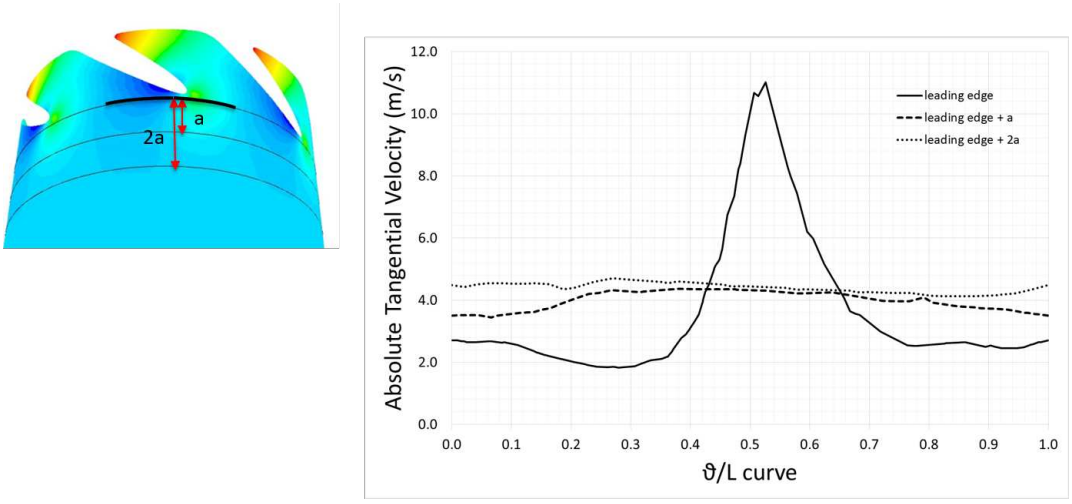

Figure 7.8: *Tangential velocity calculated at different distance from the trailing edge of the blade.*

7.3.1 Application to 1D model

As previously described, the slip factor gathers different sources of deflection, e.g. counter rotating vortex, pressure gradient at the trailing edge of the blade and 3D flow phenomena. Applying the Euler's equation in order to compute the specific work both via 1D theoretical model, Y_{1D}, and CFD calculi, Y_{CFD}, at the BEP_T, the $\sigma_{turbine}$, in which the real work in absence of experiments is substituted by CFD calculi, is equal to 0.967. Similarly to the theory of pumps where the slip factor corrects the ideal work transferred by the machine to the flow, the turbine slip factor here introduced might be applied under turbine operating mode in order to correct the ideal work extracted from the fluid by the PaT. After that, the slip factor has been computed at different operating points, i.e., different mass flow rates, and the results are shown in Fig.7.9. Then, a

model of the slip factor has been obtain by means of least-squares fitting. Numerical simulations at different flow rates are suggested for the purpose of further exploring the slip factor behavior and improving the least-square fitting.

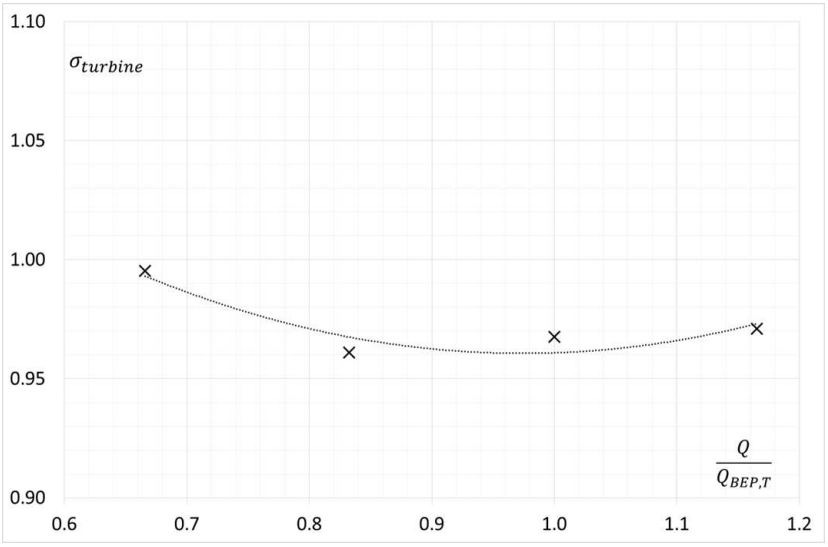

Figure 7.9: *Evolution of the slip factor at various flow rate for a blade with low-medium specific speed and 7 blades.*

Eventually, three different slip factor models have been applied to the 1D model proposed by Stefanizzi et al. [124] to predict the PaT performance from their geometric data, see Fig.7.10. The results show that by neglecting the slip factor ($\sigma_{turbine}$ = 1) [112, 118] the turbine head at the BEP is overestimated with an error of +6.4%. On the other hand, by applying either the Busemann's [122] or the Stodola's [123] model, the results at the BEP are in good agreement but the turbine head at part-loads is underestimated, with an error of -8%. Instead, by applying the least-squares fitting of the CFD results, as described in Fig.7.10, errors are minimized over a wide range of flow rates.

7.4 Conclusions

This activity shows numerical investigations of a centrifugal pump operating in reverse mode, namely working as a turbine, with emphasis on the flow field at the runner outlet with the aim to improve the accuracy of prediction model of PaT characteristic curves. The numerical analyses have been run by solving 3D U-RANS equations by means of the open-source CFD code OpenFOAM. According to Ventrone and Shi et al., the relative velocity vector at the outlet of the impeller shows a deflection in the direction of the peripheral velocity. This is due to the counter rotating vortex that is generated inside the impeller channels by Coriolis effect. In addition, another source of localized deflection is due to the pressure gradient that occurs at the trailing edge of the blades. The presence of these phenomena is pointed out by the evaluation of the tangential and axial absolute vectors components via the numerical simulation. These results have been compared with the data resulting from the blade congruent flow theory. This analysis allowed the introduction of the slip factor, $\sigma turbine$, which has been helpful in order

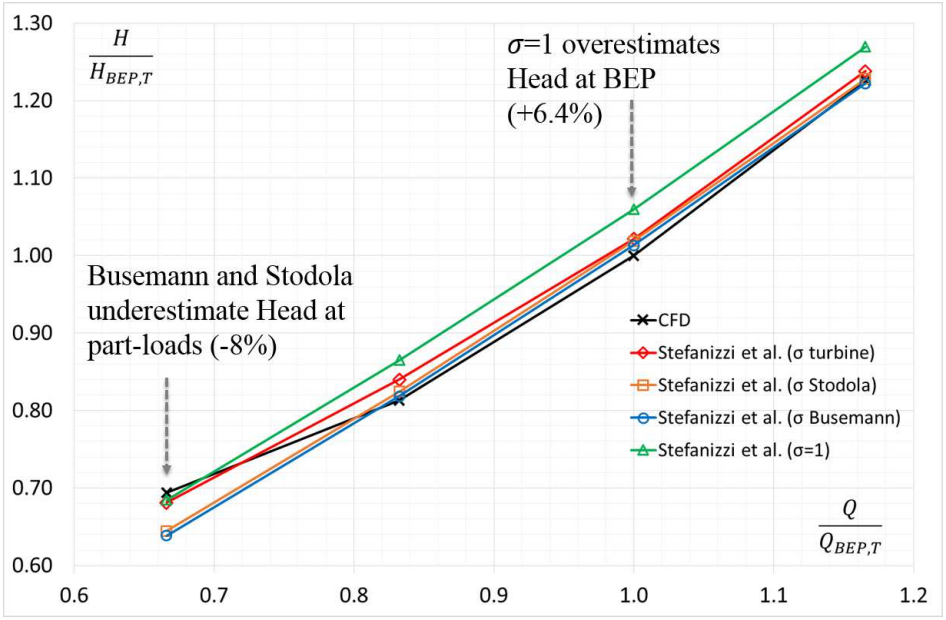

Figure 7.10: *Application of different definitions of the slip factor (σ =1, σ Busemann and σ Stodola) to a 1D model for predicting the PaT performance curve.*

to improve a 1D model developed by our research group to predict the characteristic curve of a PaT starting from the pump geometry and its characteristic curves. Indeed, the proposed 1D model shows good results in a wide range of mass flow rates.

It is recognized that in order to use this parameter for PaT performance prediction an estimation of the slip factor can not be done by means of CFD simulation. Thus, a campaign of simulations of single centrifugal pumps vanes with different number of blades working as turbines is highly recommended in order to provide a relation between the turbine slip factor (eq.7.1) and the number of blades.

CHAPTER 8

Passive control system for limiting cavitation around hydrofoils

8.1 Introduction

Cavitation is a phenomenon, which can occur in hydraulic turbomachineries, such as pumps, turbines and propellers, when the local static pressure falls below the vapour pressure. The phase change is characterized by pressure oscillations with specific amplitudes and frequencies. Cavitation also causes surface damages and induces noise and vibrations, which negatively affect the performance of the machines.

Thus, in this activity a new control system for limiting cavitation around hydrofoil has been proposed, since hydrofoils are representative of the fluid flow around the leading edge of hydraulic turbomachinery impellers. As explained in chapter 2, nowadays two kind of systems for limiting cavitation around hydrofoil are available in the literature, an active one and a passive one. Actually, the cavitation control system that will be shown in the following paragraphs belongs to this second class.

8.2 Case study

This work starts with the analysis of the cavitation developed on a two-dimensional hydrofoil since this case can be considered a simplified representation of cavitation at the leading edges of the impeller vanes. In particular, the flow past a NACA0009 hydrofoil at a fixed angle of attack equal to 2.5° has been investigated by means of OpenFOAM and the results compared against experimental data provided by P. Dupont [1]. Furthermore, a modified NACA0009 hydrofoil with slots, connecting the pressure side to the suction side of the foil, introduced as a passive cavitation control system, has been investigated in order to understand how they can affect the turbomachine performance

under fully wetted flow and when cavitation occurs.
The numerical investigation has been carried out for a cavitation number $\sigma = ((p_\infty - p_v))/((0.5\rho_\infty U_\infty^2)) = 0.81$ where p_v is the vapour pressure and ∞ indicated inlet boundary conditions. Simulations have been performed by means of the open source CFD code OpenFOAM by solving the 2D Unsteady Reynolds-Average Navier-Stokes (RANS) equations for incompressible flow with the mass transfer model proposed by Schnerr and Sauer [2] in combination with two different turbulence models, namely, k-ω SST [79] and k-kl-ω [93, 94].
Besides, different angles of attack have been simulated in order to reproduce the leading edge of a centrifugal pump impeller under off-design conditions. The selected angles of attack are $2.5°$ and $5°$. The former deals with attached cavities, thus it mainly concerns the resolution of the boundary layer phenomena. Whereas, the latter can involve vapour shedding cavity. Furthermore, in this type of applications, large variation of the Reynolds number occurs when the pressure falls below the vapour pressure, thus the k-kl-ω [93, 94] model has been used because of its capability to predict the pressure distribution over the suction side of the hydrofoil under laminar-to-turbulent boundary layer transition, as shown by Capurso [87]. Due to the operating flow conditions and for an angle of attack equal to 5°, the Reboud correction has been applied to the k-ω SST turbulence model to take into consideration the unsteadiness of the vapour pocket (see chapter 3). Eventually hydrofoils in cascade configuration have been simulated with the purpose to reproduce the influence of one blade on another one, what actually occurs in a real impeller. The performance of the hydrofoils has been evaluated in terms of force coefficients and contours of vapour volume fraction.

8.3 Numerical domain and boundary conditions

The 2D fluid domain is shown in Fig.8.1. It reproduces the height of the experimental test section of the Cavitation Research Facility at EPFL, Lausanne [1], whereas the computational domain extends $3.5c$ upstream and $5.5c$ downstream of the foil ($c = 100mm$) to reduce influence of boundary conditions at the inlet and outlet.

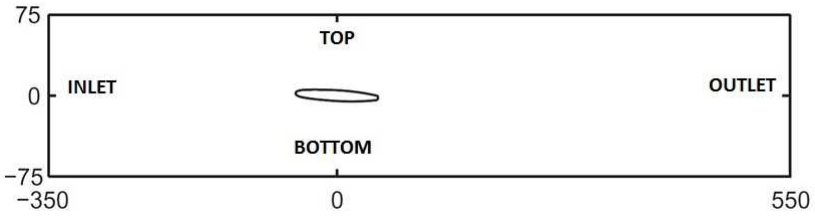

Figure 8.1: *Main dimensions of the numerical domain expressed in mm.*

The hydrofoil is a NACA0009 [1, 125] with a chord truncated at 90% of the initial chord value ($110\ mm$), maximum thickness at 50% of the initial chord and the trailing edge height equal to $3.22\ mm$ (Fig.8.3). A no-slip boundary condition is imposed along the hydrofoil surface and along the top and bottom tunnel boundaries. The pressure at the outlet is set in such a way to guarantee the desired cavitation number, $\sigma = (p_\infty - p_v)/(0.5\rho_\infty U_\infty^2)$, where p_∞ is the pressure measured at $250\ mm$ upstream

of the foil. This distance has been chosen being adequately far from the pressure disturbance due to the hydrofoil. The velocity at the inlet, U, is equal to 20.7 m/s and the properties of the fluid are assumed to be $\rho = 998.7\ kg/m^3$ and $\nu = 1.08 \cdot 10^{-6}\ m^2/s$, which corresponds to pure water at 17 °C. The vapour pressure of the water at 17 °C is $p_v = 1938.4\ Pa$ and the vapour density and kinematic viscosity are $\rho = 0.014493$ kg/m^3 and $\nu = 6.66 \cdot 10^{-4}\ m^2/s$, respectively [1]. Furthermore, for this test case a constant turbulent intensity has been assumed equal to 1% at the inlet of the domain. During calculation, the k-ω SST turbulence model was considered with k and ω equal to 0.06 and 60, respectively. The grid has been computed with the software Pointwise Gridgen®, exported in ".msh" format and then converted with the command fluentMeshToFoam in OpenFOAM. After that, the grid has been checked, to extract information about its extreme values of aspect ratio (< 1000), skewness (< 0.98) and non-orthogonal cells ($< 70°$), with the command checkMesh. About the grid sensitivity analysis, this has been carried out by considering the three grids having different prism layer initial height: a fine, a medium and a coarse mesh that are made up of 114 000, 48 000 and 31 000 cells, respectively. These grids have been tested under steady-state fully wetted (non-cavitating) condition. The grids details are shown in Fig.8.3. Each fluid mesh has been made with a different number of structured elements close to the foil surface to ensure a proper value of $y^+ = yU_\tau/\nu$, where y is the first cell height, and U_τ is the wall frictional velocity. The region outside these elements has been discretized with unstructured triangular elements. Mesh refinements are performed at both the foil leading and trailing edges (Fig.8.3). The lift and drag coefficients, have been compared with the experimental data provided by P. Dupont [1] in Table 8.1.

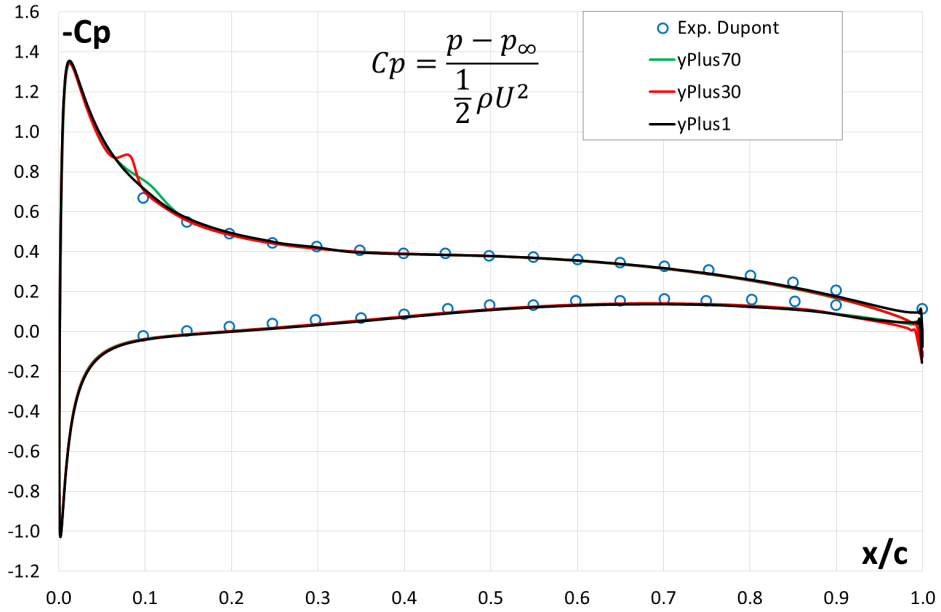

Figure 8.2: *Comparison of the pressure coefficient calculated with three different grids on the suction and pressure side of the NACA0009 hydrofoil with $\alpha = 2.5°$ in fully wetted flow condition with k-kl-ω turbulence model. The results are compared with experimental data.*

The mesh with about 114 000 cells has been selected to carry out the multi-phase

Table 8.1: *Comparison of the hydrofoil performance (lift and drag coefficient) in wetted simulation with $U = 20\ m/s$ compared with experimental data [10].*

	$n.cells$	$C_D = \frac{D}{1/2\rho U^2 c}$	$C_L = \frac{L}{1/2\rho U^2 c}$	$err.C_D$	$err.C_L$
Dupont P. (experimental)		0.0214	0.315		
Coarse mesh (y^+=70)	31000	0.0221	0.355	-3.3%	-12.7%
Medium mesh (y^+=30)	48000	0.0237	0.355	-10.7%	-12.7%
Fine mesh (y^+=1)	114000	0.0208	0.362	2.8%	-14.9%

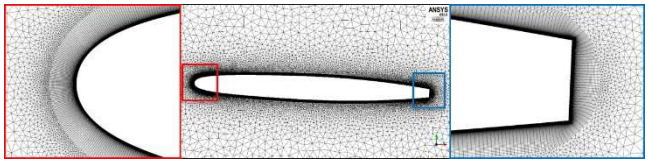

Figure 8.3: *Mesh details.*

analyses considering that only marginal deviations are observed in the results (Fig.8.2) among the three grids (see Tab.8.1). The grid with 114 000 cells presents a better resolution near the walls and the leading edge (with y^+ value approximately equal to 1) than the mesh with 48 000 cells.

The effect of turbulence models, mesh types, and mesh density on the cavitating flow dynamics have been studied in detail for the case of the NACA0009 hydrofoil at a fixed angle of attack, $\alpha = 2.5°$, under steady flow conditions for the quasi-steady sheet cavitating case ($\sigma = 0.81$ and $Re = 2 \cdot 10^6$).

8.4 Passive control system

Herein, a new passive control system for limiting cavitation has been applied to a NACA0009 hydrofoil. The basic idea is to introduce slots nearby its leading edge connecting pressure and suction sides of the hydrofoil, in order to increase locally the pressure on the suction side. The original geometry has been modified by the introduction of three slots close to the leading edge of the foil (see Fig.8.4). Both the location of the first slot with respect to the leading edge and the distance between the slots are equal to 5% of the chord. The slots have variable cross section areas and their axes are inclined $30°$ with respect to the chord. Due to the slots, a small amount of flow rate flows through the slots due to the pressure gradient. The slots angle is designed in order to avoid flow separation at the slots outlet. In addition, the main flow pushes down the flow rate coming from the slots. The slots can be realized by means of a broaching machine with specific tools and their cross section areas have been chosen not constant (they increase from pressure to suction side) in order to reduce the velocity of the flow toward the outlet of the slots. This slot configuration is applied to NACA0009 hydrofoil with angle of attack equal to $2.5°$ starting from the experimental set up proposed by Dupont. This configuration can be used to reduce cavitation phenomenon at different angle of attack trying to reproduce the operating condition of a centrifugal pump at part-load. Since there is no symmetry with respect to the chord of the foil this modification can work only either at part or at over loads.
On the other hand a symmetric configuration is preferred when the machine works

both at part and over loads. This conditions will be discussed in another work. The NACA0009, modified with the introduction of the slots from pressure to suction side, has been discretized by using the same technique previously described. Moreover, the regions inside the slots have been discretized with structured elements close to the walls in order to guarantee the same first cell height as the one applied on the adjacent walls of the foil, see Fig.8.4.

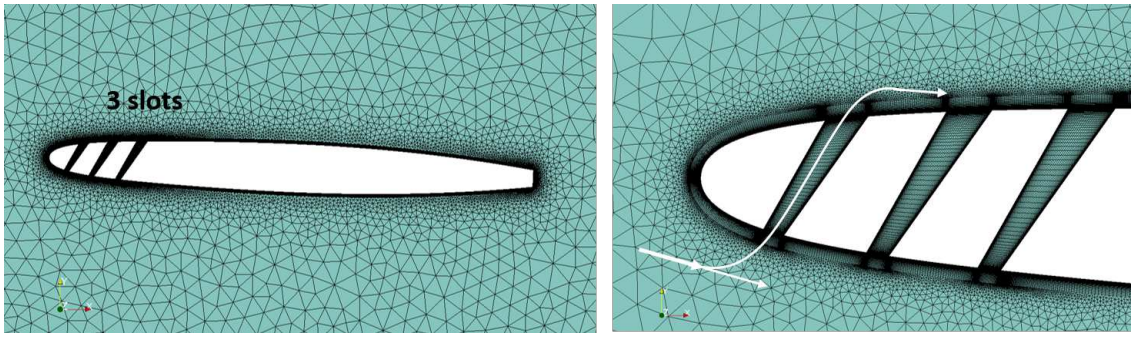

Figure 8.4: *NACA0009 hydrofoil modified with the introduction of the slots and representation of the fluid flowing through the slots from the pressure to the suction side.*

8.5 Results and Discussion - Flow analysis with AoA = 2.5 deg

The unsteady simulations in both wetted and cavitating flow conditions have been run with a $\Delta t = 5.0 \cdot 10^{-6} s = t_\infty/1000 = (c/U_\infty)/1000$ for a total time equal to 0.3 s, which corresponds to sixty passages of the flow over the hydrofoil. The results have been averaged over the time interval corresponding to twenty times the reference time ($20t_\infty$).

8.5.1 Single-phase flow

After the numerical method assessment, the regular foil and the modified geometry have been investigated. A comparison of the pressure coefficient obtained via numerical simulations for the regular geometry and the modified one is shown in Fig.8.5. They are compared with the experimental data provided by P. Dupont. The curves depicted in Fig.8.5 point out that the passive cavitation control system, acting on the forward part of the hydrofoil, increases the pressure located at the leading edge ($-C_p$ decreases) and modifies the pressure distribution up to the 30% of the chord. Furthermore, the geometry modifications and the new pressure field lead to a reduction of the lift coefficient and an increase of the drag coefficient (Table 8.2).

Table 8.2: *Comparison of the hydrofoil performance (lift and drag coefficient) under fully wetted condition with and without the passive control system.*

	C_D	C_L
Regular foil	0.0253	0.364
Passive control	0.0355	0.272
Difference %	+42%	-25%

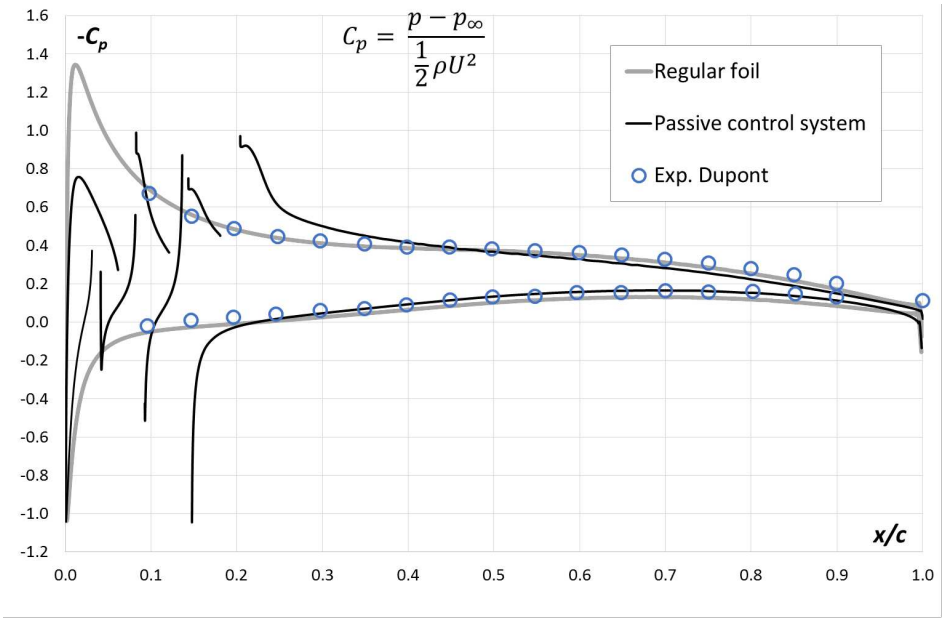

Figure 8.5: *Pressure coefficient on the suction and pressure side of the NACA0009 hydrofoil with $\alpha = 2.5°$ in fully wetted flow condition with k-ω SST turbulence model. The results of the regular and modified geometry are compared with experimental data [1].*

The introduction of the slots modifies the velocity field downstream their exit on the suction side, see Fig.8.6. Noticeable results are a higher boundary layer close to the suction side of the foil and a reduction of the viscous stress on the suction side of the foil. Looking inside the slots, flow unsteadiness and recirculation zones develop inside of them; due to their specific geometry they are able to develop a recirculation zone which decelerates the velocity flow at the exit of the slots transmitting simultaneously pressure information from the pressure to the suction side (Fig.8.7).Furthermore, the flow coming from the slots is pushed towards the trailing edge and it overlays the suction side;

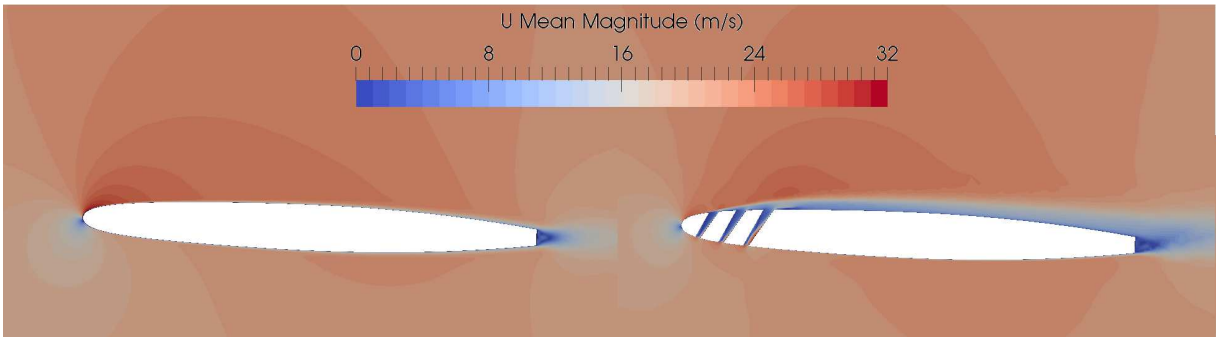

Figure 8.6: *Contours of the mean velocity around the regular and the modified foil.*

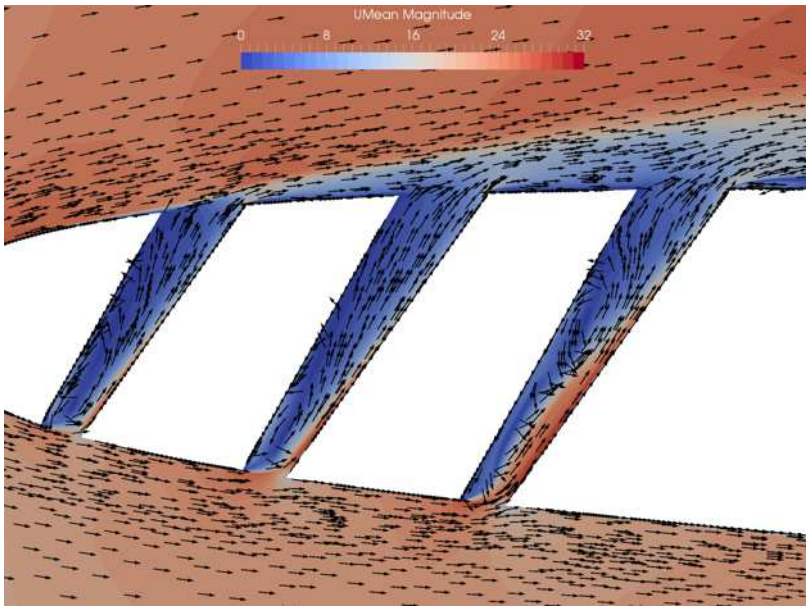

Figure 8.7: *Velocity vectors colored by mean pressure on the contours of the mean velocity inside the slots.*

8.5.2 Multi-phase flow k-kl-ω

All the multi-phase flow simulations have been run using the mass transfer model provided by Schnerr and Sauer [2] and the k-kl-ω turbulence model. The results are depicted in Figs8.9,8.10 and 8.11. The results show a good agreement between the pressure coefficient of the regular foil under cavitating flow conditions and the experimental results. Moreover, the curves of the modified geometry highlights that there are no large variation in either fully wetted and cavitating flow conditions (Figs.8.5 and 8.8).

A study of the velocity around the leading edge of the foil has been carried out in order to study the presence of flow separation. The regular foil shows a recirculation inside the cavity, whereas the flow that passes through the ducts in the modified geometry does not induce any separation of the flow downstream the exit of the channels, except around the corners, see Fig.8.9.

The comparison of the water volume fraction α_w of the regular foil against the modified geometry draw attention to the strong reduction of the cavitation phenomenon (Fig.8.10, Tab.8.3). This confirms the ability of the passive control system proposed in this work to suppress the cavitation inception at the leading edge of the hydrofoil. Indeed the channels are able to increase the pressure locally at the leading edge of the foil. Their effect is shown in Fig.8.11.

Table 8.3: *Comparison of the cavitation number (σ) and alpha water volume fraction (α_{vapour}) in cavitating flow condition with and without the passive control system.*

	σ	α_v
Regular foil	0.810	2.65E-08
Passive control	0.815	1.85E-09
Difference %	+0.6%	-93%

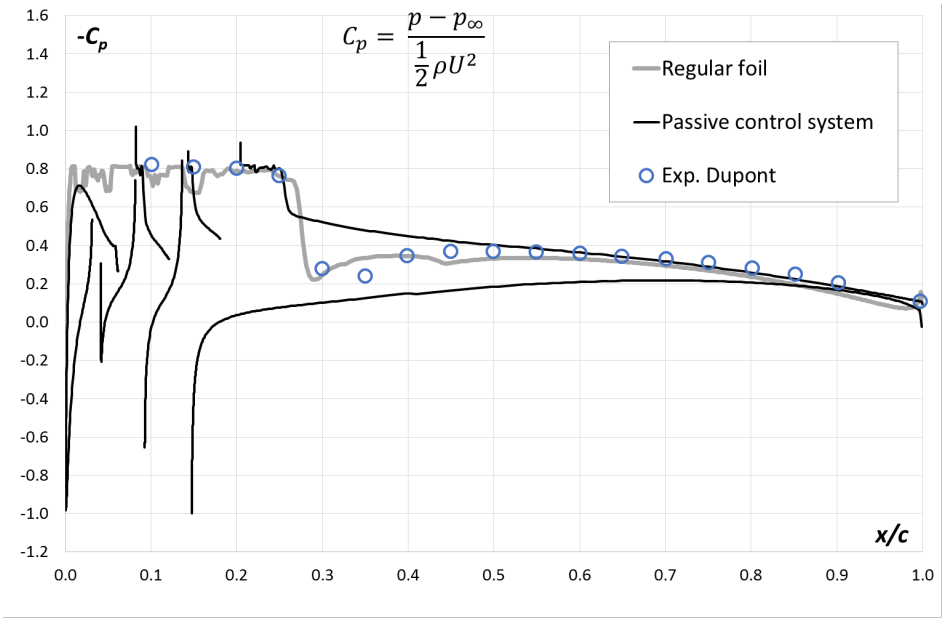

Figure 8.8: *Pressure coefficient on the suction side of the NACA0009 hydrofoil with $\alpha = 2.5°$ and $\sigma = 0.81$ with the mass transfer model proposed by Schnerr and Sauer [2] and k-kl-ω turbulence model. The results are compared with experimental data [1].*

8.5.3 Results and discussion at different AoA from 0 to 5 deg

Given the good results, the passive cavitation control system has been applied at the hydrofoil with different angles of attack in order to reproduce the flow condition that occurs at the leading edge of a centrifugal pump blades when they operate under off-design conditions. Both at 2.5 and 5 deg the regular hydrofoil is subjected to attached cavity with partial cavitation pattern. But with the introduction of the slots we have a great reduction of the vapour cavity. The alpha water contours highlight that at 2.5 deg the volume of vapour is almost totally suppressed, whereas at 5 deg the pure vapour cavity becomes a two-phase cavity.

To compare the performance of the original foil with and without the slots, at different angles of attack, the values of the C_L, C_D and C_L/C_D have been calculated. Moreover, the volumes occupied by the cavities have been calculated. The variations are resumed in Tab.8.4 and displayed in Figs.8.12, fig:Cl/Cd and fig:volume vapour.

Table 8.4: *Comparison of the hydrofoil performance at different angles of attack with and without passive cavitaion system control under multi-phase flow conditions.*

Cases	Passive control system	σ	C_D	C_L	C_L/C_D	var. C_D [%]	var. C_L [%]	var. C_L/C_D [%]	var. V_{cavity} [%]
0°	no	0.81	0.0204	0					
0°	yes	0.81	0.0570	0.0642		179			
2.5°	no	0.81	0.0248	0.3730	15.00				
2.5°	yes	0.81	0.0284	0.2404	9.15	12	-35	-39	-93
5°	no	0.81	0.0496	0.6360	12.80				
5°	yes	0.81	0.0622	0.4390	7.06	25	-31	-45	-54

The comparison of the mean liquid volume fraction, α_l, of the regular foil against the modified geometry draw attention to the strong reduction of the cavitation phenomenon

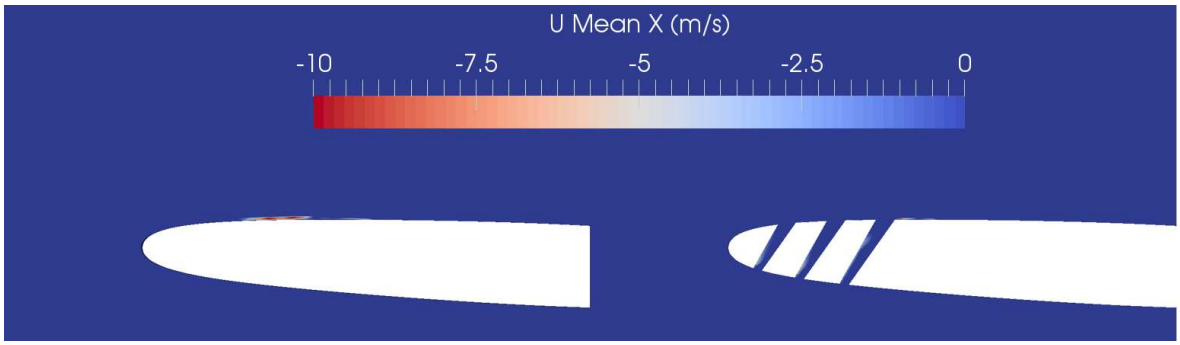

Figure 8.9: *Contours of the velocity x component mean ($UMean\ X$) in order to highlight regions affected by flow separation.*

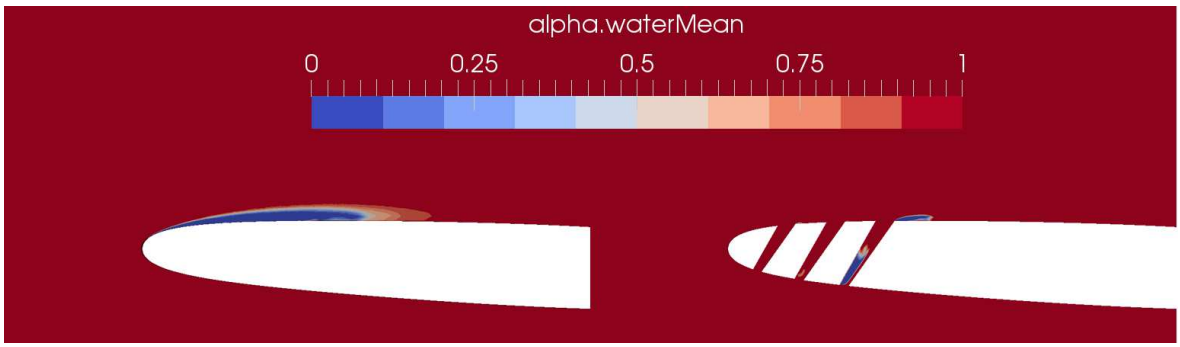

Figure 8.10: *Contours of the mean alpha water fraction, with and without the introduction of the passive cavitation control.*

(Fig.8.15). This confirms the ability of the passive control system proposed in this work to suppress the cavitation inception at the leading edge of the hydrofoil, but also when cavitation largely affects the hydrofoil, like in the case of $5°$, the system proposed is able to reduce the cavity to a significant extent. Indeed the slots are able to increase the pressure locally at the leading edge of the foil without promoting flow separation, indeed the main idea is to transfer pressure information and not to transfer flow rate from the pressure to the suction side. Their effect is shown in Fig.8.15. On the contrary these positive effects are accompanied by a loss of performance, C_L reduction (-31%) and C_D increase (+25%), respectively. This level of losses is acceptable considering that the current case aims to reproduce the forward part of impeller vanes. Actually, the impeller vanes are longer than hydrofoils therefore the losses will be localized to the leading edge whereas the benefits from suppressing cavitation would improve the entire functionality of the pump channels.

8.5.4 Multi-phase flow with k-ω, Reboud correction and hydrofoil cascade

To further investigate the regular and the modified geometries other numerical simulations have been carried out by considering modified turbulence model and different boundary conditions as proposed in the literature. As described in chapter 3 the Reboud eddy-viscosity limiter is used to take into account the dynamic of the re-entrant

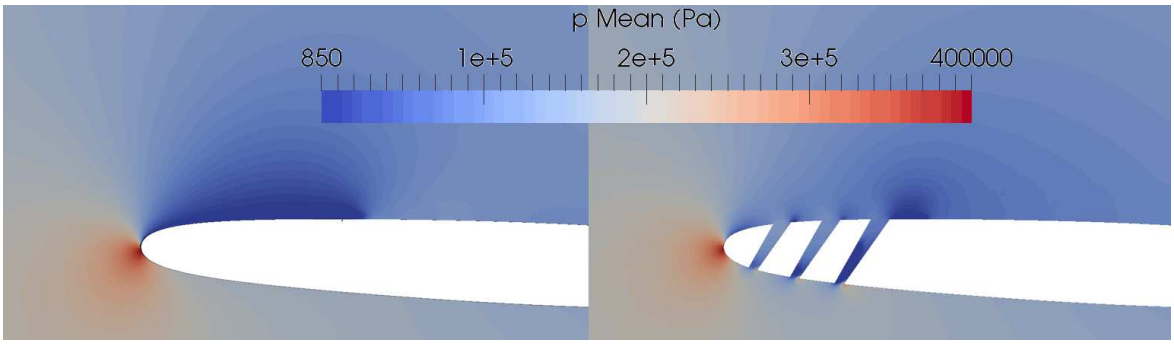

Figure 8.11: *Contours of the mean static pressure, with and without the introduction of the passive cavitation control.*

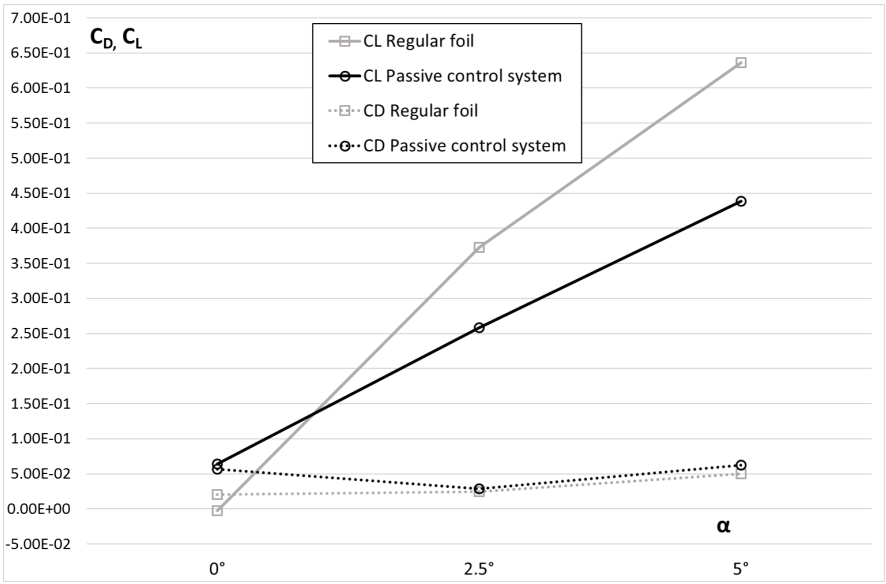

Figure 8.12: *Trend of the C_L and C_D coefficients at various angles of attack of the regular and modified geometry.*

jet. Thus, the same modified geometry previously studied with the k-kl-ω turbulence model have been simulated with k-ω SST and k-ω SST with Reboud correction. Moreover the same case has been analyzed by applying periodic boundary conditions on the top and bottom surfaces (Fig.8.1) of the domain in order to simulate the flow around a hydrofoil cascade configuration trying to reproduce the interaction between different hydrofoils.

The Reboud correction is thought to be useful for angle of attack equal to 5° where shedding vapour cavity can occur. Therefore, this case has been investigated. On the contrary, the Reboud correction applied to the regular hydrofoil with AoA = $2.5°$ overestimates the dimension of the cavity, resulting in a pressure coefficient on the suction side of the hydrofoil which does not follow the experimental results.

In Tab.8.5 the results in terms of force coefficients and vapour volume fraction are summarized.

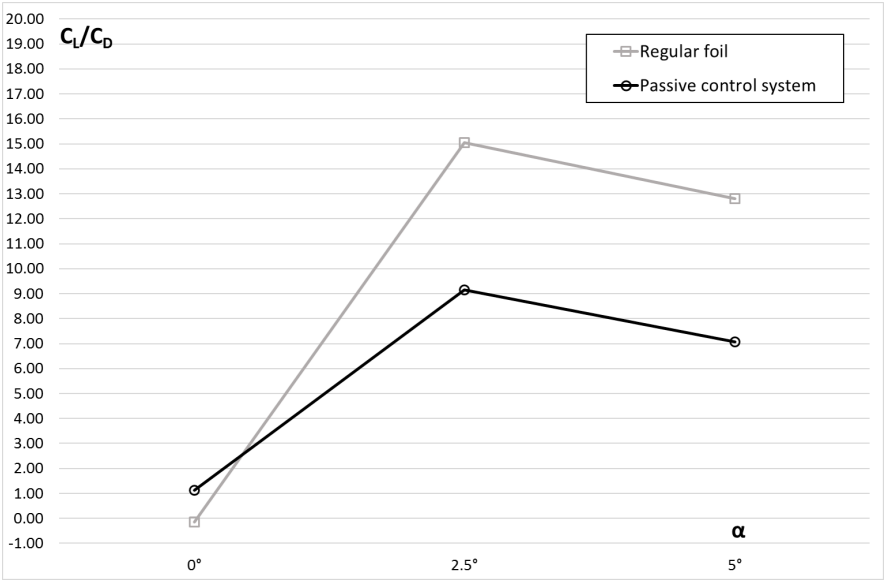

Figure 8.13: *Trend of the C_L/C_D coefficients at various angles of attack of the regular and modified geometry.*

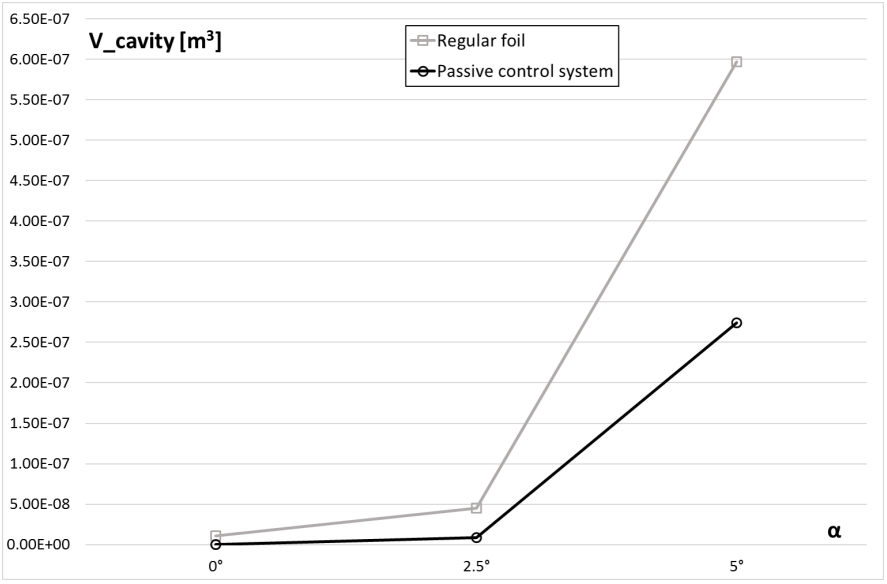

Figure 8.14: *Trend of the volume of the cavity pocket at various angles of attack of the regular and modified geometry.*

Looking at the contours of the mean velocities and vapour fraction, the two models with the standard and the modified k-ω SST models seems to provide almost the same results. The case with the introduction of the periodic boundary shows a velocity field slightly different from the confined tunnel case, however completely different values of the lift and drag coefficient have been calculated (Tab.8.5). Moreover, in the periodic case the cavitation is absent. Compared to the case with the k-kl-ω, Fig.8.15, all these case display a strong reduction of the vapour volume. The case with the period

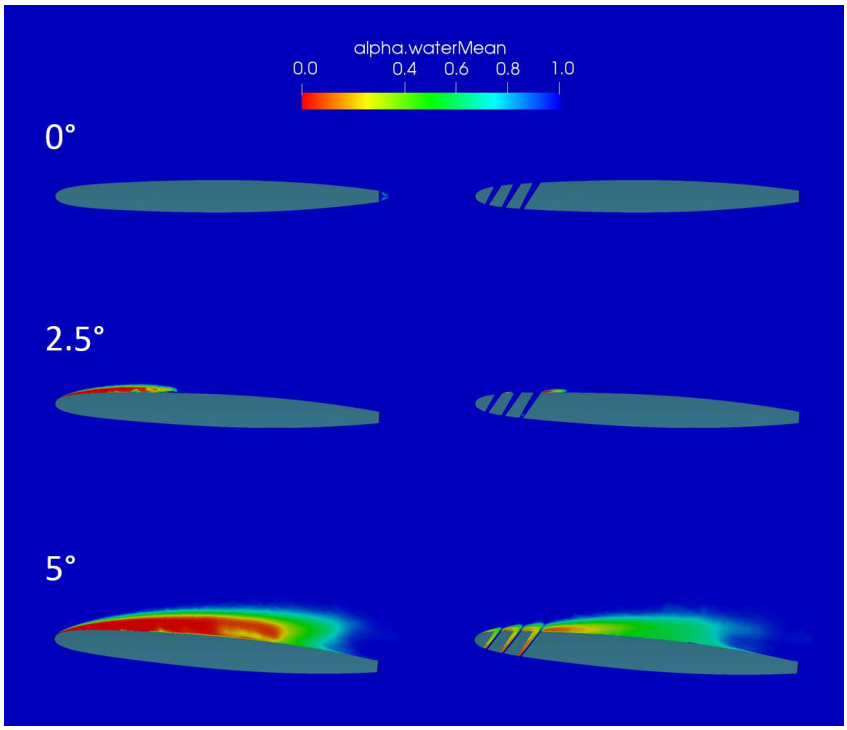

Figure 8.15: *Contours of the mean liquid volume fraction, α_l, with and without the introduction of the passive cavitation control at different angles of attack.*

Table 8.5: *Comparison of the hydrofoil performance (lift and drag coefficient) under two-phase condition with the passive control system for three different cases (k-ω SST, k-ω SST + Reboud correction and k-ω SST with periodic conditions).*

	C_D	C_L	α_v
k-ω SST	0.0690	0.3290	9.71E-09
k-ω SST + Reboud	0.0725	0.3367	1.77E-08
k-ω SST + cascade	0.0450	0.1738	2.84E-14

boundaries reproduces a cascade hydrofoil which is representative of the flow field at the impeller eye. The velocity contours show low velocities on the suction side of the foil therefore the pressure maximum shall be lower. This is also confirmed by a lower value of the lift coefficient. Thus, a comparison of the regular foil under cascade configuration is commended to evaluate the reduction of the performance. In the future numerical simulations and comparison of the regular geometry with the different turbulence models and boundary conditions are suggested. After that the slots could be applied to a real impeller and the head and the $NPSH_3\%$ compared with the original geometry.

8.6 Conclusions

In this work, the performance of the NACA0009 hydrofoil with the introduction of geometry modifications working as a passive cavitation control system has been investigated. The study focuses on understanding how these modifications affect the regular

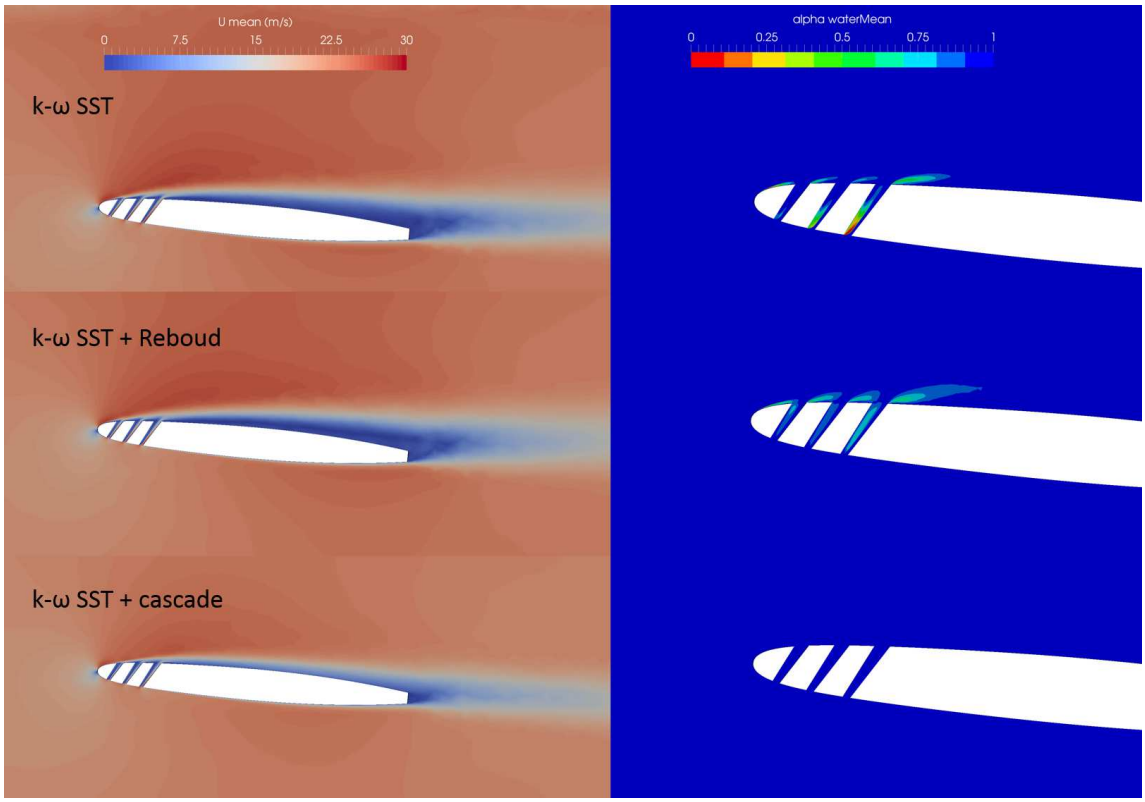

Figure 8.16: *Contours of the mean liquid volume fraction, α_l, with and without the introduction of the passive cavitation control at different angles of attack.*

performance of the system and conversely improve the performance when cavitation occurs. The passive cavitation control considers ducts passing through the body of the foil that allow the pressure transmission from the pressure side to the suction side of the foil. The numerical analyses have been performed by solving 2D U-RANS equations with the k-ω SST under wetted condition and the k-kl-ω model for multiphase flows for turbulence closure. The hydrofoils have been tested in single-phase and multi-phase flow conditions and the results compared against the experimental data [1]. The performance of the hydrofoil has been evaluated in terms of C_L, C_D and vapour volume fraction (α_v). They show remarkable advantages, i.e., strong reduction of the vapour volume fraction (up to -93%) even if accompanied by a loss of performance, C_L reduction (-31%) and C_D increase (+25%), respectively. This level of loss can be acceptable considering that the current case aims to reproduce the forward part of impeller vanes. Actually the impeller vane is longer than the foil analyzed here, therefore the losses will be localized at the leading edge whereas the benefit from suppressing the cavitation can improve the entire functionality of the pump channels. In the future work an optimization tool will be studied with the aim to design a symmetric configuration, which can be used when the hydraulic turbomachine works either at part or over loads. Moreover, a comparison of the different cases at different angles of attack with turbulence model modification and different boundary conditions is suggested.

CHAPTER 9

Conclusions

World's energy consumption is increasing year by year driven by the industrial and the tertiary sector, where most of the electrical energy is consumed by electrical motors (65%). The latter drive pumps (22%), most of which are centrifugal pumps (73% - world market = 20 billion euro per year). Due to their wide use, a great effort has been spent in the last decades in trying to improve the selection and the efficiency of pump systems with the aim to reduce their energy consumption. Besides, it has been found out that among all the rotating devices in a process plant, centrifugal pumps typically have the best overall potential for energy savings.

In this scenario the design of an innovative impeller for double suction centrifugal pumps (named BTC impeller) has been proposed since this kind of centrifugal pumps is widely used (30%) in many industrial sectors, such as: oil&water pipeline, refinery&petrol-chemical, power generation, onshore and offshore oil&gas production and fire fighting. Moreover, double suction centrifugal pumps are employed in water distribution networks, pulp&paper industry, agriculture and domestic. About energy production systems they are used in nuclear and steam power plants as main component of feed-water system (feed-water and primary pumps) and they are responsible for a significant energy absorption (e.g., up to 2% in Hualong One) affecting the balance of both the gross and net electrical energy production. In all these applications the obtained efficiency increase, even if of only a few percentage points, is a relevant result in their economy.

In this thesis, the main objective has been to introduce a completely new approach for designing novel impellers for low-medium specific speed double suction centrifugal pumps. The basic idea has been to design a novel impeller, that can easily retrofit a conventional one, embedding an innovative vane arrangement with the aim to reduce the slip phenomena at their outlet.

This new geometry has been designed respecting the following geometric (due to stator parts) and fluid dynamic constrains: to have the same specific speed number (n_q) of the baseline geometry; to guarantee a kinematic flow angle at the inlet of the volute (α_3) in accordance with the optimum α_3 of the volute (there is no bladed diffurer) and to satisfy the matching with the absolute inlet flow angle at the outlet of the inlet duct. Firstly, a 1D code has been written to design the novel impeller. To do this a completely new approach has been adopted and new methodologies have been developed to model the novel vanes. The new approach is based on the kinematic of a particle inside the impeller. Herein the trend of the velocity and the shape of the channel have been imposed in a way that the channels coming up from the two sides of the impeller intersect each other having their blades arranged circumferentially avoiding interpenetration. At the beginning different parameters have been assumed and numerical simulations of a single impeller vane have been run by means of the commercial code ANSYS Fluent® and by solving 3D steady-state RANS equations in order to evaluate the hydraulic losses and the slip factor. These values have been then passed back to the 1D code until convergence is reached. A geometrical element (chamfer) has been added to avoid channels interpenetration; indeed the section of the vane starts being four-sided polygonal and becomes five-sided at certain distance where interpenetration is highly probable. In order to detect interpenetration, before geometry generation, a specific tool has been developed on purpose. Once the final geometry has been generated, the entire geometry of the centrifugal pump has been studied via numerical simulations to take into account the interaction of the novel impeller and the stator parts. The computational fluid dynamics analysis has been performed with an open-source code named OpenFOAM by solving 3D U-RANS with the k-ω SST model for turbulence closure. The methods and the models adopted in the OpenFOAM environment have been validated against a commercial one (CFX).

Once the geometry has been manufactured experimental tests have been carried out at the hydraulic test rig of Nuovo Pignone, Bari. The numerical simulations and the experimental tests displays an impeller which is able to transfer more efficiently energy to the fluid compared to the baseline having higher value of the slip factor (+8.5%). Moreover, the novel design of the channel provides a higher efficiency (+1.2%, the new vane has lower length and higher hydraulic diameter) over the full range and a slight reduction of the fluid flow rotary stagnation pressure inside of it. This means that a more efficient machine (higher pressure rise) can be installed preserving the same dimensions of the baseline or alternatively the adoption of the new geometry can lead to a size (volume, weight and cost) reduction, -5.5%, when the same head of the baseline is required and it allows to assemble a more compact system than the ones currently used.

Velocity and vorticity fields have been numerically investigated at the outlet of the novel impeller in order to evaluate the benefits from using the novel configuration. Velocity and pressure profiles have been calculated along the axial and the circumferential direction. Furthermore, wake structures at the outlet of the impellers have been displayed by means of the "Q-criterion vortex". These analyses figures out a more homogeneous flow at the inlet of the volute, that means a reduction of the secondary flow inside of it due to non-uniform flow. The experimental data of the torque and vibrations measured on the testing cell, have confirmed a low level of stresses and vibrations

induced by the novel configurations.

According to the results shown in this thesis, it can be stated that the introduction of this technology, instead of the conventional one, can allow a reduction of the total electric motor energy consumption in industry due to centrifugal pumps, which nowadays in UE corresponds to 120 $TWh/year$. Under the hypothesis that the novel geometry provides an efficiency improvement in the order of $1 - 2\%$ and the number of double suction pumps were 10% of the total number of centrifugal pumps used in industry, then the amount of energy saved would be equal to $0.18\ TWh/year$. This amount of energy is equivalent to 600 units of 300 MW gas turbine power plants for electricity generation. The carbon footprint data related to gas-fired electricity generation is equal to 500 gCO_2eq/kWh, thus the novel geometry could allow a reduction of the CO_2 emission up to $90 \cdot 10^3\ t_{CO_2}/year$. This would give a cumulative saving of $3.96\ TWh$ and $1980 \cdot 10^3\ t_{CO_2}$ by 2040. A further analysis has been done by norrowing it down to a energy power plant, for instance the China's nuclear power plant Hualong One. This plant has three primary coolant loops with pump each driven by 6.6 MW electric motors (110 t each). Its gross energy production is 1170 MWe and the energy consumed by the pumps is equal to 19.8 MW. Under the hypotesis that the conventional and the novel geometry have the same weight, considering a 5.5% size reduction to provide the same pressure rise and the price of stainless steel = 1200 €$/t$ a money saving of the 28000 € (-15.6%) concerning the cost of the pumps can be reached by substituting the three conventional geometry with novel ones. In terms of efficiency the retrofit of the conventional geometries could lead to 0.198 MW of energy saving in the global energy consumption.

After that a second prototype has been designed with the aim to rotate at a lower rotational speed with a higher blade loading (with a reduced number of blades) than the first prototype. As in the first case, the second prototype should have the same specific speed of the first geometry at its BEP, keeping the same absolute angle at the outlet of the impeller (α_2) and at the inlet of the volute (α_3). To do this a Matlab tool based on a Harmony Search Algorithm has been written and used to select the operating point of the second impeller. Furthermore, design tools have been studied on purpose (C_L and C_p analytical calculation) to predict, during the geometry generation the blade loading and the presence of flow separation caused by the reduced number of blades. Also in this case both numerical simulations and experimental tests have highlighted a reduction of the slip phenomenon and an increase of the global efficiency. It can be observed that the second prototype has higher value of the head coefficient compared to the baseline and a stable curve towards zero flow rates. Moreover, experimental results do not show dangerous values of pressure and torque oscillations even if the number of the blades is increased and with this the pressure and the lift coefficient of the blade.

Given these results, in the future works, the design of a third impeller with a different number of blades is suggested in order to extrapolate a relation between the slip factor and the number of blades for the novel geometry proposed. Moreover, experimental tests of the baseline geometry are highly recommended to compare the experimental results of the various impellers in terms of torque, vibrations and $NPSH_{3\%}$.

Besides, the novel vane arrangement has been thought to be adequate to better guide the flow at the inlet of the runner under reverse operating conditions. Thus, the baseline and the first prototype have been simulated working as turbines by means of the 3D

U-RANS simulations with the open source CFD code OpenFOAM. The characteristic curves of the two machines have been calculated and their specific speeds compared. From the results analysis a size scaling (-3.5%) is proposed in order to reach the same performance of the baseline geometry. Once done, this size reduction moves the BEP of the novel geometry at the same value of $Q/Q_{BEP,conv} = 1$, pointing out that the novel geometry is able to extract additional energy from the fluid ΔH = +4.7%. Thus, to reach the same performance of the baseline a further scaling is required. By reducing both the size (D) and the rotational speed (n) by -4% an overlapping of the curves of the two machines is possible. This leads to a remarkable reduction of the disk friction losses (-25.96%) and an improvement of the global efficiency from +0.83% at the BEP to +14.9% at part-loads. The novel geometry seems to be more prone to extract hydraulic energy over the entire range of flow rate. Moreover, the rotary stagnation pressure has been studied inside the two impeller vanes working at their $BEPs$ showing a reduced level of losses from the inlet to the outlet of the runner.

In the future, further analyses of the rotary stagnation pressure will be carried out at part loads in order to investigate the benefits from using the novel geometry in reverse mode. Moreover, velocity profiles at the inlet and at the outlet of the runners will be compared to analyze the behavior of the novel vanes in guiding the fluid exiting from the volute and to quantify slip phenomena at the outlet of the novel runner.

The numerical analysis of the conventional pumps working as turbines, has allowed to investigate the fluid flow losses inside the stator and the rotor parts of a PaT. In order to improve the accuracy of 1D model for the prediction of PaT characteristic curves, numerical investigations of a conventional centrifugal pump operating in reverse mode, namely working as a turbine, with emphasis on the flow field at the runner outlet have been carried out. According to Ventrone and Shi, the relative velocity vector at the outlet of the impeller shows a deflection in the direction of the peripheral velocity. This is due to the counter rotating vortex that is generated inside the impeller channels by Coriolis effect. In addition, another source of localized deflection is due to the pressure gradient that occurs at the trailing edge of the blades. The presence of these phenomena has been pointed out by the evaluation of the tangential and axial absolute vectors components via numerical simulations. These results have been compared with the data resulting from the blade congruent flow theory.

This study allowed the introduction of the slip factor for centrifugal turbines with reduced number of blades compared to conventional ones (e.g., Francis turbine). This parameter, $\sigma_{turbine}$, has been helpful in order to improve a 1D model developed by our research group to predict the characteristic curve of a PaT starting from the pump geometry and its characteristic curves. Indeed, the proposed 1D model shows better results in a wide range of mass flow rates compared to models which neglects this phenomenon or models which apply correlations commonly used for centrifugal pumps. In the future works a parametric study with the purpose to correlate the slip factor at the outlet of centripetal runners with the number of blades is proposed.

Finally, with the purpose to reduce the cavity pocket that develops on the suction side of centrifugal pump impellers and consequently to enlarge their operating range, the performance of the NACA0009 hydrofoil with the introduction of geometry modifications working as a passive cavitation control system has been evaluated. The basic idea is to introduce slots nearby its leading edge connecting pressure and suction sides

of the hydrofoil, in order to increase locally the pressure on the suction side. The study focuses on understanding how these modifications affect the regular performance of the system and conversely improve the performance when cavitation occurs. Numerical analyses of the NACA0009 hydrofoil under the following operating conditions: AoA = 2.5° and σ = 0.81 have been performed by solving 2D U-RANS equations with the k-ω SST and k-kl-ω models for turbulence closure. The hydrofoils have been tested in single-phase and multi-phase flow conditions and the results compared against the experimental data provided by the researcher P. Dupont. After that, the NACA hydrofoils have been simulate with AoA equal to 5° in order to verify that the passive control system proposed is able to control and reduce the cavitation inception at different angle of attack by covering different pump operating conditions. The performance of the hydrofoil has been evaluated in terms of C_L, C_D and vapour volume fraction (α_v). They show remarkable advantages, i.e., strong reduction of the vapour volume fraction (up to -93%) even if accompanied by a loss of performance, C_L reduction (-31%) and C_D increase (+25%), respectively. This level of loss can be acceptable considering that the current case aims to reproduce the forward part of impeller vanes. Actually the impeller vane is longer than the foil analyzed here, therefore the losses will be localized at the leading edge whereas the benefit from suppressing the cavitation can improve the entire functionality of the pump channels. In the future work an optimization tool will be studied with the aim to design a symmetric configuration, which can be used when the hydraulic turbomachine works both at part and over loads.

Bibliography

[1] P. Dupont, "cavitation turbomachines hydrauliques NACA009," 1993.

[2] J. Sauer and G. H. Schnerr, *Unsteady cavitating flow - a new cavitation model based on a modified front capturing method and bubble dynamics*. 2000.

[3] E. Abdelaziz, R. Saidur, and S. Mekhilef, "A review on energy saving strategies in industrial sector," *Renewable and Sustainable Energy Reviews*, vol. 15, no. 1, pp. 150 – 168, 2011.

[4] "World energy outlook," 2009.

[5] "Policies for promoting industrial energy efficiency in developing countries and transition economies," 2008.

[6] H. Vogelesang, "An introduction to energy consumption in pumps," *World Pumps*, 2008.

[7] *Study on improving the energy efficiency of pumps*. European Commission, 2001.

[8] "A comprehensive review on energy efficiency enhancement initiatives in centrifugal pumping system," *Applied Energy*, vol. 181, pp. 495–513, 2016.

[9] T. Sahoo and A. Guharoy, "Energy cost savings with centrifugal pumps," *World Pumps*, vol. 2009, no. 510, pp. 35 – 37, 2009.

[10] "Nuclear power reactors," 2018.

[11] Z. Zou, F. Wang, Z. Yao, R. Tao, R. Xiao, and H. Li, "Impeller radial force evolution in a large double-suction centrifugal pump during startup at the shut-off condition," *Nuclear Engineering and Design*, vol. 310, pp. 410 – 417, 2016.

[12] I. Annus, D. Uibo, and T. Koppel, "Pumps Energy Consumption Based on New EU Legislation," *Procedia Engineering*, vol. 89, pp. 517–524, jan 2014.

[13] U. D. of Energy, "Improving motor and drive system performance," 2008.

[14] J. F. Gulich, *Centrifugal pumps, 2nd Edition*. 2006.

[15] C. B. Earls, "HYDRODYNAMICS OF PUMPS," tech. rep., 1994.

[16] J. P. F. Michel and J. M. Michel, *Fundamentals of Cavitation*, vol. 76. 2005.

[17] J. H. Horlock and B. Lakshminarayana, "Secondary flows: Theory, experiment, and application in turbomachinery aerodynamics," *Annual Review of Fluid Mechanics*, vol. 5, no. 1, pp. 247–280, 1973.

[18] L. BB, "Visualization Study of Flow in Axial Flow Inducer," *ASME. J. Basic Eng. 1972;94(4):777-787*, 1972.

[19] L. BB, "Analytical and experimental study of flow phenomena in noncavitating rocket pump inducers," *NASA Contractor Rep. 3471*, 1981.

[20] A. Bhattacharyya, A. Acosta, C. Brennen, and T. Caughey, "Observations on off-design flows in noncavitating inducers," *Proc. ASME Symp. on Pumping Machinery*, vol. FED-154, pp. 135–141, 1993.

[21] M. E, "Centrifugal pump hydraulic instability," *Electric Power Res. Inst. Rep. EPRI CS-1445*, 1980.

[22] R. Binder and R. Knapp, "Experimental determinations of the flow characteristics in the volutes of centrifugal pumps," *Trans. ASME, 58*, pp. 649–s661, 1936.

[23] R. Worster, "The flow in volutes and its effect on centrifugal pump performance," *Proc. Inst. of Mech. Eng., 177, No. 31*, pp. 843–875, 1963.

[24] S. Lazarkiewicz and A. Troskolanski, "Pompy wirowe. (Impeller pumps.) Translated from Polish by D.K.Rutter.," *Publ. by Pergamon Press*, 1965.

[25] J. Johnston and R. Dean, "Losses in vaneless diffusers of centrifugal compressors and pumps," *ASME J. Eng. for Power*, vol. 88, pp. 49–62, 1966.

[26] S. Chu, R. Dong, and J. Katz, "The noise characteristics within the volute of a centrifugal pump for different tongue geometries," *Proc. ASME Symp. on Flow Noise,Modelling, Measurement and Control*, 1993.

[27] K. Kaupert, "Unsteady flow fields in a high specific speed centrifugal impeller," 1997. PhD thesis.

[28] D. S. Miller, *Internal flow systems : design and performance prediction*. Houston, Tex. : Gulf Publishing Company, 2nd ed ed., 1990. First published: Cranfield, Bedfordshire : BHRA (Information Services), 1990.

[29] L. Wen-Guang, "Experiments on impeller trimming of a commercial centrifugal oil pump," *International Conference on Hydraulic Machinery and Hydrodynamics*, 2004.

[30] W. guang Li, "Impeller trimming of an industrial centrifugal viscous oil pump," 2012.

[31] M. Šavar, H. Kozmar, and I. Sutlović, "Improving centrifugal pump efficiency by impeller trimming.," *Desalination*, vol. 249, no. 2, pp. 654–659, 2009.

[32] G. Kergourlay, M. Younsi, F. Bakir, and R. Rey, "Influence of splitter blades on the flow field of a centrifugal pump: Test-analysis comparison," *International Journal of Rotating Machinery*, vol. 2007, 2007.

[33] B.-l. Cui, Y.-g. Lin, and Y.-z. Jin, "Numerical simulation of flow in centrifugal pump with complex impeller," *Journal of Thermal Science*, vol. 20, pp. 47–52, Feb 2011.

[34] Y. S, Z. J, T. Y, Y. J, and F. Y, "Research on the design method of the centrifugal pump with splitter blades," *ASME. Fluids Engineering Division Summer Meeting*, vol. 1, pp. 107–120, 2009.

[35] L. Wen-Guang, "Blade exit angle effects on performance of a standard industrial centrifugal oil pump," *Journal of Applied Fluid Mechanics*, vol. 4, pp. 105–119, 2011.

[36] W. Li, "Effect of exit blade angle, viscosity and roughness in centrifugal pumps investigated by cfd computation," 2011.

[37] M. Patel and A. Doshi, "Effect of impeller blade exit angle on the performance of centrifugal pump," *International Journal of Emerging Technology and Advanced Engineering,*, vol. 3, pp. 702–709, 2013.

[38] E. Bacharoudis, A. Filios, M. Mentzos, and D. Margaris, "Parametric study of a centrifugal pump impeller by varying the outlet blade angle," *Open Mechanical Engineering Journal*, vol. 2, pp. 75–83, 2008.

[39] M. H. S. Fard and F. Boyaghchi, "Studies on the influence of various blade outlet angles in a centrifugal pump when handling viscous fluids," *American Journal of Applied Sciences*, vol. 4, pp. 718–724, 2007.

[40] J. Skrzypacz and M. Bieganowski, "The influence of micro grooves on the parameters of the centrifugal pump impeller," *International Journal of Mechanical Sciences*, 2017.

[41] K. P. S. Chakraborty and B. Roy, "Numerical analysis on effects of blade number variations on performance of centrifugal pumps with various rotational speeds," *International Journal of Current Engineering and Technology*, vol. 2, pp. 143–152, 2012.

[42] H. Liu, Y. Wang, S. Yuan, M. Tan, and K. Wang, "Effects of blade number on characteristics of centrifugal pumps," *Chinese Journal of Mechanical Engineering*, vol. 23, pp. 742–747, 2010.

[43] K. Rababa, "The effect of blades number and shape on the operating characteristics of groundwater centrifugal pumps," *European Journal of Scientific Research*, vol. 52, pp. 243–251, 2011.

[44] T. M, L. H, Y. S, W. Y, and W. K, "Effects of blade outlet width on flow field and characteristic of centrifugal pumps," *ASME. Fluids Engineering Division Summer Meeting*, vol. 1, pp. 243–251, 2009.

[45] L. Zhou, W. Shi, and S. Wu, "Performance optimization in a centrifugal pump impeller by orthogonal experiment and numerical simulation," *Advances in Mechanical Engineering*, vol. 5, p. 385809, 2013.

[46] E. A. Ahmmed, "Study of flow field in a radial vaned impeller of a centrifugal pump & its effect on pump performance," *Mechanical Power & Energy*, 2015.

[47] M. S. Hussien, A. H. Lotfy, H. M. Abdalla, and I. Saleh, "Optimum slot size and location in a radial vane impeller for better centrifugal pump performance," *Conference on Aerospace Sciences & Aviation Technology*, 2001.

[48] C. Hongxun, L. Weiwei, J. Wen, and W. Peiru, "Impellers of low specific speed centrifugal pump based on the draughting technology," *IOP Conference Series: Earth and Environmental Science*, vol. 12, no. 1, p. 012018, 2010.

[49] Y. H. Z. W. S. Z. J. L. Y. Chen, "Modeling and multi-objective optimization of double suction centrifugal pump based on kriging meta-models," *Avanced in Engineering Software*, 2015.

[50] S. Derakhshan, M. Pourmahdavi, E. Abdolahnejad, A. Reihani, and A. Ojaghi, "Numerical shape optimization of a centrifugal pump impeller using artificial bee colony algorithm," *Computers & Fluids*, vol. 81, pp. 145–151, 2013.

[51] D. V. L. d'Agostino, A. Pasini, "A reduced order model for preliminary design and performance prediction of tapered inducers: Comparison with numerical simulations," 2008.

[52] C. Wang, W. Shi, X. Wang, X. Jiang, Y. Yang, W. Li, and L. Zhou, "Optimal design of multistage centrifugal pump based on the combined energy loss model and computational fluid dynamics," *Applied Energy*, vol. 187, pp. 10 – 26, 2017.

[53] "Api standard 610: Centrifugal pumps for petroleum heavy duty chemical and gas industry services," 2004.

[54] H. Ramos and A. Borga, "Pumps as turbines: an unconventional solution to energy production," *Urban Water*, vol. 1, no. 3, pp. 261 – 263, 1999.

[55] A. Williams, "Pumps as turbines for low cost micro hydro power," *Renewable Energy*, vol. 9, no. 1, pp. 1227 – 1234, 1996. World Renewable Energy Congress Renewable Energy, Energy Efficiency and the Environment.

[56] B. Orchard and S. Klos, "Pumps as turbines for water industry," *World Pumps*, vol. 2009, no. 8, pp. 22 – 23, 2009.

[57] N. R. Lueneburg R, "Hydraulic power recovery turbines," 1995.

[58] O. E. BALJE, "Turbomachines - a guide to design, selection, and theory," pp. 513 p : ill , 23 cm (BD0000QO: photocopies), 1981.

[59] S. V. Jain and R. N. Patel, "Investigations on pump running in turbine mode: A review of the state-of-the-art," *Renewable and Sustainable Energy Reviews*, vol. 30, pp. 841–868, feb 2014.

[60] V. G., "Deviazione della corrente relative nelle giranti delle turbine Francis," *L'Energia Elettrica*, 1972.

[61] G. Shi, X. Liu, J. Yang, S. Miao, and J. Li, "Theoretical research of hydraulic turbine performance based on slip factor within centripetal impeller," *Advances in Mechanical Engineering*, vol. 7, no. 7, p. 1687814015593864, 2015.

[62] C. E. Brennen and N. York, "Cavitation and Bubble Dynamics," 1995.

[63] C. E. Brennen, "Fundamentals of Multiphase Flows,"

[64] V. Mikhail, I. I. Zapryagaev, K. S. Pervunin, and D. M. Markovich, "Cavitating flow control through continuous tangential mass injection on a 2d hydrofoil at a small attack angle," *International symposium IPHT*, 2016.

[65] J. Huang, C. Yu, Y. Wang, C. Xu, and C. Huang, "Passive control of cavitating flow around an axisymmetric projectile by using a trip bar," *Theoretical and Applied Mechanics Letters*, vol. 7, no. 4, pp. 181 – 184, 2017.

[66] H. G. Weller, G. Tabor, H. Jasak, and C. Fureby, "A tensorial approach to computational continuum mechanics using object-oriented techniques," *Computers in Physics*, vol. 12, no. 6, pp. 620–631, 1998.

[67] H. Jasak, "Error analysis and estimation for finite volume method with applications to fluid flow," tech. rep., 1996.

[68] R. Henrik, "Computational fluid dynamics of dispersed two-phase flows at high phase fractions," tech. rep., PhD thesis, Department of Mechanical Engineering, University of London, Technology and Medicine, 2002.

[69] G. Caramia, "Numerical simulation of hydrodynamic lubrication in micro-textured surfaces," tech. rep., PhD thesis, Department of Mechanics, Mathematics and Management, 2016.

[70] S. Patankar and D. Spalding, "A calculation procedure for heat, mass and momentum transfer in three-dimensional parabolic flows," *International Journal of Heat and Mass Transfer*, vol. 15, no. 10, pp. 1787 – 1806, 1972.

[71] S. Shah, S. Jain, R. Patel, and V. Lakhera, "Cfd for centrifugal pumps: A review of the state-of-the-art," *Procedia Engineering*, vol. 51, pp. 715 – 720, 2013.

[72] G. J, F. J, B. E, and S. C., "Numerical Simulation of the Dynamic Effects Due to Impeller-Volute Interaction in a Centrifugal Pump," *ASME. J. Fluids Eng. 2002*, vol. 124(2):348-355, 2002.

[73] T. H. Wang HH, "Fundamental Analysis on Rotor-Stator Interaction in a Diffuser Pump by Vortex Method," *ASME. J. Fluids Eng. 2001*, vol. 123(4):737-747, 2001.

[74] H. Nilsson, "Evaluation of openfoam for cfd of turbulent flow in water turbines," *23rd IAHR Symposium*, 2006.

[75] *Kye B., Park K., Choi H., Lee M., Kim J.H., Flow characteristics in a volute-Type centrifugal pump using large eddy simulation, 10th International Symposium on Turbulence and Shear Flow Phenomena (TSFP10), Chicago, USA, July, 2017.*

[76] R. Mittal and G. Iaccarino, "Immersed boundary methods," *Annual Review of Fluid Mechanics*, vol. 37, pp. 239–261, 2005. cited By 1483.

[77] A. Posa, A. Lippolis, R. Verzicco, and E. Balaras, "Large-eddy simulations in mixed-flow pumps using an immersed-boundary method," *Computers & Fluids*, vol. 47, no. 1, pp. 33 – 43, 2011.

[78] *M. Specklin, Y. Delauré, A versatile immersed boundary method for pump design, Pump Users International Forum, September, 2016.*

[79] F. R. Menter, "Two-equation eddy-viscosity turbulence models for engineering applications," *American Institute of Aeronautics and Astronautics*, 1994.

[80] P. H. J. Bardina and T. Coakley, "Turbulence modeling validation, testing, and development," *NASA Technical Memorandum, vol. 110446*, 1997.

[81] S. Barre, J. Rolland, G. Boitel, E. Goncalves, and R. F. Patella, "Experiments and modeling of cavitating flows in venturi: attached sheet cavitation," *European Journal of Mechanics - B/Fluids*, vol. 28, no. 3, pp. 444 – 464, 2009.

[82] B. Stutz and J. L. Reboud, "Experiments on unsteady cavitation," *Experiments in Fluids*, vol. 22, pp. 191–198, Jan 1997.

[83] R. E. Cervone A, Bramanti C and d'Agostino L., "Thermal cavitation experiments on a naca 0015 hydrofoil," *ASME. J. Fluids Eng.*, vol. 128, no. 2, pp. 326–331, 2009.

[84] M. Dular, R. Bachert, B. Stoffel, and B. Širok, "Experimental evaluation of numerical simulation of cavitating flow around hydrofoil," *European Journal of Mechanics - B/Fluids*, vol. 24, no. 4, pp. 522 – 538, 2005.

[85] M. Morgut and E. Nobile, "Numerical predictions of cavitating flow around model scale propellers by cfd and advanced model calibration," *International Journal of Rotating Machinery*, 2012.

[86] V. H. Hidalgo, X. W. Luo, X. Escaler, J. Ji, and A. Aguinaga, "Numerical investigation of unsteady cavitation around a naca 66 hydrofoil using openfoam," *IOP Conference Series: Earth and Environmental Science*, vol. 22, no. 5, p. 052013, 2014.

[87] T. Capurso, M. Lopez, M. Lorusso, M. Torresi, G. Pascazio, S. Camporeale, and B. Fortunato, "Numerical investigation of cavitation on a naca0015 hydrofoil by means of openfoam," *Energy Procedia*, vol. 126, pp. 794 – 801, 2017. ATI 2017 - 72nd Conference of the Italian Thermal Machines Engineering Association.

[88] S. J and S. GH, "Unsteady cavitating flow - a new cavitation model based on a modified front capturing method and bubble dynamics," *In Fluids Engineering Summer Conference, Proceedings of FEDSM*, 2000.

[89] J. U. Brackbill, D. B. Kothe, and C. Zemach, "A continuum method for modeling surface tension," *J. Comput. Phys.*, vol. 100, pp. 335–354, June 1992.

[90] R. F. Kunz, D. A. Boger, D. R. Stinebring, T. S. Chyczewski, J. W. Lindau, H. J. Gibeling, S. Venkateswaran, and T. Govindan, "A preconditioned navier–stokes method for two-phase flows with application to cavitation prediction," *Computers & Fluids*, vol. 29, no. 8, pp. 849 – 875, 2000.

[91] C. L. MARKLE, "Computational modeling of the dynamics of sheet cavitation," *Proc. 3rd International Symposium on Cavitation*, vol. 2, pp. 307–311, 1998.

[92] F. A. Asnaghi A and B. R. E, "Numerical simulation of cavitating flows using openfoam," *18th Numerical Towing Tank Symposium*, 2015.

[93] J. Fürst, "Numerical simulation of transitional flows with laminar kinetic energy," 2013.

[94] W. D and C. D., "A three-equation eddy-viscosity model for reynolds-averaged navier–stokes simulations of transitional flow," *ASME. J. Fluids Eng.*, 2008.

[95] E. Goncalvès Da Silva and E. Goncalvès, "Numerical Study of Unsteady Turbulent Cavitating Flows," *European Journal of Mechanics-B/Fluids*, vol. 30, 2011.

[96] B. Charrière, J. Decaix, and E. Goncalvès, "A comparative study of cavitation models in a Venturi flow," *European Journal of Mechanics B/Fluids*, vol. 49, pp. 287–297, 2015.

[97] J. Decaix and E. Goncalvès, "Time-dependent simulation of cavitating flow with k l turbulence models," *International Journal for Numerical Methods in Fluids*, vol. 68, no. 8, pp. 1053–1072.

[98] "Patent - gb18343," 1900.

[99] "Patent - jp2012132368," 2012.

[100] "Patent - us1003542," 1911.

[101] "Patent - us2791183."

[102] K. ltd Patent JPS58155298A, "Impeller for double suction pump," 1983.

[103] "Patent - jph0687694u," 1994.

[104] E. J. Paul DeGarmo T Black Ronald A Kohser Solutions Manual by Barney E Klamecki, "Solutions Manual to Accompany MATERIALS AND PROCESS IN MANUFACTURING Ninth Edition," tech. rep., 2003.

[105] S. Kalpakjian, Serope Schmid, "Manufacturing Engineering and Technology (5th ed.)," tech. rep., 2006.

[106] "High efficiency double suction impeller," 2017.

[107] "Openfoam - checkmesh," 2015.

[108] P. J. Roache, "Perspective: A method for uniform reporting of grid refinement studies," *Journal of Fluids Engineering*, vol. 116(3):405, pp. 405–413, 1994.

[109] G. HALLER, "An objective definition of a vortex," *Journal of Fluid Mechanics*, vol. 525, p. 1–26, 2005.

[110] "Houses of parliament, parliamentary office of science and technology, carbon footprint of electricity generation," number 383, June 2011.

[111] "International energy agency, co2 emissions from fuel combustion 2017 overview," 2017.

[112] M. Binama, W.-T. Su, X.-B. Li, F.-C. Li, X.-Z. Wei, and S. An, "Investigation on pump as turbine (PAT) technical aspects for micro hydropower schemes: A state-of-the-art review," *Renewable and Sustainable Energy Reviews*, vol. 79, no. C, pp. 148–179, 2017.

[113] A. Morabito, J. Steimes, O. Bontems, G. A. Zohbi, and P. Hendrick, "Set-up of a pump as turbine use in micro-pumped hydro energy storage: a case of study in froyennes belgium," *Journal of Physics: Conference Series*, vol. 813, no. 1, p. 012033, 2017.

[114] G. Ardizzon, G. Cavazzini, and G. Pavesi, "A new generation of small hydro and pumped-hydro power plants: Advances and future challenges," *Renewable and Sustainable Energy Reviews*, vol. 31, no. C, pp. 746–761, 2014.

[115] S. Rehman, L. M. Al-Hadhrami, and M. M. Alam, "Pumped hydro energy storage system: A technological review," *Renewable and Sustainable Energy Reviews*, vol. 44, pp. 586 – 598, 2015.

[116] O. Paish, "Micro-hydropower: Status and prospects," *Proceedings of the Institution of Mechanical Engineers, Part A: Journal of Power and Energy*, vol. 216, no. 1, pp. 31–40, 2002.

[117] J. Y. Xiaohui W and Z. X, "Study on Slip Phenomenon of Pumps As Turbines in Different Working Conditions," *ASME. Fluids Engineering Division Summer Meeting, Volume 1A, Symposia: Keynotes; Advances in Numerical Modeling for Turbomachinery Flow Optimization; Fluid Machinery; Industrial and Environmental Applications of Fluid Mechanics; Pumping Machinery*, 2017.

[118] S.-S. Yang, S. Derakhshan, and F.-Y. Kong, "Theoretical, numerical and experimental prediction of pump as turbine performance," *Renewable Energy*, vol. 48, no. C, pp. 507–513, 2012.

[119] S. Derakhshan and A. Nourbakhsh, "Experimental study of characteristic curves of centrifugal pumps working as turbines in different specific speeds," *Experimental Thermal and Fluid Science*, vol. 32, no. 3, pp. 800 – 807, 2008.

[120] S. Barbarelli, M. Amelio, and G. Florio, "Predictive model estimating the performances of centrifugal pumps used as turbines," *Energy*, vol. 107, no. C, pp. 103–121, 2016.

[121] M. Stefanizzi, T. Capurso, M. Torresi, G. Pascazio, S. Ranaldo, S. M. Camporeale, B. Fortunato, and R. Monteriso, "Development of a 1-d performance prediction model for pumps as turbines," *Proceedings*, vol. 2, p. 682, Jul 2018.

[122] A. Busemann, "Das förderhöhenverhältnis radialer kreiselpumpen mit logarithmisch-spiraligen schaufeln," *ZAMM - Journal of Applied Mathematics and Mechanics / Zeitschrift für Angewandte Mathematik und Mechanik*, vol. 8, no. 5, pp. 372–384.

[123] S. A., "Dampf und gas-turbinen,"

[124] M. Stefanizzi, M. Torresi, B. Fortunato, and S. Camporeale, "Experimental investigation and performance prediction modeling of a single stage centrifugal pump operating as turbine," *Energy Procedia*, vol. 126, pp. 589 – 596, 2017. ATI 2017 - 72nd Conference of the Italian Thermal Machines Engineering Association.

[125] Y. Aït Bouziad, "Physical modelling of leading edge cavitation computational methodologies and application to hydraulic machinery," p. 209, 2005.